Preparation of Electrocatalysts for Oxygen Reduction and Water Oxidation Reactions, and Construction of Photoanodes with Covalently Bonded Chromophores

by

Chao Wang

A thesis submitted in partial fulfillment of the requirements for the degree of

Doctor of Philosophy

Department of Chemistry
University of Alberta

© Chao Wang, 2018

Abstract

Renewable fuels are essential to meet the future energy demands of our society and to alleviate the impact of the anthropogenic CO_2 on the environment. Energy conversion devices like fuel cells, water electrolyzers, and photoelectrochemical cells are the key components in the transformation to a renewable energy dependent society. This dissertation describes the synthesis and characterization of active electrocatalysts for fuel cells and water electrolyzers, as well as a novel method to prepare stable chromophore–semiconductor photoelectrodes.

Due to the sluggish kinetics at the fuel cell cathode, active oxygen reduction reaction electrocatalysts are required. The first part of the thesis describes the preparation and the oxygen reduction activity of the electrodeposited, conformal Pt overlayers on glancing angle deposited Ni nanopillar catalysts that could potentially be applied in fuel cells. Up to 30-fold enhancement in the Pt mass-normalized oxygen reduction reaction activity was observed compared to Pt directly deposited on glassy carbon substrates.

Water electrolysers are crucial devices in the long-term storage of sustainable energy as hydrogen. The water oxidation reaction at the anode of the electrolysers is kinetically sluggish, and requires active electrocatalysts. A simple bench-top aqueous synthetic method was developed to prepare extremely active water oxidation electrocatalysts for water electrolyzers. The $Ir_{0.89}Ni_{0.11}$ and $Ir_{0.89}Cu_{0.11}$ hydrous oxide nanoparticles prepared using this method are among the most active and stable water oxidation catalysts in acid published to date. The $Ni_{0.75}Fe_{0.25}$ layered double hydroxides prepared are among the most active alkaline water oxidation catalysts. The electrocatalysts were characterized

using X-ray diffraction, transmission electron microscopy, cyclic voltammetry, and X-ray photoelectron spectroscopy. Mechanisms for the water oxidation activities were proposed.

Photocatalytic water oxidation and carbon dioxide reduction reactions favors the use of alkaline conditions, but common anchoring groups, like phosphonic ester groups and carboxylic ester groups, between the visible-light chromophores and the semiconductor surfaces are only stable in acidic solutions. In this dissertation, Ru- and Ir- chromophores on semiconductor surfaces were prepared with a novel diazonium reduction and metalation method, and the bonding was between the C5 of the 1,10-phenathroline ligand of the chromophores and the ITO or TiO_2 surfaces. The chromophore–semiconductor photoelectrodes prepared using this method were active and relatively stable to photoelectrochemical oxidation of hydroquinone and triethylamine under neutral and basic conditions and potentially can be paired with electrocatalysts to carry out the photocatalytic water oxidation and carbon dioxide reduction reactions.

Preface

Chapter 1 is the introductory Chapter on the fuel cell and water electrolyzer technology.

Chapter 2 has been published as

Xu, S.; Wang, C.; Francis, S. A.; Tucker, R. T.; Sorge, J. B.; Moghaddam, R. B.; Brett, M. J.; Bergens, S. H. *Electrochim. Acta* **2015**, *151*, 537.

Xu, S. and I were responsible for the electrochemical preparation of the samples and the data collection. Dr. Francis, S. A. carried out preliminary studies and assisted in the manuscript preparation. Dr. Tucker, R. T. and Dr. Sorge, J. B. carried out the substrate preparation and the spectroscopic characterization. Dr. Moghaddam, R. B. assisted in the manuscript composition and the data analysis. Dr. Brett, M. J. was the collaborating supervisor, and Dr. Bergens, S. H. was our supervisor.

Chapter 3 has been published as

Wang, C.; Moghaddam, R. B.; Sorge, J. B.; Xu, S.; Brett, M. J.; Bergens, S. H. *Electrochim. Acta* **2015**, *176*, 620.

I was the first author and was responsible for the sample preparation and characterization, the data collection and analysis, and the manuscript composition. Dr. Moghaddam, R. B. contributed to the manuscript composition and the data analysis. Dr. Sorge, J. B. carried out the substrate preparation and the spectroscopic characterization. Xu, S. assisted in the data collection. Dr. Brett, M. J. was the collaborating supervisor, and Dr. Bergens, S. H. was our supervisor.

Chapter 4 has been published as

Moghaddam, R. B.; Wang, C.; Sorge, J. B.; Brett, M. J.; Bergens, S. H. *Electrochem.*

Commun. **2015**, *60*, 109.

Dr. Moghaddam, R. B. contributed in the concept formation, the manuscript composition, the data collection, and analysis. I was responsible for the data collection and analysis, and the characterization of the samples. Dr. Sorge, J. B. carried out the spectroscopic characterization. Dr. Brett, M. J. was the collaborating supervisor, and Dr. Bergens, S. H. was our supervisor.

Chapter 5 has been published as

Wang, C.; Moghaddam, R. B.; Bergens, S. H. *J. Phys. Chem. C* **2017**, *121*, 5480.

I was the first author and was responsible for the sample preparation and characterization, the data collection and analysis, and the manuscript composition. Dr. Moghaddam, R. B. contributed in the manuscript editing. Dr. Bergens, S. H. was our supervisor.

Chapter 6 has been published as

Wang, C.; Moghaddam, R. B.; Brett, M. J.; Bergens, S. H. *ACS Sustainable Chem. Eng.* **2017**, *5*, 1106.

I was the first author and was responsible for the sample preparation and characterization, the data collection and analysis, and the manuscript composition. Dr. Moghaddam, R. B. contributed in the data analysis and the manuscript editing. Dr. Brett, M. J. was the collaborating supervisor, and Dr. Bergens, S. H. was our supervisor.

Chapter 7 has been published as

Wang, C.; Amiri, M.; Endean, R. T.; Martinez Perez, O.; Varley, S.; Rennie, B.; Rasu, L.; Bergens, S. H. *ACS Appl. Mater. Interfaces* **2018**, DOI:10.1021/acsami.8b06605.

I was the first author and was responsible for the sample preparation and characterization, the data collection and analysis, and the manuscript composition. Dr.

Mona Amiri assisted in the data collection, the sample preparation and characterization, and the manuscript editing. Riley T. Endean, Benjamin E. Rennie, and Dr. Loorthuraja Rasu synthesized the Ru- and Ir- complexes. Octavio Martinez Perez and Samuel Varley assisted in the data collection. Dr. Bergens, S. H. was our supervisor.

Chapter 8 summarizes the findings of this thesis and provides future directions of the research.

Acknowledgements

I would like to thank Dr. Steven H. Bergens, who supervised me and impassioned me with encouragement and confidence in facing problems in all aspects of my life. Enjoyable was the time passed in discussing mechanisms behind the observed phenomena and questing for possible solutions with him. Also, I want to thank my supervisory committee: Dr. Arthur Mar, Dr. Mark McDermott, and Dr. Aicheng Chen. My thanks also go to Dr. Michael Brett, who gave me support and guidance during my projects. I would like to extend my gratitude to Dr. Anna Jordan who helped me in editing this dissertation.

The professors, staff and technicians in the department of chemistry, earth science, electrical and computer engineering, and in the National Institute for Nanotechnology, including Peng Li, Anqiang He, Shihong Xu, Nancy Zhang, Jian Chen, Jason Dibbs, Scott Stelck, Bernie Hippel, and Guangcheng Chen provided immediate help with my requests on sample analysis, chemical purchasing, and glassware design. I would like to thank them as well.

I thank my friends from the research group for their relentless help, support, advice, discussions, and friendship over the past five years, including Dr. Reza Moghaddam, Dr. Mona Amiri, Dr. Loorthuraja Rasu, Suneth Kalapugama, Dr. Jaya Pal, Lan Truong, Prabin Nepal, Shuai Xu, Octavio Martinez Perez, and Riley Endean. My thanks extend to my friends Dr. Jason Sorge, Xian Luo, Chencai Wang, Lingju Meng, and Yunong Li who supported me during my studies and research.

At last, I would love to thank my family and my girlfiend Miao Geng for their unceasing encouragement during the past five years, especially my parents, Zhixia Bi and

Xiaofang Wang, for their support throughout the years. Their words guide me to fathom the profundity of humanity and love, impinging the paradoxical pessimistic but idealistic perspectives upon my life. I love them all, and I am blessed to have them in life.

Table of Contents

List of Tables

List of Figures

List of Schemes

List of Abbreviations

® – registered trademark

AEM – anion exchange membrane

AFC – alkaline fuel cell

ALD – atomic layer deposition

AWE – alkaline water electrolyzer

BE – binding energy

BET – Brunauer–Emmett–Teller

CE – counter electrode

CF – carbon fiber paper

CNT – carbon nanotube

CV – cyclic voltammetry

DEMS – differential electrochemical mass spectroscopy

DFT – density function theory

DLFC – direct liquid fuel cell

DMFC – direct methanol fuel cell

DOS – density of states

DSPEC – dye-sensitized photoelectrochemical cell

EASA – electrochemically active surface area

EDS – energy-dispersive X-ray spectroscopy

EXAFS – extended X-ray absorption fine structure

FC – fuel cell

FTIR – Fourier-transform infrared spectroscopy

FTO – fluorine-doped tin oxide

GC – glassy carbon

GLAD – glancing angle deposition

HO-np – hydrous oxide nanoparticles

HOR – hydrogen oxidation reaction

HRTEM – high resolution transmission electron microscopy

ICP–MS – inductively coupled plasma mass spectrometry

IPCE – incident photon-to-current conversion efficiency

ITO – indium tin oxide

JCPDS – joint committee on powder diffraction standards

LC – ligand centered

LDH – layered double hydroxides

LLCT – ligand-to-ligand charge transfer

LUMO – lowest unoccupied molecular orbital

LSV – linear sweep voltammetry

MCFC – molten carbonate fuel cell

MEA – membrane electrode assembly

ML – monolayer

MLCT – metal-to-ligand charge transfer

NHE – normal hydrogen electrode

ORR – oxygen reduction reaction

PAFC – phosphoric acid fuel cell

PEC – photoelectrochemical cell

PEM – proton exchange membrane (polymer electrolyte membrane)

PEMFC – proton exchange membrane (polymer electrolyte membrane) fuel cell

PEMWE – proton exchange membrane (polymer electrolyte membrane) water electrolyzer

PMMA – poly(methylmethacrylate)

PSS – polystyrene sulfonate

PTFE – sulfonated polytetrafluoroethylene

PVD – physical vapor deposition

RDS – rate-determining step

RFC – reversible fuel cell

rGO – reduced graphene oxide

RDE – rotating disk electrode

RHE – reversible hydrogen electrode

RRDE – rotating ring-disk electrode

SC – semiconductor

SCE – saturated calomel electrode

SEM – scanning electron microscopy

SERS – surface-enhanced Raman spectroscopy

SOFC – solid oxide fuel cell

SOWE – solid oxide water electrolyzer

TEA – triethylamine

TEM – transmission electron microscopy

TOF – turnover frequency

UPS – ultraviolet photoelectron spectroscopy

UV–vis – ultraviolet–visible spectroscopy

WE – working electrode

WOC – water oxidation catalyst

WOR – water oxidation reaction

XANES – X-ray absorption near edge structure

XPS – X-ray photoelectron spectroscopy

XRD – X-ray diffraction

YSZ – Y_2O_3-stablized ZrO_2

Chapter 1 Introduction

1.1 Fuel cells

1.1.1 Definition

FCs (**f**uel **c**ells) are devices that continuously convert chemical energy stored in fuels and oxygen into electrical energy at constant temperature. A single fuel cell consists of an anode where the fuel is oxidized, a cathode where the oxidant (usually O_2) is reduced, and an electrolyte between the two electrodes. Unlike batteries, fuel cells have the distinguishing feature that no oxidant or reductant is stored, rather, with a continuous supply of the oxidant and reductant, fuel cells can operate infinitely long.[1]

Figure 1.1 shows the working principles of a hydrogen–oxygen fuel cell. The fuel (H_2) is oxidized at the anode, forming H^+ and electrons. The electrons move through the external circuit to the cathode, where the oxidant (O_2) is reduced. The proton moves through the electrolyte to the cathode to make water from reduction of O_2. The electrons that travel through the external circuit can be converted to different forms of energy, like heat, power, or magnetism, depending on the device positioned.

Since fuel cells can produce electricity directly from chemical energy stored in the fuels, they are theoretically more efficient than combustion engines. However, unlike combustion engines, fuel cells can be all solid state, meaning no moving parts, which renders the potential for silent, highly reliable, and long-lasting systems.[2] Another big advantage of the fuel cells is their low impact on the environment. Pollutants like oxidized

sulfur and nitrogen are not found since zero sulfur fuels are used and the operating temperature is not high enough to form nitrogen oxides for most of the fuel cells.

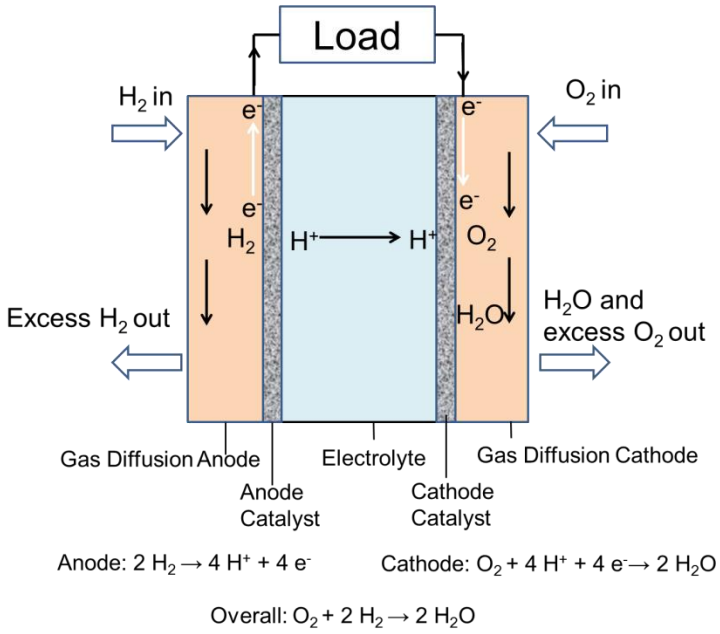

Figure 1.1 Schematic illustration of a hydrogen–oxygen fuel cell (not drawn to scale).

1.1.2 Working principles

For a H_2–O_2 fuel cell, the maximum amount of electrical work obtained from a galvanic cell is equal to the change in Gibbs free energy of the reaction (ΔG^o), which can be expressed by eq 1.1.

$$\Delta G^o = -nFE^o_{cell} \quad 1.1$$

where n is the number of electrons transferred and F is the Faraday constant (96485 C mol^{-1}). E^0_{cell} is the potential difference between two electrodes under standard conditions. E^o_{cell} = 1.23 V for a H_2–O_2 fuel cell, and ΔG^o = -237.4 kJ mol^{-1}.

The enthalpy change (ΔH^o) under standard conditions is the entire heat released by the reaction at constant pressure, and it can be calculated by eq 1.2.

$$\Delta H^{o} = \Delta H^{o}_{f,H_2O,l} - \Delta H^{o}_{f,H_2} - \frac{1}{2}\Delta H^{o}_{f,O_2} = \text{- 285.8 kJ mol}^{-1} \quad (1.2)$$

The thermal efficiency of an energy conversion device is defined as the amount of useful energy produced relative to the change in energy that is released when a fuel reacts with an oxidant.[3] Therefore, the theoretical maximum thermal efficiency of a H_2–O_2 fuel cell under standard conditions is given by eq 1.3.

$$\varepsilon = \frac{\Delta G^0}{\Delta H^0} \times 100 = 83\% \quad (1.3)$$

1.1.3 History

The first fuel cell was demonstrated in 1839 by Sir William Grove. The device converted hydrogen and oxygen into water while supplying electricity. He referred to it as a gas battery and later named as a fuel cell.[4]

Although the fuel cell technology was attractive when it was invented, the interest in fuel cells declined, and the research in this area remained relatively small in scale as the efficiency of other energy conversion systems kept increasing.

In the 1950s, General Electric invented the proton exchange membrane, and in 1959, Francis Bacon demonstrated a 5 kW alkaline fuel cell. Starting in 1962, the United States space program (Gemini and Apollo missions) first put fuel cells into practical application. The Apollo lunar mission used alkaline hydrogen–oxygen fuel cells to provide power for life support, guidance and communication, and as a source of scalable water. Fuel cells fit into the mission because they continuously supplied high power (1 kW) over 14 days, and they were lightweight.[4]

Interest in fuel cells revived after the mission to the moon. As well, the oil crisis along with the increasing awareness of environment among government, industry, and business in the 1970s prompted the development of alternative energy sources, including fuel cells. In the 1980s, the US Navy commissioned studies into the use of fuel cells in submarines where the highly efficient, zero-emission, and near-silent running features of fuel cells offered considerable operational advantages. In 1983, the Canadian company Ballard began research into fuel cells and became a major manufacturer of stacks and systems for stationary and transport applications in later years.[1]

The last decade has witnessed increasing concerns over energy security, energy efficiency, and carbon dioxide emission. Fuel cells have attracted attention as one of several potential technologies capable of delivering energy efficiently while reducing dependence on fossil fuels. Research on catalysts, electrodes, electrolytes, and system engineering, coupled with better understanding of the mass transport and the diffusion of the reactants and products within the device, flourished.

Starting in 2007, fuel cells became commercially available in a variety of applications. Today, fuel cells are used in stationary power supplies and transportation including automobiles, ships, trains, buses and submarines, depending on their type employed.[5–7]

1.1.4 Types of fuel cells

Depending on the electrolyte used, there are five types of fuel cells, summarized in Table 1.1.

1.1.4.1 Proton exchange membrane fuel cells

PEMFCs (**p**roton **e**xchange **m**embrane **f**uel **c**ells) have several advantages over other FC variants. Their power density is the highest among all types of FCs (500–2500 mW cm^{-2}), and they have a high efficiency and short start-up time compared with other FCs. The fast-start and on-off cycling features make the PEMFCs most suitable for transportation and portable power applications. At present, major car companies have focused exclusively on PEMFCs.

The reactions occurring at the anode and cathode are shown in eqs 1.4 and 1.5.

$$\text{Anode: } 2\ H_2 \rightarrow 4\ H^+ + 4\ e^- \qquad 1.4$$

$$\text{Cathode: } O_2 + 4\ e^- + 4\ H^+ \rightarrow 2\ H_2O \qquad 1.5$$

The PEM (**p**roton **e**xchange **m**embrane) is usually Nafion® by DuPont, which is a sulfonated polytetrafluoroethylene based polymer. Different types of polymer electrolyte membranes have been reviewed for fuel cell applications.[8] Generally speaking, Nafion® is more resistant towards degradation under both an oxidizing and a reducing environment than the previously used polystyrene sulfonate polymer because the C–F bonds are stronger than the C–H bonds; the bond dissociation energy is 513.8 kJ mol^{-1} for C–F versus 338.4 kJ mol^{-1} for C–H.[9] Figure 1.2 shows the structures of the PSS (**p**oly**s**tyrene **s**ulfonate) and sulfonated PTFE (**p**oly**t**etra**f**luoro**e**thylene) based polymer (Nafion®) membranes.

Table 1.1 Comparison of the fuel cell technology

	Electrolyte (Charge carrier)	Operating temperature	Fuel	Efficiency	Application
PAFC	> 85% H_3PO_4 (H^+)	150–200 °C	H_2	40%	Distributed generation
MCFC	Carbonate (CO_3^{2-})	600–700 °C	H_2, CH_4	50%	Distributed generation Electricity utility
SOFC	Yttria-stabilized zirconia (O^{2-})	600–1000 °C	H_2, CH_4, CO	60%	Auxiliary power Electricity utility Distributed generation
AFC	Aqueous KOH (OH^-)	60–220 °C	H_2	60%	Space military Subsea power
PEMFC	Perfluorosulfonic acid (H^+)	80–120 °C	H_2, CH_3OH	60%	Backup Portable power Transport Distributed generation

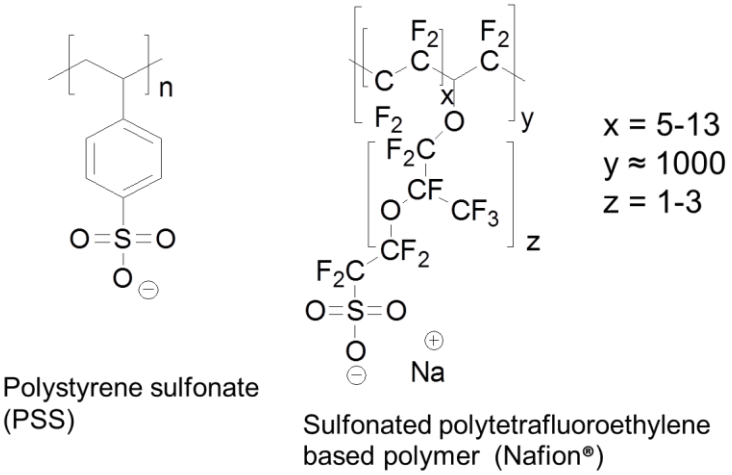

Figure 1.2 Structures of polystyrene sulfonate polymers and Nafion®.

The PEM must be hydrated to maintain adequate proton conductivity, therefore, the operating temperature ranges from 80 to 120 ^{o}C. The optimum operating temperature depends strongly on the membrane and humidification. During the operation, water is generated at the cathode, and the humidity should be balanced to avoid flooding at the cathode.[10]

On either side of the membrane, a thin layer of carbon-supported platinum-based catalysts was coated using the hot-press method. Due to the relatively low operating temperature, platinum-based catalysts are the only practical choice. Considerable efforts have been made to decrease the loading of Pt in the electrocatalysts, especially in the cathode catalysts since the ORR (**o**xygen **r**eduction **r**eaction) at the cathode is much slower compared with the HOR (**h**ydrogen **o**xidation **r**eaction) at the anode. For example, the exchange current density for the ORR is several magnitudes lower than the HOR over Pt in acid (10^{-7} to 10^{-9} A cm^{-2} for the ORR versus 10^{-3} A cm^{-2} for the HOR).[11]

Despite the high cost, another issue associated with the Pt-based catalysts is their

intolerance towards carbon monoxide. A small amount of CO is found often in the H_2 fuel, especially when using the hydrogen from reformed hydrocarbons or alcohols. CO binds strongly to the surface of Pt. To improve the CO tolerance of Pt-based catalysts, oxophilic transition metals, such as Ni, Ru, Co, and Sn, are used.[12–14] With these bimetallic catalysts, CO is oxidized easily at Pt by the adsorbed oxygenated species of the adjacent oxophilic metal. Moreover, the adsorption energy of CO on Pt can be changed through the electronic and lattice-strain effects owing to the second metal. The details of these effects are discussed in Section 1.1.5.1.[13,15] In addition, Pt catalysts tend to migrate on the surface and agglomerate, leading to decreased performance.[16]

Interested readers are directed to other excellent review articles on PEMFCs, including applications,[17–20] material degradation,[21] catalysts,[22] and system control.[23]

1.1.4.2 Alkaline fuel cells

AFCs (**a**lkaline **f**uel **c**ells) were the first fuel cells applied to commercial use. They were the primary power source used in National Aeronautics and Space Administration flights between the 1960s and 1970s.[1] In contrast with the PEMFCs, the electrolyte for AFCs is 85 wt% KOH, and OH^- is the charge carrier that moves from the cathode to the anode. The anode and cathode reactions are shown in eqs 1.6 and 1.7.

$$\text{Anode: } 2\ H_2 + 4\ OH^- \rightarrow 4\ H_2O + 4\ e^- \qquad 1.6$$

$$\text{Cathode: } O_2 + 4\ e^- + 2\ H_2O \rightarrow 4\ OH^- \qquad 1.7$$

Water is consumed at the cathode and is produced twice as fast at the anode. The excess water at the anode needs to be removed, or it will dilute the KOH electrolyte, causing degradation in performance. The ORR is faster in alkaline solutions, and

non-noble metal catalysts, like nickel, manganese oxide, or cobalt and iron macrocycles, can be used.[24,25] Since AFCs do not use Pt catalysts, CO poisoning is not an issue for AFCs.

One major issue with AFCs is that the performance is degraded by the reaction of carbon dioxide with the KOH electrolyte, as described by eqs 1.8 and 1.9.

$$CO_2 + 2\ OH^- \rightarrow H_2O + CO_3^{2-} \quad 1.8$$

$$CO_2 + OH^- \rightarrow HCO_3^- \quad 1.9$$

The resulting carbonate and bicarbonate salts reduce the conductivity of the electrolyte, and the precipitation of these salts within the pores of the electrodes hinders the mass transport. Moreover, the precipitates can damage the electrodes by inducing mechanical strain. These issues can be mitigated, partially, by using CO_2 scrubbers and resupplying with fresh KOH electrolytes, but both methods involve additional cost.[26,27]

Recent advances in AEMs (**a**nion **e**xchange **m**embranes) have led to a surge in AFC research.[28,29] Primarily, AEMs consist of immobilized cations, rather than mobile solution phase cations, precluding the formation of carbonate or bicarbonate precipitates. Typically, the immobilized cation is a quaternary ammonium group. However, AEMs are generally low in OH^- conductivity compared with PEMs, and the cationic groups are susceptible to attack by OH^-, especially at elevated temperatures, causing degradation of the polymer membrane.[30,31]

1.1.4.3 Solid oxide fuel cells

SOFCs (**s**olid **o**xide **f**uel **c**ells) operate at temperatures higher than 600 ^oC, and special materials for the cell components are required. The common solid ceramic electrolyte

material is YSZ (**Y**$_2O_3$-**s**tablized **Z**rO_2), which is an O^{2-} conductor at high temperatures.[32] The anode and cathode reactions are shown in eqs 1.10 and 1.11.

$$\text{Anode: } 2\ H_2 + 2\ O^{2-} \rightarrow\ 2\ H_2O + 4\ e^- \qquad 1.10$$

$$\text{Cathode: } O_2 + 4\ e^- \rightarrow\ 2\ O^{2-} \qquad 1.11$$

The most common material for a SOFC anode is the nickel-YSZ cement (a mixture of metal and ceramic), with Ni providing conductivity and catalytic activity. The YSZ adds ion conductivity, thermal expansion compatibility, and mechanical stability, while maintaining porosity.[33] Typical cathode materials include lanthanum–strontium manganite, lanthanum–strontium ferrite, lanthanum–strontium cobaltite, and lanthanum–strontium cobaltite ferrite. These materials show good oxidation resistance and high catalytic activity in cathodic environments.[34,35]

The catalysts do not have a CO-poisoning problem (not Pt-based), and CO can be used as a fuel for SOFCs. However, carbon forms by disproportionation of CO at high temperatures, as shown in eq 1.12, leading to a deleterious deposition of carbon on the catalyst surface.[36,37]

$$2\ CO\ \rightarrow\ C + CO_2 \qquad 1.12$$

The high operating temperatures pose challenges involving hardware, sealing, and cell interconnection issues. Mechanical faults, reliability concerns, and thermal expansion matching also need to be addressed well at elevated temperatures. In the absence of proper thermal management, a local higher temperature would cause thermal stresses and failure of the cells, and minor defects in the sealing can lead to fuel leakage and reduction in power density caused by the oxidation of the anode. Advantages of SOFCs include fuel flexibility and their ability to operate in cogeneration systems where high-quality waste

heat is generated for home and industrial use. [38–40]

1.1.4.4 Molten carbonate fuel cells

MCFCs (**m**olten **c**arbonate **f**uel **c**ells) also operate at high temperatures (600–700 ^{o}C), with an electrolyte consisting of a molten mixture of alkali carbonates, Li_2CO_3 and K_2CO_3, immobilized in a $LiO\text{-}AlO_2$ matrix;[41] CO_3^{2-} is the charge carrier. The anode and cathode reactions are shown in eqs 1.13 and 1.14.

$$\text{Anode: } 2\ H_2 + 2\ CO_3^{2-} \rightarrow 2\ H_2O + 2\ CO_2 + 4\ e^- \qquad 1.13$$

$$\text{Cathode: } O_2 + 2\ CO_2 + 4\ e^- \rightarrow 2\ CO_3^{2-} \qquad 1.14$$

CO_2 is produced at the anode and consumed at the cathode. Therefore, MCFC systems must extract CO_2 from the anode and recirculate it to the cathode. The waste steam from the anode is fed into a combustor to burn unreacted fuels in order to avoid mixing of fuels and O_2 at the cathode. The resulting CO_2 and steam are combined with fresh air and are supplied to the cathode. The heat at the combustor can be used to preheat the reactant air, enhancing the efficiency and maintaining the operating temperature of MCFCs.[42]

The catalysts for MCFCs are porous nickel stabilized by a dispersion of alumina or chromium. Nickel tends to dissolve into the electrolyte at the cathode and diffuse to the anode. The nickel ions are reduced by hydrogen and deposit as metallic Ni. The deposited Ni may form a short circuit between the anode and the cathode, which will degrade the performance severely.[43] To reduce nickel dissolution, lithiated nickel oxide and other lithiated metal oxides with low solubility in the Li_2CO_3 and K_2CO_3 melts, such as $LiFeO_2$ and $LiCoO_2$, are coated on the NiO surface.[32,44]

MCFCs deal with similar degradation, sealing, and matching challenges as SOFCs.[41]

Challenges remain in the electrolyte management and the carbon dioxide recirculation.[45] However, the relative high operating temperatures of MCFCs provide fuel flexibility, and a variety of hydrocarbons, alcohols and CO can be used as fuels.[46,47] MCFCs have been utilized in continuous and stationary power generation and could, potentially, be used as a CO_2 separator.[48,49]

1.1.4.5 Phosphoric acid fuel cells

PAFCs (**p**hosphoric **a**cid **f**uel **c**ells) utilize pure or highly concentrated H_3PO_4 as the electrolyte contained in a SiC matrix between two graphite electrodes coated with platinum catalysts. The anode and cathode reactions are the same as those in PEMFCs, shown in eqs 1.4 and 1.5. Protons are conducted through the SiC matrix/electrolyte from the anode to the cathode.[32]

The optimum operating temperatures for PAFCs range from 180 to 210 ^oC. The SiC matrix provides mechanical supports and minimizes gas crossover. During operation, the H_3PO_4 must be replenished continuously due to its gradual evaporation to the environment.

CO poisoning is still a problem since the PAFCs use Pt catalysts, though the elevated operating temperature endows better tolerance than the PEMFCs. However, the performance of the PAFCs is inherently lower than that of PEMFCs because of oxygen's low solubility in phosphoric acid and the strong interaction between PO_4^{3-} and Pt surfaces.[50] In addition, Pt catalysts tend to migrate on the surface and agglomerate, leading to decreased performance.[16] Stable materials for catalysts and hardware are hard to find due to the strong acidic conditions and the high temperatures.

Typical applications of PAFCs include power sources for stationary power plants that require a constant and stable energy supply. The waste heat can be collected for cogeneration similar to the SOFCs and MCFCs.[51]

1.1.4.6 Other types of fuel cells

DLFCs (**d**irect **l**iquid **f**uel **c**ells) generate energy from liquid fuels, such as methanol,[52] ethanol,[53,54] formic acid,[55] and borohydride[56] solutions. The DLFCs are attractive because the liquid fuels is easier to handle using the current infrastructure rather than gaseous fuels and because the liquid fuels generally have higher energy densities than hydrogen. For example, the energy density of liquid methanol is 17.3 MJ L^{-1} compared with that of compressed hydrogen at 700 bar, which is 8.3 MJ L^{-1}.[57] However, only relatively simple liquid fuels are used due to their sluggish oxidation kinetics compared with hydrogen. Moreover, the experiment efficiencies and power outputs of the DLFCs are lower compared to hydrogen–oxygen fuel cells.[42] DLFCs are studied widely as portable power sources to replace rechargeable batteries,[58] as military power systems in remote areas, and as backup power supplies.[57]

The most studied DLFC is the DMFC (**d**irect **m**ethanol **f**uel **c**ell). The electrode reactions are shown in eqs 1.15 to 1.18.

In acid

$$\text{Anode: } CH_3OH + H_2O \rightarrow CO_2 + 6\,H^+ + 6\,e^- \qquad 1.15$$

$$\text{Cathode: } 1.5\,O_2 + 6\,e^- + 6\,H^+ \rightarrow 3\,H_2O \qquad 1.16$$

In base

Anode: $CH_3OH + 6\ OH^- \rightarrow CO_2 + 5\ H_2O + 6\ e^-$ 1.17

Cathode: $1.5\ O_2 + 3\ H_2O + 6\ e^- \rightarrow 6\ OH^-$ 1.18

In acid, the catalysts are Pt-based. Since one intermediate in the methanol oxidation is CO, Pt alloys with oxophilic metals Ru,[59] Sn,[60] Ni,[61] etc. perform better as electrocatalysts for the methanol oxidation. Ru is the most effective in providing CO tolerance. Surface Ru generates surface adsorbed OH groups (OH^{ads}), which oxidizes CO^{abs} at adjacent surface Pt atom to form CO_2.[59,62] Another challenge in DMFCs is the crossover of the methanol from the anode to the cathode, decreasing efficiency.[57]

Under basic conditions, the methanol oxidation kinetics is faster than in acid. Catalysts like Ni and Fe can be used, which reduces the cost of fabrication. However, similar to AFCs, challenges like the electrolyte degradation by CO_2 exist.[57]

RFCs (**r**eversible **f**uel **c**ells) are the devices that can function both in fuel cell mode and water electrolyzer mode. In electrolyzer mode, water is split into hydrogen and oxygen gases by electrical energy input to the cell. In fuel cell mode, RFCs utilize the stored hydrogen with stored oxygen or air to regenerate electricity and form water.[63] When coupled with hydrogen and oxygen storage systems, RFCs can constitute a long-term electrical energy storage system. Though RFCs are still in the research and development stage, potential applications involve areas such as space vehicles and satellites, submarines, and power supply systems in remote regions where there is variable energy input, such as solar or wind power.[64,65]

1.1.5 Oxygen reduction reaction

1.1.5.1 Mechanism

Unlike the HOR at the anode, the ORR at the cathode is kinetically sluggish. Tireless efforts have been expended in developing active ORR catalysts.[66–68] The ORR proceeds through two possible pathways: a 4-electron pathway and a 2-electron pathway suggested by Wroblowa et al.[69]

The 4-electron reduction process is shown in eqs 1.19 and 1.20.

In acid: $O_2 + 4\ e^- + 4\ H^+ \rightarrow 2\ H_2O$ $\quad E^o = 1.23$ V 1.19

In base: $O_2 + 4\ e^- + 2\ H_2O \rightarrow 4\ OH^-$ $\quad E^o = 0.40$ V 1.20

The 2-electron reduction process is shown in eqs 1.21 to 1.24.

In acid: $O_2 + 2\ e^- + 2\ H^+ \rightarrow H_2O_2$ $\quad E^o = 0.70$ V 1.21

$H_2O_2 + 2\ e^- + 2\ H^+ \rightarrow 2\ H_2O$ $\quad E^o = 1.76$ V 1.22

In base: $O_2 + 2\ e^- + H_2O \rightarrow OH^- + HO_2^-$ $\quad E^o = -0.056$V 1.23

$HO_2^- + 2\ e^- + H_2O \rightarrow 3\ OH^-$ $\quad E^o = 0.87$ V 1.24

The 4-electron reduction process is preferred in fuel cells because it does not involve peroxide species that may degrade the electrodes and the membrane.[70] Also, higher operating potentials and current densities could be generated through a 4-electron reduction process.[71] Numerous reports have shown that Pt-based catalysts go through the 4-electron reduction process.[72–75] For the less active metals, like Hg and Au, the 2-electron reduction process is reported. One application of the 2-electron reduction process is the production of hydrogen peroxide in industry.[66]

Scheme 1.1.

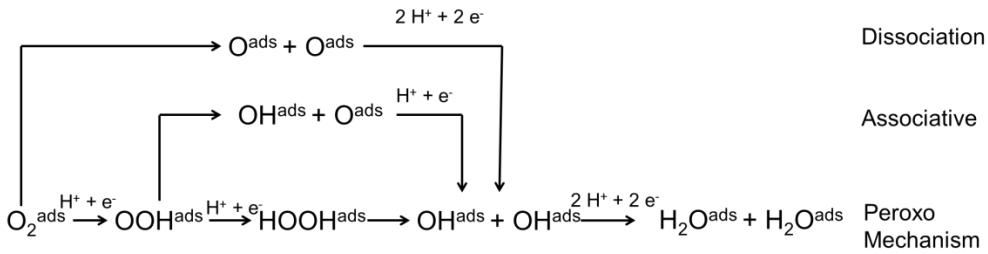

DFT (**d**ensity **f**unctional **t**heory) uses the electron density to evaluate the energy of a system with any configuration of nuclei and electrons, and it can be used in predicting chemical reaction pathways. Keith et al. provided detailed 4-electron reduction pathways on Pt(111) catalysts based on DFT, as shown in Scheme 1.1.[66,76–78] The key difference between the three mechanisms is the point at which the oxygen–oxygen bond breaks.

1. *Dissociation mechanism.* After O_2 is adsorbed on the catalyst surface as O_2^{ads}, the oxygen double bond breaks, forming 2 O^{ads}. Two electrons coupled with protons (e^-/H^+) reduce the 2 O^{ads}, resulting in 2 OH^{ads}. Another 2 e^-/H^+ reduce the two OH^{ads}, making surface adsorbed water, H_2O^{ads}. However, according to the DFT calculation by Hyman et al, the cleavage of the oxygen double bond requires > 0.5 eV energy, rendering this pathway less likely to happen.[79]

2. *Associative mechanism*. After O_2 is adsorbed on the catalyst surface as O_2^{ads}, the proton-coupled electron transfer results in OOH^{ads}. The O–O single bond breaks and forms OH^{ads} and O^{ads}. A second e^-/H^+ reduces the O^{ads}, forming OH^{ads}. Eventually, H_2O^{ads} is formed by a further proton-coupled electron-transfer process.

3. *Peroxide mechanism*. Upon forming OOH^{ads}, the proton-coupled electron-transfer process happens at the O that binds with the surface metal atom, followed by the cleavage

of the O–O bond. The resulting two OH^{ads} are reduced by electrons coupled with protons and form two H_2O^{ads}.

The reaction intermediates (OOH^{ads}, OH^{ads} and O^{ads}) are considered crucial in determining the catalyst activity by Nørskov et al.[80,81] They obtained a volcano plot (Figure 1.3) of the ORR activity versus oxygen binding energy[a] (ΔE_O) on different metal surfaces by DFT calculations.[80] Catalysts sitting on the left side of the volcano plot bind with the O^{ads} so strongly that the formation of OH^{ads} hinders the overall activity, while for catalysts at the right side of the volcano plot, the weak adsorption of O^{ads} is the rate-limiting step of the ORR.[80] The metal sitting near the top of the volcano plot is Pt.

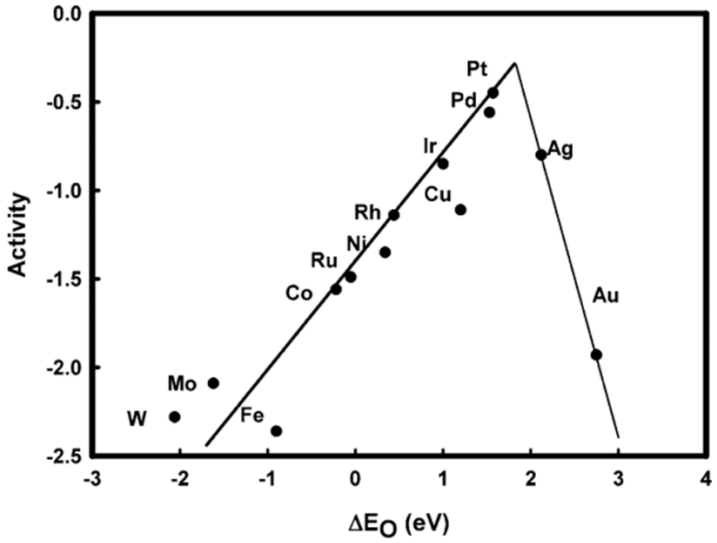

Figure 1.3 ORR activity versus oxygen binding energy (ΔE_O) at different metal surfaces. Reprinted with permission from American Chemical Society.

[a] *Biniding energy here refers to the minimum energy required to remove an atom or a molecule at the metal surface.*

Furthermore, the BE (**b**inding **e**nergy) of a species on the transition metal surface is related to the relative position of the metal d-band center and the Fermi level according to the d-band model.[82,83] The d-band center (ε_d) is defined as the average energy of the electron d states, and the Fermi level (ε_f) is the highest energy state occupied by electrons in a material at absolute zero temperature.[84] Figure 1.4 shows the change in local electronic structure of the O atom upon adsorption on the Pt surface. The Pt d-band states couple with the O 2p states to form bonding and antibonding states below and above the O 2p states. The extent of the filling of the antibonding states is dependent on the local electronic structure of the metal at the surface. As the metal d-band center shifts down relative to the Fermi level, the filling of the antibonding states increases, destabilizing the metal–oxygen interaction (weaker binding). In reverse, the upshift of the d-band center relative to the Fermi level will depopulate the antibonding states, leading to strong binding of oxygen on the metal surface.[82] Therefore, the catalytic activity and metal electronic structure are related, and the d-band model serves as guidance to screen new active ORR catalysts efficiently.

On the basis of the volcano plot and the d-band theory, the O binding energy on Pt has to be lowered by 0.2 eV to reach the optimum activity, which can be achieved by down-shifting the Pt d-band center relative to the Fermi level.[80] Alloying Pt with other transition metals, like Ni, Cu, and Co, has proven effective in optimizing the ORR activity. Theories explaining the enhanced activity observed by the addition of a second metal, including the electronic effect and the strain effect, are established.[67]

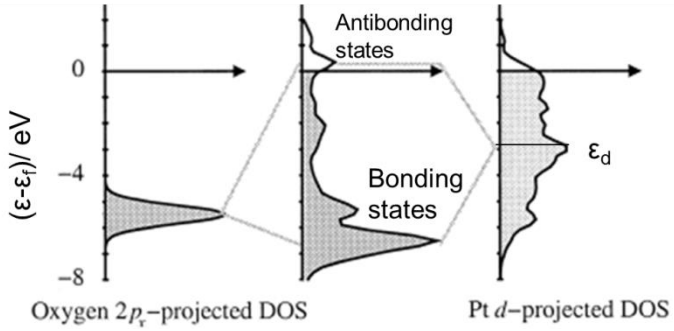

Figure 1.4 Illustration of the change in local electronic structure of the O atom upon adsorption on the Pt surface. (DOS (**d**ensity **o**f **s**tates), which reveals the number of states per band available to be occupied by electrons.) Reprinted with permission from Elsevier.

The electronic effect refers to the modification of the Pt electronic structure by the adjacent metal site.[82] The interaction of the adjacent metal atoms changes the electronic structure of Pt, causing the change in binding energy of the adsorbate at Pt atoms. The electronic effect can be probed using XPS (**X**-ray **p**hotoelectron **s**pectroscopy) and UPS (**u**ltraviolet **p**hotoelectron **s**pectroscopy). The working principle of XPS and UPS is illustrated in Figure 1.5: a valence or core electron is excited by X-ray or UV light, respectively, and ejected to the vacuum in the spectrometer; ε_f is the Fermi level shared by the spectrometer and the sample since they are in electrical contact; ε_{vac} is the vacuum level; KE is the **k**inetic **e**nergy; φ_{sample} is the work function of the sample; and φ_s is the work function of the spectrometer. By measuring the kinetic energy of the excited electrons, the binding energy of the electrons in the material can be calculated by eq 1.25[85]

$$BE = h\nu - KE - \varphi_s \qquad 1.25$$

where h is the Plank constant, and ν is the incident radiation frequency. The core-level

electron BE shifts provide an idea of the electronic structure of atoms in the solid. Relative to the neutral atom, an increase in electron density around an atomic site would result in higher repulsion, causing a shift to lower binding energy, and vice versa. This explanation assumes that the remaining electrons in the final states are the same as they were before the ejection event.[86] However, the final state effects could also come into play. The electrons at the final states experience less shielding, and the BE would be lower since it is easier to remove the electron,[87] making the interpretation of the electronic effect from XPS and UPS data indefinite.

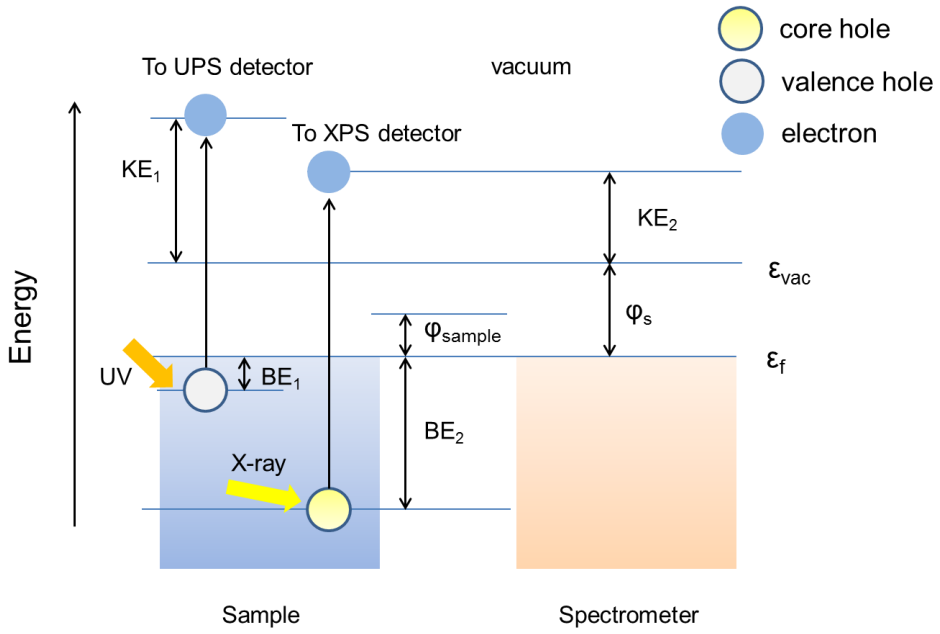

Figure 1.5 Scheme showing the working principles of XPS and UPS.

Down-shifting in Pt core-level electrons[b] binding energies has been reported for various Pt–Ni systems, including a graphene-supported PtNi alloy catalyst,[88] Ni core and

[b] *Core-level electrons refer to the electrons that are not participating in forming bonds.*

Pt shell nanoparticles,[89] and PtNi nanoparticles.[90,91] This shift was explained wholly or in part by Ni donating electron density to Pt sites according to Pauling electronegativity values, which are a measure of the atom's ability to attract an electron when the electron is still attached to the other atom (1.91 for Ni and 2.28 for Pt).[90] Stamenkovic et al. utilized UPS on the $Pt_3Ni(111)$ alloy with a Pt skin surface and found a down-shift of the d-band center relative to the Pt(111) surface, which is caused by the electronic effect. Cyclic voltammograms also showed an impeded hydrogen and hydroxide adsorption process for the $Pt_3Ni(111)$ alloy with Pt skin compared with Pt(111), indicating weaker surface adsorbate binding energy and supporting the d-band model.[92]

The strain effect refers to the differences in the positions of the surface layer Pt atoms caused by underlying metal layers due to the differences in lattice parameters between Pt and the underlying atoms. If the underlying layer has a larger atomic radius than Pt, the expansive strain is experienced. The compressive strain in the Pt layer occurs when the underlying atoms have a smaller radius than Pt. A DOS calculation shows that the expansive strain narrows the d-band of Pt due to less orbital overlap and less electronic repulsion. It follows that the highest energy state will be lower than the metal's Fermi level. Therefore, in order to conserve the d-band filling, the energy-band will up-shift (Figure 1.6). Similarly, the compressive strain widens the d-band and shifts the d-band center down.[93] Zhang et al. have reported an expansive strain of the Pt **m**ono**l**ayer (ML) on the Au(111) surface.[94] The up-shift of the Pt surface d-band center was suggested, leading to a stronger Pt–O adsorption, as predicted by the d-band model.[80] Pt ML on Ir(111) experienced the compressive strain, resulting in weaker Pt–O surface bonds.[95] In reality, both the electronic effect and the strain effect would occur simultaneously, and it is hard to

distinguish between them.

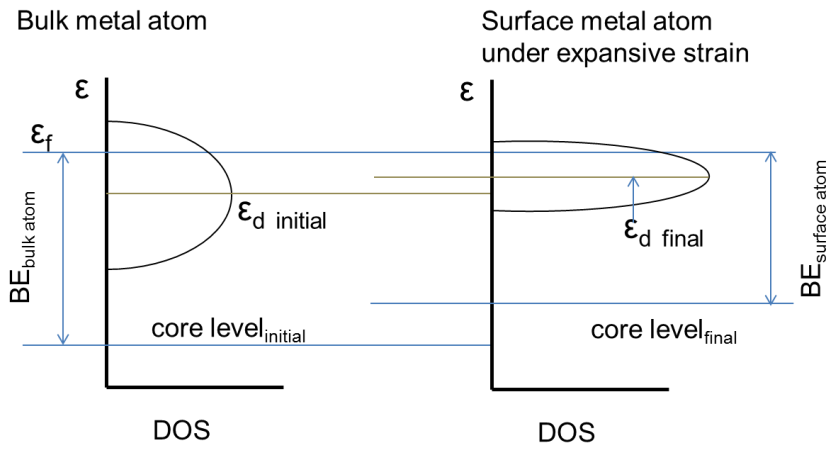

Figure 1.6 DOS for a metal with more than half-filled d-bands under expansive strain. Energy levels and BE in the bulk (left) and surface band narrowing accompanied with d-band shift (right).

The d-band theory has been confirmed experimentally by many systems.[96–98] However, discrepancies are reported for several systems where d-band models are not applicable.[99–101] In these systems, factors not included in the d-band model may play a significant role. One such case is the bifunctional mechanism, where the presence of two metals allows for an additional reaction to occur, increasing the catalytic activity. An exemplary reaction is the methanol oxidation on PtRu catalyst. When a surface Pt atom (Pt^{surf}) is poisoned by adsorbed CO, the OH groups at an adjacent surface Ru atom (Ru^{surf}) will facilitate the oxidation of CO to CO_2, thus depoisoning Pt (eq 1.26).[102] The presence of Ru significantly enhances the catalytic activity of Pt, while the electronic factors play a minor role.[103]

$$Pt^{surf}–CO^{ads} + Ru^{surf}–OH^{ads} \rightarrow CO_2 + H^+ + e^- + Pt^{surf} + Ru^{surf} \quad 1.26$$

1.1.5.2 Pt-based ORR electrocatalysts

Methods to synthesize Pt-based alloy catalysts with enhanced activities follow the strategies summarized below.

1. *Monolayer Pt catalysts.*

Adzic et al. have reported a monolayer of Pt deposited on a non-platinum metal substrate (e.g. single crystal Pd (111) and Au(111),[104] Ru,[105] Pd–Au,[106] Ir, Re,[107] PtPb, PdFe, PdPb,[108] Pd_3Co,[109] PdAu,[110] and AuNi[111]) through replacement of a second metal (e.g., Cu) adlayer template that has been formed by underpotential deposition.[94,112–114] For example, a layer of Cu was deposited first on a commercial Pd(111) electrode using underpotential deposition in a 0.05 M $CuSO_4$ and 0.1 M H_2SO_4 solution. The applied potential for the Cu monolayer deposition is higher than the Nernst potential of bulk Cu deposition so that Cu only deposits on the Pd surface, forming a monolayer. Then, the electrode was dipped in a 1 mM K_2PtCl_6 and 0.05 M H_2SO_4 solution under N_2 to allow the displacement of the Cu monolayer by the Pt monolayer.[104] This method yields extremely low Pt loading catalysts with high ORR activity. The ORR mass activity for the monolayer Pt shell on the AuNi core nanoparticles supported on carbon (1.52 A mg_{Pt}^{-1} at 0.9 V versus the **r**eversible **h**ydrogen **e**lectrode (V_{RHE})) was 7 times higher than the commercial Pt/C catalyst (0.2 A mg_{Pt}^{-1} at 0.9 V_{RHE}).[111] The peak of the reduction of adsorbed oxygen species shifted to a higher potential for the Pt_{ML}AuNi nanoparticles compared with Pt, indicating weakened oxygen affinity. This was explained by the addition of the NiAu core donating electron density to the Pt site, leading to a downshift of the d-band center and a weakening of the

oxygen binding energy, as predicted by the d-band model. In addition, they also proposed that the Pt–Pt bond in the deposited surface monolayer Pt was contracted, shifting down the d-band center compared with Pt. Both the electronic effect and the strain effect contributed to the enhanced ORR activity on the Pt monolayer shell AuNi core nanoparticle catalysts.[111,112]

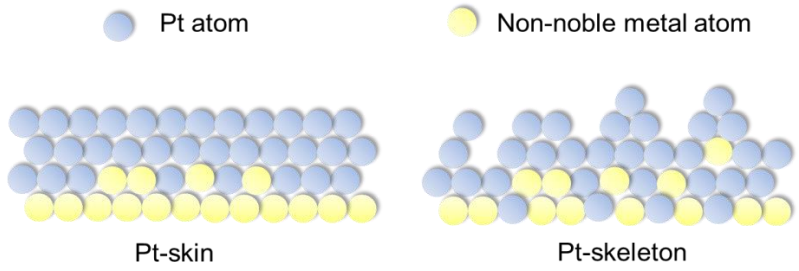

Figure 1.7 Illustration of the "Pt-skin" and the "Pt-skeleton" surface layer structures (side view).

2. *Pt-skin and Pt-skeleton catalysts.*

In this method, a few atomic Pt layers were deposited on a transition metal-rich substrate. Stamenkovic et al. have reported "Pt-skin" catalysts synthesized in an ultra-high vacuum argon-filled arc-melting furnace.[115] The surface aggregation of Pt atoms leads to the formation of a Pt-skin type structure on PtM alloys (M = Co, Ni, and Fe), with the depletion of Pt atoms at the sub 2 to 3 layers.[92,116] Strasser et al. utilized the electrochemical dealloying process (multiple potential cycling in an acidic solution at high sweep rates, e.g. 0.5 to 1 V_{RHE}, 50–100 mV s^{-1} for 200 cycles),[117] which incompletely removed the less noble components from the metallic alloy precursors, resulting in an atomically rough surface of Pt atoms with low lateral coordinations; this was referred to as a "Pt-skeleton" structure at the surface. An illustration of the "Pt-skin" and the "Pt-skeleton" structure is

shown in Figure 1.7. The "Pt-skin" and the "Pt-skeleton" structures have surface layers of Pt protecting the inner transition metal atoms from dissolution, while the electronic effect and the strain effect of the surface Pt are preserved.

The dealloyed catalysts are more active ORR catalysts in acidic solutions. A survey of the PtM_3 (M = Cu, Co, Ni) and $PtNiM_3$ (M = Cu, Co, Fe, Cr) was carried out by Strasser et al.[117119,120] The best ORR activity was acquired by the dealloyed composition of $Pt_{48}Ni_{48}Cu_4$ (from the $Pt_{20}Ni_{60}Cu_{20}$ alloy precursor), which reached 0.47 A mg_{Pt}^{-1} and 406 μA cm_{Pt}^{-1} at 0.9 V_{RHE}.[117] Further investigation on $Pt_{1-x}Ni_x$ (x = 0.14–1) catalysts revealed that the $Pt_{0.25}Ni_{0.75}$ catalyst, after dealloying for 200 cycles of potential sweep (0.06 to 1 V_{RHE}, 500 mV s^{-1}) and 400 stability cycles (0.5 to 1 V_{RHE}, 50–100 mV s^{-1}), achieved a kinetic current density of 0.44 A mg_{Pt}^{-1} and 1185 μA cm_{Pt}^{-1} at 0.9 V_{RHE}.[118,119] Later, they reported $Pt_{71}Rh_3Ni_{26}$ catalysts synthesized using a hydrothermal method;[120] the kinetic current after 20 activation cycles reached 1.14 A mg_{Pt}^{-1} and 3.25 mA cm_{Pt}^{-1}. The increased activity by doping a transition metal to Pt is believed to occur through the compressive strain and the electronic effect that affect the chemisorption of the ORR intermediates.[73,119]

Catalysts with record-breaking ORR activities have been reported by various research groups.[121–123] Recently, Duan et al. synthesized jagged platinum nanowires with a 2–3 nm diameter. $Pt(acac)_2$ (acac = acetylacetonate), $Ni(acac)_2$, and glucose were dissolved in a mixture of 1-octadecene and oleylamine, and polyvinylpyridine and $W(CO)_6$ were added to the solution. The mixture was heated up to 140 ^oC over 6 h in a sealed vessel to obtain Pt/NiO core/shell nanowires. The as-prepared Pt/NiO nanowires were loaded onto carbon black and annealed at 450 ^oC in Ar/H_2: 97/3 atmosphere. Cyclic voltammetry was performed in a N_2-saturated 0.1 M $HClO_4$ solution (0.05 V to 1.1 V_{RHE}) with a sweep rate

of 100 mV s^{-1} to dissolute Ni, forming jagged Pt nanowires. Extremely high ORR activity (13.6 A mg_{Pt}^{-1} and 11.5 mA cm_{Pt}^{-1} at 0.9 V_{RHE}) was observed. The EXAFS (**e**xtended **X**-ray **a**bsorption **f**ine **s**tructure) analysis and the computational simulation revealed that the surface Pt is under coordinated (coordination number 6–8 compared to 9 for a crystalline Pt(111) facet). The author proposed that a large EASA (**e**lectrochemically **a**ctive **s**urface **a**rea, 118 m^2 g_{Pt}^{-1}) and the presence of ORR-favorable rhombus structures[c] at the surfaces of nanowires contributed to the enhanced ORR activity.[124,125]

Challenges remain for synthesizing active and stable ORR catalysts. Compared with extended structure ORR catalysts, nanoparticle catalysts are susceptible to the loss of surface active sites due to the particle size increase. The abundant edges and corners are preferential sites to adsorb inactive oxygenated spectator species, thus decreasing the ORR activity. Therefore, synthesis of "Pt-skin" catalysts with an extended structure is promising in obtaining active and stable ORR catalysts.

[c] *A rhombus structure is a set of 4 Pt atoms forming two triangles sharing one edge. The structure is crystalline, but Pt atoms are highly under coordinated.*

1.2 **Water electrolyzers**

1.2.1 Definition

Electrolysis of water is the process of using electricity to split water into hydrogen and oxygen gases. This process takes place in a unit called an electrolyzer. In principle, when a direct current is passed between two electrodes immersed in an aqueous electrolyte, hydrogen and oxygen are formed at the cathode and the anode, respectively. The amount of hydrogen and oxygen produced is directly proportional to the current passing through the electrodes. Implementation of a diaphragm or a separator is necessary to avoid recombination of hydrogen and oxygen to preserve efficiency and ensure safety. The electrodes, the separator, and the electrolyte form the electrolyzer. Figure 1.8 shows an example of a water electrolyzer under acidic conditions. Water electrolyzers and fuel cells use similar technology, but the process in fuel cells is the reverse.

Compared with other hydrogen production methods, like the reforming of natural gas,[126] gasification of coal[127] and petroleum coke,[128] and gasification and reforming of heavy oil,[129] water electrolysis produces extremely pure hydrogen (> 99.5%), ideal for the high-value added processes, like the manufacture of electronic components.[130] Additionally, production of hydrogen from renewable energy (e.g., wind, solar, hydro etc.) by water electrolysis is one of the solutions to a sustainable energy supply.

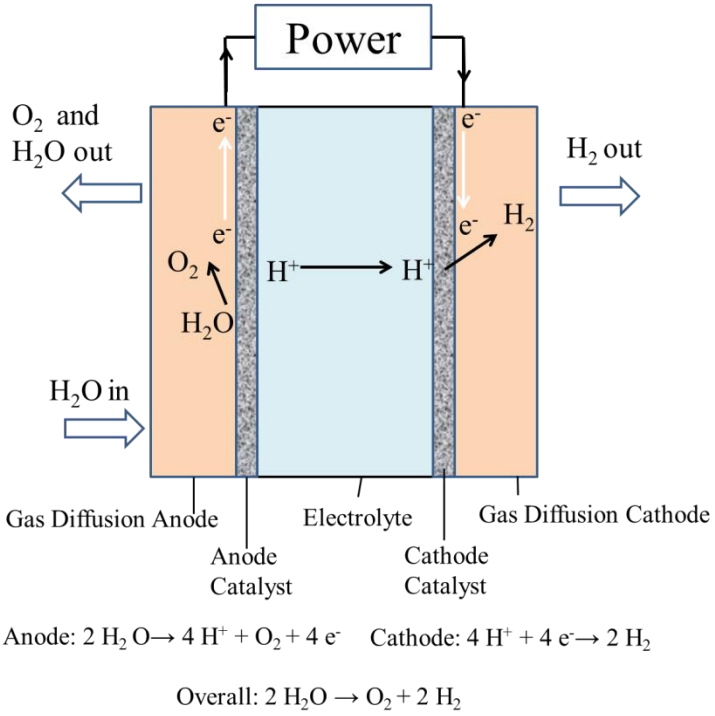

Figure 1.8 Schematic illustration of an acidic water electrolyzer (not drawn to scale).

1.2.2 Working principles

In water electrolyzers, electrical energy is converted into chemical energy. The total energy required for water splitting is given by the enthalpy of formation of water. Under standard conditions (298.15 K and 1 atm), the enthalpy change (ΔH^o), free energy change (ΔG^o), and entropy change (ΔS^o) of water splitting is 285.8 kJ mol^{-1}, 237.2 kJ mol^{-1}, and 0.163 kJ mol^{-1} K^{-1}, respectively.[131]

The difference between enthalpy change and free energy change at constant temperature (eq 1.27) gives the entropy change term ($T\Delta S$).[130]

$$T\Delta S^o = \Delta H^o - \Delta G^o = 285.8 - 237.2 = 48.6 \text{ kJ mol}^{-1} \quad 1.27$$

The energy used for entropy change under standard conditions, 48.6 kJ mol^{-1}, is absorbed

spontaneously from the surroundings. The water oxidation reaction is expressed in eq 1.28.

$$H_2O + \text{electrical energy } (\Delta G^o) + \text{heat } (T\Delta S^o) \rightarrow 2\,H_2 + O_2 \qquad 1.28$$

The reversible cell potential (E^o), which is the minimum voltage required to split water, is given by eq 1.29, where ΔG^o is the total energy required to supply as electricity, n is the number of electrons transferred, and F is the Faraday constant (96485 C mol^{-1}).

$$E^o = \frac{\Delta G^o}{nF} = \frac{237.2\ \text{kJ mol}^{-1}}{2 \times 96485\ \text{C mol}^{-1}} = 1.23\ \text{V} \qquad 1.29$$

In an isolated system, the thermoneutral potential (E_{th}^o) required to satisfy the thermodynamic requirement as given by eq 1.30,

$$E_{th}^o = \frac{\Delta H^o}{nF} = \frac{285.8\ \text{kJ mol}^{-1}}{2 \times 96485\ \text{C mol}^{-1}} = 1.48\ \text{V} \qquad 1.30$$

which means that at 1.48 V, no heat exchange occurs with the surroundings.[132] Since practical water electrolyzers operate at potentials higher than 1.48 V, excess heat is generated in the cell.

The efficiency of a water electrolyzer is defined as the ratio of the total energy input to the total energy output.[133] The energy input can be expressed as the free energy change (ΔG) or the enthalpy change of the reaction (ΔH), hence, two efficiencies (η_1 and η_2) are given by eqs 1.31 and 1.32 at 25 °C.[134,135]

$$\eta_1 = \frac{E_{\Delta G}}{E_{cell}} \times 100 = \frac{1.23\ \text{V}}{E_{cell}} \times 100 \qquad 1.31$$

$$\eta_2 = \frac{E_{\Delta H}}{E_{cell}} \times 100 = \frac{1.48\ \text{V}}{E_{cell}} \times 100 \qquad 1.32$$

Eq 1.31 is the percentage of the theoretical energy needed to split the water molecule

in a real cell voltage and is a measurement of the efficiency from the cell voltage point of view. Eq 1.32 means that an additional cell voltage, above the thermodynamic reversible voltage, is needed to maintain the thermal balance, and the percentage of the actual energy needed in the real voltage defines the thermal efficiency.

The electrolysis cell voltage can be expressed, in eq 1.33, by the sum of various voltage losses in the cell,[131]

$$E_{\text{cell}} = E_{\text{rev}} + E_{\text{ohm}} + E_{\text{act}} + E_{\text{con}} \quad 1.33$$

where E_{rev} is the thermodynamic reversible cell potential, E_{ohm} is the voltage loss due to the ohmic resistance (electrodes, current collectors, interconnections etc.), E_{act} is the activation overvoltage due to the electrode kinetics (activation energy required for reactions to occur), and E_{con} is the concentration overpotential caused by the mass transport processes (convection and diffusion).

1.2.3 History

After the discovery of electricity, the phenomenon of water splitting into hydrogen and oxygen was observed first by Nicholson and Carlisle in 1800. They used Volta's pile, which consists of zinc and silver with a piece of cloth soaked in conducting liquids, as the electrical supply.[136] The relationship between the electricity consumed and the amount of gas produced was established through Faraday's law of electrolysis, and the concept of water electrolysis was defined scientifically and acknowledged.[137]

Driven by the demand for hydrogen in industry, mainly in the production of ammonia fertilizers, several large water electrolysis 100 MW-size plants were built worldwide in the 1920s.[138] In 1948, the first pressurized water electrolyzer was built by Zdansky and

Lonza.[136] The period between 1920 and 1970 marks a significant progress in water electrolysis technology; the prototype water electrolyzers contained components that are still in use today.[139] One concept is the adoption of a membrane that allows selective ions to pass while it separates the hydrogen and oxygen gases, and the first commercial membrane was asbestos. However, due to its vulnerability under a strong alkaline environment at elevated temperatures and its potential hazard to human health, the gas separation material gradually shifted to polymers such as perfluorosulphonic acid and polytetrafluoroethylene.[140,141]

The oil crisis in the 1970s provoked a new interest in water electrolysis using hydrogen as a sustainable and clean energy source.[142] The PEM electrolyzers have been applied in a small scale in the military.[143]

Today, water electrolyzers are applied in many areas that require hydrogen, including marine, rocket, spacecraft, electronic production, food industries, chemical processing, and medical applications. Water electrolyzers could also couple with fuel cells to form energy conversion and storage devices. The Jupiter Independence system fabricated by FutureE (a German fuel cell company) integrated fuel cells, water electrolyzers, and hydrogen storage cylinders, and it is currently used as a power backup system to supply power for a few hours in case of outage.[144,145]

1.2.4 Types of water electrolyzers

Like fuel cells, which depend on the electrolyte used in the system, water electrolyzers can be divided into three categories, AWEs (**a**lkaline **w**ater **e**lectrolyzers), PEMWEs (**p**roton **e**xchange **m**embrane **w**ater **e**lectrolyzers), and SOWEs (**s**olid **o**xide **w**ater **e**lectrolyzers).

1.2.4.1 Alkaline water electrolyzers

AWE is a mature technology for hydrogen production.[146] The cathode and anode are separated by a diaphragm that keeps the product gas apart for efficiency and safety. Ni- and Co-based oxides are used as cathode and anode catalysts, respectively, and steels are the cell construction materials. The electrolyte is 20–40% KOH. The electrode reactions are shown in eqs 1.34 and 1.35.[147]

$$\text{Anode: } 4\ OH^- \rightarrow O_2 + 2\ H_2O + 4\ e^- \qquad 1.34$$

$$\text{Cathode: } 2\ H_2O + 4\ e^- \rightarrow 2\ H_2 + 4\ OH^- \qquad 1.35$$

The major issues associated with the AWEs are low partial load range, limited current density, and low operating pressure.[146] The diaphragms used in AWEs are a ceramic, a mesh of titanium oxide and potassium titanate, or a ZrO_2-embedded polysulfone matrix.[148] However, these diaphragms do not prevent gas diffusion completely, posing a potential safety hazard, and the crossover of gas reduces the overall efficiency. The high ohmic loss across the liquid electrolyte and diaphragm leads to a low achievable maximum current density. In addition, the low operating pressure caused by the use of a liquid electrolyte requires additional facilities to pressurize the gases. Like AFCs, the electrolyte KOH may react with CO_2 in the atmosphere to form carbonates, introducing mechanical and gas diffusion issues. AEMs are being developed for modern alkaline electrolyzers (lab scale).[130,149] The low OH^- conductivity and degradation limit the current density and performance of these devices. Research in AWEs focuses on developing alternative efficient catalysts for water oxidation and durable AEMs with good OH^- conductivity.

Table 1.2 Comparison of AWEs and PEMWEs

Specifications	Alkaline Electrolysis	PEM Electrolysis
Cell temperature (^{o}C)	60–80	50–80
Current density (mA cm^{-2})	0.2–0.4	0.6–2.0
Cell voltage (V)	1.8–2.4	1.8–2.2
Voltage efficiency	62–82%	67–82%
Gas purity	> 99.5%	99.99%
Lifetime stack (h)	< 90000	< 60000
Lifetime system (years)	20–30	10–20

1.2.4.2 Proton exchange membrane water electrolyzers

PEMWEs are the most attractive and efficient devices to split water into H_2 at low temperatures.[150] A PEMWE consists of an anode, a cathode, and a PEM. Water is supplied to the anode where it is split into protons, electrons, and oxygen by the catalyst. The protons move through the membrane to the cathode and are reduced by the electron from the external circuit to form hydrogen.[146]

Anode: $2\ H_2O \rightarrow 4\ H^+ + O_2 + 4\ e^-$ 1.36

Cathode: $4\ H^+ + 4\ e^- \rightarrow 2\ H_2$ 1.37

Owing to the good proton conductivity of the membrane, PEMWEs can operate at high current densities, which reduces the operational cost. The utilization of Nafion® allows for a compact design of the device, a high operational pressure, and a low gas

crossover, thus producing hydrogen and oxygen with higher purity and efficiency.[151] However, the strong acidic corrosive environment and anodic potentials limit the selection of the materials for catalysts, current collectors, and separator plates.[148] Currently, only limited materials are stable in such a harsh acidic environment. Scarce, expensive materials, such as platinum-group metals and iridium oxide, are used for catalysts, and titanium based materials for current collectors and separator plates.[146]

Currently, the research in PEMWEs is focused mainly on developing an alternative membrane to Nafion®, low cost and stable water oxidation catalysts, and new materials for current collectors and separator plates.

Table 1.2 compares the technological parameters of the PEMWEs and the AWEs. The AWEs could obtain a higher hydrogen production rate as a stacked system, the lifetime of which is proven longer than the PEM electrolysis.

1.2.4.3 Solid oxide water electrolyzers

SOWEs operate at high temperatures (600–900 °C). Steam passes through the cathode forming H_2 and O^{2-}, and the O^{2-} ion diffuses through the ceramic electrolyte to the anode, where O_2 is produced. The anode and cathode reactions are shown in eqs 1.38 and 1.39.

$$\text{Anode: } 2\ O^{2-} \rightarrow O_2 + 4\ e^- \qquad 1.38$$

$$\text{Cathode: } 2\ H_2O + 4\ e^- \rightarrow 2\ H_2 + 2\ O^{2-} \qquad 1.39$$

Similar to SOFCs, yttria-stabilized zirconia is used as the electrolyte material.[152] The most commonly used cathode material is Ni-Y_2O_3 stabilized ZrO_2 (Ni-YSZ) cermet, which is the same as the HOR electrode in SOFCs. The anode in SOWEs uses the same material (e.g. lanthanum–strontium cobaltite) as the ORR electrode in SOFCs.[153] Therefore, the

SOFC/SOWE can operate reversibly.[154] Since water electrolysis is an endothermic reaction, the electrical energy demand is lower at high temperatures for a water splitting process to occur.[155] One important advantage of SOWEs is that they could be used for the electrolysis of CO_2 to CO, and for the co-electrolysis of H_2O/CO_2 to H_2/CO (syngas).[40,146,156] Like SOFCs, SOWEs would be a beneficial part of a combined heat and power generation system since the excess heat from industries could be used in SOWEs.[157,158] However, the thermal stability of the materials and the system sealing pose additional challenges, and facilities to separate the hydrogen from the steam increase the cost.[150] Currently, the SOWE technology is relatively young and untested and is not yet commercially available on a large scale.

1.2.5 Water oxidation reaction

Although the thermodynamic potential for water electrolysis is 1.23 V, the slow kinetics of the reaction requires extra overpotential[d] to be applied to drive the reaction. Since the hydrogen evolution reaction has faster kinetics relative to the WOR (**w**ater **o**xidation **r**eaction), most of the overpotential loss in the water electrolyzers is on the anode side. The water oxidation reaction occurs at a potential higher than the potential of the metal/metal oxide redox couple, therefore, water oxidation only takes place at the metal oxide surface.[159]

[d] *Overpotential is the potential difference between thermodynamic potential and experimentally determined potential.*

1.2.5.1 Mechanisms of the water oxidation reaction

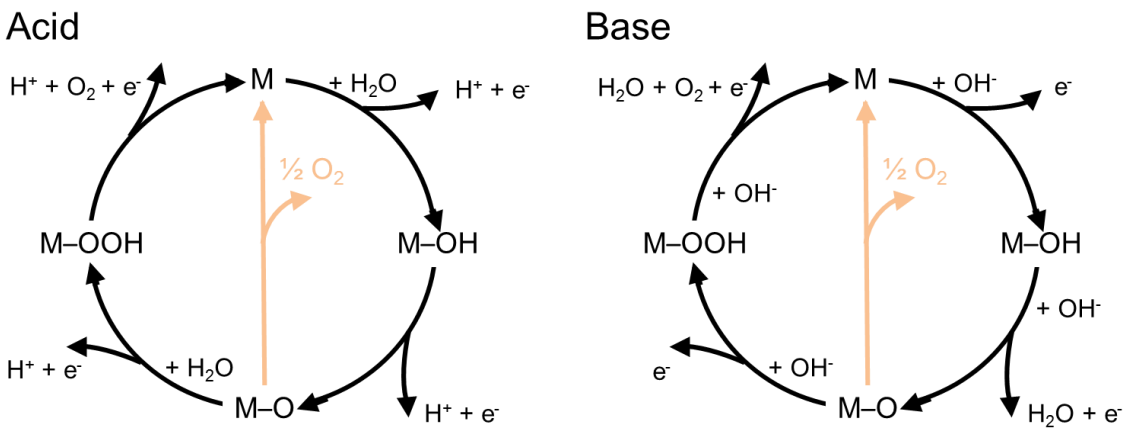

Figure 1.9 WOR mechanism in acid (left) and in base (right). The black line shows the mechanism pathway involving the formation of the peroxide intermediate (M–OOH), while another route for the direct reaction of two adjacent adsorbed oxygens (M–O) (red line) is also possible.

Figure 1.9 shows the mechanism pathways proposed for water oxidation in acid and in base for heterogeneous electrocatalysts. In acid, the overall water oxidation reaction at the anode can be expressed by eq 1.40,

$$2\ H_2O \rightarrow O_2 + 4\ H^+ + 4\ e^- \qquad 1.40$$

and also described in eqs 1.41 to 1.45. [153,154]

$$H_2O + M \rightarrow M\text{–}OH + H^+ + e^- \qquad 1.41$$

$$M\text{–}OH \rightarrow M\text{–}O + H^+ + e^- \qquad 1.42$$

$$2\ M\text{–}O \rightarrow 2\ M + O_2 \qquad 1.43$$

$$M\text{–}O + H_2O \rightarrow M\text{–}OOH + H^+ + e^- \qquad 1.44$$

$$M\text{–}OOH \rightarrow M + H^+ + e^- + O_2 \qquad 1.45$$

In base, the overall water oxidation reaction at the anode can be expressed by eq

1.46,[160,161]

$$4\ OH^- \rightarrow O_2 + 2\ H_2O + e^- \quad (1.46)$$

and also described in eqs 1.47 to 1.51.

$$OH^- + M \rightarrow M\text{–}OH + e^- \quad (1.47)$$

$$OH^- + M\text{–}OH \rightarrow M\text{–}O + H_2O + e^- \quad (1.48)$$

$$2\ M\text{–}O \rightarrow 2\ M + O_2 \quad (1.49)$$

$$M\text{–}O + OH^- \rightarrow M\text{–}OOH + e^- \quad (1.50)$$

$$M\text{–}OOH + OH^- \rightarrow M + H_2O + e^- + O_2 \quad (1.51)$$

The major difference is at the reactions that form oxygen. There are two proposed mechanistic pathways for the formation of O_2 from M–O (surface adsorbed oxygen). One is the direct coupling mechanism (red route shown in Figure 1.9, eqs 1.43 and 1.49), where two adjacent M–O directly combine to produce oxygen.[162] The other is the acid–base mechanism (black route shown in Figure 1.9 and eqs 1.44, 1.45, 1.50, and 1.51) involving the formation of the M–OOH peroxide intermediate, which subsequently decomposes to form oxygen.[163,164]

Similar with the ORR, the catalytic activity of a catalyst towards water oxidation was correlated to the energy states of two adsorbed intermediates, M–O and M–OH, on the surface. If the M–O bonding is weak, the overpotential is limited by the oxidation of M-OH. In the opposite case, if there is strong M–O bonding, the overpotential is limited by the further reaction occurring at the M–O sites.[165]

1.2.5.2 Experimental evidence of water oxidation mechanism in acid

RuO_2 generally is considered to have the highest water oxidation activity in acid among the

single-transition metal oxides.[166] But RuO_2 is not stable under prolonged anodic potentials and dissolves as RuO_4 based on XPS and RRDE (**r**otating **r**ing-**d**isk **e**lectrode) measurements.[167]

IrO_2 is less active than RuO_2 but is significantly more stable. Therefore, the great majority of studies on water oxidation catalysts in acid are focused on IrO_2-based materials. Interested readers are directed to these excellent reviews concerning other materials for the water oxidation reaction.[168–170]

In situ studies on IrO_x-catalyzed water oxidation have been presented by several reports, and the active species towards water oxidation is under debate. Casalogue et al. have observed the Ir^{5+} 4f peak (62.2 eV) using ambient temperature XPS based on the shift of the Ir 4f peak to a higher binding energy than the Ir^{4+}.[171] But Pfeifer et al. have pointed out that the observed species might be the Ir^{3+} rather than Ir^{5+} because in $IrCl_3$, the Ir^{3+} 4f peak (62.6 eV) has a higher binding energy than the Ir^{4+} peak in IrO_2 (61.9 eV).[172] Minguzzi et al. proposed the presence of both Ir^{3+} and Ir^{5+} species during the WOR, based on XANES (**X**-ray **a**bsorption **n**ear **e**dge **s**tructure) spectroscopy.[173] However, the identification of Ir^{5+} species is under debate since Ir^{5+} species are not included in the standard reference material for XANES, and the author assigned the observed edge-position shift to the presence of Ir^{5+} simply based on the redox state.[174]

DEMS (**d**ifferential **e**lectrochemical **m**ass **s**pectroscopy) using labeled electrolyte ($H_2{}^{18}O$ enriched) showed that about 1% of the lattice oxygen in IrO_2 (several surface monolayers) are involved in the formation of O_2.[175] However, this study did not reveal if the O_2 originated from the two lattice-related surface O atoms coming together (direct coupling mechanism) or by one O atom reacting with water to form oxygen (acid–base

mechanism). Sivasankar et al. detected M–OOH species transiently during water oxidation by FTIR (**F**ourier-**t**ransform **i**nfrared **s**pectroscopy) on Ir oxide by the absorption band at 830 cm^{-1}.[176] A SERS (**s**urface **e**nhanced **R**aman **s**pectroscopy) study on electrochemically prepared IrO_x indicated that surface coverage of M–OOH is likely low during the WOR.[177] Based on all these in situ analyses, neither the acid–base nor the direct coupling mechanism could be confirmed or rejected for IrO_x conclusively. More research is needed to understand the mechanism of IrO_x towards water oxidation fully. For example, by using online DEMS with Ir–^{18}OH labelled catalysts and $H_2{}^{16}O$, the presence of $^{18}O^{18}O$ at the early stage of the reaction would be a clear evidence for a direct coupling mechanism.

1.2.5.3 Catalysts for water oxidation in acid

The traditional methods to prepare IrO_2 catalysts for PEMWEs include the Pechini–Adams method,[178] the modified Adams fusion method,[179] the ethylene glycol colloidal method,[180] the sulfite complex method,[181] and the magnetron sputtering method.[182,183] For example, the modified Adams fusion method follows the chemical reactions in eqs 1.52 and 1.53.

$$H_2IrCl_6 + 6\ NaNO_3 \rightarrow 6\ NaCl + Ir(NO_3)_4 + 2\ HNO_3 \qquad 1.52$$

$$Ir(NO_3)_4 \rightarrow IrO_2 + 4\ NO_2 + O_2 \qquad 1.53$$

Also, catalyst supports like TiO_2 can be added to the metal precursor H_2IrCl_6, $NaNO_3$ is added, and the mixture is heated at 500 ^oC for 1 h. Then, the product is washed with water and dried.

Most efforts on IrO_2-based catalysts are directed towards enhancing the activity and reducing the Ir loading. Also, the mechanism is under intense investigation. Approaches to lower the Ir content involve dispersing the IrO_x nanoparticles on high surface area

substrates or mixing them with an inert component, such as oxides of Ti,[184] Ta,[184] Nb,[185] Sn,[186] or Si.[187] For example, De Pauli and Trasatti studied the activity and stability of thermally prepared Ir–Sn mixed oxides from chloride precursors on a Ti substrate after heating at 500 ^{o}C.[188] Similar Tafel slopes were observed, indicating that the mixed oxide catalysts have the same water oxidation mechanism as pure IrO_x. Marshall et al. later showed that up to 20% Sn in IrO_x has no significant influence on the activity in aqueous acidic solutions.[186]

The intrinsic activity and stability of IrO_x can be tuned by doping it with Ni,[189–197] Cu,[198–202] or Co.[203,204] Strasser et al. demonstrated that core-shell structures using NiIr as a core and IrO_2 as a shell are more active than pure IrO_2. The step-wise addition of Ni(II) acetate and Ir(III) acetate into oleylamine, oleic acid, 1,2-tetradecandiol, and dibenzyl ether at 240 ^{o}C, followed by electrochemical oxidation and dealloying, formed NiIr core/IrO_2 shell nanoparticles (36 A g_{Ir}^{-1} at 1.48 V_{RHE}), which were three times more active than IrO_2 (12 A g_{Ir}^{-1} at 1.48 V_{RHE}).[189] The higher activity resulted from the increased electrochemically active surface area, electronic and strain effects due to the presence of the Ni-containing core, and by the reduction of the Ir loading since the Ir only existed at the catalyst surface. Nong et al.[189,191] also concluded that the enhanced water oxidation activity of $IrNiO_x$ nanoparticles is not merely a result of an increased number of surface active sites, leading to further investigations on the structural related factors. Xia et al. reported thermally prepared Ir–Ni composite oxide electrodes by treating $IrCl_3$ and $NiCl_2$ at 450 ^{o}C for 1 h and proposed that the higher activity of, for example, $Ir_{0.7}Ni_{0.3}O_x$ catalyst was caused, partially, by increased proton and electron conductivity within the oxide lattice.[197]

While studying thermally prepared IrNi–mixed oxide thin films, Reier et al. showed that the WOR activity likely is related to active surface hydroxyl groups that are generated by surface leaching of Ni from $IrNiO_x$.[193] Furthermore, the possible presence of the electrophilic O^{1-} species in $IrNiO_x$, as observed by Pfeifer et al. using in situ XPS and in situ XANES, also might be responsible for the improved WOR activity.[172,205] They proposed that the electrophilic nature of O^{1-} species accelerates the nucleophilic attack of water, formed a peroxide intermediate and, subsequently, evolve oxygen (eq 1.54).

$$IrO_xO^{1-} + H_2O \rightarrow IrO_xO^{1-}–O^{1-}–H + H^+ + e^- \rightarrow IrO_x + O_2 + 2\,H^+ + 3\,e^- \qquad 1.54$$

Studies on thermally prepared Cu-doped IrO_x by Sun et al. showed that on doping with 30% Cu into an IrO_x lattice, the Jahn–Teller effect of octahedral $Cu^{II}O_6$ and the existing oxygen vacancies change the adsorption energy of the intermediates, contributing to the enhanced activity. [199]

Recently, non-precious metal-based water oxidation catalysts in acid have been developed. Rossmeisl et al. have developed TiO_2 modified MnO_2 catalysts by sputtering. In 0.05 M H_2SO_4, the catalyst showed a 0.27 V onset overpotential[e] and a 0.42 V overpotential to reach 1 mA cm^{-2}.[206] Lewis et al. reported crystalline nickel manganese antimonite ($Ni_{0.5}Mn_{0.5}Sb_{1.7}O_y$), which catalyzed the water oxidation at 0.672 V overpotential to reach 10 mA cm^{-2} in 1.0 M H_2SO_4 with a loading of 0.5 μmol cm^{-2}. This catalyst was stable for more than 165 h under a 10 mA cm^{-2} galvanostatic test.[207] These are promising catalysts for PEMWEs owing to their low cost.

[e] *Onset overpotential is the overpotential at which the reaction starts to happen.*

1.2.5.4 Experimental evidence of water oxidation mechanism in base

In alkaline and near neutral solutions, oxides and hydroxides of the late first row transition metals (Ni, Fe, Co, Mn) have promising performance,[208–211] and hydroxides incorporating Ni and Fe together show the lowest overpotential towards the WOR under strong alkaline conditions.[209,212,213] Efforts have been made to develop water oxidation catalysts with higher activity and better stability, as well as in understanding the mechanism of NiFe hydroxides towards the WOR.

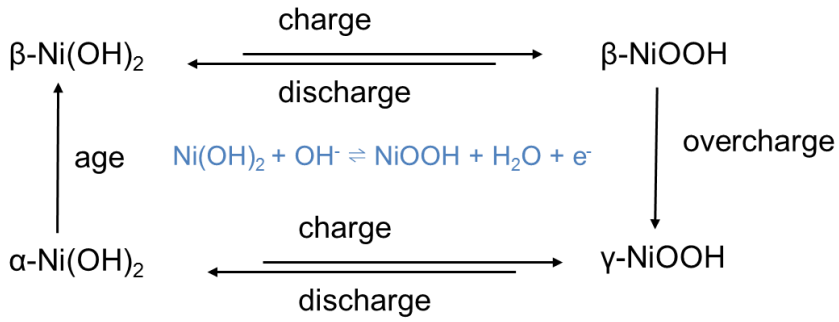

Figure 1.10 A general scheme of the phase transformation of nickel hydroxides and oxyhydroxides involving chemical and electrochemical processes.

Figure 1.10 shows the general scheme of the nickel hydroxide phase transformation during chemical and electrochemical processes.[214] The α-$Ni(OH)_2$ (with oxidation state 2^+) is highly hydrated and poorly crystalline, and it can be oxidized to γ-NiOOH. The average oxidation state of Ni in γ-NiOOH is 3.6^+ (Ni^{4+} and Ni^{3+} present). β-$Ni(OH)_2$ (with oxidation state 2.2^+) is mainly anhydrous and crystalline, and it can be oxidized to β-NiOOH (with oxidation state 3^+). Ageing of the α-$Ni(OH)_2$ in a strong base slowly forms β-$Ni(OH)_2$, while β-NiOOH could be transformed to γ-NiOOH upon overcharging at anodic potentials.[215] A detailed discussion of the different phases of nickel hydroxides

and oxyhydroxides can be found in these review articles.[215–217]

Earlier, it was thought that β-NiOOH is the active phase for water oxidation because the catalytic activity improved after ageing, which was believed to transform α-$Ni(OH)_2$ to β-$Ni(OH)_2$ and then to β-NiOOH under anodic conditions.[214] However, recent in situ studies showed that the active phase was, in fact, γ-NiOOH formed by oxidation of α-$Ni(OH)_2$.[218,219] In situ XANES on a NiOOH film deposited from a nickel-containing borate electrolyte exhibited a oxidation state of 3.6^+, indicating a predominant portion of γ-NiOOH during water oxidation.[220]

Trotochaud et al. argued that during the aging process, NiOOH could collect Fe impurities gradually from the electrolyte, changing the surface electronic properties and contributing to the improved activity.[221] They found an increase of over 30 times in conductivity by incorporating Fe into the α-$Ni(OH)_2$ films. However, conductivity alone is not a complete explanation. In situ EXAFS revealed that under water oxidation conditions, the average coordination number of Fe atoms increased, indicating that Fe participates in the WOR.[222]

In situ Raman spectroscopy by Louie et Bell indicated that NiOOH is the possible active phase for the WOR.[223] They also observed that the Ni–O environment was modified by Fe, according to the change in relative peak intensity at 475 and 555 cm^{-1} (assignable to the NiOOH band). Their relative intensity reflects the local structure of Ni–O, which could be affected by factors like Ni–O interlayer spacing, the presence of ions (e.g. K^+) between the sheets, structural disorder of the sheet, and metal oxidation states. They later correlated the water oxidation activity trend to the Ni–O vibration, implying that the Ni plays an active role in the WOR.

Nocera et al. observed by in situ XANES that Fe^{3+} induced the formation of Ni^{4+} in the NiFe layered double hydroxides film, which contributed to the enhanced activity, supporting the previous conclusion that Ni is the catalytic active center towards the WOR.[224]

Gewirth et al. explored the kinetic isotope effect to probe the nature of the RDS (**r**ate-**d**etermining **s**tep) using Ni oxide films deposited on an Au substrate in 1 M NaOH and 1 M NaOD solutions. They found that the k_H/k_D value was 0.5 for Ni oxide, suggesting that the OH bond is not directly cleaved during the RDS and that the RDS involves forming or breaking of a bond within the vicinity of OH, and/or with a change of the metal center from a less hybridized state to a more hybridized state.[225] Further studies in determining the active sites, the RDS, and identifying the reaction pathways (e.g. oxygen formation by direct coupling or acid–base mechanism) are crucial to better understand the WOR process and to develop new active catalysts.

1.2.5.5 Catalysts for water oxidation in base

Soon after their discovery of Ni-based alkaline batteries, Edison and Junger found that Fe could poison the Ni oxide material. Such an effect could be observed with concentrations below 1% Fe and was attributed to the catalytic behavior of conducting ferric oxide in the study by Mlynarek et al. [226–228] In the 1980s, Corrigan first investigated the catalytic WOR activity of NiFe hydroxides.[229] This initial work laid the foundation for future development of NiFe water oxidation catalysts. In addition, as a special class of LDH (**l**ayered **d**ouble **h**ydroxides) materials, NiFe LDH arouse interest owing to their good water oxidation activity.[230]

Layered double hydroxides are a class of layered materials consisting of positively charged layers and charge balancing anions in the interlayer regions. The excessive positive charge is generated by partially replacing divalent cations (e.g. Mg^{2+}, Ni^{2+}, Ca^{2+}, Mn^{2+}, Co^{2+}, Cu^{2+}, Zn^{2+}) or monovalent cations (e.g. Li^{+}) in the hydroxide layers by trivalent cations (e.g. Al^{3+}, Fe^{3+}, Co^{3+}, Cr^{3+}). The intercalated ions could be CO_3^{2-}, NO_3^{-}, Cl^{-}, SO_4^{2-}, and OH^{-}.[231,232] The layered structure leads to more surface accessible sites, thus the LDH materials are attractive candidates as electrochemical catalysts.

Synthesis of NiFe LDH includes solvothermal or hydrothermal methods, the co-precipitation at a constant pH, and the cathodic or anodic electrodeposition.

1. *Solvothermal or hydrothermal methods*

A solution containing metal salt precursors is mixed with a weak base (amines or ammonia), to form NiFe LDH; urea[233–235] and dimethylformamide[236] are typical bases. This method requires an elevated temperature to process the hydrolysis in autoclaves. Well crystallized nanoplates generally are obtained in hexagonal shapes, reflecting the symmetry of the layers. Gong et al. first reported NiFe LDH materials prepared by slow hydrolysis of metal salts ($Ni(CH_3COO)_2$ and $Fe(NO_3)_3$) at 85 ^{o}C, followed by hydrothermal reaction at 120 ^{o}C for 12 h and 160 ^{o}C for 2 h in the presence of dimethylformamide.[236] They obtained ultrathin LDH nanoplates (~ 5 nm). With the addition of a chelating reagent (e.g. ethylene glycol), different morphologies can be obtained, such as flower-like nanoparticles.[233,237] This method allows the growth of NiFe LDH onto a wide variety of substrates like graphene,[238] carbon quantum dots,[239] and Ni foam substrates.[235]

2. *Co-precipitation at constant pH*

One of the most used methods is to synthesize NiFe LDH by the co-precipitation of the metal precursors (Ni^{2+} and Fe^{3+} or Fe^{2+}) at constant pH (9 to 13) by adding a base or a carbonate (e.g. KOH, Na_2CO_3).[240,241] Increasing the temperature favors the crystallinity of the materials. The mechanism for the formation of NiFe LDH was studied by Gregoire et al. by titrating an aqueous solution of the two precursors.[242] They proposed that the precipitation of ferric oxyhydroxide occurs first, followed by the adsorption of cationic complexes, like $[Ni(OH)(H_2O)_5]^+$, which further evolve into molecular clusters. Ultimately, NiFe LDH are formed by diffusion of ions from the ferric oxyhydroxide phase into the α-$Ni(OH)_2$ phase and anion intercalation. The particles formed by this method usually show nanoplate morphologies.

3. *Electrodeposition*

Electrodeposition is another common method to synthesize NiFe LDH. Cathodic electrodeposition at a constant current in a solution containing nickel and iron precursors results in NiFe based hydroxides.[221,243,244] The pH of the deposition solution is generally close to 7. One proposed mechanism for the deposition is based on NiFe precipitation onto substrates due to the local basic pH upon reduction of anions (e.g. nitrate, eq 1.55), though the hydrogen evolution and reduction of metal ions could happen simultaneously.

$$NO_3^- + H_2O + 2\ e^- \rightarrow NO_2^- + 2\ OH^- \qquad 1.55$$

Usually, the film prepared is rough and amorphous or poorly crystallized. A variation of the cathodic galvanostatic deposition is reported by Boettcher et al., in which they used a sequential 2 s pulsed -10 mA cm^{-2} current with 10 s intervals for 20 cycles; this method is proven effective to prepare thick films.[244] Anodic electrodeposition is rarely used; however, Morales-Guio et al. showed the anodic deposition of $FeNiO_x$ on FTO (**f**luorine doped **t**in

oxide) and Au substrates.[245] Electrodeposition of a NiFe alloy in an ionic liquid was reported by Lo et al. In this work the film was deposited on a Cu substrate under potentiostatic conditions, and it was later converted to a hydroxide after cycling in a 0.1 M NaOH solution.[246]

The large interlayer distance on the NiFe LDH materials makes the exfoliation[f] of the nanoplates possible. Song and Hu reported a synthetic route in which they exfoliated NiFe LDH with formamide.[247] The exfoliated LDH have a thickness of ~ 0.8 nm, implying single or double layer structures. The WOR activity improved significantly upon exfoliation, and they proposed that after exfoliation, increased number of electrochemically active atoms were exposed.

[f] *Exfoliation of the layered double hydroxides refers to the process that forms intact single layers of hydroxides with nanometer thickness.*

1.3 **Dye-sensitized photoelectrochemical cells**

PECs (photo**e**lectrochemical **c**ells) are devices that convert solar energy to chemical fuels, e.g. water into hydrogen and oxygen. An ideal PEC should combine low cost materials with high quantum efficiency, selectivity, and longevity. DSPECs (**d**ye-**s**ensitized **p**hoto**e**lectrochemical **c**ells) integrate SC (**s**emi**c**onductor), molecular chromophores (photosensitizers) that absorb light, and surface-bound catalysts, and this separation of functions allows for independent optimization, and to some extent, it separates the processes that occur within the DSPEC for study.[248,249]

In the 1970s, Fujishima and Honda reported the first UV-light water splitting electrochemical cell. The cell was built with anatase TiO_2 and a Pt CE (**c**ounter **e**lectrode).[250] The TiO_2 absorbed light, forming a hole–electron pair. Then, the hole migrated to the TiO_2 surface where H_2O was oxidized, and the electron migrated to the Pt wire where H_2 was evolved. In the first reported DSPEC in 1999, 2-propanol was dehydrogenated to acetone over the Ru polypyridyl chromophore-catalyst assembly (Ru1 in Figure 1.11) on TiO_2, and water was reduced to hydrogen at the Pt counter electrode.[251] Mallouk et al. reported a visible light water splitting DSPEC in 2009 using IrO_x nanoparticles as the water oxidation catalysts and Ru2 as the chromophore (Figure 1.12).[252] Many developments have been made based on these systems in recent years.[253–263]

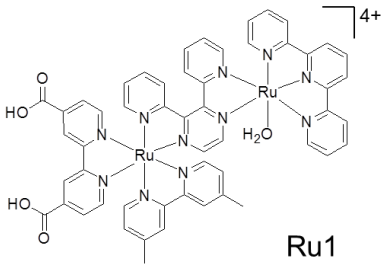

Figure 1.11 Molecular structure of Ru chromophore-catalyst assembly.

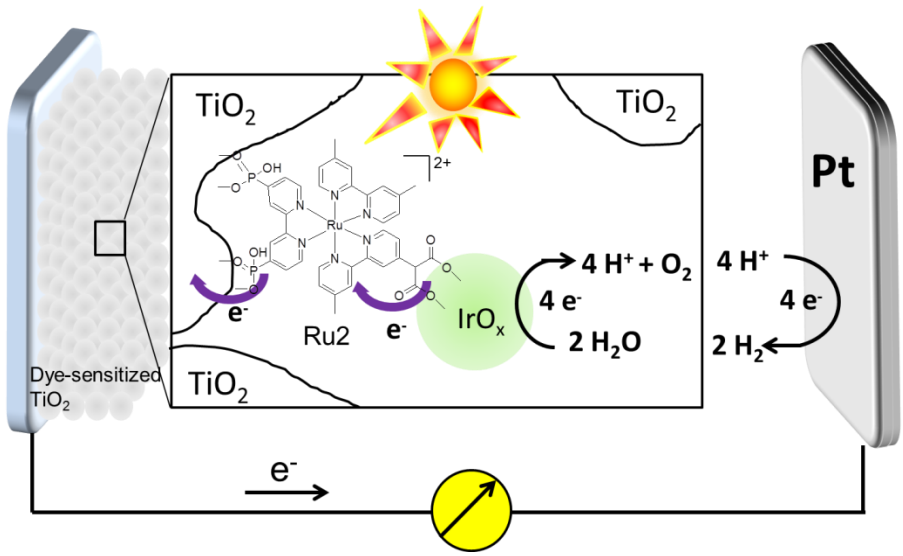

Figure 1.12 Illustration of the first visible light DSPEC for water oxidation.

1.3.1 Photoanodes for DSPECs

Photoanodes for DSPEC consist of three major components: a light-absorbing chromophore (dye, photosensitizer), a water oxidation catalyst, and a semiconductor. Under light irradiation, a sequence of events take place at the photoanode: (1) light absorption by a surface-bound chromophore forms an excited state; (2) electron injection from the excited state of the chromophore to the conduction band of the n-type

semiconductor (in this case anatase TiO_2) forms an oxidized chromophore; (3) electron transport to a cathode or, ideally, a photocathode, generates hydrogen; (4) electron transfer from the WOC (**w**ater **o**xidation **c**atalyst) to the oxidized chromophore; and (5) repetition of the process four times generates oxygen.[248] However, the recombination process could happen between the oxidized chromophore and the electron in the SC conduction band or in the trapped states[g] at the surface, leading to decreased performance.

The following requirements must be fulfilled to successfully fabricate an efficient photoanode:

- The oxidation potential of the chromophore must be higher than the operating potential of the WOC.
- The chromophore's excited states must have a lower reducing potential than the conduction band of the SC.
- The chromophore should be able to transfer four electrons consecutively to the catalyst before any unfavorable recombination process occurs.
- The WOC should have long-lived intermediate oxidation states to accumulate multiple oxidizing equivalents before recombination happens.
- The chromophores and WOCs must be stable under operating conditions.
- The electron transfer between injection of the excited-state chromophore to the SC

[g] *The trapped states assume that the charge carriers are confined to the surface or in the bulk of a system and cannot participate in the charge transport. Their wave function is localized relative to the distance between trapped states, therefore, the transfer probability between states is low.*

conduction band, from WOC to oxidized chromophore, and from water to the WOC needs to be fast.

- The surface anchoring group between the chromophore and the SC surface is crucial to avoid desorption, to facilitate electron injection, and to survive the oxidizing environment with long-term solar irradiation.[264]

Interested readers are directed to these excellent reviews on DSPECs.[248,264–266]

To date, the most active photoelectrochemical water oxidation system was reported by Sun et al. The $[Ru(bpy)_2(4,4'\text{-}PO_3H_2)_2bpy]^{2+}$ (bpy = 2,2'-bipyridine) chromophore (Ru3 in Figure 1.13) and Ru molecular water oxidation catalyst (Ru4 in Figure 1.13) were co-adsorbed on a TiO_2 coated FTO electrode. With Pt as the counter electrode, the water oxidation current reached 1.7 mA cm^{-2} at 0.2 V versus **n**ormal **h**ydrogen **e**lectrode (V_{NHE}) bias under 300 mW cm^{-2} Xenon lamp irradiation (> 410 nm) in a pH 6.8 phosphate buffer solution.[259]

The nanoparticle IrO_x also has been reported as a WOC, though its activity was inferior to that of the molecular water oxidation systems. Mallouk et al. prepared the photoanode based on the chromophore Ru5 and the IrO_x catalyst bonded with a benzimidazole–phenol (BIP) electron mediator to facilitate the electron transfer from IrO_x to the excited Ru chromophore (Figure 1.14). This electron mediator was designed to mimic the tyrosine/histidine pair of residues in Photosystem II. The 2-carboxyethylphosphonic acid (CEPA) binds the IrO_x to the TiO_2 surface. A 80 uA cm^{-2} photocurrent was generated with 0.55 V_{RHE} using a 150 W Xe lamp (> 410 nm) as the light source in pH 5.8 Na_2SiF_6–$NaHCO_3$ (2:3) silicate buffer with a 0.1 M $NaClO_4$ solution.[267] Interested readers are directed to these excellent review papers on other

photoelectrochemical water oxidation systems.[248,265]

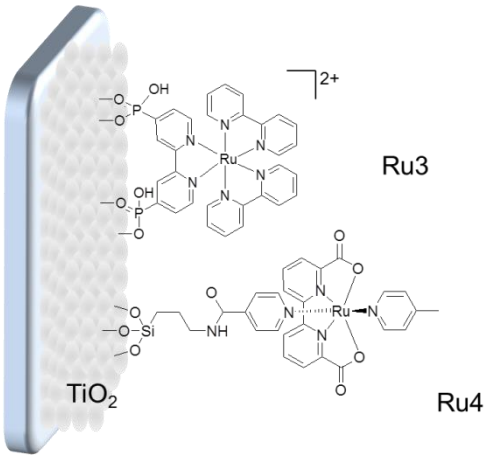

Figure 1.13 Structure of the photoanode reported by Sun et al. for DSPEC.

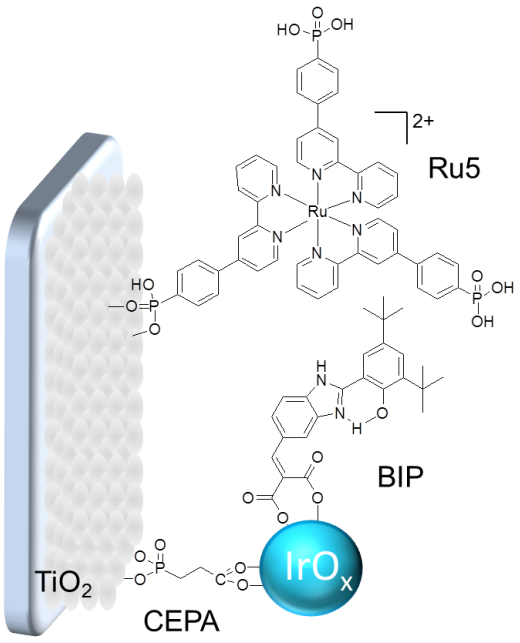

Figure 1.14 Structure of the photoanode reported by Mallouk et al. for DSPEC.

1.3.2 Anchoring groups

The most commonly used anchoring groups to attach chromophores and catalysts to the SC surfaces are carboxylic acids and phosphonic acids.[268–270] Recent research into hydroxamic acids and silatrane anchoring groups also shows promising results (Figure 1.15).[271–275]

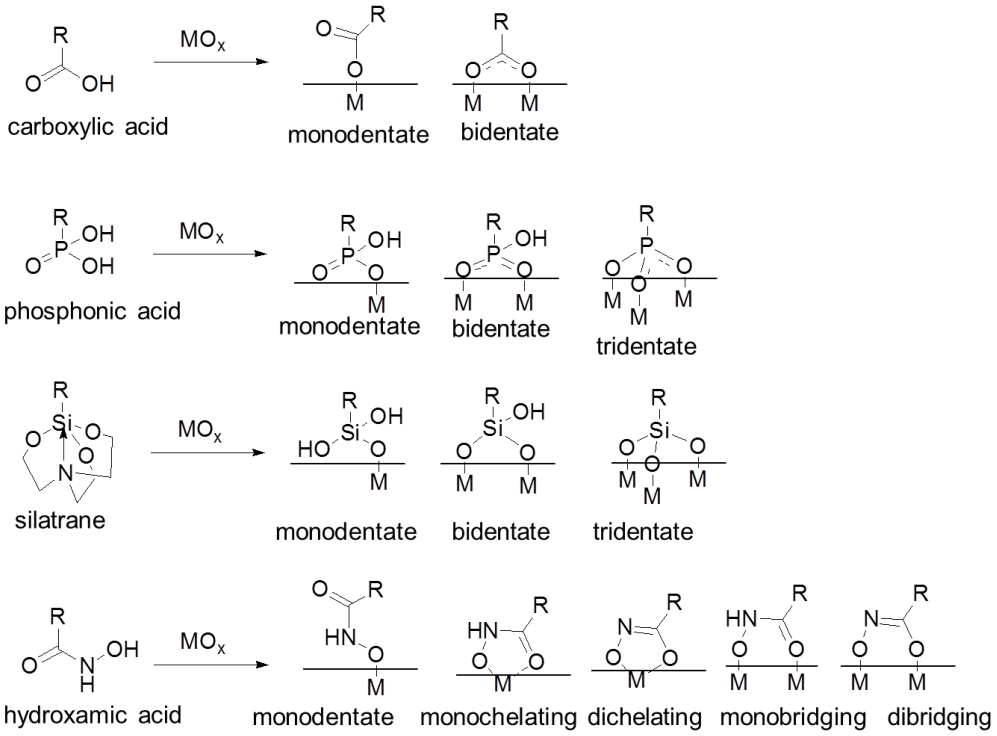

Figure 1.15 Possible binding modes of carboxylic acid, phosphonic acid, silatrane and hydroxamic acid groups bound to a metal oxide surface (MO_x).

The binding modes of these anchors to the surface were investigated by FTIR and computational simulation. Figure 1.15 summarizes the most possible binding modes of the surface anchoring groups on an oxide SC surface (MO_x). The hydrogen bonding between the anchoring group and the surface hydroxyl group or between adjacent surface

anchoring groups is not shown here. Carboxylic acid groups bind with the surface preferably through the bidentate mode, with monodentate binding observed but less favored (Figure 1.15).[269,276,277] It is well-known that the carboxylic acid anchoring groups are only stable in pH < 4 in aqueous conditions.[271,277] At higher pHs, hydrolysis occurs, leading to the release of the bound molecule.[269,278]

The phosphonic acid anchors show three binding modes, with the bidentate mode preferred.[269,271,277] They show better stability than the carboxylic acid anchors and are stable in pH < 7 solutions.[254,277,279] Transient absorption spectroscopy on the perylene derivatives with carboxylic acid and with phosphonic acid groups on TiO_2 revealed that the electron injection rate for carboxylic acid anchors was twice as high, implying stronger electronic coupling of the carboxylic acid groups with TiO_2. This strong coupling was explained by the DFT calculation, which revealed that the extension of the LUMO (**l**owest **u**noccupied **m**olecular **o**rbital) wave functions onto the anchoring group was significantly different for the carboxylic acid groups and the phosphonic acid groups. The higher degree of the LUMO extension to carboxylic acid anchoring groups was related to their sp^2 hybridization, compared with the sp^3 hybridization of the phosphonic acid anchoring groups, which has less degree of LUMO extended to it.[269,279,280]

Silatrane also has three binding modes with the surface, predominantly bidentate. The loss of the silatrane cage is believed to happen through nucleophilic attack by the surface hydroxyl groups, releasing the triethanolamine group.[271,273] The silatrane anchoring groups are stable over a wide range of pH (2–11).[271] The electron injection efficiency using the silatrane anchoring groups is less studied. Transient absorption spectroscopy comparing the decay of the porphyrin radicals with the carboxylic acid or

silatrane anchoring groups on SnO_2 showed that the one with carboxylic acid anchoring groups decayed faster, suggesting that the electron injection efficiency was lower on silatrane anchoring groups.[281]

The hydroxamic acid anchors show five different binding modes, with monochelating by using two oxygen atoms the preferred mode.[274,278] In aqueous solutions, the hydroxamic acid anchors are stable at pH 2–10.[271] The hydroxamic acid anchoring groups show efficient electron injection. The time constant for electron injection of the hydroxamic acid groups was twice that of the carboxylic acid groups, as shown by time resolved picosecond terahertz spectroscopy. However, the recombination rate was three times higher than that of the carboxylic acid anchoring groups, leading to an overall lower electron injection efficiency than for the carboxylic acid anchoring groups.[272,275,282]

1.3.3 Stabilization of chromophore surface bindings

Surface desorption of the chromophore is observed to be accelerated by illumination of carboxylic acid and phosphonic acid anchored ruthenium bipyridine chromophores.[280] In addition, hydrolysis of these surface chromophores bound by ester groups is catalyzed by OH^- (Scheme 1.2), but the WOR rates typically increase with increasing pH.[248,283,284] Therefore, stabilizing the surface bindings, as well as developing alternative stable bindings between chromophores and the SC, is desirable.

Scheme 1.2.

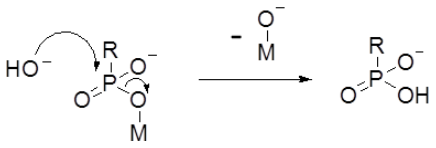

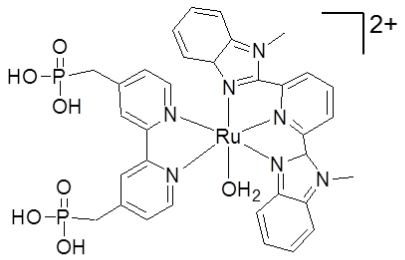

Ru6

Figure 1.16 Molecular structures of water oxidation catalyst Ru6.

Strategies have been developed to stabilize the linkage between chromophores and metal oxide surfaces. The most effective strategy is ALD (**a**tomic **l**ayer **d**eposition) of oxide overlayers, such as TiO_2 and Al_2O_3, after surface binding.[285,286] In the ALD technique, a reactive gas ($Al(CH_3)_3$ for Al_2O_3 and $TiCl_4$ for TiO_2) is exposed to the sensitized photoelectrode. Reaction of the precursor with the surface, followed by hydrolysis, yields one or few atomic layers of the oxides, and these layers function like a glue to bind the molecules to the surface.[248] Lapides et al.[287] first deposited a layer of ALD Al_2O_3 on a $[Ru(bpy)_2(4,4'\text{-}(PO_3H_2)_2bpy)]^{2+}$ (Ru3) sensitized nano-**i**ndium **t**in **o**xide (ITO) electrode, then the Ru6 water oxidation catalyst was adsorbed on top of the ALD Al_2O_3 layer, followed by another ALD Al_2O_3 layer to protect the Ru6 catalyst. Figure 1.16 shows the structures of the Ru catalyst. The resulting electrode was used to photoelectrochemically oxidize water in a 0.1 M $H_2PO_4^-$ /HPO_4^{2-} (pH 8.8) and 0.4 M $NaClO_4$ splution at 0.64 V_{NHE}, and the photocurrent was stable for 6 h at 6 μA cm^{-2} under continuous irradiation. In addition, the use of ALD to deposit an alumina overlayer incorporates the benefits of hindering the recombination process. However, high cost and sophisticated instrumentation are required to carry out the ALD deposition.

Dip-coating the sensitized photoanodes with PMMA (**p**oly(**m**ethyl**m**eth**a**crylate)) also has been studied as a way to stabilize the surface.[261,288] Compared with the ALD process, the dip-coating process can be applied by soaking the electrodes in a PMMA solution. The coating thickness can be controlled by the soaking time and the PMMA concentration. Wee et al. coated the $[Ru(bpy)_2(4,4'\text{-}(PO_3H_2)_2bpy)]^{2+}$ (Ru3) sensitized TiO_2 electrode with a PMMA overlayer, and a 10% decrease in photocurrent was observed in 1000 s in a 0.1 M phosphate buffer (pH 7), with 0.4 M $NaClO_4$ and 20 mM hydroquinone as the sacrificial electron donor.[288] However, thicker PMMA layers will block the pores since the polymer is hydrophobic, and the electron transfer rate between the electrode and the electrolyte may be hindered. To solve the insulating problem, Ding et al. mixed the molecular catalyst Ru7 (Figure 1.17) with 2 wt% PMMA and coated it on the $[Ru(bpy)_2(4,4'\text{-}(PO_3H_2)_2bpy)]^{2+}$ (Ru3) sensitized TiO_2 electrode. The incorporation of the catalyst molecule activates the PMMA layer for the WOR, and a photocurrent of 1.1 mA cm^{-2} was observed in a pH 6.8 phosphate buffer under 300 mW cm^{-2} illumination with 0.2 V_{NHE} applied bias.[261]

A direct binding method between the pyridine group on the Ru8 (Figure 1.17) chromophore with the TiO_2 surface was demonstrated by Takijiri et al. by immersing the TiO_2 coated FTO electrode in a solution containing Ru8.[289] A sustained photocurrent was observed with 30 mM EDTA as the sacrificial electron donor in a 0.1 M $NaClO_4$ and 0.1 M acetate buffer solutuion (pH 5.0). The binding of the chromophore to the surface was confirmed by UV–vis (**u**ltra**v**iolet–**vis**ible spectroscopy). The photocurrent degraded by 7% after 100 min under continuous irradiation. However, the electron injection properties have not been evaluated on these pyridine anchoring groups.

Although these methods can protect the chromophores from desorption under slightly basic conditions, the photocurrent generation ability under strong alkaline conditions (e.g. pH = 13) using these systems is unknown. Considering the fact that it is desirable to carry out photoelectrochemical water oxidation in strong alkaline conditions, developing stable chromophore–SC binding is crucial in the development of DSPECs.[248]

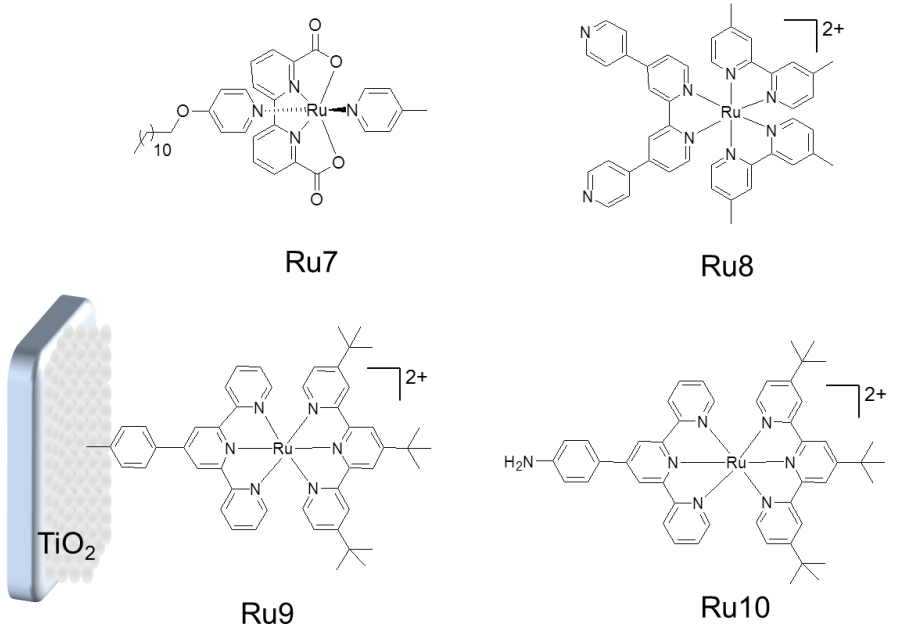

Figure 1.17 Structures of the Ru complexes.

Meyer et al. used Ru-diazonium electro-grafting to form direct C–O^{surf} covalent bonding of Ru9 on a TiO_2 surface. A 2 mM Ru10 sensitizer (Figure 1.17) in 100 mM tetrabutylammonium perchlorate CH_3CN solution was mixed with 1.5 mM *tert*-butyl nitrite at 0 ^oC. The TiO_2 electrode was held at a potential ranging from -0.1 to 0.1 V_{NHE}

for 30 min. The resulting electrode was active and stable at pH 12 towards triethanolamine oxidation.[290] XPS indicated that the Ti–O–C bonding was formed. This approach, however, requires excess amounts of Ru organometallic–diazonium compound that cannot be reused, and the lifetime of the radical intermediate depends upon the nature of the compound.[291] An alternative is to deposit the ligand using a diazonium-reduction method first, then metalation to form desired chromophores on the surface. Diazonium-based ligand modified surfaces are suitable for binding organometallic complexes as well as macromolecules, and this process is cost-effective since it does not involve the formation of precious-metal based radicals.[292] In addition, the versatility of this method allows a variety of metal complexes to be grafted on the surface following a similar protocol.

1.4 **Research Objectives**

1. Developing active ORR electrocatalysts for fuel cells

Active ORR electrocatalysts are required in acid and in base because the ORR is significantly slower than the HOR. Nanoparticle ORR catalysts are susceptible to sintering over time, reducing the number of surface active sites. I aim to prepare Pt overlayers on Ni GLAD (**gl**ancing **a**ngle **d**eposition) nanopillars, and investigate their surface properties, ORR activity, and stability. My goals include optimization of the deposition method, and to investigate possible mechanisms (e.g., electronic effect, strain effect) that the Ni GLAD substrate enhances the ORR activity of Pt. These results are described in Chapter 2 and Chapter 3.

2. Developing active WOR electrocatalysts for water electrolysers

The kinetics for the WOR are lower than the HER, leading to the largest energy efficiency losses in water electrolysers. Therefore, active catalysts are required for the WOR in acid and in base. Ideally, for large-scale industrial applications, the synthetic procedure for electrocatalysts should be simple and easily-scalable. I aim to find a one-step aqueous method to synthesize a series of active water oxidation catalysts.

For WOR electrocatalysts in acid, the goal is to find active Ir–transition metal hydrous oxide nanoparticles with high mass-normalized, and electrochemically active site-normalized WOR activity with good stability. Attempts will be made to understand the mechanism of the enhancement of WOR activity caused by doping with earth-abundant transition metals. These results are described in the Chapter 4 and Chapter 5 for $Ir_{1-x}Ni_x$ and $Ir_{1-x}Cu_x$ HO-np (**h**ydrous **o**xide **n**ano**p**articles), respectively.

A series of binary HO-np consisting of first-row transition metals will be investigated as WOR electrocatalysts in base. The results from $Ni_{1-x}Fe_x$ HO-np are described in Chapter 6. Besides understanding the origins of the enhanced activity of $Ni_{1-x}Fe_x$ HO-np over Ni HO-np and Fe HO-np, I also aim to explore the influence of the catalyst support on the WOR activity.

These studies will, in principle, provide an economic route to industrial-scale WOR catalysts, and promote the widespread application of the water electrolysers. Also, the acquired insights on the WOR mechanism will guide catalysts preparation and optimization in future studies.

3. Construction of stable chromophore–semiconductor photoelectrodes

Common groups that anchor chromophores to semiconductors in DSPECs are stable only under acidic conditions. Alkaline conditions are desireable for the WOR and the CO_2 reduction reaction. I aim to develop a new and reliable method to form base-stable covalent bonds between chromophores and semiconductor surfaces using diazonium chemistry. Spectrocopic characterizations will be carried out to investigate the surface bond. The photocurrent responses will be evaluated, and the stability will be compared to the photoelectrodes with typical phosphonic ester anchoring groups. Chapter 7 describes this new method and the results. This research will pave the way for the utilization of DSPEC in alkaline conditions, and ultimately lead to its wide application as a solar-to-fuel energy conversion device.

Chapter 2 Glancing Angle Deposited Ni Nanopillars Coated with Conformal, Thin Layers of Pt by a Novel Electrodeposition: Application to the Oxygen Reduction Reaction[a]

2.1 Introduction

Tireless efforts have been directed towards improving the sluggish ORR over Pt because Pt is a common component of the most active ORR catalysts.[67,72,75,293] The most studied approach is to prepare alloys or composite structures containing Pt with various non-noble metals and then study their properties in acidic or basic electrolytes.[294–297] Such alloys often undergo dealloying (i.e., selective dissolution of the non-noble metals in acid) or lose activity due to the destructive electrodissolution of the active materials in acid.[298] In most cases, the initial use of basic conditions to study a newly developed combinatory catalyst would minimize significant changes in its structure and composition due to the dissolution. The use of alkaline electrolytes allows for convenient screening of the near as-prepared

[a] *A version of this Chapter has been published. Xu, S.; Wang, C.; Francis, S. A.; Tucker, R. T.; Sorge, J. B.; Moghaddam, R. B.; Brett, M. J.; Bergens, S. H. Electrochimica Acta 2015, 151, 537.*

structure, activity, and durability of the ORR electrocatalysts. Furthermore, the results of such studies are relevant to the development of alkaline fuel cells.[299,300]

A great deal of attention has been focused on the study of the ORR in alkaline media using Pt as a catalyst in binary and ternary combinations with non-noble transition metals.[301,302] For instance, Garcia-Contreras et al. reported that PtNi and PtNiCo made by chemical vapor deposition were both more active than Pt in KOH solution, with the latter giving the best activity.[303] A comparative theoretical and experimental survey of the ORR in 0.1 M KOH by Pasti et al. showed that the Pt–In alloy was 2.6 times more active than Pt.[304] Later, Jaeger and coworkers showed that a Pt–C(Mo_2C) catalyst was more active than the Pt/Vulcan carbon towards the ORR in base.[305]

Vacuum sputtering/deposition methods have been used to prepare electrocatalysts reproducibly with control over structure and composition.[306–319] The use of GLAD materials as oxygen reduction electrocatalysts also was reported recently.[311–318] GLAD is a PVD (**p**hysical **v**apor **d**eposition) technique performed in vacuum, and the microstructural control is achieved by the precise motion of the substrate relative to the incoming vapor flux.[319,320] Figure 2.1 illustrates the GLAD process.

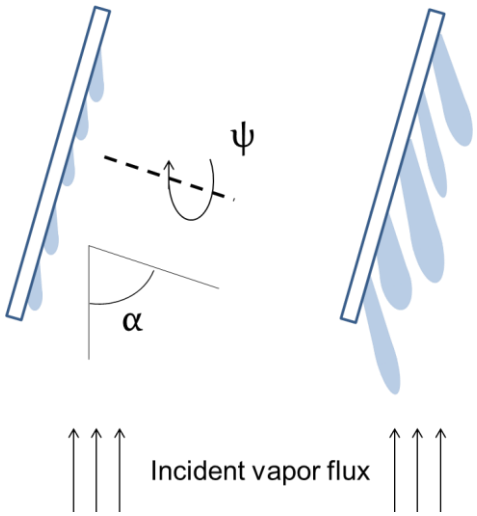

Figure 2.1 A schematic illustration of the oblique deposition angle, α, and the rotation angle relative to the substrate normal ψ, as defined in the GLAD process.

The oblique deposition angle, α, is the angle between the incident vapor flux and the substrate normal, while the angle of rotation relative to the substrate normal is denoted as ψ. During the deposition, the obliquely incident atoms are able to nucleate only onto the highest points of the substrate surface due to a self-shadowing effect. With increasing flux deposition, this self-shadowing effect leads to columnar or pillar-shaped growth. The porosity and nanopillar spacing can be controlled by changing α. Further morphology control can be achieved by modulating the substrate rotation in ψ, and this allows the formation of various structures (e.g. vertical columns, slanted posts, chevrons, square spirals, helices, and combinations thereof). The high level of morphology control, inherent to GLAD, would lead to well-tailored nanostructures that can be used in a variety of

applications, including electrocatalysis. Moreover, large-area GLAD films have been prepared in a prototype roll-to-roll system that can be extended to the mass production of these materials.[321]

The Gall group reported various studies of GLAD-based electrodes in PEM fuel cells.[311–314] For example, 100 to 500 nm GLAD Pt nanorods were sputtered at $\alpha = 87°$ directly onto gas diffusion layers and incorporated into PEMFCs as cathodes. These were compared to Pt cathodes prepared at the normal incidence of $\alpha = 0°$. The GLAD Pt cathode had a lower electrochemically active surface area but a higher porosity than the cathode prepared at $\alpha = 0°$. The mass specific activity of the GLAD-based cell was higher than the $\alpha = 0°$ system, suggesting that mass transport was more facile in the GLAD-based cathode.[314] In another report, Pt sputtered onto 500 nm GLAD carbon nanorods were incorporated into a fuel cell and etched in situ by applying cell voltages between 1.2 and 1.7 V. The etching improved the performance of the cell, suggesting that mass transport was also more facile in the etched cathode.[312]

Brett et al. collaborated with the research groups of Wilkinson and Dahn to report Pt sputtered on GLAD annealed niobium oxide and titanium nanopillars, respectively.[315,316] Both reports showed 11 to 13 times surface area enhancement of the catalyst due to the high surface area of the GLAD supports. The room-temperature ORR studies in 0.1 M $HClO_4$ showed that Pt/GLAD Ti could achieve current densities of 0.5 mA cm^{-2}, while the

annealed niobium oxide-supported Pt displayed current densities ≥ 1 mA cm^{-2} at 0.9 V_{RHE}. Moreover, the latter catalyst withstood aggressive electrochemical testing up to 1.4 V_{RHE}, and its morphology was stable at 1000 °C.

The Bergens group reported the first study of alcohol oxidation with GLAD-based electrocatalysts.[322] Specifically, Pt was deposited electrochemically onto 500 nm long Ni_{GLAD} nanopillars supported on Si wafers (Ni_{GLAD}/Si). Two Pt deposition methods were compared. The first was a traditional potentiostatic deposition from Pt salts dissolved in acidic electrolytes. This deposition mainly placed the Pt on the tops of the Ni_{GLAD} nanopillars to give a layered structure with Ni on the bottom and Pt on the top (referred to herein as $Pt_{Tr}Ni_{GLAD}$/Si). The second Pt deposition was an unconventional, self-limiting, galvanostatic one (J = -100 mA cm^{-2}, normalized to the geometric area of the Si support under the Ni_{GLAD}), with a Pt counter electrode as the source of Pt in a 2.0 M NH_4Cl electrolyte resulting in a conformal Pt coating on the Ni_{GLAD}/Si.[323,324] This core-layer catalyst is referred to as Ni_{GLAD}{Pt}/Si. Both $Pt_{Tr}Ni_{GLAD}$/Si and the core-layer Ni_{GLAD}{Pt}/Si were more active in the electro-oxidation of 2-propanol in base than Pt foil or Ni_{foam}{Pt} (made by a similar Pt CE deposition on a Ni foam).[324] At low overpotentials (0.05–0.30 V_{RHE}), the electrochemically active surface atom normalized activity of Ni_{GLAD}{Pt}/Si was higher than the unsupported Pt and Pt–Ru nanoparticles as well. Interestingly, the Ni_{GLAD}/Si substrate without added Pt was active towards 2-propanol

electro-oxidation at low potentials.

This Chapter presents the first ORR study on GLAD Ni supports over which Pt was electrochemically deposited using a rotating disc electrode. Using the versatile GLAD methodology we have been able to cast Ni on a bare glassy carbon electrode with control over shape, quantity, and distribution. Here, a higher value of α (α = 88°) than previous studies with Ni_{GLAD}/Si (α = 85°) was set to decrease the surface density of the nanopillars in an attempt to facilitate the mass transport of O_2 in the catalyst layer.[325,326] As well, we used a modified version of the Pt CE deposition with the WE (**w**orking **e**lectrode) rotating at high rates to prepare Ni_{GLAD}{Pt}/GC core-layer nanopillars with minimal mass transport effects. This technique appears to deposit controlled amounts of Pt uniformly over the Ni pillars. The resulting structures survived fast WE rotation during the ORR tests in the absence of binders such a Nafion®. This approach is beneficial for mechanistic studies, for benchmarking catalysts, and for testing novel catalyst materials while avoiding intrinsic complications (e.g. mass transport and stability problems) commonly encountered with binding agents.

2.2 **Results and Discussion**

2.2.1 Morphology and electrochemistry of Ni_{GLAD}/GC

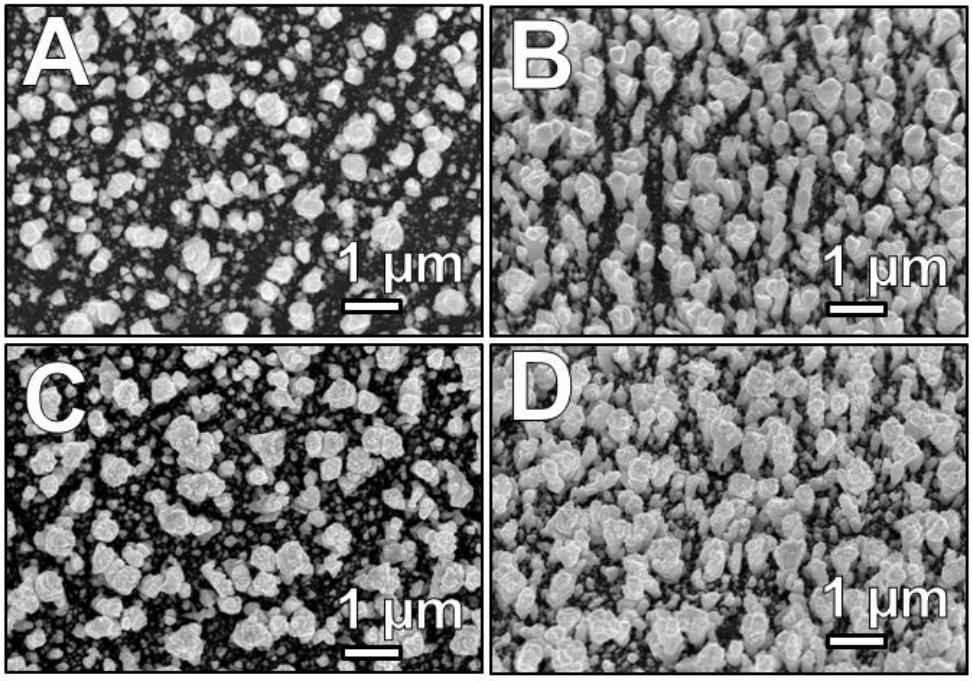

Figure 2.2 Scanning electron micrographs showing the (A) top-down and (B) 45 degree oblique side view of a Ni_{GLAD}/GC electrode, as well as the (C) top-down and (D) 45 degree oblique side view of an as prepared Ni_{GLAD}{Pt}/GC electrode.

Figure 2.2 shows top (A) and 45° oblique side (B) views of SEM (**s**canning **e**lectron **m**icroscopy) results of the as-prepared Ni_{GLAD}/GC electrode. The Ni nanopillars are columnar, roughly perpendicular to the surface of the glassy carbon, ~ 500 nm tall, and widen with increasing height, with an average maximum diameter of ~ 200 nm, and are distributed evenly on the surface. The typical mass of the Ni deposits was 62.5 μg (1.06 ×

10^{-6} mole Ni), or 500 μg cm^{-2} (8.35×10^{-6} mole cm^{-2}), as determined by ICP–MS (**i**nductively **c**oupled **p**lasma–**m**ass **s**pectrometry) after dissolution of the Ni deposit.

Figure 2.3 shows typical CVs (**c**yclic **v**oltammograms) of five consecutive cycles for the Ni_{GLAD}/GC substrate in 1.0 M KOH in the range 0–0.40 V_{RHE} (sweep rate = 10 mV s^{-1}). This range covers the reversible, 2-electron Ni/α-$Ni(OH)_2$ conversion, and it avoids the irreversible formation of β-$Ni(OH)_2$ at higher potentials.[327–329] This process is shown in eq 2.1.

$$Ni + 2\ OH^- \rightarrow\ \alpha\text{-}Ni(OH)_2 + 2\ e^- \qquad 2.1$$

The first scan displayed a weak anodic wave at ~ 0.05 V_{RHE} on the forward sweep, which disappeared in the subsequent cycles. This anodic peak likely arises from the oxidation of adsorbed hydrogen that would have formed during the initial polarization at 0 V_{RHE}.[328] Unlike previous reports with bulk polycrystalline Ni that typically contain a well-defined anodic peak at ~ 0.23 V_{RHE},[327–329] the anodic sweeps for Ni_{GLAD}/GC only showed an oxidative region with two broad peaks at ~ 0.12 and ~ 0.25 V_{RHE}, ascribed to the Ni/α-$Ni(OH)_2$ conversion. A similar broadening was observed previously in the CVs of Ni_{GLAD}/Si in base.[324] This broadening likely is due to differences in the nature and distribution of the active sites on the Ni_{GLAD} nanopillars and on bulk, polycrystalline Ni. A previous study reported only slight differences in the peak potentials of the anodic waves in the Ni (110), (100), and (010) crystal faces, further suggesting that the broad nature of this

wave is a unique property of Ni_{GLAD}/GC or Ni_{GLAD}/Si. A large reduction peak at ~ 0.06 V_{RHE}, which is due to the reduction of α-$Ni(OH)_2$ to Ni, is the prevailing feature of the cathodic scan.[327–329] The cathodic features of the CVs did not change appreciably with cycling. The evolution of H_2 over Ni_{GLAD}/GC commences at ~ 0.02 V_{RHE}, which is more positive than that over bulk, polycrystalline Ni.[323,324] The charge under the fifth sweep of the cathodic wave, down to the onset of the H_2 evolution, was used to approximate the EASA of Ni_{GLAD}/GC. For a typical sample, this charge was 1182 μC. The charge acquired by integration of the area in a cyclic voltammogram can be used to estimate the electrochemically active surface atoms based on eq 2.2,

$$m = \frac{Q}{nF} \qquad 2.2$$

where m is the mole of electrochemically active surface atoms, Q is the charge, n is the electron transfer number, and F is the Faraday constant. Assuming a 2-electron process for the Ni/α-$Ni(OH)_2$ couple, this charge corresponds to 6.1×10^{-9} mole surface atoms of Ni, compared to 1.06×10^{-6} mole total Ni (63 μg) in the deposit. Using the charge density of 514 μC cm^{-2} for Ni towards 2-electron oxidation forming α-$Ni(OH)_2$, this charge would correspond to an EASA of ~ 2.3 cm^2 (on 0.126 cm^2 GC).[327]

After characterization by CV, we washed the Ni_{GLAD}/GC electrode and cell with deoxygenated H_2O under an atmosphere of nitrogen, added the 2.0 M NH_4Cl electrolyte, and then carried out the rotating WE galvanostatic deposition in the same cell without

exposing Ni_{GLAD}/GC to air.

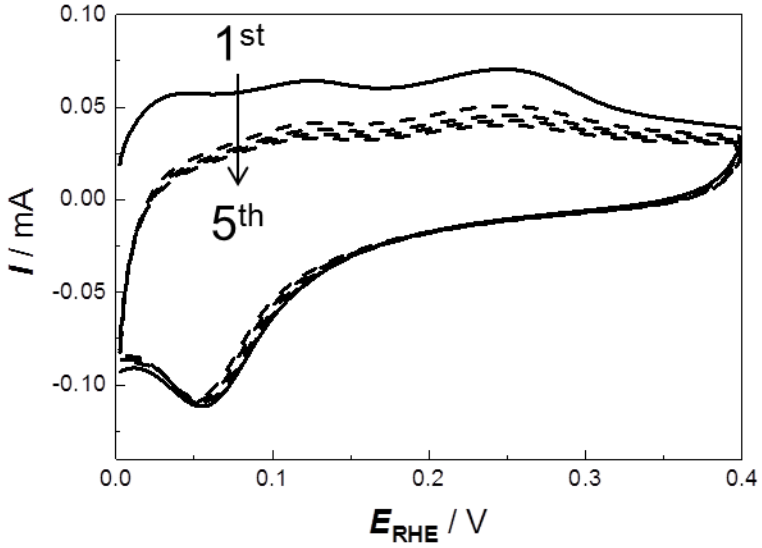

Figure 2.3 The first 5 sweeps of the cyclic voltammetry for the Ni_{GLAD}/GC substrate in 1.0 M KOH under N_2 at 25 °C. The potential sweep rate was 10 mV s^{-1}.

2.2.2 Rotating WE, galvanostatic deposition onto Ni_{GLAD}/GC

The deposition was carried out galvanostatically in 2.0 M NH_4Cl with a Pt black gauze CE as the Pt source. The CE was exposed to H_2 (1 atm) before the deposition in order to reduce the surface Pt oxides.[322–324] As was the case in 1.0 M KOH, H_2 evolution at the Ni_{GLAD}/GC WE started at a lower overpotential than that of bulk, polycrystalline Ni in 2.0 M NH_4Cl. Indeed, the H_2 evolution at Ni_{GLAD}/GC was significant, and the gas bubbles blocked the electrolyte access to the WE even at the beginning of the deposition when little or no Pt

existed on the surface. Therefore, we performed the depositions at a high rate of WE rotation (ω = 1700 rpm) to dislodge the bubbles continuously as they formed. This high rate of rotation would also minimize the mass transport effects on the distribution of the Pt deposit within the catalyst layer. As well, a lower current density than in our previous reports (j = -64 mA cm^{-2}_{GC} or j_{EASA} = -5.5 mA cm^{-2} Ni_{surf} from the initial EASA of the Ni_{GLAD} deposit) was used.[322] Under these conditions, we expected to obtain a more uniform deposit of Pt on Ni_{GLAD}. We note that the nature of the Ni_{GLAD}/GC deposit, i.e. with the Ni nanopillars attached directly to the surface of the GC disc, uniquely allowed the rotating WE deposition without the need of binders such as Nafion® that could interfere with the deposition and activity measurements of the resulting electrocatalysts. The potential of the WE increases (decreasing the overpotential) as the Ni surface is covered progressively by Pt, until it levels out when the Ni is fully covered by Pt.[322] As can be seen in Figure 2.2C and D (SEM for a Ni_{GLAD}{Pt}/GC electrode), there appear to be no significant changes in the overall shape and morphology of the GLAD pillars before and after the rotating deposition. Thus, it is likely that Pt has been deposited uniformly, on this scale, over the Ni_{GLAD} nanopillars. Closer inspection of the nanopillars before and after Pt deposition reveals the appearance of some fine structures that presumably are due to partial surface deposition of Pt, which is also consistent with the E_{WE} changes over the course of electrodeposition.

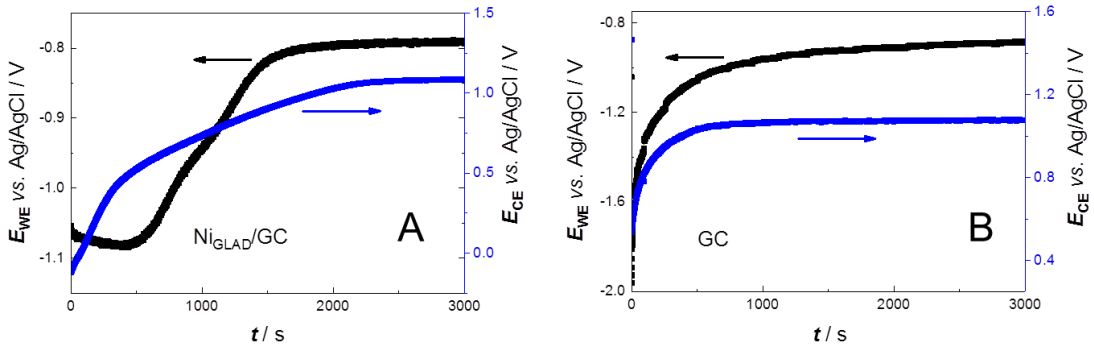

Figure 2.4 Potential profiles of the E_{WE} and E_{CE} during the Pt depositions for (A) a Ni_{GLAD}/GC electrode and (B) a bare GC electrode.

Figure 2.4A shows profiles of E_{WE} (working electrode potential) and E_{CE} (counter electrode potential) versus time during the rotating WE, galvanostatic deposition of a Ni_{GLAD}/GC electrode. For comparison, the same procedure was carried out over a bare GC disk (Figure 2.4B) to prepare a control {Pt}/GC electrode. The initial stages (up to ~ 400 s) of the deposition over Ni_{GLAD}/GC largely represent H_2 evolution over the rotating Ni_{GLAD}/GC electrode, with E_{WE} ranging -1.06 to -1.08 V versus Ag/AgCl ($V_{Ag/AgCl}$). The Pt deposition largely begins once the Pt black CE potential rises to values adequate to dissolve significant amounts of Pt in 2.0 M NH_4Cl (~ 0.47 $V_{Ag/AgCl}$).[322–324] Starting at 410 s, we believe that a mixed H_2 evolution system exists over the Ni_{GLAD}{Pt}/GC electrode, with H_2 evolution occurring over both Pt and Ni and then mainly over Pt when the Ni is fully covered with Pt (i.e. after t = 1500 s). E_{WE} increased almost linearly in the mixed

potential region for ~ 1200 s and then leveled off asymptotically towards -0.81 $V_{Ag/AgCl}$. This behavior of E_{WE} with time indicates that the Pt coverage increases almost linearly during the early stages of the deposition (~ 1200 s). As expected, the initial WE potential is more negative over bare GC than over Ni_{GLAD}/GC. Also, the polarization of the CE initiates at potentials larger than 0.47 $V_{Ag/AgCl}$, suggesting that the electrodissolution from the CE and Pt deposition onto the WE started almost immediately. Indeed, E_{WE} over GC started to increase at the onset of the deposition. Over bare GC (Figure 2.4B), the initial surge in E_{WE} likely is due to the nucleation and the growth of the Pt deposit. The WE potential increase levels off much earlier over {Pt}/GC than over Ni_{GLAD}{Pt}/GC (around 1000 s). We note, however, that the overall deposition time for both electrodes (start of the potential increase up to the plateau) seems quite similar, and is roughly 1000 ± 50 s. The difference in the WE potentials near the end of the depositions likely reflects differences in the overpotentials for hydrogen evolution over the {Pt}/GC and Ni_{GLAD}{Pt}/GC surfaces.

2.2.3 Electrochemistry of Ni_{GLAD}{Pt}/GC

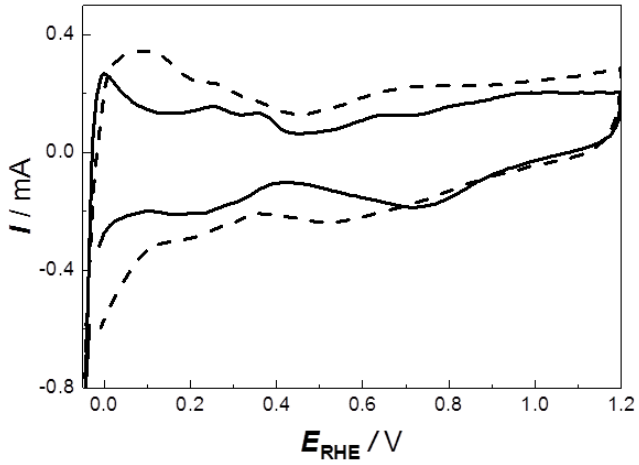

Figure 2.5 Typical cyclic voltammograms for the {Pt}/GC (solid) and Ni_{GLAD}{Pt}/GC (dashed) electrodes in 1.0 M KOH under N_2 (25 °C) at 100 mV s^{-1}.

Figure 2.5 shows typical voltammograms of the Ni_{GLAD}{Pt}/GC and {Pt}/GC electrodes in 1.0 M KOH (100 mV s^{-1}). The CVs were recorded without exposing the Ni_{GLAD}{Pt}/GC WE to air after the rotating WE galvanostatic deposition. Typical features of Pt are observed for both electrodes, with hydrogen desorption (anodic, eq 2.4) and adsorption (cathodic, eq 2.3) below 0.45 V_{RHE}, while oxide formation (anodic, eq 2.5) and stripping (cathodic, eq 2.6) are at potentials higher than 0.5 V_{RHE}.[330]

$$Pt + H_2O + e^- \rightarrow Pt–H + OH^- \quad 2.3$$

$$Pt–H + OH^- \rightarrow Pt + H_2O + e^- \quad 2.4$$

$$Pt + 2\ OH^- \rightarrow Pt\text{–}O + H_2O + 2\ e^- \quad 2.5$$

$$Pt\text{–}O + H_2O + 2\ e^- \rightarrow Pt + 2\ OH^- \quad 2.6$$

We note, however, that the oxide stripping peak over Ni_{GLAD}{Pt}/GC is at 0.53 V_{RHE}, compared to 0.71 V_{RHE} over {Pt}/GC. Using the charge under the cathodic wave, and assuming that the Pt electrochemistry is dominant, the EASA of Ni_{GLAD}{Pt}/GC is 0.76 cm^2 and, similarly, 0.75 cm^2 was obtained for the {Pt}/GC.[331] The CV of {Pt}/GC was stable over the course of these experiments in the absence of a binder, showing that this deposition approach can be used successfully over bare carbon surfaces as well.

2.2.4 Oxygen reduction reaction on Ni_{GLAD}{Pt}/GC

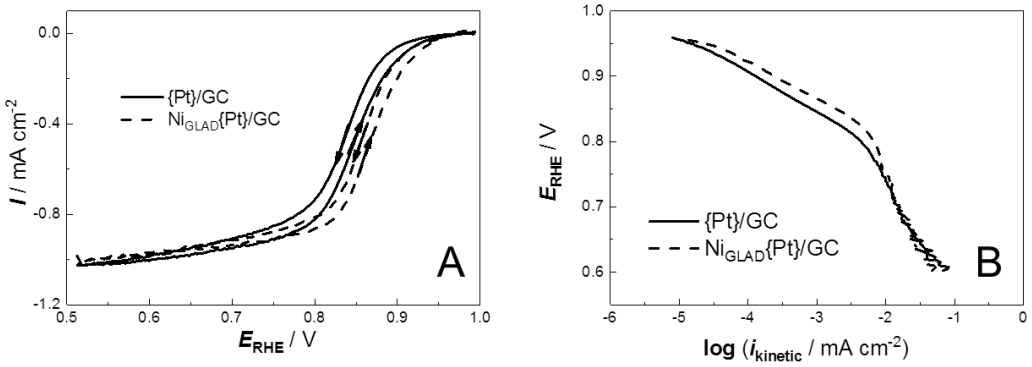

Figure 2.6 (A) The baseline-corrected fifth cathodic and anodic sweeps of the hydrodynamic CVs of the {Pt}/GC (solid) and Ni_{GLAD}{Pt}/GC (dashed) electrodes in O_2-saturated 1.0 M KOH at 25 °C, 1600 rpm, and 10 mV s^{-1}. Current densities are normalized to EASA. (B) Tafel plots extracted from the anodic sweeps. The data are not *iR*-corrected.

Figure 2.6 compares the ORR activities of the Ni_{GLAD}{Pt}/GC and {Pt}/GC electrodes in O_2-saturated 1.0 M KOH. The Figure shows the fifth negative going (cathodic) and positive going (anodic sweeps) (ω = 1600 rpm, 1.00 to 0.50 V_{RHE}, 10 mV s^{-1}) of the hydrodynamic CVs corrected for the baseline CV (measured in the absence of O_2). The current densities are normalized to the estimated EASA of the deposits. We note that, based on the charges under the hydrogen adsorption/desorption regions (Figure 2.5), the EASA of the Ni_{GLAD}{Pt}/GC and {Pt}/GC electrodes were 0.76 and 0.75 cm^{-2}, respectively. As such, both electrodes produced similar mass transport controlled activities. The onset of the ORR was ~ 30 mV less negative over Ni_{GLAD}{Pt}/GC, resulting in about a 2–3 fold superior activity for Ni_{GLAD}{Pt}/GC over {Pt}/GC in the range 0.90 to 0.75 V_{RHE} (cathodic sweeps). A comparison of the anodic sweeps showed similar improvements (somewhat better). This signifies the role of Ni_{GLAD} structures in improving the sluggish ORR activity of Pt. Kariuki et al. reported that Pt–Ni (both deposited by GLAD) nanorods gave similar ORR activity improvements compared with Pt in acidic electrolytes.[332] Table 2.1 summarizes key data of the two catalysts where the EASA and mass-normalized activities have been reported at 0.9 V_{RHE} of the anodic scans.

Table 2.1 Key parameters for the {Pt}/GC and Ni_{GLAD}{Pt}/GC electrodes

Catalyst	ORR onset (V_{RHE})	EASA (cm^2)	EASA activity ($mA\ cm_{Pt}^{-2}$)	Mass activity ($A\ g_{Pt}^{-1}$)	Normalized activity* ($A\ g_{Pt}^{-1}\ cm_{Pt}^{-2}$)
{Pt}/GC	0.93	0.75	0.105	5.53	7.37
Ni_{GLAD}{Pt}/GC	0.96	0.76	0.202	13.23	17.40

* Activity normalized both to the mass and the EASA of Pt.

Based on the Butler–Volmer equation, the potential-dependent current density could be expressed by eq 2.7,

$$i = i_0 \left[e^{\frac{-\alpha n F \eta}{RT}} - e^{\frac{(1-\alpha) n F \eta}{RT}} \right] \qquad 2.7$$

where i is the current density, i_0 is the exchange current density (the current density at the thermodynamic equilibrium potential), F is the Faraday constant, n is the number of electrons transferred in the rate-determining step, α is the transfer coefficient describing the fraction of the applied potential that favors the reaction, and η is the overpotential. The first and second terms of eq 2.7 are used to describe the electrochemical kinetics of the cathodic and anodic reaction, respectively. In the case of ORR, the anodic component of the equation is negligible since the reaction is highly irreversible.

By taking the logarithm of the current over potential, eq 2.8 is derived.

$$\eta = -\frac{2.3RT}{\alpha nF}\log i + \frac{2.3RT}{\alpha nF}\log i_0 \qquad 2.8$$

The transfer coefficient, α, of the electrochemical reaction can be determined from the Tafel slope, given by $2.3RT/\alpha nF$. A larger α indicates how much more efficiently a reaction proceeds.[333,334]

Figure 2.6B displays E_{WE} versus the logarithm of the kinetic current density (cathodic) normalized to the EASA. The kinetic current is expressed by eq 2.9, where $i_{kinetic}$, i_{obs}, and i_{lim} are the kinetic current, raw current, and limiting current, respectively.

$$i_{\text{kinetic}} = \frac{i_{\text{obs}} i_{\text{lim}}}{i_{\text{lim}} - i_{\text{obs}}} \qquad 2.9$$

For both electrodes, there were two regions of the Tafel plots with different slopes, indicating a change in the RDS with overpotential. At low overpotentials, down to E_{WE} ~ 0.80 V_{RHE}, the Tafel slopes were 63 and 58 mV dec^{-1}, while at E_{WE} between ~ 0.80 V and ~ 0.60 V_{RHE} Tafel slopes of as large as 172 and 227 mV dec^{-1} were obtained for {Pt}/GC and Ni_{GLAD}{Pt}/GC, respectively. Other authors also have reported two regions with different Tafel slopes for the ORR over Pt in KOH electrolytes, typically 60 mV dec^{-1} down to E_{WE} = ~ 0.80 V_{RHE} and ~ 121 mV dec^{-1} at E_{WE} < 0.80 V_{RHE}.[332,335] The reasons for the overly large Tafel slope at large overpotentials for Ni_{GLAD}{Pt}/GC are unknown at this point. It has been hypothesized that such high Tafel slopes would be indicative of the RDS being the adsorption of O_2;[335] therefore, higher ORR activities of Ni_{GLAD}{Pt}/GC than {Pt}/GC

could be related with the increased affinity with O_2. From the corresponding O_2-free voltammetry (Figure 2.5), the oxide stripping peak for Ni_{GLAD}{Pt}/GC appeared about 0.2 V less positive than that for {Pt}/GC. Such a shift is suggestive of a higher oxide adsorption energy with Ni present in the Ni_{GLAD}{Pt}/GC catalyst; both factors will affect the ORR activity. Further investigation is required, however, to fully explain the differences in the ORR activities between Ni_{GLAD}{Pt}/GC and {Pt}/GC.

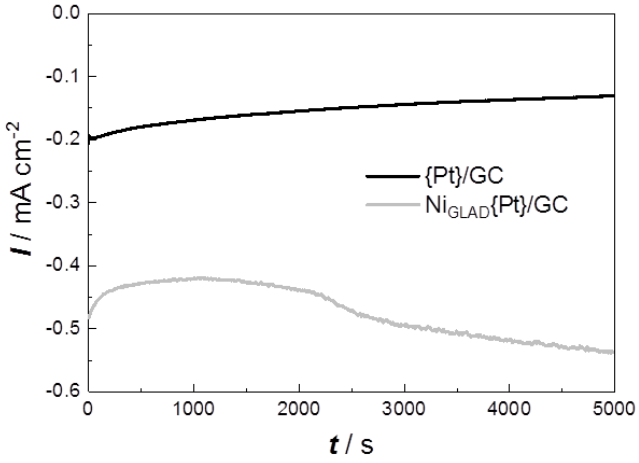

Figure 2.7 Potentiostatic ORR measurements in O_2-saturated 1.0 M KOH at 0.85 V_{RHE}. The rotation rate was 1600 rpm.

Moderate-term potentiostatic ORR tests (E_{WE} = 0.85 V_{RHE}) over 5000 s were carried out with the {Pt}/GC and Ni_{GLAD}{Pt}/GC electrodes as a preliminary comparison of the durability of these catalysts (Figure 2.7). The Ni_{GLAD}{Pt}/GC electrode retained its initial performance and also showed some improvement (-0.48 mA cm^{-2} at t = 0 and -0.55 mA

cm^{-2} at t = 5000 s), while the activity of the {Pt}/GC electrode decreased by 38% after 5000 s (-0.21 mA cm^{-2} at t = 0 and -0.13 mA cm^{-2} at t = 5000 s, respectively). This result is consistent with the report of Zhang et al. who overviewed influences of metal oxide supports in sustaining the ORR activity of Pt.[336]

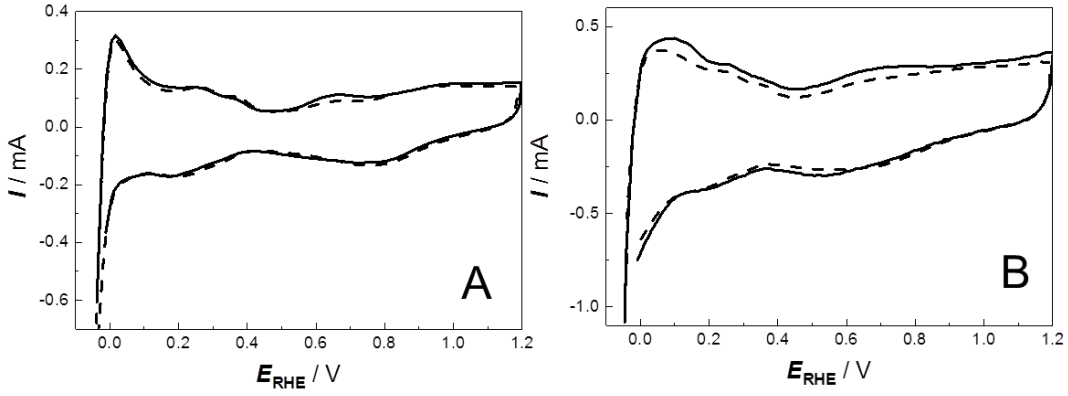

Figure 2.8 CVs before (solid) and after (dash) 5000 s ORR at 0.85 V_{RHE} for the (A) {Pt}/GC and (B) Ni_{GLAD}{Pt}/GC electrodes in 1.0 M KOH under N_2 at 100 mV s^{-1}.

Figure 2.8 shows the baseline CVs in O_2-free 1.0 M KOH for {Pt}/GC and Ni_{GLAD}{Pt}/GC before and after the moderate-term ORR tests. The before and after EASA of Ni_{GLAD}{Pt}/GC were 0.76 cm^2 and 0.74 cm^2, respectively. The corresponding values for {Pt}/GC were both 0.75 cm^2. Thus, the EASA of both surfaces were not changed significantly by the moderate-term potentiostatic ORR.

These results show that the deposition method described gives rise to Pt particles that are attached strongly to the GC support. On this basis, we propose that the superior ORR

activity and moderate-term durability of the Ni_{GLAD}{Pt}/GC over {Pt}/GC are due to the promotional effects of the Ni_{GLAD} support on the Pt layer.

2.3 **Conclusions**

Glancing angle deposition was employed to cast Ni nanopillars on glassy carbon supports. Then, a rapid rotating WE, galvanostatic deposition approach was used to incorporate Pt. This resulted in uniform deposition of Pt over the Ni structures, while SEM indicated that trace amounts of Pt have also been deposited as an overlayer. It is noteworthy that the underlying morphology of the Ni_{GLAD} apparently did not change by the deposition. Preliminary tests showed that the Ni_{GLAD}{Pt} on GC was 2–3 fold more active towards the ORR than the {Pt} on GC under identical conditions. Typically, for both catalyst layers, the Tafel plots showed two distinctive slope regions, similar to the bulk polycrystalline Pt, demonstrating the change in the ORR mechanism with potential. Moderate-term potentiostatic ORR studies showed that the Pt layer at the Ni_{GLAD} support was more durable; this should be of interest in the development of commercial catalysts for alkaline fuel cells.

The preparation of the Ni_{GLAD} deposit on GC is easy to perform, reproducible, and reasonably fast (about one hour is required for the simultaneous deposition on multiple GC electrodes). However, we emphasize that the methodology described in this Chapter is in its preliminary stages. This approach is extended to the ORR studies in acidic media as well. Chapter 3 describes this rotating WE, galvanostatic deposition on Ni_{GLAD} nanopillars for the ORR application in acid.

2.4 **Experimental**

2.4.1 General

The following chemicals were used as received from the supplier: Nitrogen (Praxair), oxygen (Praxair), concentrated sulfuric acid (Caledon), hydrochloric acid (EMD chemicals), nitric acid (EMD chemicals), perchloric acid (Anachemia Corporation), potassium permanganate (Fisher Scientific), 30% hydrogen peroxide (Fisher Scientific), potassium hydroxide (Caledon Laboratory Chemicals), ammonium chloride (Caledon Laboratory chemicals), ethanol (Greenfield Ethanol Incorporated), acetone (EMD chemicals), and potassium hexachloroplatinate (Aithica Chemical Corporation). The following materials were used as received from the supplier: platinum gauze (Alfa Aesar, 52 mesh woven from 0.1 mm wire, 99.9% metals basis) and nickel metal chunks (Cerac, Inc., 99.9% purity). The glassy carbon discs (Pine Research Instrumentation, 5 mm outer diameter × 4 mm thick, 0.196 cm^2 geometric surface area) were polished and cleaned before use, as described below.

Triply distilled H_2O was used to prepare all aqueous solutions. 2-Propanol (ACS reagent grade, Sigma-Aldrich) was distilled under N_2 from Mg. Analytical grade reagents were used to prepare all electrolyte solutions. All aqueous solutions were saturated with N_2 gas by purging for 30 min before use. All electrochemical experiments were carried out under N_2 using the standard Schlenk techniques. The rinse water and electrolytes were

transferred under flushing N_2 with cannulas. The ORR experiments were carried out in O_2-saturated 1.0 M KOH under an atmosphere of O_2. The glassware was cleaned with Piranha solutions (5:1 by volume concentrated H_2SO_4 and 30% H_2O_2), rinsed thoroughly with the triply distilled H_2O, and then dried at 80 °C. The blackened platinum gauze used as counter electrodes were prepared as described previously.[322] All electrochemical experiments were carried out at room temperature.

2.4.2 Preparation of Ni_{GLAD}/GC

The GC discs were polished with a Pine Research Instrumentation polishing kit (5, 0.3, and 0.05 μm alumina slurry with a nylon or rayon microcloth) and cleaned with acetone, 2-propanol, and water before being placed in the high vacuum deposition chamber (Kurt J. Lesker). The deposition chamber was evacuated to below 0.1 mP, and Ni was deposited from Ni metal chunks via electron beam deposition. The flux rate was maintained at 1 nm s^{-1} while a film of ~ 500 nm vertical nanopillars was deposited at $\alpha = 88^{\circ}$. The substrates were rotated constantly at a rate of one rotation every 10 nm of film growth. The Ni_{GLAD}/GC discs were stored under glass in air.

2.4.3 Rotating WE, galvanostatic deposition

The experiments in Sections 2.4.3 and 2.4.4 typically were completed on the same day to minimize ageing effects on the activity and characteristics of the resulting electrodes. The

Ni_{GLAD}/GC disc was loaded into the RRDE tip under air using a homemade, hands-free mounting tool that also removed the outer 0.5 mm-thick ring of the Ni_{GLAD} deposit, leaving 0.126 cm^2 of the GC covered with Ni_{GLAD}. The Ni_{GLAD}/GC was cleaned with triply distilled water and then fitted to a 100 mL, three-neck flask with a Pine AC01TPA6M Gas-Purged Bearing Assembly. All gases were handled with needles attached to feed and bubbler lines. The Pt gauze CE (in a glass filter tube with a coarse sinter tip) and the H_2 (1 atm)/1.0 M KOH/Pt RHE reference electrode were fitted to the flask through holes in rubber septa. The vessel was flushed with N_2 for 20 min and then filled with ~ 50 mL, N_2-saturated 1.0 M KOH through a cannula. Immediately after immersion, E_{WE} was held at -0.10 V_{RHE} for 180 s, following which CV was recorded to characterize the Ni_{GLAD} surface (0–0.40 V_{RHE}, 10 mV s^{-1}, 5 sweeps). The results are described in Section 2.2.1 and Figure 2.3.

The KOH solution was removed through a cannula. With rapid N_2 flushing, the CE was replaced with unprotected, fresh Pt black gauze, and the RHE was replaced with a Ag/AgCl (4.0 M KCl) reference electrode, both fitted through rubber septa. The picture of the setup is shown in Figure 2.9.

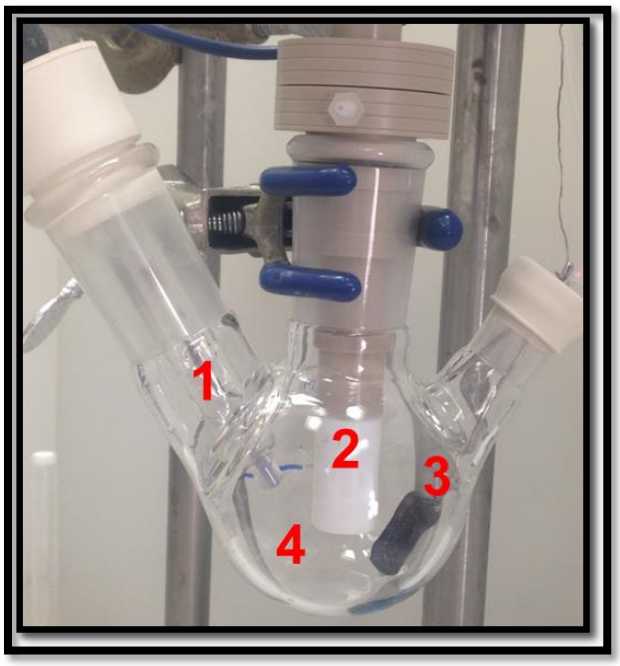

Figure 2.9 Experimental apparatus for the rotating WE, galvanostatic deposition. 1: Ag/AgCl (4.0 M KCl) reference electrode; 2: working electrode; 3: blackened Pt counter electrode; 4: 2 M NH_4Cl electrolyte.

Using cannulas, the vessel was washed 3 times with N_2-saturated H_2O (~ 50 mL each), emptied, and the Pt CE surface was reduced by exposure to a stream of H_2 (1 atm) for 10 min. The H_2 was flushed with N_2, and 30 mL of N_2-saturated 2.0 M NH_4Cl was added through a cannula. Thereafter, the WE was rotated at $\omega = 1700$ rpm, and the current density was set to j = -64 mA cm^{-2}_{GC}, normalized to the total area of the GC disc (0.196 cm^2). A detailed discussion of the galvanostatic deposition of Pt on Ni_{GLAD} can be found in Section 2.2.2.

After the deposition, the NH_4Cl solution was removed through a cannula. Under flushing N_2, the CE was exchanged for a Pt black gauze in a filter tube with a coarse sinter, and the reference electrode was exchanged for a RHE, both fitted through rubber septa. Next, the reaction vessel and working electrode were rinsed through cannulas 3 times (~ 50 mL each) with N_2-saturated triply distilled water, and ~ 50 mL aqueous 1.0 M KOH was introduced into the vessel. Voltammetry was conducted to characterize the Ni_{GLAD}{Pt}/GC catalyst (11.6 μg by ICP–MS), and this is discussed in Section 2.2.3. The same steps were carried out with a bare GC electrode to prepare the {Pt}/GC electrode (14.5 μg by ICP–MS).

2.4.4 Oxygen reduction reaction measurements

After the electrode was characterized by CV in 1.0 M KOH under N_2, oxygen (1 atm) was bubbled through the electrolyte for 30 min while the WE was at open circuit. The ORR measurements were carried out with 1600 rpm WE rotation, as described in Section 2.2.4 and Figure 2.6. The Ni_{GLAD}{Pt}/GC or {Pt}/GC catalyst layers were washed with water and stored in air between use. Each experiment has been repeated at least three times to ensure the reproducibility, and the experimental errors between measurements are less than 10%.

2.4.5 Instrumentation

The electrochemical experiments were performed with a Solartron SI 1287 Electrochemical Interface controlled by CorrWare for Windows Version 2–3d software. The rotating disc electrode experiments were performed with a Pine Research Instrumentation Modulated Speed Rotator equipped with an AFE6MB RRDE shaft and E5TQ series change-disk tip. The shaft and tip were connected to the reaction flask with a Pine AC01TPA6M Gas-Purged Bearing Assembly.

SEM was performed with a Hitachi S-4800 instrument. ICP–MS data were measured with an Agilent 7500 ce ICP–MS coupled with Cetac ASX-510 autosampler. Samples were prepared by dissolving the deposits in aqua regia.

Chapter 3 Oxygen Reduction over Dealloyed Pt Layers on Glancing Angle Deposited Ni Nanostructures[a]

3.1 Introduction

The results from the Ni_{GLAD}{Pt}/GC catalysts for the ORR in base inspired us to optimize the conditions further and to apply the catalysts towards the ORR in acid. The ORR in acid is a fundamental process that occurs in all PEMFCs.[334,337,338] The overpotential for the ORR is detrimentally higher than that for the hydrogen oxidation reaction in H_2–O_2 fuel cells, and much research has been directed towards developing active and practical ORR catalysts.

Platinum is a proven component of stable, active ORR catalysts in acid.[339–342] Consequently, most ORR research is focused on reducing the loading by increasing the activity of Pt-containing catalysts. For example, combining Pt with a non-noble transition metal, such as Ni, Co, Cu, or Fe, can improve the activity of the catalyst dramatically.[74,334,338,343–345] The mechanism of the ORR in acid is well-studied,[11,346–348] and the non-Pt components in these catalysts increase the activity of Pt by contracting the Pt–

[a] *A version of this Chapter has been published. Wang, C.; Moghaddam, R. B.; Sorge, J. B.; Xu, S.; Brett, M. J.; Bergens, S. H. Electrochimica Acta 2015, 176, 620.*

Pt lattice (geometric strain)[112,349] and/or by an electronic effect.[346,350] Both the strain and the electronic effect optimize the surface–oxygen bond strengths by shifting the d-band to minimize the adsorption of oxides, hydroxides, and related species that inhibit the ORR. The downward shift in the d-band center brings the antibonding state of the interaction between the adsorbed oxygen's valence p level and the Pt d-band below the Fermi level, weakening the surface–adsorbate bond.[118,351–353] However, these non-noble transition metal components are quite soluble in acid, and their dissolution is accelerated at the operating potentials of the ORR.

A widely-known approach to stabilize such multicomponent ORR catalysts is dealloying, where the non-noble metal is electro-dissolved to a controlled extent either at a constant potential[344] or under potential cycling.[120,298,353] It is believed that the catalysts formed by dealloying are core-shell systems with Pt-rich shells that prevent further dissolution of the non-noble metal(s) and that the cores activate the Pt shell towards the ORR by lattice strain and/or an electronic effect. Strasser et al. extensively studied the dealloying of Pt intermetallic nanoparticles to produce active ORR catalysts in acid.[120,343,351–354] The early reports described dealloyed catalysts that were evaluated in RDEs (**r**otating **d**isk **e**lectrodes) and in MEAs (**m**embrane **e**lectrode **a**ssemblies).[351–353] In the MEA, ternary Pt–Co–Cu catalysts were dealloyed, and the resulting Cu and Co ions were extracted from the membrane by ion exchange with a mineral acid.[352] The mass

activities of the resulting catalysts were over five times greater than that of Pt.[352] Later, they reported a dealloyed $PtNi_3$ catalyst that operated with 0.29 A mg_{Pt}^{-1} at 0.9 V_{RHE} at room temperature in O_2-saturated 0.1 M $HClO_4$. This mass activity was 7–8 times that of a heat-treated Pt catalyst with similar particle sizes and 2–3 times that of a commercial Pt catalyst.[118,119] The area-specific activities were 6–7 times that of the pure Pt catalysts.[118,119]

This Chapter describes the utilization of GLAD to grow Ni nanopillars on GC rotating disk electrodes. Thin and conformal Pt layers are deposited onto Ni_{GLAD}/GC from a blackened[355] Pt gauze CE using a rotating WE, galvanostatic deposition at low current densities in 2.0 M NH_4Cl, as described in Chapter 2.[323] A detailed study of these systems as ORR catalysts in acid is carried out, and the optimal coverage of Ni_{GLAD} by Pt for the ORR in acid is determined. In addition, the effect of dealloying on their activities towards the ORR is investigated.

3.2 **Results and Discussion**

3.2.1 Cyclic voltammetry

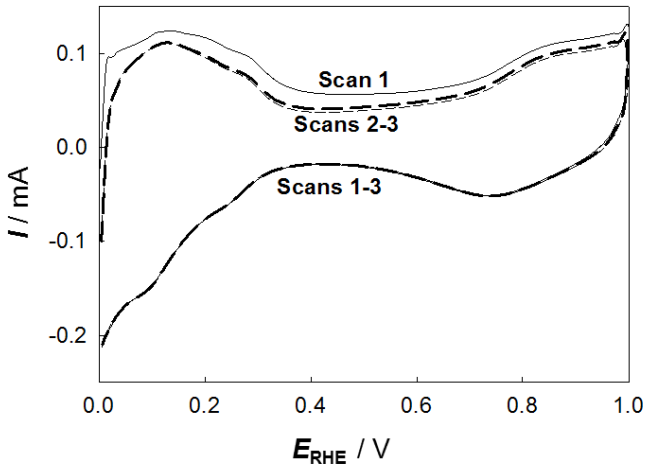

Figure 3.1 First three CVs of an as-prepared Ni_{GLAD}{Pt-800}/GC electrode at 50 mV s^{-1}in N_2-saturated 0.1 M $HClO_4$.

Figure 3.1 shows the first three consecutive cyclic voltammograms (50 mV s^{-1}) of an as-prepared Ni_{GLAD}{Pt}/GC electrode (Ni_{GLAD}{Pt-800}/GC) in 0.1 M $HClO_4$. The electrode was prepared by interrupting the Pt deposition after 800 s. Based upon the E_{WE} versus time curve for the deposition (Figure 3.10), 800 s corresponds with the point when E_{WE} begins to level off, presumably when most of the Ni is covered by Pt. The EASA of the Ni_{GLAD}/GC electrode was estimated from CV in base before the Pt deposition.[356] The CVs of Ni_{GLAD}{Pt-800}/GC in 0.1 M $HClO_4$ contained the features of Pt electrochemistry in

acid, with the anodic peaks assignable to the hydrogen desorption ($E < 0.37\ V_{RHE}$) and the surface oxide formation ($E > 0.70\ V_{RHE}$), and with the oxide layer stripping followed by the hydrogen adsorption dominating the cathodic sweep. The EASA of the as-prepared Ni_{GLAD}{Pt-800}/GC electrode was estimated by integrating the hydrogen adsorption area (corrected for the background current), taking into account the charge density of 0.210 mC cm^{-2} for one electron transfer at Pt (eq 3.1)[357] and the estimated hydrogen adsorption charge of 0.37 mC, the EASA was 33.5 $m^2\ g_{Pt}^{-1}$.

$$Pt + H^+ + e^- \rightarrow Pt–H \qquad 3.1$$

As shown in Figure 3.1, the EASA (estimated from the hydrogen adsorption region) of the deposit remained almost unchanged over the subsequent scans. The mass loadings of Pt and Ni in this electrode were 5.2 and 21.5 μg, respectively, as determined by the destructive ICP–MS after the electrochemical measurements.

3.2.2 Oxygen reduction reaction activity

Figure 3.2 shows the RDE (ω = 1600 rpm) voltammetric ORR current for the same Ni_{GLAD}{Pt-800}/GC electrode (weight composition ~ $Pt_{27}Ni_{73}$) in O_2-saturated 0.1 M $HClO_4$ (10 mV s^{-1}). The ORR onset potential was ~ 0.8 V_{RHE} in the forward scan (cathodic) of the first cycle. The onset potentials in the second and third scans were both at ~ 0.93 V_{RHE}, ~ 0.13 V higher (less overpotential) than in the first cycle. The kinetic current at 0.9 V_{RHE} (eq 2.9[358]) was 0.014 mA, corresponding to mass (Pt) and EASA activities of 0.003 A

mg_{Pt}^{-1} and 0.008 mA cm_{Pt}^{-2}, respectively.

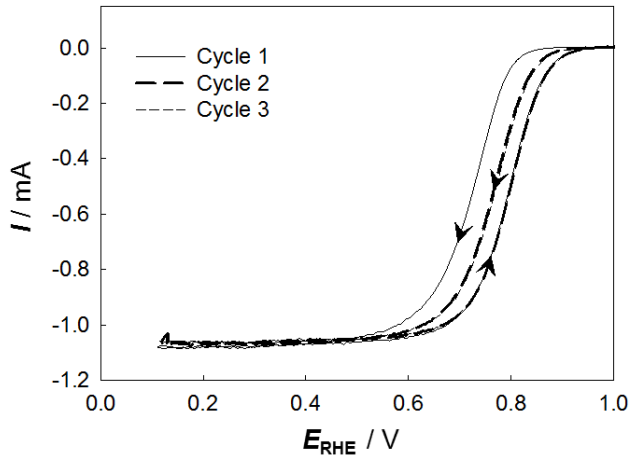

Figure 3.2 Oxygen reduction at Ni_{GLAD}{Pt-800}/GC (10 mV s^{-1}) in an O_2-saturated 0.1 M $HClO_4$ solution before dealloying.

3.2.3 Effect of dealloying on ORR activity

The dealloying protocol developed by Strasser et al.[359] (200 cycles at 500 mV s^{-1} over 0.05 to 1 V_{RHE}) was applied to the Ni_{GLAD}{Pt-800}/GC electrode. Figure 3.3 shows the CV patterns at 50 mV s^{-1} for a Ni_{GLAD}{Pt-800}/GC electrode (Pt loading = 5.2 μg) before and after the dealloying treatment. Upon dealloying, the general voltammetric features of Pt were preserved. However, the peak areas of both the oxide and hydrogen regions have decreased. The EASA (from the hydrogen adsorption region) after dealloying was ~ 32.1 m^2 g_{Pt}^{-1}, corresponding to about 4.0% decrease compared with the initial EASA. The

origins of this small decrease in EASA may be related to the changes in structure caused by dealloying. Further, the signals in the sweeps became more distinct, and the capacitive current decreased after dealloying. Similar observations were reported in the literature for other PtNi systems.[118] In addition, the oxide stripping peak potential shifted to a more positive value, indicating that the adsorption of the oxide layer was weakened.[360,361]

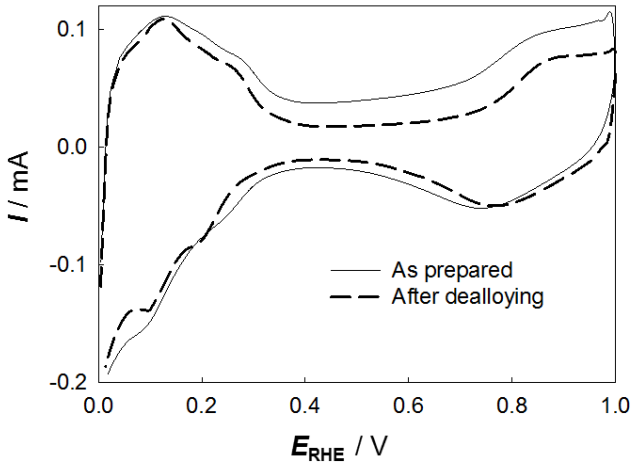

Figure 3.3 Voltammograms at 50 mV s^{-1} of the Ni_{GLAD}{Pt-800}/GC electrode in O_2-free 0.1 M $HClO_4$ before (solid) and after dealloying (dashed).

Figure 3.4 shows the ORR activity of the Ni_{GLAD}{Pt-800}/GC electrode before and after dealloying in O_2-saturated 0.1 M $HClO_4$. The ORR profiles are normalized to EASA in each case (33.4 m^2 g_{Pt}^{-1} before, and 32.1 m^2 g_{Pt}^{-1} after dealloying); the raw data are shown in the inset for comparison. Dealloying results in an impressive increase in the ORR activity, giving a kinetic current density of 0.33 mA cm_{Pt}^{-2} at 0.9 V_{RHE}, which is over 41

times that of an untreated Ni_{GLAD}{Pt-800}/GC electrode (0.008 mA cm_{Pt}^{-2}). These results show that the Ni_{GLAD}{Pt-800}/GC system can sustain the dealloying process in acid. This, combined with the observations that during the deposition to prepare Ni_{GLAD}{Pt-800}/GC the potential of the WE had risen to the plateau region by 800 s and that the CVs were consistent with the electrochemistry of Pt in acid, is good evidence that the surface of the Ni_{GLAD}{Pt-800}/GC electrode is quite rich in Pt. This interpretation also is consistent with the relatively small changes that occurred during the dealloying treatment of this electrode (Figure 3.3). Nevertheless, the substantive increase in the ORR activity induced by dealloying suggests that electrochemically accessible Ni was present near the Ni_{GLAD}{Pt-800}/GC surface and that this Ni was removed to some extent by dealloying. As shown in Figure 3.3, the EASA of Ni_{GLAD}{Pt-800}/GC decreased slightly during the dealloying process, yet the ORR activity increased, showing, as concluded by Strasser et al.[351,352] for other systems, that a simple increase in EASA does not explain the enhancement of the ORR activity produced by dealloying.

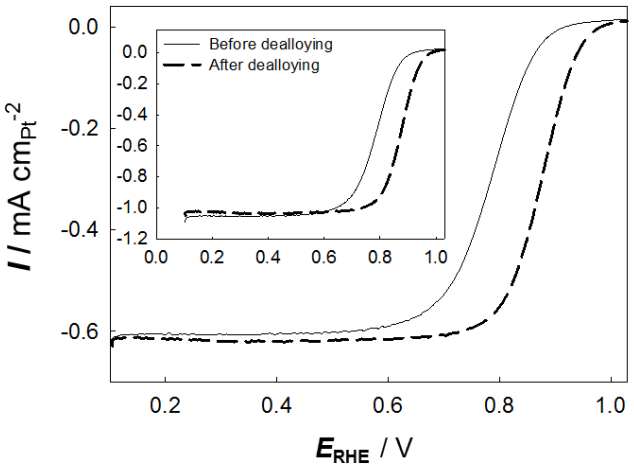

Figure 3.4 Oxygen reduction profiles at 10 mV s^{-1} (anodic sweeps) and 1600 rpm for the Ni_{GLAD}{Pt-800}/GC electrode in O_2-saturated 0.1 M $HClO_4$ before (solid) and after dealloying (dashed). Inset: raw data (not normalized to the EASA).

3.2.4 Effect of Pt deposition time on ORR activity

Using the procedure detailed in Chapter 2, the time for the rotating WE, galvanostatic deposition of Pt upon similar Ni_{GLAD}/GC substrates was varied to prepare a series of Ni_{GLAD}{Pt}/GC electrodes with different Pt loadings. Figure 3.5 shows typical CVs of the Ni_{GLAD}{Pt}/GC electrodes in N_2-saturated 0.1 M $HClO_4$ after dealloying. The CV for the electrode with the lowest loading of Pt, Ni_{GLAD}{Pt-400}/GC, was essentially featureless. During the Pt deposition at 400 s (see Figure 3.10), the potential of the Ni_{GLAD}{Pt}/GC WE is still rising, which indicates that Ni is not covered substantively by Pt in

Ni_{GLAD}{Pt-400}/GC. The lack of features in the CV of the dealloyed Ni_{GLAD}{Pt-400}/GC electrode shows that the Ni_{GLAD} support likely dissolves during the dealloying process, unless the Ni_{GLAD} underlayer is protected by the Pt coating. Apart from the relative magnitudes of the peaks, the electrochemical characteristics are quite similar for all the other Ni_{GLAD}{Pt}/GC electrodes and resemble the electrochemistry of the polycrystalline Pt in 0.1 M $HClO_4$. The longer deposition times obviously gave rise to stronger Pt signals, as expected.

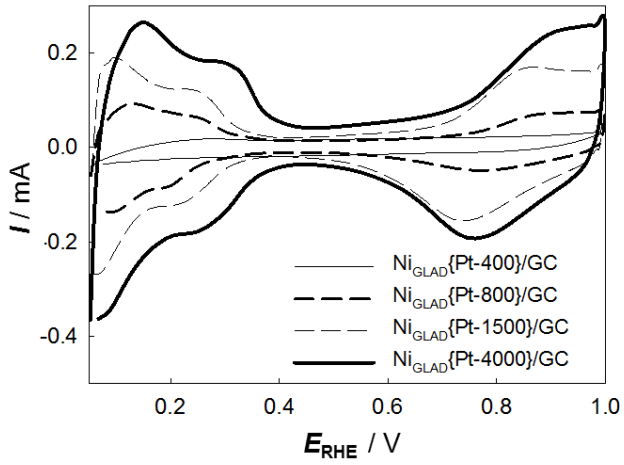

Figure 3.5 Cyclic voltammograms of the Ni_{GLAD}{Pt}/GC electrodes at 50 mV s^{-1} in N_2-saturated 0.1 M $HClO_4$.

Figure 3.6 shows the corresponding ORR responses (10 mV s^{-1}) of the Ni_{GLAD}{Pt}/GC electrodes reported in Figure 3.5. The voltammograms were recorded subsequent to the dealloying protocol, and only the anodic sweeps are shown. The ORR

activity of the Ni_{GLAD}{Pt-400}/GC electrode before dealloying is shown because this deposit did not survive the dealloying procedure. Figure 3.6 also shows the ORR profile of a {Pt}/GC electrode made with the same deposition upon bare GC over 1500 s (i.e. {Pt-1500}/GC) for comparison. For consistency, we applied the dealloying procedure to the {Pt-1500}/GC control electrode prior to the ORR test. The EASA of {Pt-1500}/GC did not change significantly over dealloying (8.1 m^2 g_{Pt}^{-1} before, and 8.2 m^2 g_{Pt}^{-1} after), and neither did the ORR activity.

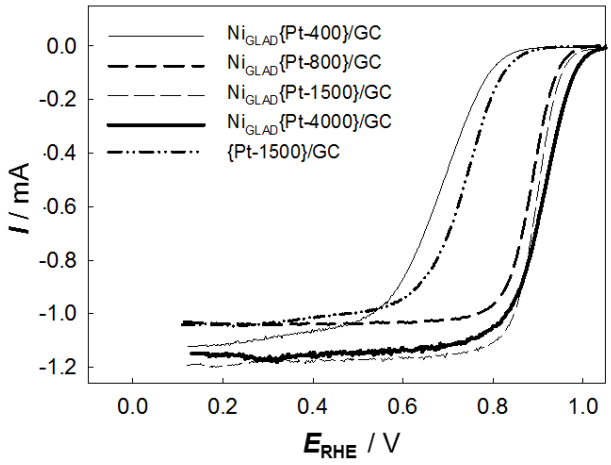

Figure 3.6 Oxygen reduction profiles at 10 mV s^{-1} (anodic sweeps) for the Ni_{GLAD}{Pt}/GC and the {Pt-1500}/GC electrodes in O_2-saturated 0.1 M $HClO_4$. The rotation rate was 1600 rpm. Except for the Ni_{GLAD}{Pt-400}/GC electrode, all the other electrodes were dealloyed before use.

All the Ni_{GLAD}{Pt}/GC electrodes, except Ni_{GLAD}{Pt-400}/GC, are more active than

the {Pt-1500}/GC control. The ORR onset potential over Ni_{GLAD}{Pt-1500}/GC (~ 1 V_{RHE}) was ~ 0.2 V more positive than that over {Pt-1500}/GC. Table 3.1 lists the key parameters for the Ni_{GLAD}{Pt}/GC and {Pt}/GC electrodes to demonstrate the promoting role of the Ni_{GLAD}. Kinetic currents (eq 2.9) were used to determine the data. The values for Ni_{GLAD}{Pt-400}/GC were calculated based on the activity before dealloying. The amount of Pt in each electrode was determined by ICP–MS after the experiment.

The potentiodynamic ORR profile of the highest loading of Pt (Ni_{GLAD}{Pt-4000}/GC) electrode suggested that it is superior to the other Ni_{GLAD}{Pt}/GC electrodes. However, it produced much lower mass and EASA activities than both the Ni_{GLAD}{Pt-800}/GC and the Ni_{GLAD}{Pt-1500}/GC electrodes, but the EASA activity of the Ni_{GLAD}{Pt-4000}/GC electrode was 23 times that of the {Pt-1500}/GC control. The Ni_{GLAD}{Pt-800}/GC and the Ni_{GLAD}{Pt-1500}/GC electrodes had similar activities and likely represent the close to optimal Pt loadings deposited on these 500 nm Ni_{GLAD} nanopillars. We note that smaller Ni_{GLAD} features would require less Pt to form deposits that are stable to dealloying in acid. The Ni_{GLAD}{Pt-800}/GC catalyst possessed the highest EASA activity (0.33 mA cm_{Pt}^{-2}), while the Ni_{GLAD}{Pt-1500}/GC catalyst possessed the highest mass activity (~ 0.204 A mg_{Pt}^{-1}). Based upon the ICP–MS data, the composition of another as-prepared Ni_{GLAD}{Pt-1500}/GC electrode was determined as $Pt_{0.22}Ni_{0.78}$. The composition of the dealloyed Ni_{GLAD}{Pt-1500}/GC used for the ORR experiments was $Pt_{0.26}Ni_{0.74}$ (Table 3.1).

The composition of the dealloyed, ORR-evaluated {Pt-800}/GC electrode was similar, $Pt_{0.27}Ni_{0.73}$. Stevens et al. reported that the highest mass activity for the ORR was obtained after dealloying a Pt–Ni alloy with an initial composition of $Pt_{0.27}Ni_{0.73}$.[362] In addition, the Pt content of the dealloyed, ORR-evaluated Ni_{GLAD}{Pt-4000}/GC electrode was significantly higher, ($Pt_{0.52}Ni_{0.48}$). Taken together, these results show that dealloying dramatically improved the activity of the Ni_{GLAD}{Pt}/GC deposits without dissolution of all the Ni initially in the deposit. Presumably, the structure and the size of the Ni_{GLAD} deposit can be optimized further for the ORR.

Table 3.1 Key parameters after dealloying for the {Pt}/GC and the Ni_{GLAD}{Pt}/GC electrodes

Electrode	Activity at 0.9 V_{RHE}			Onset	Composition
	mA cm_{Pt}^{-2}	A mg_{Pt}^{-1}	A cm_{Pt}^{-2} g_{Pt}^{-1}	(V_{RHE})	(wt.)
{Pt-1500}/GC	0.01	0.0069	1.19	0.85	Pt
Ni_{GLAD}{Pt-400}/GC*	0.01	0.0023	3.71	0.85	-
Ni_{GLAD}{Pt-800}/GC	0.33	0.111	63.46	1.00	$Pt_{0.27}Ni_{0.73}$
Ni_{GLAD}{Pt-1500}/GC	0.31	0.204	48.43	1.00	$Pt_{0.26}Ni_{0.74}$
Ni_{GLAD}{Pt-4000}/GC	0.23	0.048	10.22	1.03	$Pt_{0.52}Ni_{0.48}$

* Before dealloying

The Koutecky-Levich equation (eq 3.2) was used to estimate the electron transfer number of the ORR process,[358]

$$i_{lim} = 0.620\, nFACD^{2/3}v^{-1/6}\omega^{1/2} \qquad 3.2$$

where the i_{lim} is the limiting current in A, n is the electron transfer number, F is the Faraday constant (96485 C mol^{-1}), A is the geometric surface area in cm^2, C is the concentration of the electrolyte in mol L^{-1}, D is the diffusion coefficient in cm^2 s^{-1}, v is the kinematic viscosity of the solution in cm^2 s^{-1}, and ω is the rotation rate in rad s^{-1}. In a 0.1 M $HClO_4$ solution, 25 °C and 1 atm O_2, the following values are determined: D = 2.0 × 10^{-5} cm^2 s^{-1}, C = 1.2 × 10^{-3} mol L^{-1} and v = 0.01 cm^2 s^{-1}. Based on the hydrodynamic ORR profiles for the Ni_{GLAD}{Pt-1500}/GC electrode (Figure 3.8A), the electron transfer number was measured to be 3.98 (Figure 3.7), indicative of the desirable full reduction of oxygen to water. This number for the {Pt-1500}/GC electrode was lower, 3.63 (Figure 3.7 and Figure 3.8B), suggesting that there was a contribution from incomplete oxygen reduction (e.g. to H_2O_2) over the Pt control. Nevertheless, a detailed product analysis should be undertaken for a comprehensive explanation. Also, as a kinetic measurement of the ORR,[363] Tafel slopes over low overpotentials (0.95 to 0.87 V_{RHE}) were compared for the {Pt-1500}/GC and the Ni_{GLAD}{Pt-1500}/GC electrodes. The slope for the Ni_{GLAD}{Pt-1500}/GC electrode was ~ 58 mV dec^{-1}, while the {Pt-1500}/GC electrode gave a slope of ~ 75 mV dec^{-1} over the same potential range, showing that the ORR is faster

over the Ni_{GLAD}{Pt-1500}/GC catalyst. Chen et al. reported 73 mV dec^{-1} for a commercial Pt/C, while their highly active Pt_3Ni catalyst produced 46 mV dec^{-1}.[341] A Tafel slope of 54 mV dec^{-1} was reported for a PtNi–multiwalled carbon nanotube catalyst by Du et al.[364]

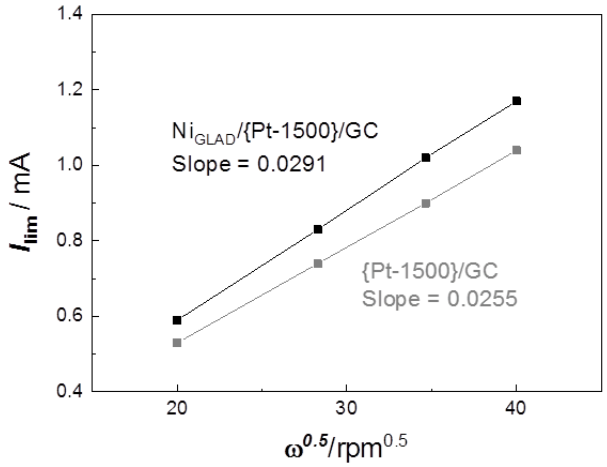

Figure 3.7 The limiting current as a function of the rotation rate for the Ni_{GLAD}{Pt-1500}/GC catalyst.

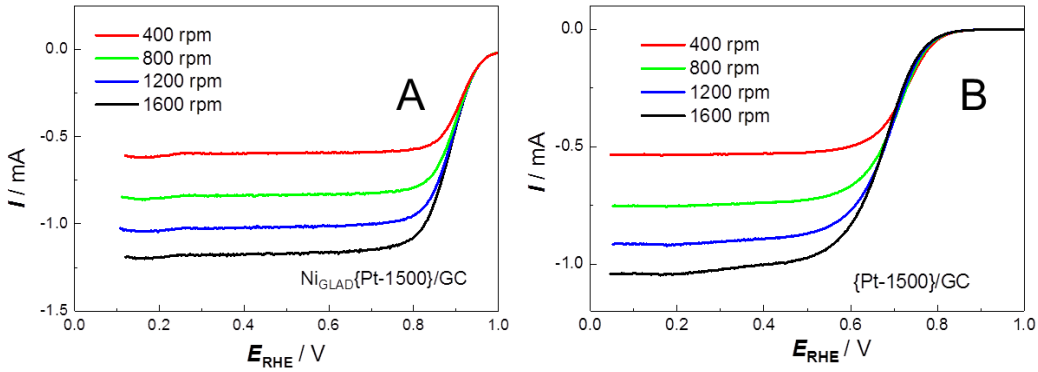

Figure 3.8 ORR profiles recorded at various rotation rates in O_2-saturated 0.1 M $HClO_4$ for (A) the Ni_{GLAD}{Pt-1500}/GC and (B) the {Pt-1500}/GC electrodes. The potential sweep rate was 10 mV s^{-1}.

3.2.5 Microscopic surface characterization

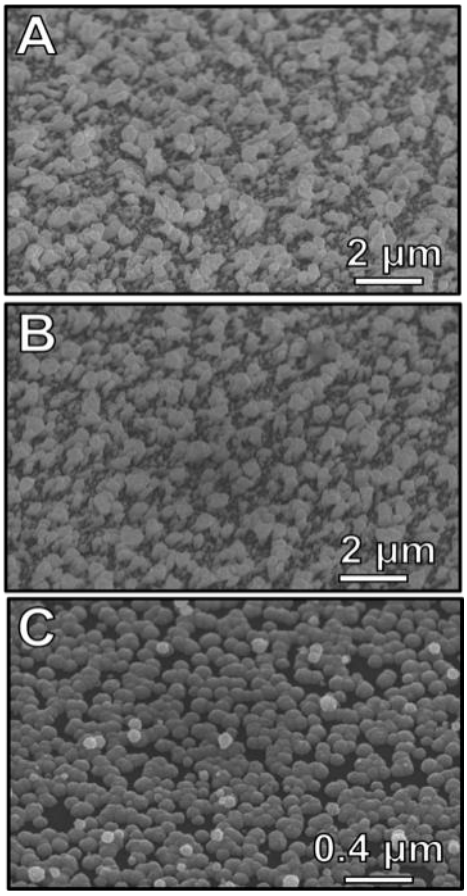

Figure 3.9 Scanning electron micrographs for Ni_{GLAD}{Pt-1500}/GC (A) before and (B) after dealloying, and (C) {Pt-1500}/GC.

Figure 3.9 shows the SEM images of the Ni_{GLAD}{Pt-1500}/GC electrode before (A) and after dealloying (B). The SEM image for a control {Pt-1500}/GC electrode is shown as well (C). The rotating WE, galvanostatic deposition of Pt upon bare GC gave uniform, spherical particles. As discussed in Chapter 2 and in our previous reports, the Pt deposition on the Ni_{GLAD}/GC electrodes mostly covered the columnar Ni_{GLAD} clusters without

detectable separate Pt particles.[322,365] The cross-section views of these columnar structures before and after Pt deposition can be found in our previous publications.[322] It is notable that the original morphology of the Ni_{GLAD}{Pt-1500}/GC layer was preserved after dealloying, and the overall structure remained intact, although there exist slightly less quantities and smaller clusters of Pt on the surface after the treatment. This is consistent with the Pt masses of 6.4 and 4.9 μg (ICP–MS) obtained before and after dealloying, respectively, of separate Ni_{GLAD}{Pt-1500}/GC samples.

Table 3.2 Summary of the XPS measurements for the {Pt-1500}/GC and Ni_{GLAD}{Pt-1500}/GC electrodes

Electrode	Binding energy (eV)		
	O 1s	C 1s	Pt 4f
{Pt-1500}/GC	531.8	284.8	71.6
Ni_{GLAD}{Pt-1500}/GC	531.5	284.8	71.1

Table 3.2 summarizes the binding energy values for C, O, and Pt obtained from the XPS studies of the {Pt-1500}/GC and the dealloyed Ni_{GLAD}{Pt-1500}/GC electrodes. The BE of the Pt 4f core electrons in the dealloyed Ni_{GLAD}{Pt-1500}/GC was ~ 0.5 eV lower than that in the {Pt-1500}/GC. This negative shift suggests that a weak electronic interaction exists between the underlying Ni_{GLAD} substrate and the Pt deposit.[366] We note

that the negative shift in BE for inner-core Pt orbitals has been observed also in other PtNi alloy systems and could be correlated to the down-shift of the Pt d-band center, supporting the proposal that a lowered d-band center leads to weakened Pt surface binding, further leading to increased ORR activity.[367,368] However, a detailed spectroscopic analysis is required to understand the origins of these shifts in BE fully. Our preliminary XPS studies do not address possible geometric effects of the underlying Ni_{GLAD} substrate on the ORR activity of Pt directly. It is likely, as has been observed by others,[112,349,351,369] that the underlying Ni_{GLAD} substrate is compressing the Pt deposit.

3.3 **Conclusions**

Developed by Brett et al.,[320] the GLAD method is suitable for tailoring mechanically stable, nanostructured, and porous metal films. It is a precise and relatively simple process, and it can be extended to casting carbon or other substrates. This Chapter demonstrates that it can be combined with the rotating WE, galvanostatic deposition to prepare Ni_{GLAD} nanopillars conveniently with controlled and thin Pt coatings that can be used as ORR catalysts in acid. The Ni_{GLAD}{Pt}/GC electrodes are prepared without the use of a binder, and they are able to sustain dealloying and ORR studies in acid, provided the Pt layer is sufficient. All the Ni_{GLAD}{Pt}/GC systems were more active towards the ORR in acid than the {Pt}/GC control. The deposition of relatively small Pt loadings that did not fully cover the Ni_{GLAD} substrate produced Ni_{GLAD}{Pt}/GC catalysts that were not stable towards dealloying in acid. The mass activities (relative to Pt) of the Ni_{GLAD}{Pt}/GC catalyst were relatively low when the Pt deposition time exceeds 1500 s. The optimized Ni_{GLAD}{Pt}/GC catalysts, made by the depositions lasting 800 and 1500 s, were at least an order of magnitude more active than the {Pt-1500}/GC electrode towards the ORR in acid.

Consistent with prior reports, we propose that the improvement in the ORR activity is caused by the strain and electronic effects of the underlying Ni substrate upon the Pt outer layer. Further studies are required to address the origin(s) of the observed ORR activity improvements fully. While the absolute activity of the Ni_{GLAD}{Pt-1500}/GC electrode is

moderate compared with the benchmark catalysts in the literature,[370,371] this Chapter demonstrates that the procedure is suitable to assess directly the activity of the catalysts in the absence of the effects from high surface area carbons and proton transport accelerators (i.e. binders such as Nafion®).

Practically, it is preferable to prepare catalysts with optimized structures directly, without activation procedures like dealloying. Further, the construction of durable PEMFCs requires that the catalyst inks be hot pressed into the membrane.[372] The temperatures, pressures, and duration of the hot pressing may restructure delicate catalyst nanostructures that were prepared under kinetic control. Further investigation is needed to determine whether our Ni_{GLAD} based composite ORR catalysts fulfill these practical requirements.

3.4 **Experimental**

3.4.1 Chemicals

The following chemicals were used as received from the supplier: Nitrogen (Praxair), oxygen (Praxair), concentrated sulfuric acid (Caledon), hydrochloric acid (EMD chemicals), nitric acid (EMD chemicals), perchloric acid (Sigma-Aldrich, 70%, 99.999% trace metal basis), 30% hydrogen peroxide (Fischer Scientific), ammonium chloride (Fisher Scientific), ethanol (Greenfield Ethanol Incorporated), acetonitrile (Sigma-Aldrich), potassium hexachloroplatinate (Aithica Chemical Corporation), nickel metal chunks (Cerac, Inc., 99.9% purity), and alumina (Allied High Tech. Products Inc.). Triply distilled water was used throughout the experiments. All experiments were performed at room temperature (298±2 K).

3.4.2 Preparation of working electrodes

The same procedure as described in Section 2.4.2 is used to prepare the Ni_{GLAD}/GC electrodes. The mass of the Ni deposit was typically 20–25 μg (ICP–MS after the ORR measurement). The perpendicular Ni nanopillars were ~ 500 nm tall with an average diameter of about 200 nm, and the density of the pillars was 4×10^8 pillars cm^{-2} (measured by counting the pillars in random SEM square areas of 25 μm^2). The EASA of the Ni_{GLAD}/GC deposits was typically 1.6–2 cm^2.

Next, thin layers of Pt were deposited onto the Ni_{GLAD}/GC electrodes to make Ni_{GLAD}{Pt}/GC electrodes, using the same procedure as in Section 2.4.3 and our previous reports.[322,365] Various deposition charges (times) were used, which resulted in different loadings of Pt. A typical deposition profile is shown in Figure 3.10. Table 3.3 lists Pt masses determined by ICP–MS for the Ni_{GLAD}{Pt}/GC electrodes prepared under various deposition times. ICP–MS samples were prepared by dissolving the deposits in aqua regia. Also, the ICP–MS result for a {Pt-1500}/GC electrode is included.

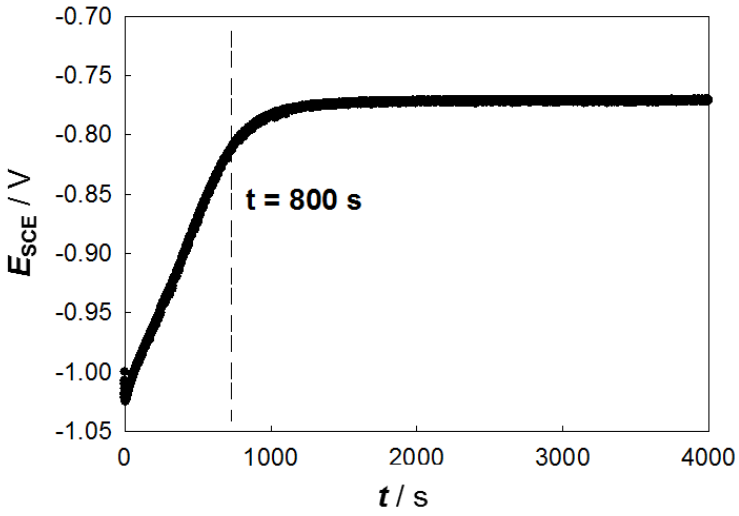

Figure 3.10 Potential profile of the WE during the deposition of Pt at a Ni_{GLAD}/GC electrode from a blackened Pt gauze in 2.0 M NH_4Cl.

Table 3.3 The amounts of Pt deposited (mass) for the {Pt}/GC and a series of Ni_{GLAD}{Pt}/GC electrodes as determined by ICP–MS

Electrode	Mass (μg)
{Pt-1500}/GC	8.4
Ni_{GLAD}{Pt-400}/GC	2.7
Ni_{GLAD}{Pt-800}/GC	5.2
Ni_{GLAD}{Pt-1500}/GC	6.4
Ni_{GLAD}{Pt-4000}/GC	22.5

Dealloying was carried out using the procedure reported by Strasser et al.[359] Briefly, the Ni_{GLAD}{Pt}/GC and the {Pt}/GC electrodes were cycled over 0.05–1 V_{RHE} at 500 mV s^{-1} in N_2-saturated 0.1 M $HClO_4$ (see Figure 3.11 for typical CVs of dealloying). CVs were recorded at 50 mV s^{-1} in the same solution before and after the process to monitor changes over dealloying. Then, the dealloyed electrodes were tested against the ORR in another O_2-saturated 0.1 M $HClO_4$ solution without any further treatment.

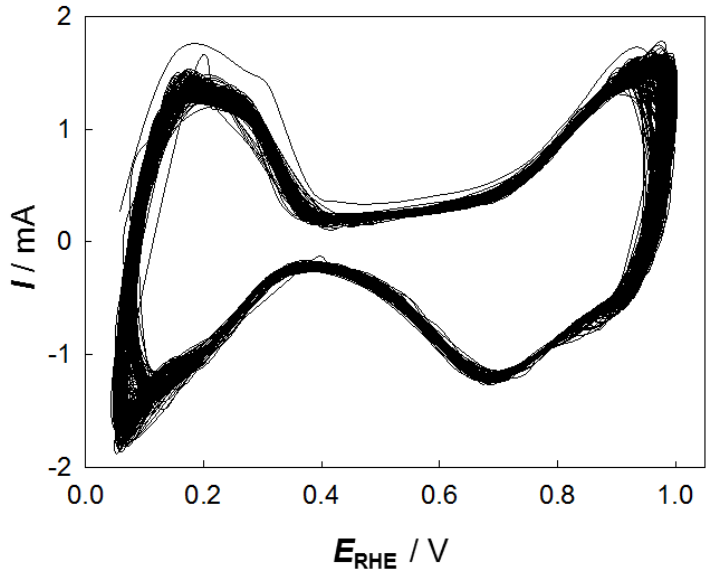

Figure 3.11 Typical voltammetric dealloying profile for a Ni_{GLAD}{Pt-1500}/GC electrode in N_2-saturated 0.1 M $HClO_4$. The potential sweep rate was 500 mV s^{-1}.

3.4.3 Electrochemistry

The electrochemical experiments were performed with a Solartron SI 1287 Electrochemical Interface controlled by CorrWare for Windows Version 2-3d software. RDE experiments were performed with a Pine Research Instrumentation Modulated Speed Rotator equipped with an AFE6MB RRDE shaft and E5TQ series Change-Disk tip. The shaft and tip were connected to the reaction flask with a Pine AC01TPA6M Gas-Purged Bearing Assembly. A Pt gauze (Alfa Aesar, 52 mesh woven from 0.1 mm wire, 99.9% metals basis) formed the counter electrode. The reference electrode was a SCE (saturated

calomel **e**lectrode). Uncompensated resistance was estimated by impedance (20 Ω) and corrected for in the ORR experiments. For each electrode, the background current in the absence of O_2 (i.e. N_2-saturated) was subtracted for the ORR tests. Each experiment has been repeated at least three times to ensure the reproducibility, and the experimental errors between measurements are less than 12%.

3.4.4 Instrumentation

SEM was performed with a Hitachi S-4800 instrument. The ICP–MS data were measured with an Agilent 7500 ce ICP–MS coupled with Cetac ASX-510 auto sampler. XPS measurements were performed on an AXIS 165 spectrometer (Kratos Analytical); the base pressure was kept below 3×10^{-8} Pa, a monochromatic Al Kα source (hv = 1486.6 eV) was used at a power of 168 W, and the analysis spot size was 400 μm × 700 μm.

Chapter 4 Easily Prepared, High Activity Ir–Ni Hydrous Oxide Catalysts for Water Oxidation in Acid[a]

4.1 Introduction

Renewable energy systems, such as photovoltaic devices,[373] require that electrical energy be stored and released efficiently. A promising method to store the electrical energy on a large scale is the electrolysis of water.[129,374–376] The resulting hydrogen can be converted back into electricity with fuel cells (e.g. PEMFCs).[377] The WOR at the anode of an electrolyzer requires electrocatalysts.[146,189,191,378–380] While the standard potential for the WOR is 1.23 V_{RHE}, the kinetics of the WOR are slow, resulting in significant anode overpotentials in water electrolyzers.

Many single and multicomponent metallic catalysts have been investigated to accelerate the WOR in acid.[170,189,191,204,379–382] Catalysts containing Ir (regarded as derivatives of Ir^{IV}–oxo species) have the most favorable combination of activity and stability in acid to date. Catalysts containing Ru are active, but Ru is not stable to prolonged operation at WOR potentials in acid.[383,384] As a result, Ir oxide nanoparticles are the benchmark for the WOR in acid, [212] and much of the research in this area is directed

[a] *A version of this Chapter has been published. Moghaddam, R. B.; Wang, C.; Sorge, J. B.; Brett, M. J.; Bergens, S. H. Electrochemistry Communications 2015, 60, 109.*

towards optimizing the utilization of Ir.[170,189,204,209,212,379,385–390] For example, Berlinguette et al. published a photochemical decomposition of Ir(acetylacetonate)$_3$ deposits to form amorphous IrO_x films that were active for the WOR in acid.[387] Among the most active acid WOR catalysts are those reported by Strasser et al.[189,191,379,380] With a series of dealloyed Ir oxide catalysts, they obtained mass activities in acid of ~ 40 A g_{Ir}^{-1} at 0.25 V overpotential.[189] The most active IrNi@IrO_x core-shell catalyst in this series was three times more active than the pure IrO_x. Recently, this group reported a mass activity of ~ 90 A g_{Ir}^{-1} at 0.28 V overpotential, using a $IrNiO_x$ catalyst on antimony-doped tin oxide annealed at 180 °C.[191]

Colloidal suspensions of IrO_x nanoparticles typically contain organic stabilizers that protect the surface of the oxide particles.[391–395] In 2010, Berkerman reported that small (~ 1 nm) IrO_x nanoparticles could be prepared in relatively high concentrations as stable suspensions in water by a simple, bench-top reaction between $IrCl_3$ and hydroxide solutions in the presence of oxygen.[382] In this Chapter, we adopted this methodology to prepare colloidal $Ir_{1-x}Ni_x$ hydrous oxide nanoparticles (x = 0–0.50) suspensions. The hydrous oxide nanoparticles were characterized and were found to be remarkably active towards the WOR in acid.

4.2 **Results and Discussion**

4.2.1 Characterization of Ir HO-np

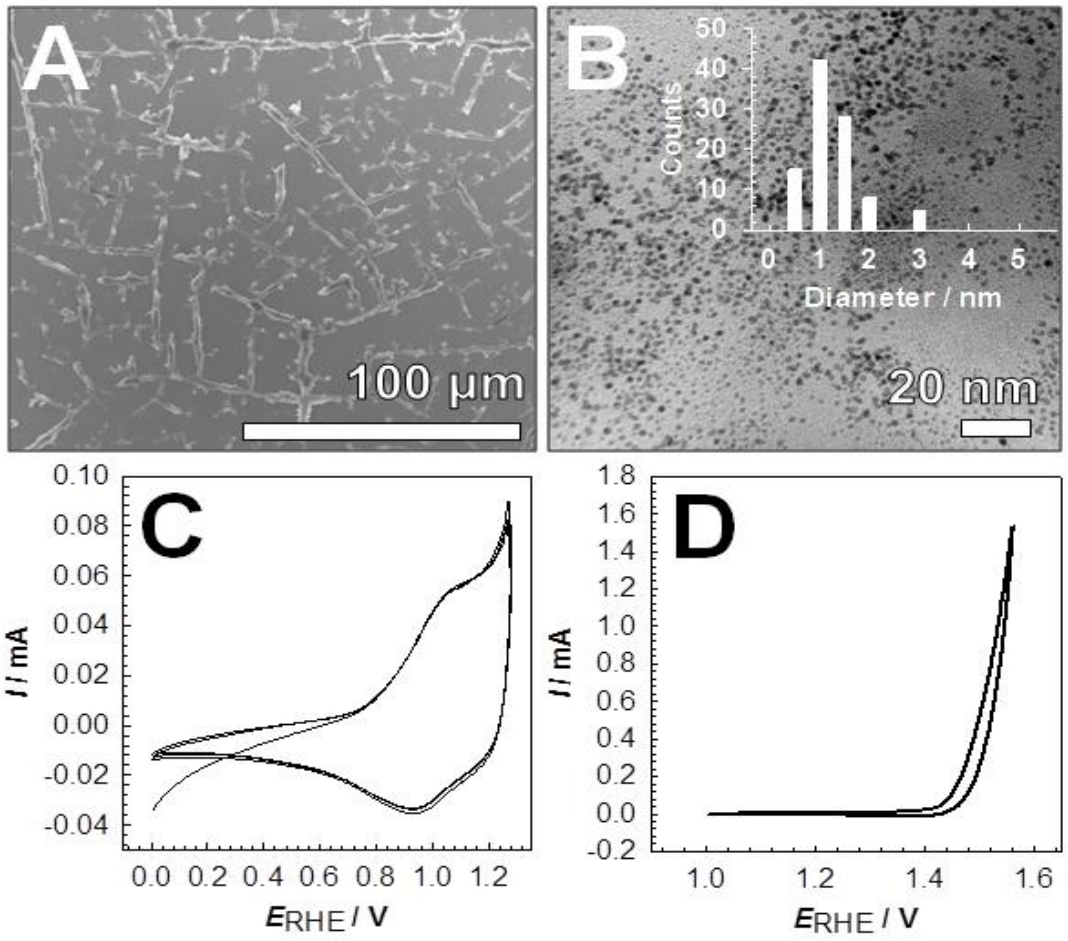

Figure 4.1 (A) SEM image of the HO-np deposits on GC. (B) TEM image of Ir HO-np supported by a Cu grid. Voltammetric profiles (C) at 50 mV s^{-1} and (D) at 10 mV s^{-1} in 0.1 M H_2SO_4 of HO-np deposits on GC containing 17 μg_{Ir} cm^{-2} and 1 wt% Nafion®. The size distribution (B, inset) was determined by measuring ~ 100 particles.

Figure 4.1A shows the SEM image of the HO-np deposits on a GC electrode with Nafion® as a binder, and Figure 4.1B shows the TEM (**t**ransmission **e**lectron **m**icroscopy) image of Ir HO-np supported by a Cu grid. The average particle size is 1.30 nm, and the size distribution histogram is consistent with those reported previously.[382] Figure 4.1C shows the voltammetric profile (0–1.25 V_{RHE}, 50 mV s^{-1}) of the Ir HO-np deposit on GC (Ir HO-np/GC) in 0.1 M H_2SO_4. The profile contains $Ir^{3+/4+}$ redox peaks at 1.07 (anodic) and 0.93 V_{RHE} (cathodic).[396] The oxidation and reduction process happens with proton coupled electron transfer, as shown in eq 4.1.[397]

$$Ir^{III}–OH_2 \rightleftharpoons Ir^{IV}–OH + e^- + H^+ \qquad 4.1$$

There were no hydrogen signals, indicating that metallic Ir is absent from the deposit. Figure 4.1D shows the WOR activity of the Ir HO-np deposit (with 17 μg_{Ir} cm^{-2}) in the extended anodic range in 0.1 M H_2SO_4. The water oxidation onset is ~ 1.42 V_{RHE}, corresponding to ~ 0.19 V overpotential. The mass-normalized WOR activity at 1.48 V_{RHE} (0.25 V overpotential) is ~ 93 A g_{Ir}^{-1}.

4.2.2 Water oxidation activity of $Ir_{1-x}Ni_x$ HO-np

A series of $Ir_{1-x}Ni_x$ HO-np were prepared using the same procedure with $NiCl_2$ added. Figure 4.2A shows the LSV (**l**inear **s**weep **v**oltammetry) in 0.1 M H_2SO_4. A bare glassy carbon electrode did not show any water oxidation activity in the 1.40–1.56 V_{RHE} potential region. All $Ir_{1-x}Ni_x$ HO-np were active for water oxidation, with the onset

potential at ~ 1.42 V_{RHE}.

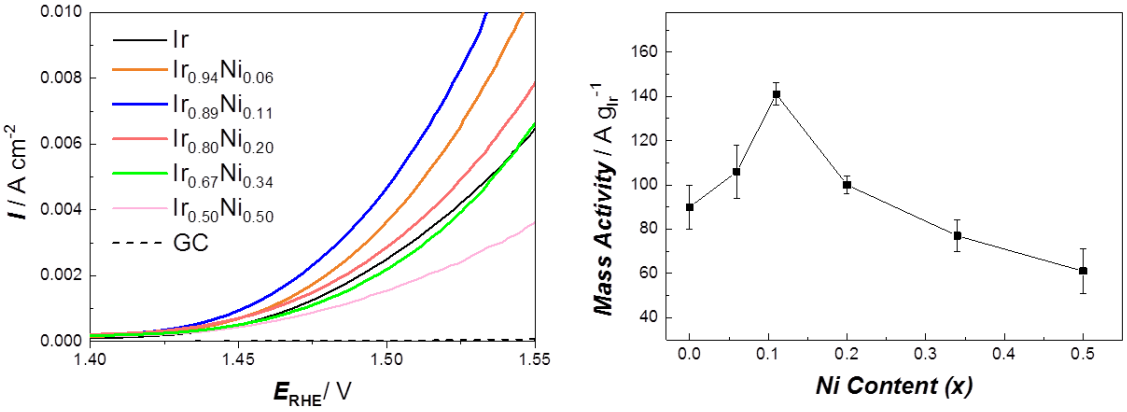

Figure 4.2 (A) LSVs of $Ir_{1-x}Ni_x$ HO-np (17μg_{Ir} cm^{-2}) on GC in 0.1 M H_2SO_4 at 10 mV s^{-1}. (B) Mass-normalized activities (A g_{Ir}^{-1}) of the $Ir_{1-x}Ni_x$ HO-np/GC electrodes at 1.48 V_{RHE}.

Figure 4.2B is a plot of the Ir mass-normalized activities of the $Ir_{1-x}Ni_x$ HO-np/GC electrodes at 1.48 V_{RHE} (0.25 V overpotential) in 0.1 M H_2SO_4 against composition. Increased activities were observed with the presence of Ni up to x = 0.11 ($Ir_{0.89}Ni_{0.11}$ HO-np/GC, 142 A g^{-1}), beyond which the activity decreases. The mass activities of x = 0.33 ($Ir_{0.67}Ni_{0.33}$ HO-np/GC) and x = 0.50 ($Ir_{0.50}Ni_{0.50}$ HO-np/GC) were ~ 76 and 61 A g_{Ir}^{-1} at 1.48 V_{RHE}, respectively, significantly lower than that of the Ir HO-np/GC electrode (93 A g_{Ir}^{-1}). All these electrochemical experiments were performed at least three times to ensure reproducibility.

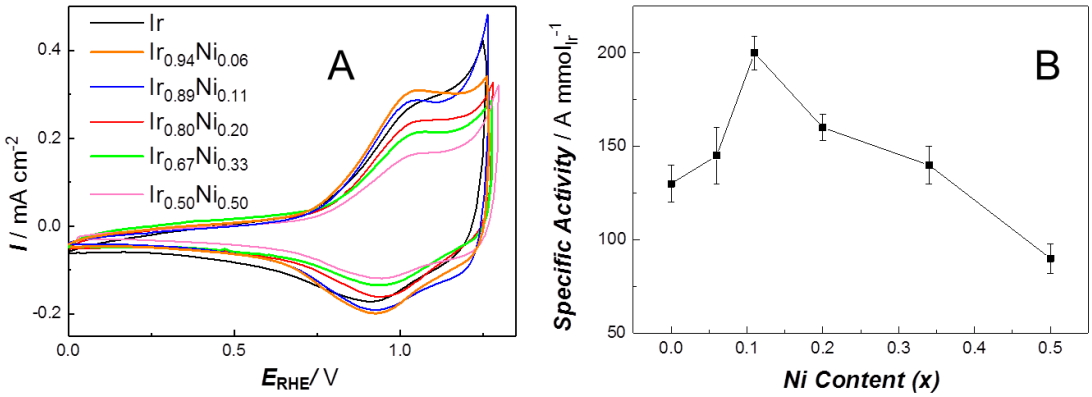

Figure 4.3 (A) CVs of the $Ir_{1-x}Ni_x$ HO-np/GC electrodes in 0.1 M H_2SO_4 at 50 mV s^{-1} (loadings: 17 μg_{Ir} cm^{-2}). (B) Specific activities at 1.48 V_{RHE} (A $mmol_{Ir}^{-1}$) obtained by the current normalized to the number of electrochemically active Ir atoms.

Figure 4.3A shows the cyclic voltammograms of the $Ir_{1-x}Ni_x$ HO-np/GC electrodes, and the electrochemical parameters are summarized in Table 4.1. The $Ir^{3+/4+}$ oxidation peak shifted to lower potentials with increased amount of Ni, which suggests a higher electron density at the Ir sites. The number of electrochemically active Ir atoms are estimated by integrating the anodic voltammetric currents over the range 0.8–1.2 V_{RHE} (corrected using the capacitive charge in 0.1 M H_2SO_4 at 10 mV s^{-1}) and assuming one electron transfer for the $Ir^{3+/4+}$ redox couple (eq 4.1).[189] The highest number of electrochemically active Ir atoms was observed with the $Ir_{0.94}Ni_{0.06}$ HO-np/GC electrode.

Figure 4.3B shows the specific activities (current normalized to the number of electrochemically active Ir atoms, A $mmol_{Ir}^{-1}$) of the $Ir_{1-x}Ni_x$ HO-np/GC electrodes against composition. A similar trend as the mass activity is shown, with the $Ir_{0.89}Ni_{0.11}$ HO-np/GC

electrode the most active. Compared with the Ir HO-np/GC electrode at 130 A $mmol_{Ir}^{-1}$, the higher specific activity (203 A $mmol_{Ir}^{-1}$) for the $Ir_{0.89}Ni_{0.11}$ HO-np/GC electrode indicates that the enhancement in the WOR activity is not caused only by the increased number of electrochemically active Ir atoms.

Table 4.1 Key electrochemical parameters from the CVs of the $Ir_{1-x}Ni_x$ HO-np/GC electrodes

	$Ir^{3+/4+}$ oxidation potential (V_{RHE})	Electrochemically active Ir atoms (nmol)
Ir	1.070	2.36
$Ir_{0.94}Ni_{0.06}$	1.057	2.49
$Ir_{0.89}Ni_{0.11}$	1.046	2.31
$Ir_{0.80}Ni_{0.20}$	1.043	2.07
$Ir_{0.67}Ni_{0.33}$	1.032	1.83
$Ir_{0.50}Ni_{0.50}$	1.028	1.72

4.2.3 Tafel plots

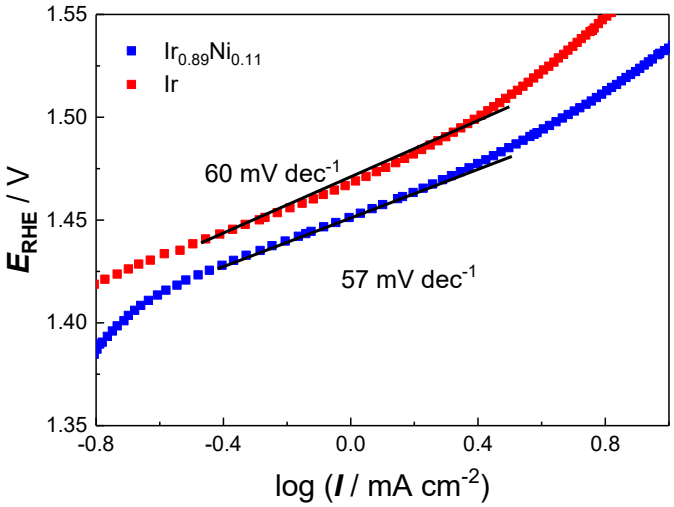

Figure 4.4 Tafel plots of the $Ir_{0.89}Ni_{0.11}$ HO-np/GC and the Ir HO-np/GC electrodes.

Figure 4.4 shows the Tafel plots of the $Ir_{0.89}Ni_{0.11}$ HO-np/GC and Ir HO-np/GC electrodes. Both electrodes showed close to 60 mV dec^{-1} Tafel slopes in the potential region 1.42–1.48 V_{RHE}, suggesting that the WOR mechanism is the same for both electrodes. The slope of 60 mV dec^{-1} matches that of the well-known mechanism for IrO_x WOR in acid (eqs 4.2 to 4.5).[159,398–401]

$$M + H_2O \rightarrow M\text{–}OH^{*ads} + H^+ + e^- \quad 4.2$$

$$M\text{–}OH^{*ads} \rightarrow M\text{–}OH^{ads} \quad 4.3$$

$$M\text{–}OH^{ads} \rightarrow M\text{–}O^{ads} + H^+ + e^- \quad 4.4$$

$$M\text{–}O^{ads} + M\text{–}O^{ads} \rightarrow 2M + O_2 \quad 4.5$$

In eqs 4.2 to 4.5, M is an active site, and $M\text{–}OH^{ads}$ is an adsorbed hydroxyl group formed

by the rearrangement of M–OH^{*ads}.[402] This mechanism predicts a Tafel slope ~ 60 mV dec^{-1} if eq 4.3 is the RDS and eq 4.2 is a pre-equilibrium electrochemical step. The lower Tafel slope for the $Ir_{0.89}Ni_{0.11}$ HO-np/GC electrode indicates faster kinetics towards the water oxidation, likely caused by the addition of Ni leading to the relative rate change of step 4.2 and 4.3 via introducing oxygen vacancies or lattice strain (vide infra).

4.2.4 Stability comparison

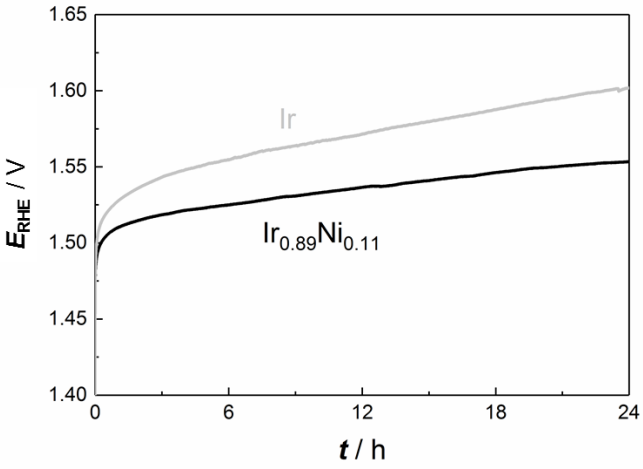

Figure 4.5 Long-term galvanostatic measurements of $Ir_{0.89}Ni_{0.11}$ HO-np and Ir HO-np deposited on CF in 0.1 M H_2SO_4 at 1 mA cm^{-2}. The loadings were 17 μg_{Ir} cm^{-2}.

The stability of Ir HO-np and $Ir_{0.89}Ni_{0.11}$ HO-np were tested in 0.1 M H_2SO_4 supported by CF (**c**arbon **f**iber paper). Figure 4.5 shows the galvanostatic 24 h WOR profile. Both electrodes produced similar durability patterns, and no significant potential increase was observed over the measurement timescale. The overpotential of the $Ir_{0.89}Ni_{0.11}$ HO-np/CF

electrode increased by 45 mV during the 24 h, compared with the 90 mV increase for the Ir HO-np/CF electrode. 1.87 μg (11% of the initial mass of Ir on the electrode) and 1.71 μg (10% of the initial mass) Ir were found in the electrolyte after a galvanostatic test for the Ir HO-np/CF and $Ir_{0.89}Ni_{0.11}$ HO-np/CF electrodes, respectively. These data indicate the enhanced stability of the $Ir_{0.89}Ni_{0.11}$ HO-np/CF electrode towards the WOR. In addition, only 6% of the initial mass of Ni on the electrode was found in the electrolyte after 24 h for the $Ir_{0.89}Ni_{0.11}$ HO-np/CF electrode. This observation indicates that Ni is stabilized in the IrO_x matrix, perhaps by forming Ir–O–Ni–O–Ir structures. Smith et al. prepared an amorphous IrO_x catalyst on the electrode with a loading of 100 μg cm^{-2}, and the WOR overpotential increased by 30 mV during 24 h 1 mA cm^{-2} galvanostatic test in 1.0 M H_2SO_4.[387] Nong et al. loaded 10.2 μg cm^{-2} $IrNiO_x$ on the mesoporous antimony doped tin oxide, and the overpotential increased by 60 mV in 20 h in 0.05 M H_2SO_4.[191] Our $Ir_{0.89}Ni_{0.11}$ HO-np are among the most active and stable IrO_x based catalysts for water oxidation in acid.

4.2.5 Characterization of $Ir_{0.89}Ni_{0.11}$ HO-np

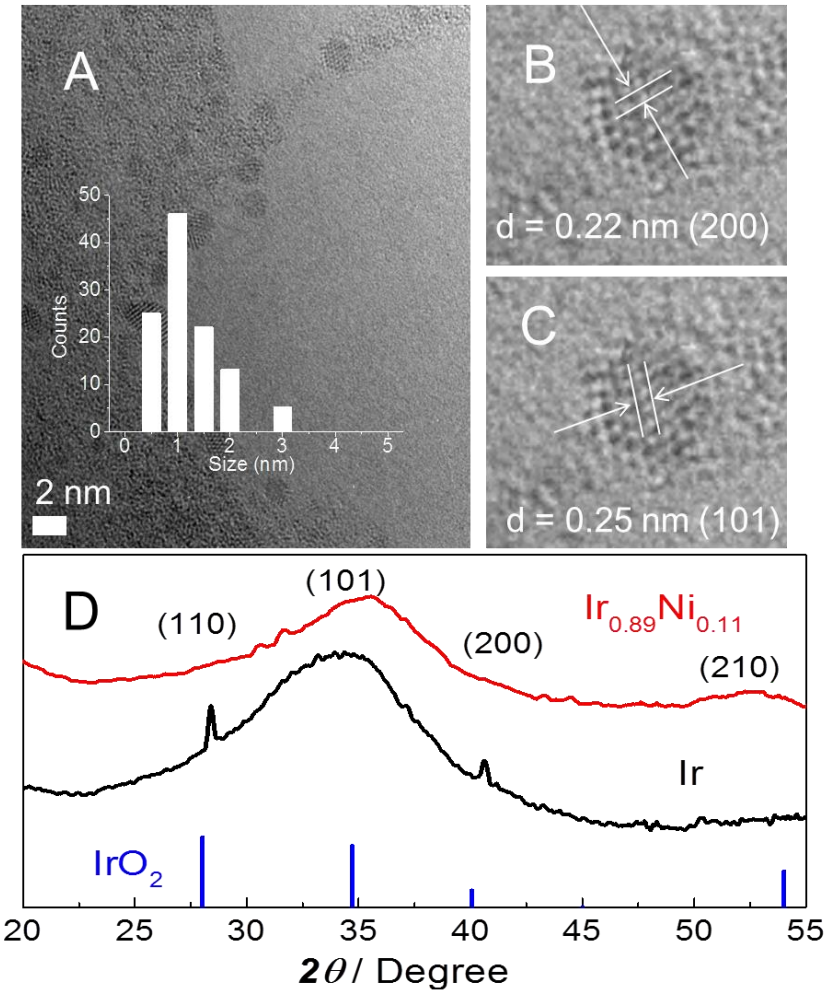

Figure 4.6 (A, B and C) HRTEM images of $Ir_{0.89}Ni_{0.11}$ HO-np, with interpalnar distances measured. (A) shows the size distribution histogram of the HO-np. (D) XRD patterns on $Ir_{0.89}Ni_{0.11}$ HO-np and Ir HO-np.

Figure 4.6A shows the HRTEM (**h**igh **r**esolution **t**ransmission **e**lectron **m**icroscopy) image of $Ir_{0.89}Ni_{0.11}$ HO-np. The $Ir_{0.89}Ni_{0.11}$ HO-np crystals had similar size distribution with Ir HO-np, with the average particle size 1.33 nm.[190] Figure 4.6B and C show that the

interplanar distances of $Ir_{0.89}Ni_{0.11}$ HO-np were 0.22 and 0.25 nm, corresponding to the (200) and (101) planes of the tetragonal IrO_2. The powder XRD (**X**-**r**ay **d**iffraction) pattern of $Ir_{0.89}Ni_{0.11}$ HO-np (Figure 4.6D) showed a similar structure with the tetragonal IrO_2 with space group P42/mnm (JCPDS No. 86-0330). The presence of both sharp and broad diffraction peaks indicates that the sample contains small crystalline regions and large amorphorous regions. We note that studies like XRD are of the isolated solid-state oxide. The results may not apply to the active catalysts in aqueous acid at various potentials.[403]

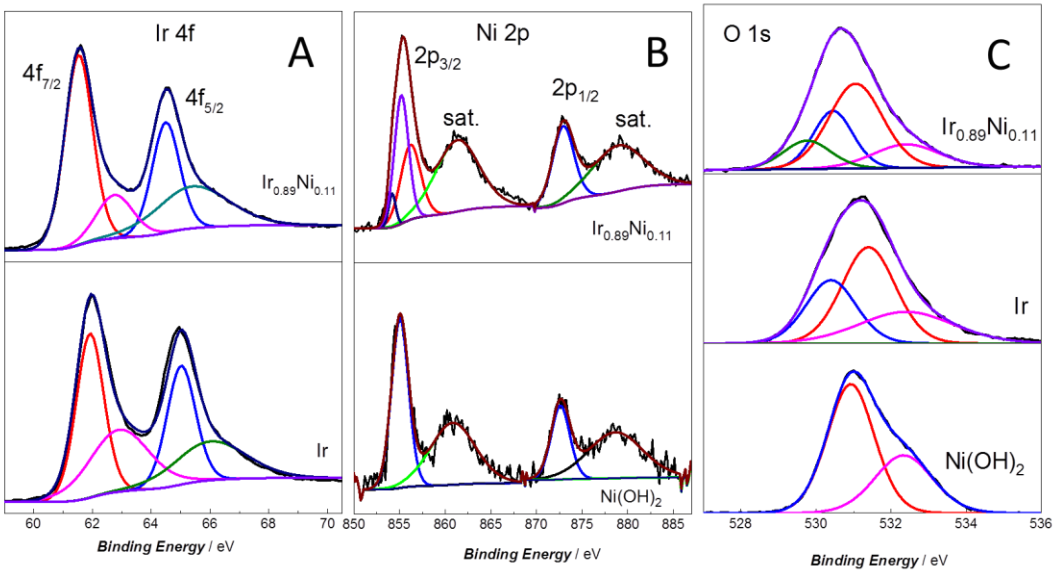

Figure 4.7 Deconvoluted XPS spectra of Ir HO-np, $Ir_{0.89}Ni_{0.11}$ HO-np, and $Ni(OH)_2$. (A) Ir 4f region, (B) Ni 2p region, and (C) O 1s region.

Figure 4.7 shows the XPS spectra of Ir HO-np, $Ir_{0.89}Ni_{0.11}$ HO-np, and $Ni(OH)_2$ prepared using the same method. In Figure 4.7A, the $4f_{7/2}$ (61.6 eV) and $4f_{5/2}$ (64.5 eV) Ir peaks in the $Ir_{0.89}Ni_{0.11}$ HO-np and the $4f_{7/2}$ (61.9 eV) and $4f_{5/2}$ (65.0 eV) Ir peaks in the Ir HO-np show that Ir is mainly in the 4^+ oxidation state in both.[404] The shift to lower binding energy in the 4f peak indicates that the electron density at the Ir site is higher in $Ir_{0.89}Ni_{0.11}$ HO-np. A similar down shift of the Ir 4f binding energy is observed in $Ir_{0.89}Cu_{0.11}$ HO-np.[405] Figure 4.7B shows the XPS spectra of the Ni 2p region of $Ir_{0.89}Ni_{0.11}$ HO-np and $Ni(OH)_2$ with the Ni $2p_{3/2}$ peaks deconvoluted. The binding energy of the Ni 2p peaks for $Ir_{0.89}Ni_{0.11}$ HO-np (Ni $2p_{3/2}$ (855.4 eV), satellite (861.3 eV), Ni $2p_{1/2}$ (873.3 eV), and satellite (879.4 eV) are higher than those of $Ni(OH)_2$ (Ni $2p_{3/2}$ (854.9 eV), satellite (860.6 eV), Ni $2p_{1/2}$ (872.3 eV), and satellite (879.1 eV)).[406] Deconvolution on the Ni $2p_{3/2}$ peak of $Ir_{0.89}Ni_{0.11}$ HO-np gave three components at 853.9 eV (NiO, 6%)[407], 855.3 eV ($Ni(OH)_2$, 42%)[408,409], and 856.3 eV (51%). The origin of the 856.3 eV peak is unknown, but this higher binding energy indicates decreased electron density at the Ni sites. Roberts et al. reported a binding energy of 856.1 eV for the Ni^{3+} species.[410] Therefore, we tentatively assign this component to Ni^{3+}. Figure 4.7C shows the deconvoluted O 1s region of Ir HO-np, $Ir_{0.89}Ni_{0.11}$ HO-np and $Ni(OH)_2$. For Ir HO-np, three deconvoluted peaks were shown at 530.4 eV, 531.3 eV and 532.5 eV, and could be assigned to the lattice oxygen, the hydroxide groups and the adsorbed water, respectively.[193,407] For $Ni(OH)_2$, only two deconvoluted peaks at 531.0 eV and 532.3 eV were shown, indicating the hydroxide

species with adsorbed water. However, the deconvoluted O 1s spectrum for $Ir_{0.89}Ni_{0.11}$ HO-np contained a new peak at 529.7 eV, which does not exist in that of Ir HO-np, and could be assigned to the oxygen atom bridging Ir and Ni in the lattice.[193,405]

Taking into consideration the HRTEM, XRD and XPS analysis, we propose that $Ir_{0.89}Ni_{0.11}$ HO-np have a similar structure with IrO_2, with 11% Ir replaced by Ni.

4.3 **Conclusions**

To our knowledge, $Ir_{1-x}Ni_x$ HO-np synthesized under alkaline conditions in air are among the most active WOR catalysts in acid reported to date,[191,379] with onset potentials of ~ 1.42 V_{RHE} and an optimized mass activity of ~ 140 A g_{Ir}^{-1} (1.48 V_{RHE}), obtained with $Ir_{0.89}Ni_{0.11}$ HO-np (see Table 5.3 for activity comparison with literature). The number of electrochemically active Ir atoms and specific activity showed that the improvement in activity upon the addition of Ni was not caused only by an increased number of electrochemically active Ir atoms. $Ir_{0.89}Ni_{0.11}$ HO-np have a similar structure with IrO_2, with 11% Ni replacing Ir in the lattice. The replacement of Ir^{4+} by Ni^{2+} or Ni^{3+} leads to the reduction of the overall positive charge, possibly introducing oxygen vacancies to the lattice. In addition, the differences in size of Ir^{4+} (63 pm) and Ni^{2+} (83 pm) or Ni^{3+} (70 pm) would lead to the expansion of the lattice, causing the strain in the lattice.[411] Both these effects would affect the WOR activity. Preliminary studies on the mechanism show that the presence of Ni does not alter the mechanism pathway for water oxidation significantly. A detailed mechanistic study is necessary to fully understand the effect of the promotion of Ni to Ir for the WOR.

4.4 **Experimental**

4.4.1 Chemicals

Sulfuric acid (Alfa Aesar; 99.9999%), potassium hydroxide (Sigma-Aldrich, semiconductor grade, 99.99%), iridium chloride trihydrate (A.B. Mackay Chemicals), nickel chloride (Alfa Aesar, anhydrous, 98%), carbon fiber paper (ElectroChem, Inc.), *tert*-butanol (Sigma-Aldrich, > 99%), and Nafion® (5 wt%, ElectroChem, Inc.) were used as received. Triply distilled water was used throughout the experiments.

4.4.2 Preparation of nanoparticle solutions

Colloidal suspensions of the mixed metal hydrous oxide nanoparticles were prepared by modifying the procedure described for iridium oxides.[382] To prepare a pure Ir HO-np suspension, 0.0704 g $IrCl_3 \cdot 3H_2O$ was dissolved in 20 mL water (i.e. 0.01 M solution of Ir^{3+}) to form a dark brown solution. Then, 2.5 mL 0.8 M KOH was added dropwise over 5 min. Upon adding the KOH, the dark brown color changed first to green, then to blue after two days; the color did not change afterwards. The obtained Ir HO-np solution was stored at room temperature. Control experiments (CV in 0.1 M H_2SO_4) confirmed that the Ir HO-np suspension was stable for about two months at room temperature. $Ir_{1-x}Ni_x$ HO-np (x = 0.06–0.50) were prepared by adding 1 M KOH to 20 mL solutions of $IrCl_3$ and $NiCl_2$ with the weights and volumes shown in Table 4.2. The molar ratios of the precursor mixtures were $Ir_{0.94}Ni_{0.06}$, $Ir_{0.89}Ni_{0.11}$, $Ir_{0.80}Ni_{0.20}$, $Ir_{0.67}Ni_{0.33}$, and $Ir_{0.50}Ni_{0.50}$. There was no visual

evidence of precipitates after several weeks for the suspensions with x = 0–0.11, but precipitates formed from suspensions with $x \geq 0.20$. The nanoparticles can be washed and separated. An equal volume of *tert*-butanol was added to the HO-np suspensions to precipitate the catalysts. After agitation for 10 min, the solution was allowed to rest for 30 min, followed by the centrifugation at 4500 rpm for 20 min. The supernatant was decanted, and the remaining precipitates were washed twice with 1:1 volume *tert*-butanol: H_2O (15 mL). After another centrifugation at 4500 rpm for 20 min, the black precipitates were dried in air at room temperature and used for XRD. The precipitates were dispersed in water by sonication for 10 min prior to the XPS and HRTEM analysis.

Table 4.2 Amounts used for the synthesis of $Ir_{1-x}Ni_x$ HO-np

Ir/Ni ratio	$IrCl_3 \cdot H_2O$ (g)	$NiCl_2$ (g)	0.8 M KOH (mL)
Ir	0.0704	-	2.5
$Ir_{0.50}Ni_{0.50}$	0.0704	0.0259	5
$Ir_{0.67}Ni_{0.33}$	0.0706	0.0130	3.8
$Ir_{0.80}Ni_{0.20}$	0.0706	0.0065	3.1
$Ir_{0.89}Ni_{0.11}$	0.0707	0.0032	2.8
$Ir_{0.94}Ni_{0.06}$	0.0705	0.0016	2.7

4.4.3 Preparation of working electrodes

The $Ir_{1-x}Ni_x$ HO-np (x = 0–0.50) suspensions were diluted by a factor of five using water that contained the appropriate amounts of Nafion® to give a final 1wt% Nafion® per total mass of Ir + Ni, calculated from the amounts in Table 4.2. Using a micropipette and graded microtips, 10 μL of the Ir HO-np/Nafion® suspensions (sonicated for 2 min) were drop-coated onto a bare GC (0.196 cm^2) electrode. Appropriate volumes of the $Ir_{1-x}Ni_x$ HO-np/Nafion® suspensions were drop-coated to give 3.4 μg Ir on the electrodes. The ink was dried at 60 °C for 20 min then left at room temperature for 20 min. Five times the amount of the HO-np/Nafion® suspensions were used to load the catalysts on the carbon fiber paper electrode (1 cm^2 surface area). To check the accuracy of the metal weighing, aliquots of the HO-np suspensions that nominally contained 3.4 μg Ir were analyzed by ICP–MS. The accuracy of the nominal mass was ~ 95% that of the actual ICP–MS value.

4.4.4 Electrochemistry

The electrochemical experiments were performed with a Solartron SI 1287 Electrochemical Interface controlled by CorrWare for Windows Version 2-3d software. The reference electrode was a SCE. A graphite rod formed the CE. Uncompensated resistance was estimated by impedance (20 Ω) and corrected for. All the electrochemical experiments were carried out at room temperature in N_2-saturated solutions.

4.4.5 Instrumentation

SEM was performed with a Hitachi S-4800 instrument. A JEOL 2011 transmission electron microscope (The Microscopy and Microanalysis Facility, University of New Brunswick) was used for TEM analysis. Samples for ICP–MS analysis were measured with Perkin Elmer Elan 6000. The HRTEM images were acquired using Titan 80-300 LB high resolution transmission microscopy. The XRD patterns were measured with an Inel diffractometer equipped with a curved position-sensitive detector (CPS 120) and a Cu Kα1 radiation source at 40 kV and 20 mA ($\lambda_{1/2}$ = 1.54060/1.54439 Å).

XPS measurements were performed on a Kratos Axis 165 instrument. Charge neutralization was applied to stabilize spectra during spectra collecting because the samples were not conductive adequately. To account for charging effects, all spectra have been referred to C 1s at 284.8 eV. Casa XPS software was used to fit the XPS data. The binding energies of the peaks were calculated from the background-subtracted spectra using Shirley background. The intensity ratio of the Ir $4f_{7/2}$ and $4f_{5/2}$ peaks was set to 4:3 with a spin-orbit coupling of 3.0 eV. The Ni $2p_{3/2}$ and $2p_{1/2}$ peaks were set to have an intensity ratio of 2:1. The peaks were fitted with Gaussian (70%)–Lorentzian (30%) curves.

Chapter 5 Active, Simple Ir–Cu Hydrous Oxide Electrocatalysts for Water Oxidation in Acid[a]

5.1 Introduction

The production of hydrogen by water electrolysis is a promising method to store energy from renewable sources, such as wind and solar.[145,374,375,412–414] Ideally, PEMs are suitable for water electrolyzers because they provide low ohmic losses, large partial load ranges, high current densities, and high gas purity.[146,166,415] However, the anode catalysts of PEMWEs must operate at oxidizing potentials for long periods of time under acidic conditions at moderate to high temperatures.[166,193,204,378] Non-noble catalysts mostly dissolve under these conditions, and oxides of noble metals are required in the most stable catalysts for the WOR in acid.[146,166,415] Further, the kinetics of the 4-electron water oxidation reaction are slow and requires high catalyst loadings in the electrolyzer anodes to produce practical current densities at moderate overpotentials.[76] Because of these challenges, developing stable and active electrocatalysts is the major barrier to the widespread utilization of PEMWEs.

---

[a] *A version of this Chapter has been published. Wang, C.; Moghaddam, R. B.; Bergens, S. H. Journal of Physical Chemistry C 2017, 121, 5480.*

Typically, catalysts containing Ru are the most active for the WOR in acid, but RuO_x undergoes severe dissolution during prolonged operation.[164,416,417] Pure Ir hydrous oxides have promising activity and good stability for the water oxidation in acid, but the scarcity of Ir restricts their widespread use in electrolyzers.[146,170,189,387,418–420] A high priority in WOR research is to increase the activity of Ir WOR catalysts while maintaining their stability. It was shown that combining Ir with a 3d-transition metal like Ni reduces the Ir content and increases the activity of WOR catalysts.[189–191,199,200,203,204] Also, the structures of Ir-containing WOR catalysts have been modified to increase their activities.

The previous Chapter describes a one-pot synthesis of a range of $Ir_{1-x}Ni_x$ hydrous oxide nanoparticles prepared by stirring $IrCl_3$ and $NiCl_2$ in aqueous base under air. The resulting $Ir_{0.89}Ni_{0.11}$ HO-np catalyzed the WOR at > 140 A g_{Ir}^{-1} at 0.25 V overpotential with good stability in 0.1 M H_2SO_4 (loading 17.3 μg_{Ir} cm^{-2}).[190] Despite its high abundance and widespread use as an electrocatalyst, we are aware of only four reports of the incorporation of Cu into IrO_x catalysts for the WOR in acid. Zou et al. synthesized Cu–Ir nanocages by a galvanic replacement method and reported 73 A g_{Ir}^{-1} mass activity for $Cu_{1.11}Ir$ nanocages at 0.28 V overpotential in 0.05 M H_2SO_4 (loading 143 μg cm^{-2}).[200] Later, they reported the preparation of Co doped Cu–Ir nanocages and the NiCuIr nanoframes synthesized by hydrolysis of metal precursors, followed by selectively leaching of surface non-noble metals. Their water oxidation activities reached 300 A g_{Ir}^{-1} (the nanocage) and 275 A g_{Ir}^{-1} (the nanoframe), at 0.28 V overpotential (loading 20 μg cm^{-2}).[198,421] The catalysts reported

by Sun et al. obtained 50 A g_{Ir}^{-1} mass activity at 0.35 V overpotential in 0.1 M $HClO_4$ (loading 200 μg cm^{-2}) with $Cu_{0.3}Ir_{0.7}$ oxides prepared by the hydrothermal method.[199]

In this Chapter, we describe the preparation of a series of $Ir_{1-x}Cu_x$ HO-np by stirring $IrCl_3$ and $CuCl_2$ hydrates in aqueous KOH under air.[190] The HO-np were characterized and were extremely active towards the WOR in acid.

5.2 **Results and Discussion**

5.2.1 Characterization of $Ir_{0.89}Cu_{0.11}$ HO-np

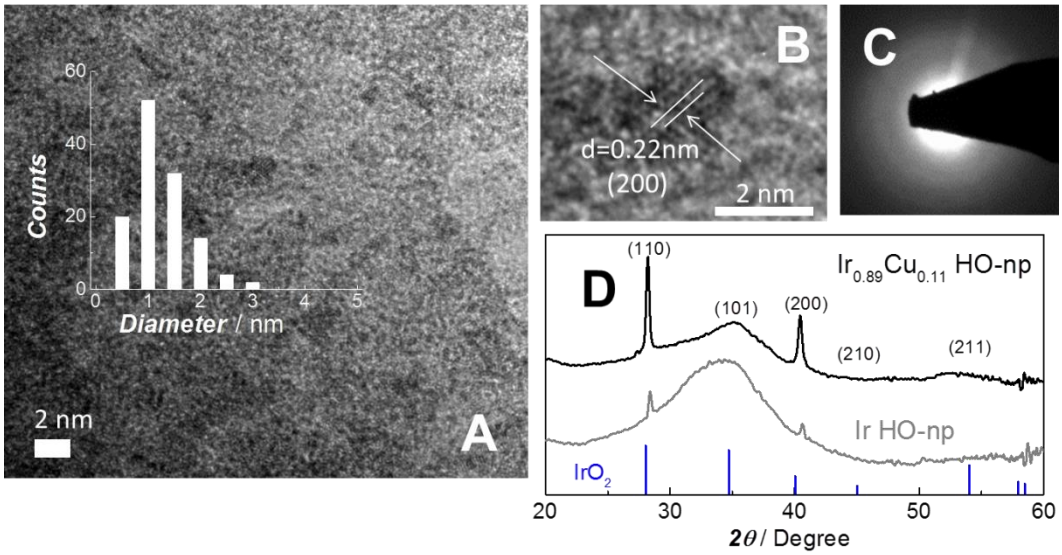

Figure 5.1 (A and B) HRTEM images of $Ir_{0.89}Cu_{0.11}$ HO-np. (C) Selected area electron diffraction pattern of $Ir_{0.89}Cu_{0.11}$ HO-np. (D) Powder XRD patterns of $Ir_{0.89}Cu_{0.11}$ HO-np and Ir HO-np.

$Ir_{1-x}Cu_x$ HO-np (x = 0–0.34) were prepared by reacting $IrCl_3$ hydrates and $CuCl_2$ hydrates with aqueous KOH under air. Figure 5.1A and B show the HRTEM images and the size-distribution histogram of $Ir_{0.89}Cu_{0.11}$ HO-np. This catalyst is the most active water oxidation catalyst in the series (vide infra). The sample consists of a mixture of small, crystalline nanoparticles. The average diameter was ~ 1.30 nm, which is similar to Ir HO-np and $IrNi_{0.125}$ HO-np that we reported previously.[190] Figure 5.1C shows that the

selected area diffraction pattern lacks bright rings, which suggests that the sample is a mixture of small crystalline nanoparticles as well.[422] The measured interplanar spacing was ~ 0.22 nm, which corresponded to the (200) plane of the IrO_2 structure with tetragonal symmetry. Similar interplanar spacings were reported for crystalized IrO_2[403,423] and Cu-doped IrO_2.[199] Figure 5.1D shows the powder XRD patterns of $Ir_{0.89}Cu_{0.11}$ HO-np and Ir HO-np. Both hydrous oxides had common IrO_2 rutile structures with tetragonal symmetry (JCPDS No. 86-0330, space group P42/mnm). The presence of both sharp and broad diffraction peaks indicates that the sample contains small crystalline regions and large amorphorous regions. We note that studies like XRD are of the isolated solid-state oxide. The results may not apply to the active catalysts in aqueous acid at various potentials.

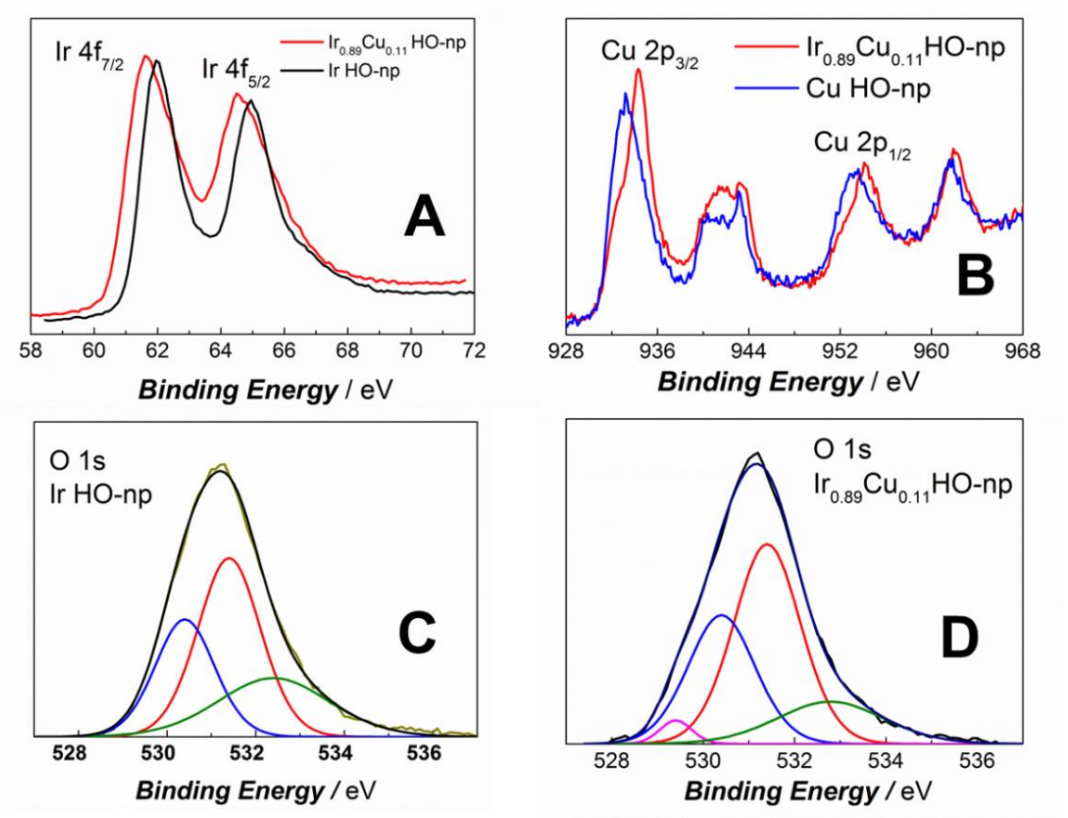

Figure 5.2 XPS spectra of $Ir_{0.89}Cu_{0.11}$ HO-np, Ir HO-np, and Cu HO-np. (A) Ir 4f region, (B) Cu 2p region, and (C and D) O 1s region.

Figure 5.2 shows the results from the XPS analysis of Ir HO-np, $Ir_{0.89}Cu_{0.11}$ HO-np, and Cu HO-np. The $4f_{7/2}$ (61.6 eV) and $4f_{5/2}$ (64.5 eV) Ir binding energies in $Ir_{0.89}Cu_{0.11}$ HO-np, as well as those in Ir HO-np ($4f_{7/2}$ (61.9 eV) and $4f_{5/2}$ (64.9 eV)) show that Ir is mainly in the 4^+ oxidation state in both these catalysts (Figure 5.2 A).[404] The 4f binding energies in Ir HO-np also match those reported for IrO_2.[404,424] The Ir 4f peaks in $Ir_{0.89}Cu_{0.11}$ HO-np occurred at lower binding energies than that of Ir HO-np, suggesting that the electron density at Ir is higher in the presence of Cu. Figure 5.2B shows the XPS spectra of

the Cu 2p region for Cu HO-np and $Ir_{0.89}Cu_{0.11}$ HO-np. The Cu $2p_{3/2}$ (934.3 eV) and $2p_{1/2}$ (954.1 eV) binding energies were similar and indicate that Cu is in the 2^+ oxidation state in both. [199,425]

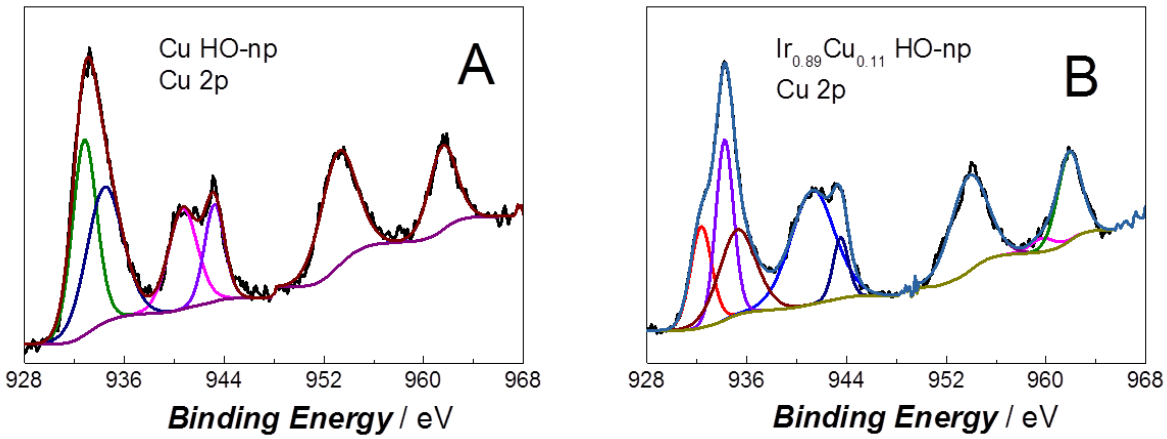

Figure 5.3 Deconvolution of the Cu 2p spectra of (A) Cu HO-np and (B) $Ir_{0.89}Cu_{0.11}$ HO-np.

Figure 5.3 shows the deconvoluted Cu $2p_{3/2}$ peak. For Cu HO-np, two deconvoluted peaks at 933.0 eV and 934.5 eV correspond to Cu^{II} oxide and hydroxide, respectively.[425] For $Ir_{0.89}Cu_{0.11}$ HO-np, another deconvoluted peak at 935.5 eV was present, which was proposed by Sun et al. to arise from Cu–O–Ir structures in the hydrous oxide.[199] As Ir is mainly in the 4^+ state, and Cu is 2^+, replacing Ir with Cu will reduce the net positive charge from the metals and may result in oxide vacancies in the HO-np lattice. Also, the decreased net positive charge may account for the lower binding energies of the Ir 4f peaks in $Ir_{0.89}Cu_{0.11}$ HO-np. Figure 5.2C shows the deconvoluted O 1s signal from Ir HO-np. The

deconvolution yielded three peaks with binding energies at ~ 530.3, 531.4, and 532.8 eV, assigned to the lattice oxygen, the hydroxyl groups, and the adsorbed water, respectively.[193,407,426] Figure 5.2D shows the deconvoluted O 1s signal for $Ir_{0.89}Cu_{0.11}$ HO-np that contained a new peak at 529.5 eV that was not present either in Ir HO-np or in Cu HO-np, between the binding energies for Cu–O–Cu (528.8 eV) (Figure 5.4) and Ir–O–Ir (530.3 eV). Therefore, we assign this peak to the lattice oxygen atoms bridging Ir and Cu. Strasser et al. observed similar peaks in the IrNi oxides, which they assigned to the Ir–O–Ni bridging oxides.[193]

Based upon the results of the HRTEM and XPS studies, we propose that $Ir_{0.89}Cu_{0.11}$ HO-np have a structure similar to IrO_2, with ~ 11% of the Ir^{4+} atoms replaced by Cu^{2+}. The distribution of Cu atoms is unknown, but the lack of Cu–O–Cu signals and the uniform shift of the Ir 4f signals suggests that the distribution of Cu is somewhat uniform within the lattice. The uniform replacement of Ir^{4+} by Cu^{2+} and the larger radius of Cu^{2+} (73 pm) versus Ir^{4+} (63 pm)[411] likely both influence the WOR activity of the catalysts.

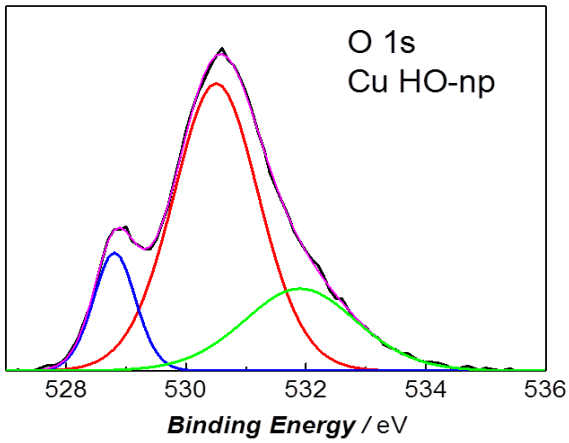

Figure 5.4 The deconvolution of the O 1s spectra of the Cu HO-np.

5.2.2 Water oxidation activity of $Ir_{1-x}Cu_x$ HO-np

Figure 5.5A shows the voltammetric profiles (1.35–1.55 V_{RHE}, 10 mV s^{-1}) in 0.1 M $HClO_4$ for the $Ir_{1-x}Cu_x$ HO-np series deposited on carbon fiber paper using Nafion® as a binder. The WOR onset potential over the $Ir_{0.89}Cu_{0.11}$ HO-np/CF electrode was ~ 1.42 V_{RHE}, corresponding to ~ 0.19 V overpotential. The mass activity at 1.48 V_{RHE} reaches 142 A g_{Ir}^{-1}. This activity is higher than other reported IrCu catalysts,[199,200] and it is comparable to $Ir_{0.89}Ni_{0.11}$ HO-np described in Chapter 4, which is among the most active in the literature (Table 5.3).[189–191,193] Figure 5.5C shows a plot of the mass activity at 1.48 V_{RHE} of the $Ir_{1-x}Cu_x$ HO-np/CF electrodes against composition. The highest mass activity was obtained with x = 0.11, which was 1.6 times higher than that of Ir HO-np. Catalysts with a higher fraction of Cu (x) had lower mass activities.

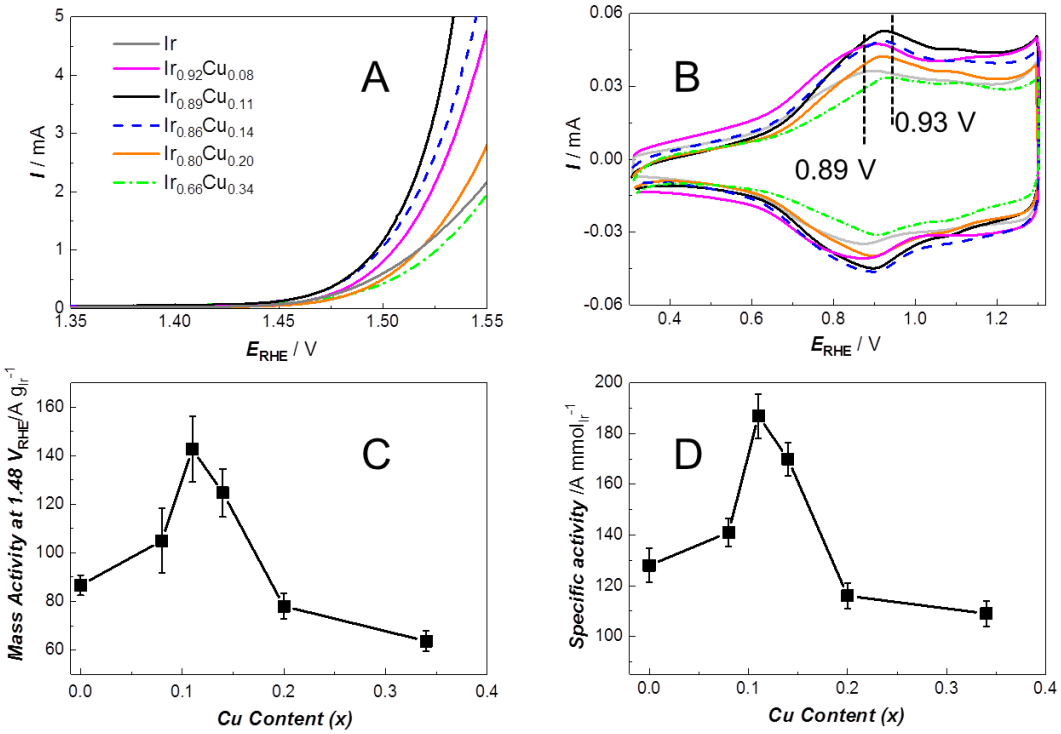

Figure 5.5 (A) Voltammetric (10 mV s^{-1}) water oxidation profiles by the $Ir_{1-x}Cu_x$ HO-np/CF electrodes (x = 0–0.34) in 0.1 M $HClO_4$. (B) Cyclic voltammograms of the $Ir_{1-x}Cu_x$ HO-np/CF electrodes in 0.1 M $HClO_4$ at 50 mV s^{-1}. (C and D) Mass and active Ir atoms normalized activity at 1.48 V_{RHE}. The mass loadings of Ir were 3.4 μg cm^{-2} for all electrodes.

Figure 5.5B shows the voltammograms (0.30–1.30 V_{RHE}, 50 mV s^{-1}) of the $Ir_{1-x}Cu_x$ HO-np/CF electrodes. The $Ir^{3+/4+}$ oxidation peaks were centered at ~ 0.9 V_{RHE} in the anodic scan and the $Ir^{4+/3+}$ reduction peaks at ~ 0.87 V_{RHE}. This behavior corresponds to that of IrO_2.[190,193,200,427] Table 5.1 summarizes the electrochemical parameters obtained for these catalysts. As shown in Table 5.1, the $Ir^{3+/4+}$ redox peak potential shifted anodically with

higher amounts of Cu, indicating that the electron density at Ir^{3+} decreases as the amount of Cu is increased in the lattice.[193] This trend appears to be opposite to the results from the XPS study. We point out that XPS measurements were of Ir^{4+}–Cu^{2+} HO-np under vacuum, whereas the CV results would be influenced to some extent by the interaction between Ir^{3+} and Cu^{2+} within the hydrated HO-np in aqueous acid.

The charge (Q) under the $Ir^{3+/4+}$ oxidation peak was used to estimate the electrochemically active Ir atoms. Table 5.1 lists the mole of electrochemically active Ir per gram catalyst calculated from eq 5.1.

$$\text{Active Ir atoms per gram} = \frac{Q}{96485 \times 3.4 \times 10^{-6}} \qquad 5.1$$

The active Ir atoms per gram increases by ~ 16.1% from x = 0 to x = 0.11 and then drops by ~ 13.2% from x = 0 to x = 0.34. Figure 5.5D shows the WOR activity (at 0.25 V overpotential) normalized to the mole of active Ir versus the content of Cu (x) in the HO-np. The same trend as the mass activity was observed, with the $Ir_{0.89}Cu_{0.11}$ HO-np/CF electrode being the most active. The accessible Ir site normalized activity of $Ir_{0.89}Cu_{0.11}$ HO-np was 1.5 times that of Ir HO-np. The mechanism of promotion of Ir by Cu is, therefore, not simply a surface area phenomenon.

Table 5.1 The key electrochemistry parameters of the $Ir_{1-x}Cu_x$ HO-np/CF electrodes

	η_{Onset} (V)	η at 1 mA cm^{-2} (V)	Electrochemically active Ir atoms per gram ($mmol_{Ir}$ g^{-1})	Tafel Slope (mV dec^{-1})	$Ir^{3+/4+}$ oxidation peak (V)
Ir	0.20	0.29	0.68	60	0.89
$Ir_{0.92}Cu_{0.08}$	0.20	0.28	0.75	58	0.90
$Ir_{0.89}Cu_{0.11}$	0.19	0.26	0.79	52	0.91
$Ir_{0.86}Cu_{0.14}$	0.19	0.27	0.76	59	0.92
$Ir_{0.80}Cu_{0.20}$	0.20	0.29	0.67	61	0.92
$Ir_{0.66}Cu_{0.34}$	0.20	0.30	0.59	73	0.93

5.2.3 Stability and Tafel plots

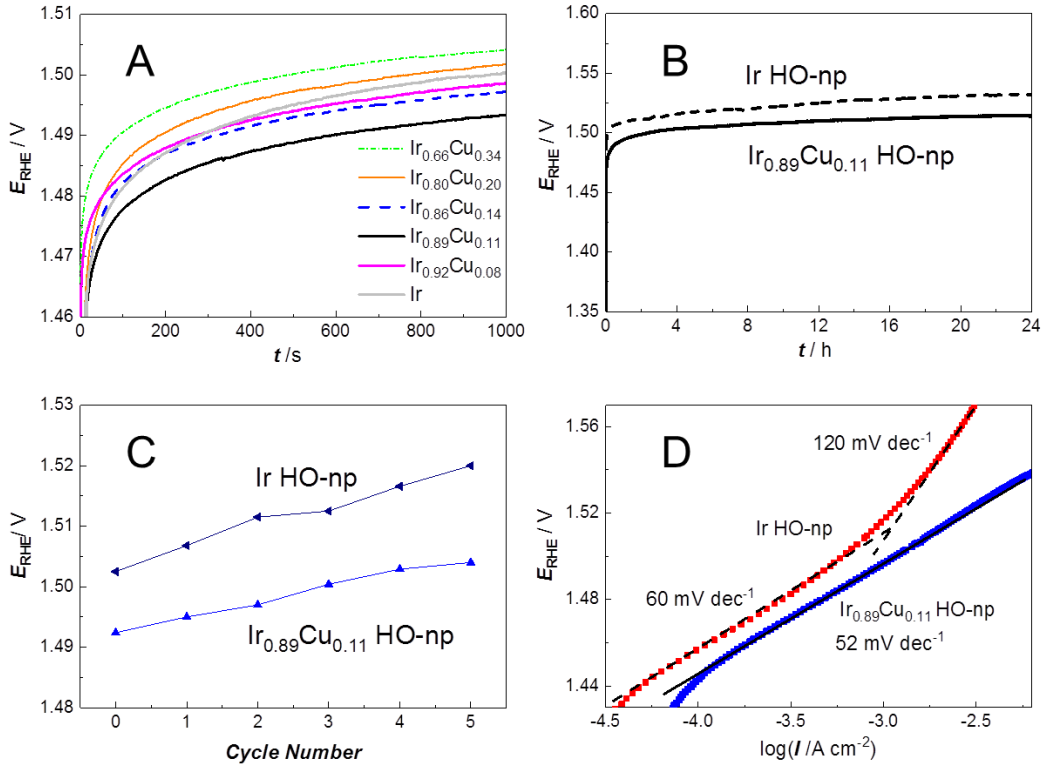

Figure 5.6 (A) Short-term 1 mA cm^{-2} galvanostatic test on the $Ir_{1-x}Cu_x$ HO-np/CF electrodes (Ir loading: 17 μg cm^{-2}). (B) 24 h galvanostatic test on the $Ir_{0.89}Cu_{0.11}$ HO-np/CF and the Ir HO-np/CF electrodes (Ir loading: 17 μg cm^{-2}). (C) Duty cycle results for the $Ir_{0.89}Cu_{0.11}$ HO-np/CF and the Ir HO-np/CF electrodes. (D) Tafel slopes of the $Ir_{0.89}Cu_{0.11}$ HO-np/CF and Ir HO-np/CF electrodes.

Figure 5.6A shows the results from a short-term galvanostatic WOR at 1 mA cm^{-2} test with the $Ir_{1-x}Cu_x$ HO-np/CF electrodes. The $Ir_{0.89}Cu_{0.11}$ HO-np/CF electrode maintained the set current density at the lowest overpotential among all the catalysts, which leveled out at

~ 0.26 V (1.49 V_{RHE}) after 1000 s. In 24 h galvanostatic tests carried out with the $Ir_{0.89}Cu_{0.11}$ HO-np/CF and the Ir HO-np/CF electrodes (Figure 5.6B), both electrodes were quite stable under 1 mA cm^{-2} galvanostatic polarization in acid. The potential for the $Ir_{0.89}Cu_{0.11}$ HO-np/CF rose from 1.47 V_{RHE} to 1.50 V_{RHE} within the first 1.5 h and then leveled out, rising very slowly to 1.51 V_{RHE}, which is ~ 20 mV lower than the Ir HO-np/CF electrode and lower than other IrO_x based catalysts in the literature.[189,191] ICP–MS measurements of the electrolyte showed that less than 10% of the Ir or Cu was dissolved during the 24 h galvanostatic oxidation (Table 5.2).

Table 5.2 The ICP–MS results of the electrolyte after the 24 h galvanostatic test of the $Ir_{1-x}Cu_x$ HO-np electrodes

	Mass of Ir (μg)	Mass of Cu (μg)
Ir	1.68	-
$Ir_{0.89}Cu_{0.11}$	1.35	0.05

The duty cycle test developed by Strasser et al. is a good measure of the stability of the catalysts under close to real electrolyzer conditions (experimental details in Section 5.4.5).[191] Figure 5.6C shows the results from duty cycle tests performed with the $Ir_{0.89}Cu_{0.11}$ HO-np/CF and the Ir HO-np/CF electrodes. After 5 duty cycles, the potential required to reach 1 mA cm^{-2} increased by only 10 mV for the $Ir_{0.89}Cu_{0.11}$ HO-np/CF electrode, while it

increased by 18 mV for Ir HO-np/CF. This stability is comparable to the $IrNiO_x$ core-shell particles reported by Strasser et al.[191]

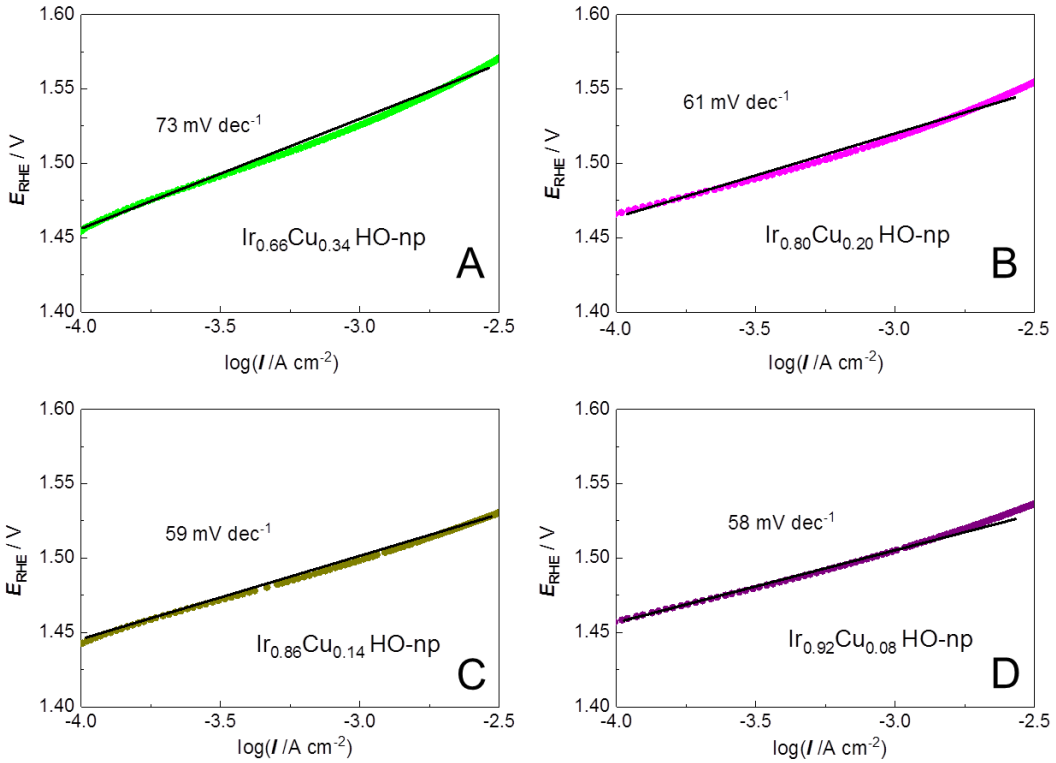

Figure 5.7 Tafel plots of the $Ir_{1-x}Cu_x$ HO-np/CF electrodes in 0.1 M $HClO_4$.

Figure 5.6D shows the WOR Tafel plots of the $Ir_{0.89}Cu_{0.11}$ HO-np/CF and Ir HO-np/CF electrodes. The Tafel slope of the Ir HO-np/CF was ~ 60 mV dec^{-1} at low overpotentials and ~ 120 mV dec^{-1} at high overpotentials. This behavior is well-known for IrO_x catalysts.[400,401,428] Figure 5.7 shows the Tafel plots for other $Ir_{1-x}Cu_x$ HO-np/CF electrodes. The Tafel slope of the $Ir_{0.89}Cu_{0.11}$ HO-np/CF electrode was ~ 52 mV dec^{-1} over the range overpotentials employed for this study. The 60 mV dec^{-1} Tafel slope matches the

mechanism (see eqs 4.2–4.5) where a fast pre-equilibrium electrochemical step (eq 4.2) is followed by the RDS, which is a chemical step involving rearrangement of the surface hydroxide group (eq 4.3).[159,398–401] The shift to 120 mV dec^{-1} can be explained provided that the turnover-limiting step changes to eq 4.2 at higher overpotentials over the Ir HO-np/CF.[191,402,428] The lower Tafel slope over the $Ir_{0.89}Cu_{0.11}$ HO-np/CF electrode (~ 52 versus 60 mV dec^{-1}) suggests that the presence of Cu does not alter the mechanism of the WOR significantly but perhaps changes the relative rates of eqs 4.2 and 4.3 to some extent due to the resulting oxide vacancies or the expansion of the oxide lattice. More research is required to investigate the role of Cu in promoting the water oxidation activity of Ir HO-np.

5.3 Conclusions

$Ir_{1-x}Cu_x$ HO-np synthesized with this straightforward, scalable manner are among the most active water oxidation catalysts in acid (see Table 5.3 for activity comparison with the literature systems). The onset overpotential is 0.19 V and the mass activity is over 140 A g_{Ir}^{-1} at 0.25 V overpotential with the most active catalyst in the series, $Ir_{0.89}Cu_{0.11}$ HO-np. $Ir_{0.89}Cu_{0.11}$ HO-np are stable under an anodic acidic environment. Preliminary mechanistic investigations showed that the activity enhancement by Cu is not just a surface area effect, and the presence of Cu does not appear to alter the mechanism of the WOR significantly.

Table 5.3 Comparison of the water oxidation activity in acid with the literature data

Catalyst	Onset (V_{RHE})	*E* at 1 mA cm^{-2} (V_{RHE})		Mass activity (A g_{Ir}^{-1})		Tafel Slope (mV dec^{-1})
	LSV	LSV	Galv.	1.48 V_{RHE}	1.51 V_{RHE}	
$Ir_{0.89}Cu_{0.11}$ HO-np	1.42	1.49	1.51	142	521	52
Ir HO-np	1.43	1.51	1.53	90	253	60
$Ir_{0.89}Ni_{0.11}$ HO-np[190]	1.42	1.50	1.52	141	352	57
$Cu_{1.11}Ir$ nanocage[200]	1.43	1.49	1.51	-	73	43.8
$Cu_{0.3}Ir_{0.7}O_x$[199]	1.46	1.53	-	50 (1.58 V_{RHE})		63
$IrNi_{3.3}$[189]	1.47	-	1.53	37	170	-
$IrNi_{0.67}O_x$[193]	1.45	1.49	-	350(1.53 V_{RHE})		-
$IrNiO_x$/Meso-ATO[191]	1.49	1.51	1.54	-	90	-
Ir/C[192]	1.54	1.55	-	8	40	55.6
$Ir_{0.7}Ni_{0.3}O_{2-y}$[197]	1.47	1.50	-	-	-	57
Amorphous IrO_x[387]	1.46	-	1.45	-	-	34
Ir nanowire[388]	1.43	1.46	-	97	323	43.6
Co-IrCu nanocage[198]	1.45	1.46	-	100	300	50
NiCuIr nanoframe[421]	1.46	1.47	-	60	275	48

5.4 **Experimental**

5.4.1 Chemicals

Perchloric acid (Sigma-Aldrich, 70%, 99.999% trace metal basis), sulfuric acid (Caledon), hydrogen peroxide (Fischer Scientific, 30%), L-ascorbic acid (Fisher Scientific; reagent grade), potassium hydroxide (Sigma-Aldrich, semiconductor grade, 99.99%), carbon fiber paper (ElectroChem, Inc.), iridium chloride trihydrate (A.B. Mackay Chemicals), cupric chloride dihydrate (BDH Chemicals Ltd. Poole England, 98%), *tert*-butanol (Sigma-Aldrich, > 99%), and Nafion® (5 wt%, ElectroChem, Inc.) were used as received. Triply distilled water was used throughout the experiments. All the glassware was cleaned with Piranha solution (5:1 volume ratio of sulfuric acid to 30% hydrogen peroxide) before use.

5.4.2 Preparation of $Ir_{1-x}Cu_x$ HO-np

Colloidal suspensions of $Ir_{1-x}Cu_x$ HO-np (x = 0–0.34) were prepared by adding 0.8 M KOH to 20 mL solutions of $IrCl_3 \cdot 3H_2O$ and $CuCl_2 \cdot 2H_2O$. The amount of Ir was kept constant, with $CuCl_2 \cdot 2H_2O$ added to give the desired fraction x. The amount of KOH added was ~ 10 times the mole of Ir + Cu. Table 5.4 shows the amounts used. The molar ratios of the precursor mixtures were $Ir_{0.66}Cu_{0.34}$, $Ir_{0.80}Cu_{0.20}$, $Ir_{0.86}Cu_{0.14}$, $Ir_{0.89}Cu_{0.11}$ and $Ir_{0.92}Cu_{0.08}$. The mixtures were stirred under air for 3 days after addition of the KOH solution. The colloidal suspensions could be stored in glass vials under air at room temperature for at least two

months without losing activity.

Table 5.4 The amounts of the reagents in the synthesis of $Ir_{1-x}Cu_x$ HO-np (x = 0–0.34)

Ir/Cu ratio	$IrCl_3 \cdot 3H_2O$ (g)	$CuCl_2 \cdot 2H_2O$ (g)	0.8 M KOH (mL)
Ir	0.0704	0	2.5
$Ir_{0.92}Cu_{0.08}$	0.0706	0.0029	2.7
$Ir_{0.89}Cu_{0.11}$	0.0704	0.0043	2.8
$Ir_{0.86}Cu_{0.14}$	0.0703	0.0057	2.9
$Ir_{0.80}Cu_{0.20}$	0.0705	0.0086	3.1
$Ir_{0.66}Cu_{0.34}$	0.0704	0.0171	3.8

5.4.3 Preparation of working electrodes

A similar procedure as described in Section 4.4.3 was used to deposit 3.4 μg Ir on 1 cm^2 carbon fiber paper. The actual amount of metal deposited was determined by the dissolution in $HClO_4$ in the presence of ascorbic acid, followed by ICP–MS analysis. The theoretical mass, based upon the volume of the suspension, was ~ 96% that of the value measured by ICP–MS (Table 5.5). For galvanostatic tests, five times higher amounts of the ink were used to deposit 17 μg Ir on the electrode.

Table 5.5 The ICP–MS data on some of the $Ir_{1-x}Cu_x$ HO-np deposits (theoretical mass of Ir was 3.4 μg)

	Mass of Ir (μg)	Mass of Cu (μg)	Ir:Cu atomic ratio (μg)	Ir:Cu mass ratio (μg)
Ir	3.35	-	-	-
$Ir_{0.89}Cu_{0.11}$	3.42	0.14	8.26	24.43
$Ir_{0.86}Cu_{0.14}$	3.32	0.18	6.14	18.44

A similar procedure as described in Section 4.4.2 was used to separate $Ir_{1-x}Cu_x$ HO-np from the synthesis solution. A control experiment showed that this washing procedure does not change the water oxidation activity of the catalyst (Figure 5.8).

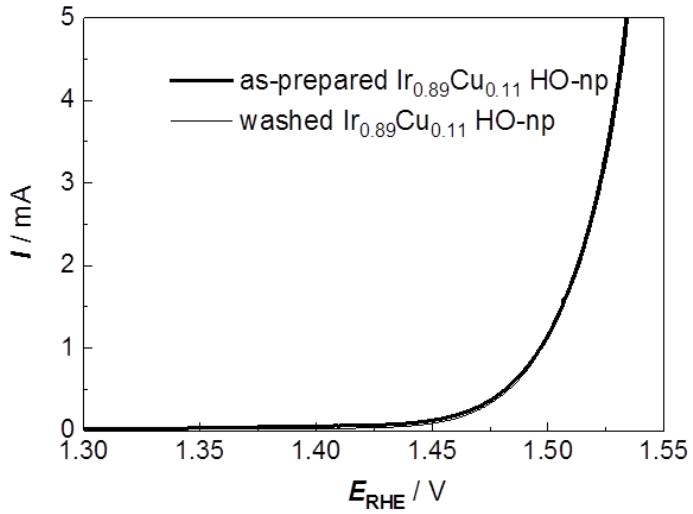

Figure 5.8 Voltammetric WOR on the $Ir_{0.89}Cu_{0.11}$ HO-np/CF electrodes before and after washing, in 0.1 M $HClO_4$, 10 mV s^{-1} (Ir loading: 3.4 μg cm^{-2}).

5.4.4 Electrochemistry

The electrochemical experiments were performed in 0.1 M $HClO_4$ solutions, with a Solartron SI 1287 Electrochemical Interface controlled by CorrWare for Windows Version 2-3d software. The reference electrode was a SCE. The potential of the SCE was calibrated against a Pt electrode in a H_2-saturated 0.1 M $HClO_4$ solution at room temperature (Figure 5.9). The average of the cathodic and anodic scan points of 0 current was 0.303 V_{SCE} and was used to convert the measured potential to the RHE scale. A graphite rod formed the CE. Uncompensated resistance was measured by AC impedance (8 Ω) and corrected for. All the other electrochemical experiments were carried out at room temperature in N_2-saturated solutions.

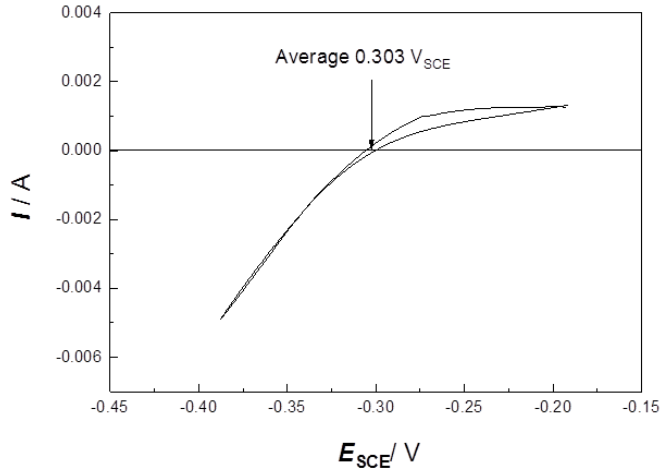

Figure 5.9 Calibration of the SCE potential to RHE in a H_2-saturated 0.1 M $HClO_4$ solution (sweep rate 1 mV s^{-1}).

5.4.5 Duty cycle test

The potential of the WE was set at E^5 (potential at which the current density reaches 0.5 mA cm^{-2}) and was increased in 0.02 V steps every 10 min (last potential E^{Final} would be $E^5 + 0.1$ V). The process of stepping the potential from E^5 to E^{Final} is one duty cycle. The duty cycle was repeated five times. After each cycle, a CV was collected, and the voltammetric potential at 1 mA cm^{-2} was plotted as a function of the duty cycle number.

5.4.6 Instrumentation

ICP–MS analyses were performed with Perkin Elmer Elan 6000. The HRTEM images were acquired using a Titan 80-300 LB high resolution transmission electron microscope. The XRD patterns were measured with an Inel diffractometer equipped with a curved position-sensitive detector (CPS 120) and a Cu Kα1 radiation source at 40 kV and 20 mA ($\lambda_{1/2}$ = 1.54060/1.54439 Å).

XPS measurements were performed on a Kratos Axis 165. Charge neutralization was applied to stabilize spectra during spectra collecting since the samples were not conductive adequately. To account for charging effects, all spectra have been referred to C 1s at 284.8 eV. Casa XPS software was used to fit the XPS data. The binding energies of the peaks were calculated from the background-subtracted spectra using Shirley background. The peaks were fitted with Gaussian (70%)–Lorentzian (30%) curves.

Chapter 6 A Simple Aqueous Preparation of High Activity and Stability NiFe Hydrous Oxide Catalysts for Water Oxidation[a]

6.1 Introduction

This Chapter describes a simple synthesis of active, stable catalysts for the WOR from common earth-abundant precursors. The large-scale electrolysis of water is a promising method to store energy from solar, wind, and other CO_2-free sources of electricity.[129,374,429,430] The resulting hydrogen can be combusted or converted into electricity with fuel cells.[18,431] Alternatively, carbon dioxide can be reduced at the electrolyzer cathode to form carbon monoxide or liquid fuels.[432,433] Alkaline water electrolyzers possess advantages over acidic systems.[146,434] Among the most significant one is that non-noble metals catalyze the WOR in base.[209,212,213] However, the major challenge to the widespread application of electrolyzers for energy storage is the sluggish WOR at the anode (eq 6.1, $E° = 1.23\ V_{RHE}$).[134,139]

$$4\ OH^- \rightarrow O_2 + 4\ e^- + 2\ H_2O \qquad 6.1$$

There are numerous reports of combinations of the first row metals, such as Ni, Fe, Co,

[a] *A version of this Chapter has been published. Wang, C.; Moghaddam, R. B.; Brett, M. J.; Bergens, S. H. ACS Sustainable Chemistry & Engineering 2017, 5, 1106.*

and Cu, that are promising alkaline WOR catalysts.[166,211,221,230,236,435–442] Table 6.1 represents the most active catalysts in the literature, and most of them contain Ni and Fe. Berlinguette et al. used 5.8 W UV irradiation to decompose Fe^{III} 2-ethylhexanoate and Co^{II} 2-ethylhexanoate on FTO, followed by heat treatment at 100 ^{o}C for 1 h to prepare amorphous FeCo catalyst (Table 6.1, entry 1).[438] A galvanostatic deposition with a current density of -0.25 A cm^{-2} in a $NiSO_4$, $FeSO_4$, and $(NH_4)_2SO_4$ solution using a Pt working electrode was carried out by Dougherty et al. to prepare a NiFe/Pt foil catalyst.[443] Duan et al. carried out the electrodeposition in a solution containing $Ni(NO_3)_2$ and $FeSO_4$ at -1 V_{SCE} under N_2 using a Ni foam working electrode. The deposit was oxidized in air and formed the active NiFe-LDH WOR catalyst (entries 3).[30] Hydrothermal and solvothermal methods are applied to prepare NiFe LDH catalysts, with the addition of rGO (**r**educed **g**raphene **o**xide) (entry 4)[238] or CNT (**c**arbon **n**ano**t**ubes) (entry 5)[236] in order to enhance the WOR activity. For example, Yang et al. hydrothermally treated a solution containing $NiCl_2$, $FeCl_2$, urea, trisodium citrate, and graphene oxide at 150 ^{o}C for 24 h to synthesize NiFe-GO LDH. Then, the graphene oxide in the catalyst was reduced by ammonia and hydrazine in water at 95 ^{o}C for 1 h to yield the NiFe-rGO LDH catalyst.[238] Sargent et al. prepared active FeCoW oxyhydroxides catalysts by careful hydrolysis of the $FeCl_3$, $CoCl_2$, and WCl_6, followed by sol-gel formation with propylene oxide, then drying with supercritical CO_2 (entry 6).[444]

Ideally, an industrial catalyst synthesis is inexpensive, simple, quick, and

scalable.[146,440] This Chapter describes the preparation and study of a series of $Ni_{1-x}Fe_x$ HO-np prepared in a similar manner as in previous Chapters for the WOR in base.

Table 6.1 Reported active water oxidation catalysts in base

	Catalyst	η_{Onset} (V)	η at 10 mA cm^{-2} (V)	Tafel slope (mV dec^{-1})	Loading (mg cm^{-2})
1	FeCo[438]	0.18	NA	31	NA
2	NiFe/Pt foil[443]	NA	NA	14.8	NA
3	NiFe-LDH/Ni foam[243]	0.20	0.23	52.8	1.0
4	FeNi-rGO LDH[238]	0.19	0.21	39	0.25
5	NiFe LDH-CNT hybrid[236]	0.22	0.25	31	0.25
6	FeCoW/Au plated Ni_{foam}[444]	NA	0.19	NA	0.39
	This work	0.19	0.23	24	0.135

NA: Not available.

6.2 **Results and Discussion**

6.2.1 Characterization of $Ni_{0.75}Fe_{0.25}$ HO-np

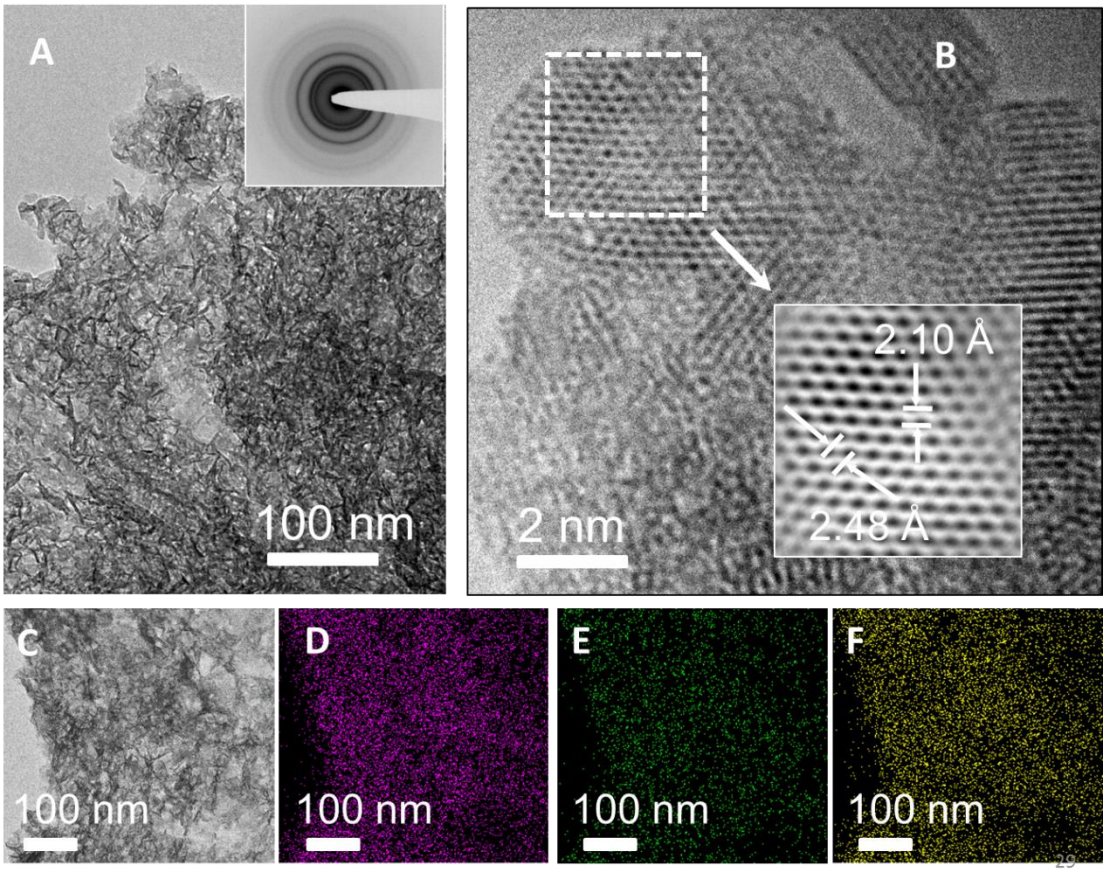

Figure 6.1 (A and B) HRTEM images of isolated, washed $Ni_{0.75}Fe_{0.25}$ HO-np. The inset of (A) shows the selected area electron diffraction pattern. EDS elemental mappings for (D) Ni, (E) Fe, (F) O, and the scanning transmission electron microscopy image of the corresponding area (C).

Figure 6.1A shows the HRTEM images of the isolated, washed $Ni_{0.75}Fe_{0.25}$ HO-np catalyst. This is the most active mass-normalized WOR catalyst in the series prepared for this study (vide infra). The selected area electron diffraction pattern contains several rings (Figure 6.1A inset), indicating regions with polycrystalline structure. Figure 6.1B shows that the catalyst consists of regions with mostly clear lattice images, indicating largely polycrystalline $Ni_{0.75}Fe_{0.25}$ HO-np. The measured lattice distances are 0.248 nm and 0.210 nm, corresponding to the (012) and (015) planes of α-$Ni(OH)_2$, respectively. A similar lattice distance (0.25 nm) was reported by Dai et al. for the (012) lattice plane in their NiFe-LDH/CNT hybrid WOR catalyst.[236] The powder XRD pattern of isolated $Ni_{0.75}Fe_{0.25}$ HO-np also contained peaks corresponding to the (00n) planes of LDH structures, consistent with the known NiFe-LDH (JCPDS 51-0460) (Figure 6.2).[231,236,241,247,445,446] In comparison, the major phase of Ni HO-np was β-$Ni(OH)_2$ (JCPDS 14-0117).

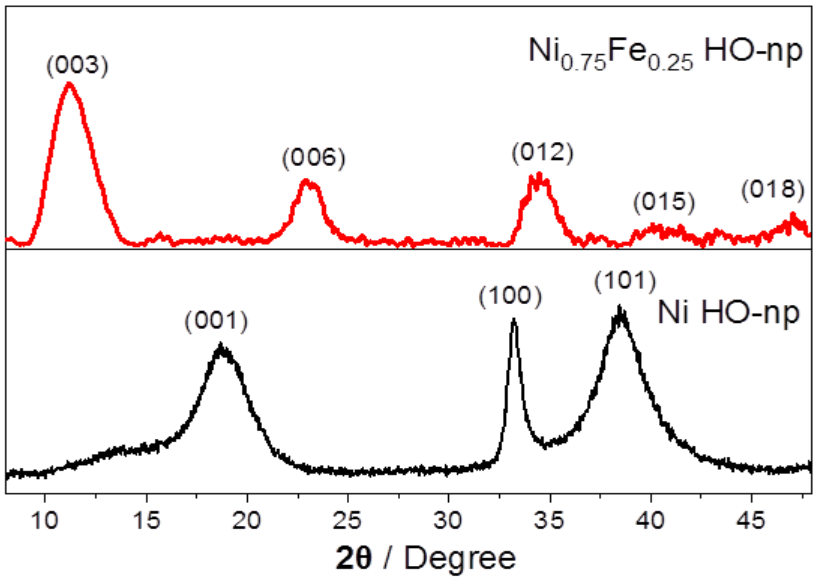

Figure 6.2 Powder X-ray diffraction patterns of $Ni_{0.75}Fe_{0.25}$ and Ni HO-np.

The Brunauer–Emmett–Teller (BET) surface area of the isolated, vacuum-dried $Ni_{0.75}Fe_{0.25}$ HO-np powder was 68.64 m^2 g^{-1}. The BET surface areas reported for other NiFe LDH materials in the literature range from 7 to 385 m^2 g^{-1}.[238,447–449]

The EDS (**e**nergy **d**ispersive X-ray **s**pectroscopy) elemental mapping indicates that the distribution of Ni, Fe, and O in the catalyst is uniform, with the ratio of Ni to Fe close to 3:1. The same ratio was measured by XPS and by ICP–MS after dissolving $Ni_{0.75}Fe_{0.25}$ HO-np in 0.1 M $HClO_4$ (Table 6.1). Potassium and chloride ions were not detected by XPS (Figure 6.3) nor EDS (Figure 6.4) in the isolated, washed catalyst. Thus, the initial ratio of Ni and Fe precursors is present in the isolated hydrous oxide nanoparticle product. Also, the absence of Cl^- shows that the anionic species in the LDH structure are oxides or hydroxides.

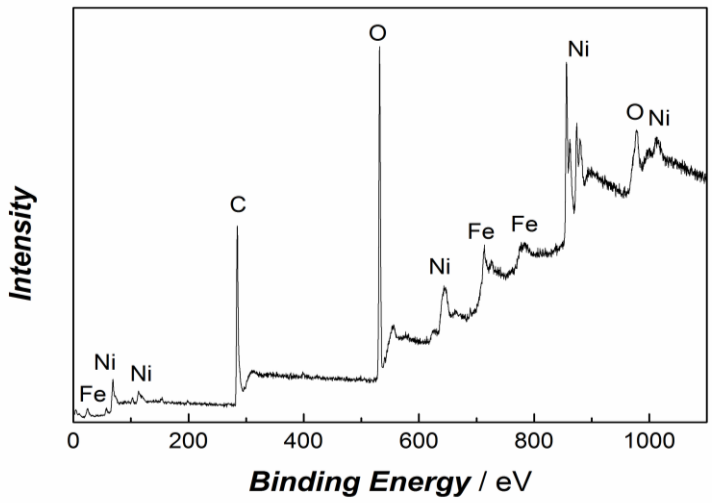

Figure 6.3 XPS spectra of washed $Ni_{0.75}Fe_{0.25}$ HO-np.

Table 6.2 Comparison of as-synthesized and washed $Ni_{0.75}Fe_{0.25}$ HO-np composition from the ICP–MS, XPS, and EDS measurements, and the ICP–MS data for $Ni_{1-x}Fe_x$ HO-np

		Mass		Mass ratio	Atomic ratio
		Ni (μg)	Fe (μg)	(Ni:Fe)	(Ni:Fe)
As-synthesized	ICP–MS	51.33	16.87	3.04	2.90
$Ni_{0.75}Fe_{0.25}$ HO-np	EDS	-	-	3.18	3.02
	XPS	-	-	3.12	2.96
Washed	ICP–MS	52.04	16.25	3.20	3.03
$Ni_{0.75}Fe_{0.25}$ HO-np	EDS	-	-	3.12	2.96
	XPS	-	-	3.22	3.06
Washed	ICP–MS	45.05	20.93	2.15	2.04
$Ni_{0.66}Fe_{0.34}$ HO-np					
Washed	ICP–MS	53.51	13.50	3.96	3.76
$Ni_{0.80}Fe_{0.20}$ HO-np					
Washed	ICP–MS	60.31	7.41	8.14	7.73
$Ni_{0.89}Fe_{0.11}$ HO-np					

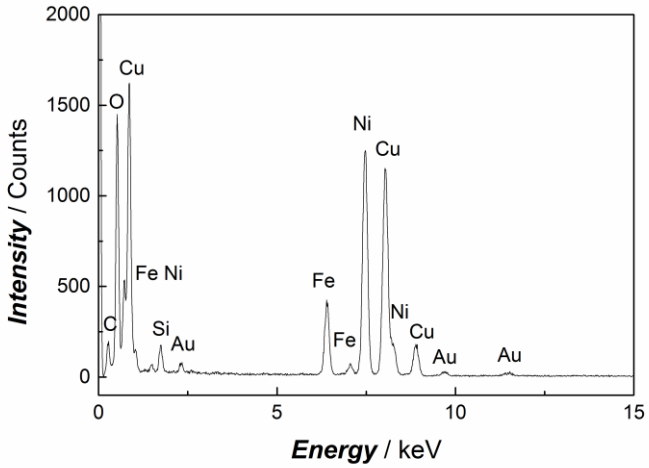

Figure 6.4 EDS spectra of washed $Ni_{0.75}Fe_{0.25}$ HO-np. The small amount of Au detected was from the detector, and Si came from the glass vial container.

The XPS spectra (Figure 6.5) of $Ni_{0.75}Fe_{0.25}$ HO-np show that Fe is predominantly in the 3^+ oxidation state, resulting from the oxidation of Fe^{2+} by the oxygen in air during the synthesis.[450] We note that the use of $FeCl_3$ as a precursor formed the catalyst with the same activity. Deconvolution of the O 1s signal at ~ 530–533 eV shows that the oxygen mainly exists as OH^- incorporated into the lattice or on the surface, with only ~ 1% of lattice O^{2-} present (Figure 6.5).[407,440] The Ni XPS signals of washed and isolated $Ni_{0.75}Fe_{0.25}$ HO-np encompass two spin-orbit doublet peaks at 855.4 eV (Ni $2p_{3/2}$), 861.0 eV (satellite), 872.7 eV (Ni $2p_{1/2}$), and 879.5 eV (satellite), matching the binding energy of Ni^{2+} in $Ni(OH)_2$.[236,440] The Ni and O peaks in the XPS spectra of the Ni HO-np control were quite similar to those of $Ni_{0.75}Fe_{0.25}$ HO-np. Deconvolution of the O 1s signal indicated that less than 1% O^{2-} was present in both $Ni_{0.75}Fe_{0.25}$ HO-np and Ni HO-np.[409] Also, the

detected presence of Fe^{3+}, OH^-, and $Ni(OH)_2$, are consistent with the NiFe LDH catalyst structure.

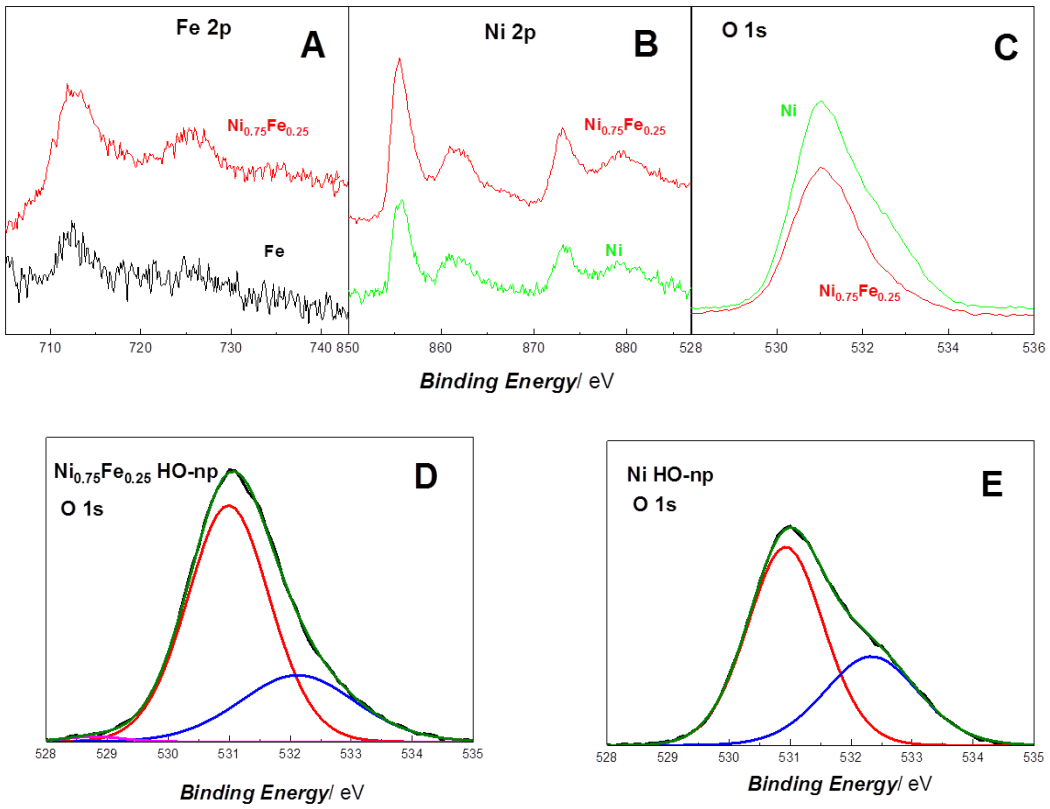

Figure 6.5 The XPS patterns for Ni, Fe, and $Ni_{0.75}Fe_{0.25}$ HO-np. (A) Fe 2p region, (B) Ni 2p region, (C) O 1s region, and the deconvolution of O 1s peak of (D) $Ni_{0.75}Fe_{0.25}$ HO-np and (E) Ni HO-np.

The combined results from the characterization studies show that $Ni_{0.75}Fe_{0.25}$ HO-np predominantly exist as NiFe LDH structures,[231,247] containing $Ni^{II}(OH)_2$ and $Fe^{III}(OH)_2^+$ octahedral centers in the hydroxide layers, with OH^- and H_2O intercalated between the layers. The overall equation for its formation is shown by eq 6.2.

$$3\ Ni^{2+} + Fe^{2+} + 7.25\ OH^- + 0.25\ O_2 + 0.5\ H_2O \rightarrow 4\ [Ni_{0.75}Fe_{0.25}(OH)_2]^{0.25+}\ OH^-_{0.25} \quad 6.2$$

6.2.2 Water oxidation activity of $Ni_{1-x}Fe_x$ HO-np/CF

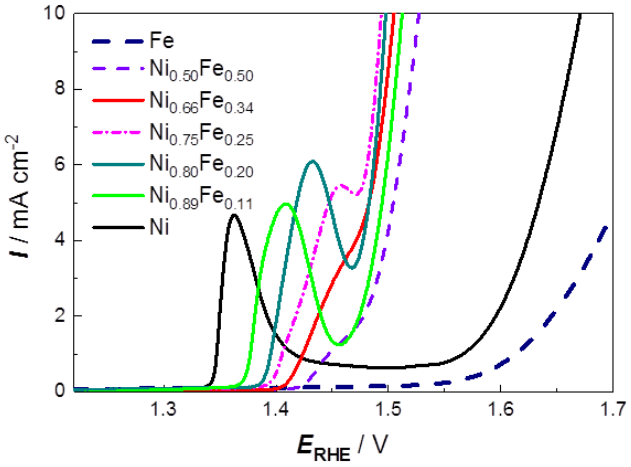

Figure 6.6 Voltammetric WOR over the $Ni_{1-x}Fe_x$ HO-np/CF electrodes in 1.0 M KOH at 5 mV s^{-1}. All loadings of Ni + Fe = 0.0675 mg cm^{-2}.

Figure 6.6 shows the positive-going LSVs in 1 M KOH for a series of $Ni_{1-x}Fe_x$ HO-np deposited upon carbon fiber paper. The total mass loading of Ni + Fe was the same (0.0675 mg cm^{-2}) for all the electrodes. The LSV of the Fe HO-np/CF electrode is essentially featureless up to ~ 1.58 V_{RHE} (~ 0.35 V overpotential) where the WOR current spikes up. The LSV of the Ni HO-np/CF electrode contains a distinctive peak at 1.37 V_{RHE}, corresponding to the $Ni(OH)_2$/Ni(O)OH redox couple.[451] This peak shifts to higher potentials when the mole fraction of Fe increases. Similar observations have been reported by others.[229,452–454] The shift to higher potentials may result in part from an increasing

electron deficiency in the layered double hydroxides as Ni^{2+} is replaced by Fe^{3+} in the lattice. The WOR onset over the Ni HO-np/CF electrode (x = 0) was ~ 1.56 V_{RHE} (~ 0.33 V overpotential), which compares to the literature value after all traces of Fe were removed from the KOH.[453,455] The mixed systems are more active than the pure Ni or Fe catalysts for the WOR, with the $Ni_{0.75}Fe_{0.25}$ HO-np/CF electrode being the most active when normalized to the total mass of Ni + Fe. Table 6.3 summarizes the data. With increasing fractions of Fe, the onset potential decreased from 1.56 V_{RHE} over the Ni HO-np/CF electrode to 1.44 V_{RHE} (0.21 V overpotential) over the $Ni_{0.75}Fe_{0.25}$ HO-np/CF electrode. The onset potential then increased to ~ 1.58 V_{RHE} over the Fe HO-np/CF electrode. The Ni(O)OH/$Ni(OH)_2$ peak in the cathodic sweeps of the LSVs did not overlap with the WOR (Figure 6.9A) and could be used to estimate the number of electrochemically accessible Ni atoms of the catalysts. Table 6.3 lists the WOR overpotentials for the HO-np at 6×10^4 A mol_{Ni}^{-1} in order to investigate the intrinsic activities of Ni within this series. The data show that the activity of Ni increases when the mole fraction of Fe (x) increases, even as x exceeds 0.25 (the mole fraction within the most active mass-normalized WOR catalyst). Although this trend does not exclude other possibilities, it does suggest that $Ni_{0.75}Fe_{0.25}$ HO-np is the most active catalyst by mass because the combination of Ni activation by Fe and the number of Ni atoms with the HO-np is optimized for the WOR.

Table 6.3 Key electrochemical results for the $Ni_{1-x}Fe_x$ HO-np/CF and the $Ni_{0.75}Fe_{0.25}$ HO-np/Ni_{foam} electrodes (loadings: 0.0675 mg cm^{-2})

Catalyst	η_{Onset} * (V_{RHE})		η at 10 mA cm^{-2}(V)		η at 6 × 10^4 A mol_{Ni}^{-1} ** (V)	Tafel Slope (mV dec^{-1})
	LSV	Tafel	LSV	Galv.		
Ni	0.33	0.31	0.44	0.45	0.47	62
$Ni_{0.89}Fe_{0.11}$	0.24	0.23	0.28	0.29	0.31	34
$Ni_{0.80}Fe_{0.20}$	0.22	0.23	0.27	0.27	0.29	30
$Ni_{0.75}Fe_{0.25}$	0.21	0.22	0.26	0.27	0.28	29
$Ni_{0.66}Fe_{0.34}$	0.23	0.22	0.27	0.28	0.26	34
$Ni_{0.50}Fe_{0.50}$	0.24	0.22	0.30	0.29	0.25	42
Fe	0.35	0.34	0.54	0.58	-	120
$Ni_{0.75}Fe_{0.25}/Ni_{foam}$ ***	0.19	0.20	0.23	0.24	0.28	24

* The onset overpotential was estimated by the intercept of the negative-going LSV with the *E* axis (Figure 6.9A and Figure 6.16A) and the beginning of the linear region in Tafel plots (Figure 6.7 and Figure 6.8).

** The current density was chosen arbitrarily. The electrochemically accessible Ni normalized cyclic voltammograms are shown in Figure 6.9B and Figure 6.16B.

*** Catalyst loading on Ni foam Ni + Fe = 0.135 mg cm^{-2}.

6.2.3 Tafel analysis and proposed WOR mechanism

In Figure 6.7, the Tafel slopes for the Ni HO-np/CF and the Fe HO-np/CF electrodes were ~ 62 and 120 mV dec^{-1}, respectively. The slopes were substantially less over the most active $Ni_{0.75}Fe_{0.25}$ HO-np/CF and $Ni_{0.80}Fe_{0.20}$ HO-np/CF electrodes (~ 29 and 30 mV dec^{-1}, respectively). The Tafel slopes were all near 40 mV dec^{-1} for the series of $Ni_{1-x}Fe_x$ HO-np (Figure 6.7 and Figure 6.8). As proposed by Gervasi et al., this Tafel slope is consistent (at low overpotentials and under steady-state conditions) with a mechanism with two net steps. The first is a reversible one-electron oxidation accompanied by coordination of hydroxide to a Ni^{IV} active site (eq 6.3). The second is a turnover limiting one-electron oxidation that occurs by reaction between dissolved hydroxide and Ni^{IV}–OH^{ads} to generate O_2 (eq 6.4).[235,456] Eqs 6.3 and 6.4 likely represent multi-step processes. The turnover-limiting eq 6.4 possibly resembles an attack by hydroxide on an electron-deficient oxygen species bonded to Ni^{IV}.

$$Ni^{IV} + OH^- \rightleftharpoons Ni^{IV}–OH^{ads} + e^- \quad (6.3)$$

$$Ni^{IV}–OH^{ads} + OH^- \rightarrow Ni^{IV} + 0.5\ O_2 + H_2O + e^- \quad (6.4)$$

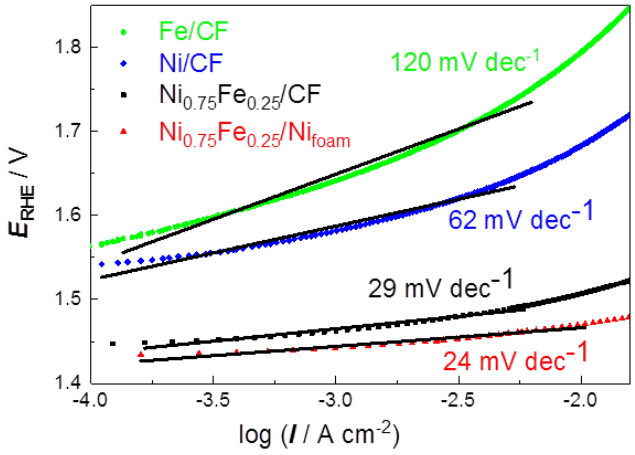

Figure 6.7 Tafel plots of the $Ni_{1-x}Fe_x$ HO-np/CF and the $Ni_{0.75}Fe_{0.25}$ HO-np/Ni_{foam} electrodes in 1.0 M KOH.

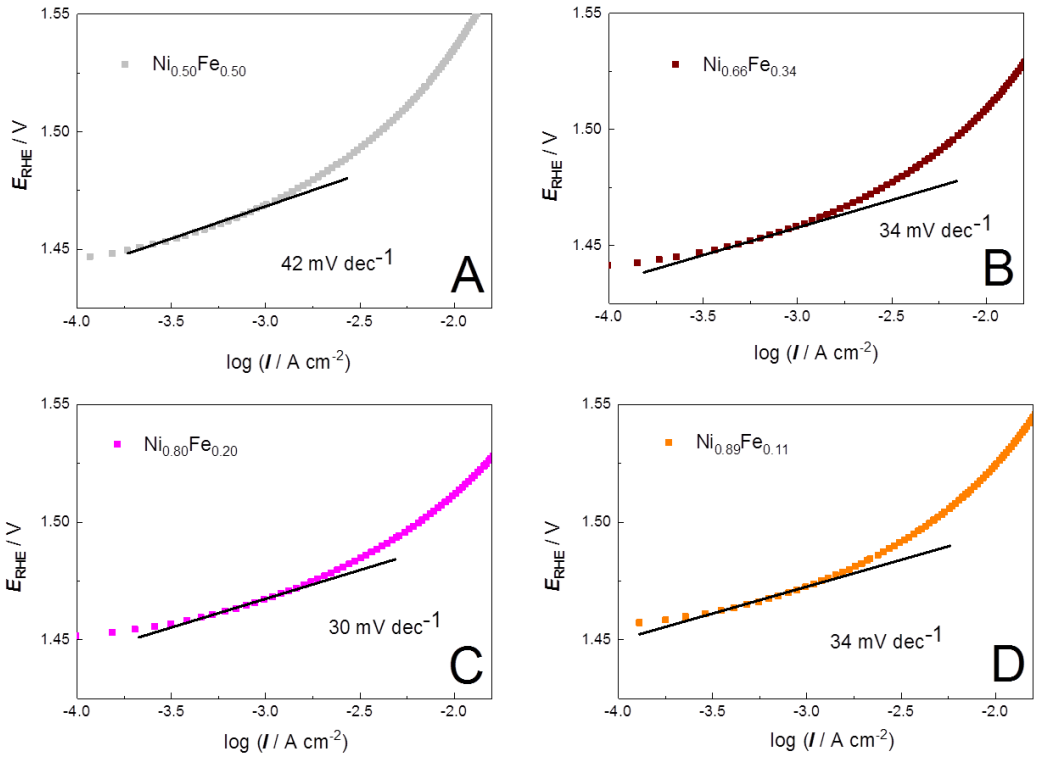

Figure 6.8 Tafel plots of the $Ni_{1-x}Fe_x$ HO-np/CF electrodes in 1.0 M KOH.

Cyclic voltammetry studies in the literature[223,454,457] and our own both indicate that the electron deficiency at Ni increases with the fraction of Fe in the lattice. Combining this observation with the mechanism proposed by Gervasi et al.,[456] we propose one way that Fe enhances eq 6.4 is by reducing the electron density at Ni, thereby increasing the reactivity of Ni-bound O-containing species towards attack by OH^-. This enhancement increases with the mole fraction of Fe in the HO-np, but the mass activity of the catalyst also depends upon the mole fraction of Ni. Again, this proposal does not exclude other possibilities.

Table 6.3 also summarizes the LSV and galvanostatic WOR potentials of the series at 10 mA cm^{-2} (geometric). The mixed catalyst $Ni_{0.75}Fe_{0.25}$ HO-np was the most active (E ~ 1.49–1.50 V_{RHE}, 0.26–0.27 V overpotential) by mass Ni + Fe.

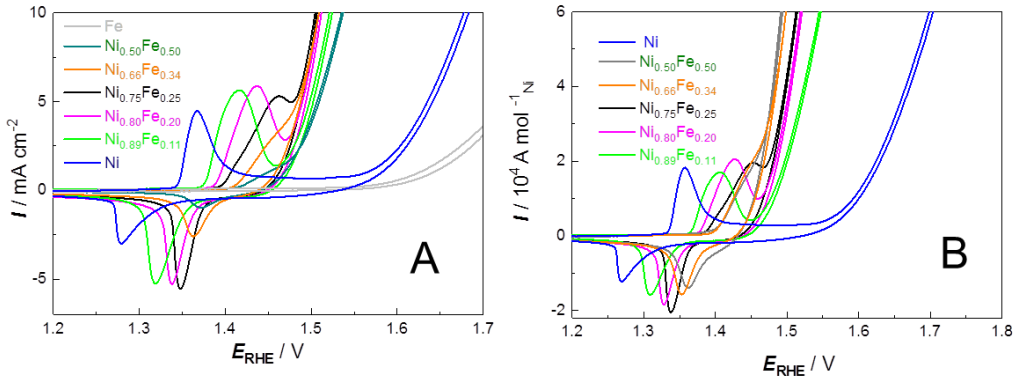

Figure 6.9 (A) CVs and (B) the current normalized to the mole of electrochemically accessible Ni of the $Ni_{1-x}Fe_x$ HO-np/CF electrodes in 1.0 M KOH (sweep rate 5 mV s^{-1}, loading 0.0675 mg cm^{-2}).

6.2.4 Stability comparison

The stability of $Ni_{0.75}Fe_{0.25}$ HO-np towards the WOR was investigated by galvanostatic and duty cycle experiments. Figure 6.10 shows the 24 h galvanostatic WOR polarization curves over the Ni HO-np/CF and the $Ni_{0.75}Fe_{0.25}$ HO-np/CF electrodes at 10 mA cm^{-2} with the loading Ni + Fe = 0.0675 mg cm^{-2}. Both catalysts displayed sustained polarization patterns during the entire galvanostatic water oxidation. The CVs (Figure 6.11) and XPS spectra (Figure 6.12) of the $Ni_{0.75}Fe_{0.25}$ HO-np/CF electrode were measured after the 24 h galvanostatic WOR. The area under the $Ni(O)OH/Ni(OH)_2$ cathodic peak (Figure 6.11) increased slightly (~ 4%), suggesting that a major restructuring of the catalyst did not occur over the 24 h WOR. The XPS peaks ($2p_{3/2}$ and $2p_{1/2}$) of the Ni and Fe regions shifted by 0.5–1.0 eV to higher binding energies after the 24 h galvanostatic test (Figure 6.12), and the deconvolution of the O 1s peak showed that the amount of O^{2-} increased from < 1% to ~ 3%. Taken together, the increases in the 2p binding energies and in the amount of O^{2-} suggest that the fraction of high oxidation state species, perhaps resembling Ni(O)OH and Fe(O)OH, increased over the 24 h WOR. However, this interpretation is tentative because other factors, such as the degree of hydration and the proportion of OH^- versus O^{2-} in the intercalated layers, could change over the 24 h WOR as well.

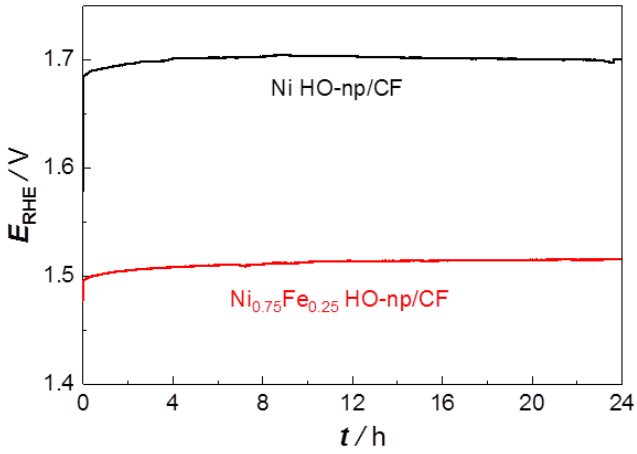

Figure 6.10 The 24 h galvanostatic (10 mA cm^{-2}) WOR profiles over the Ni HO-np/CF and the $Ni_{0.75}Fe_{0.25}$ HO-np/CF electrodes (loading: 0.0675 mg cm^{-2}).

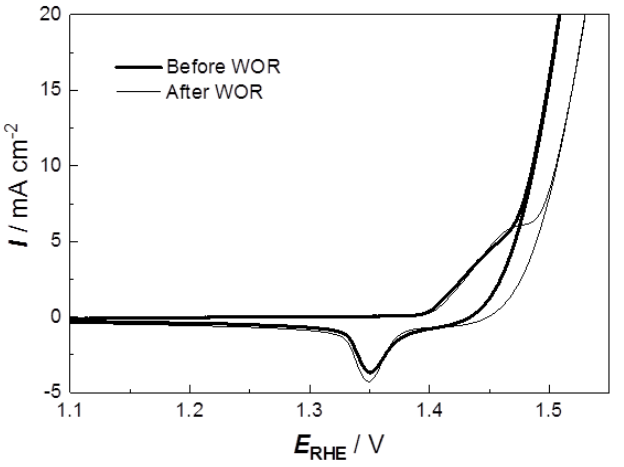

Figure 6.11 CVs of a $Ni_{0.75}Fe_{0.25}$ HO-np/CF electrode before and after 24 h galvanostatic test (loading: 0.0675 mg cm^{-2}).

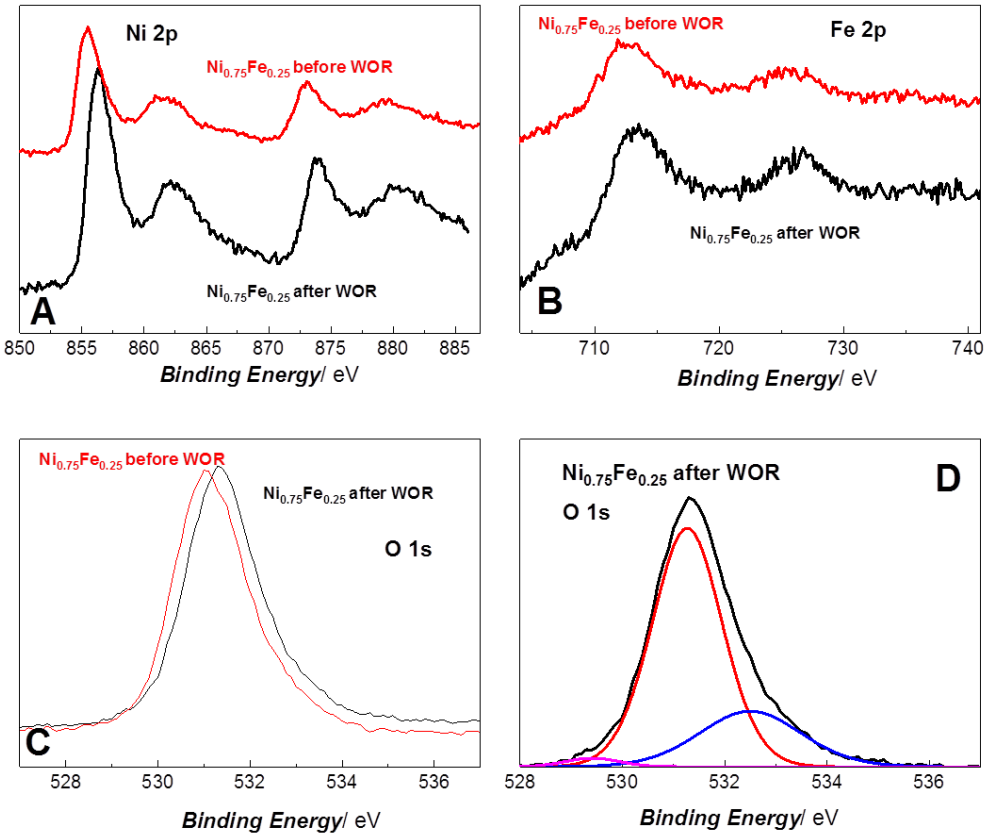

Figure 6.12 XPS spectra of a $Ni_{0.75}Fe_{0.25}$ HO-np/CF electrode after water oxidation (black line in A, B, and C) compared with the isolated $Ni_{0.75}Fe_{0.25}$ HO-np before water oxidation (red line in A, B, and C). And (D) the deconvolution of the O 1s peak of the $Ni_{0.75}Fe_{0.25}$ HO-np/CF electrode after water oxidation.

Strasser et al. developed duty cycle tests that assess the durability of $IrNiO_x$ acidic WOR catalysts under conditions closer to an operating electrolyzer.[191] We applied similar duty cycle tests to a $Ni_{0.75}Fe_{0.25}$ HO-np/CF electrode for the WOR in base, except that we measured the WOR activity after each cycle at 10 mA cm^{-2}, rather than the reported 1 mA

cm^{-2}. We utilized this harsher current density to keep up with the conventions of the alkaline WOR literature. Figure 6.13 shows plots of WOR potential at 10 mA cm^{-2} (E^{10}) versus number of duty cycles for the Ni HO-np/CF and $Ni_{0.75}Fe_{0.25}$ HO-np/CF electrodes. Both catalysts demonstrated high stabilities that are comparable to the acid $IrNiO_x$ systems reported by Strasser et al. Specifically, E^{10} rose by 30 mV, over 5 duty cycles with the Ni HO-np/CF electrode and by only 17 mV, over 5 duty cycles with the $Ni_{0.75}Fe_{0.25}$ HO-np/CF electrode. Thus, $Ni_{0.75}Fe_{0.25}$ HO-np were robust to 24 h galvanostatic and duty cycle tests.

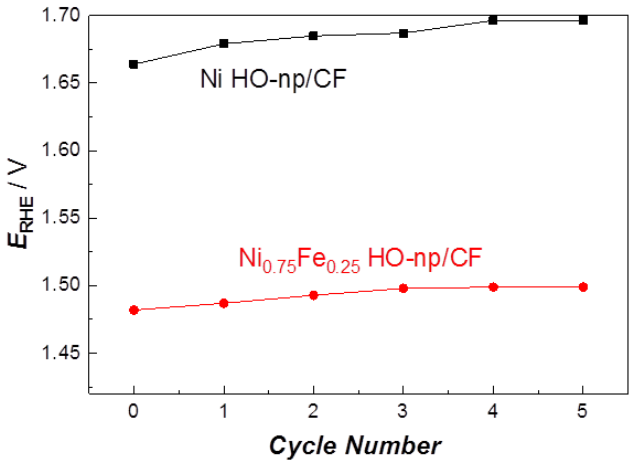

Figure 6.13 Voltammetric potential at 10 mA cm^{-2} versus duty cycle numbers for the Ni HO-np/CF and $Ni_{0.75}Fe_{0.25}$ HO-np/CF electrodes (loading: 0.0675 mg cm^{-2}).

6.2.5 Comparison of the carbon fiber paper and Ni foam as substrates

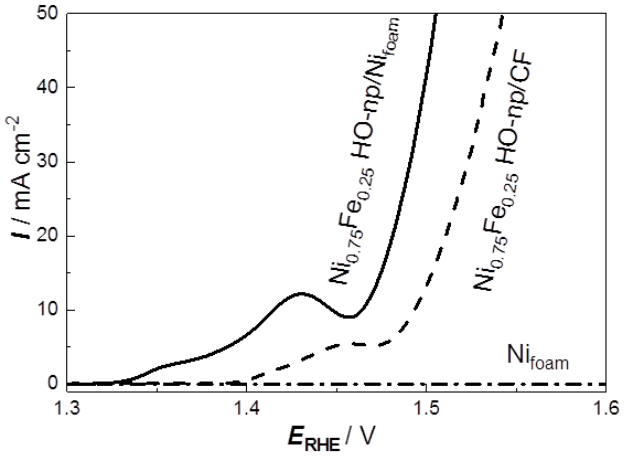

Figure 6.14 LSVs of $Ni_{0.75}Fe_{0.25}$ HO-np on the Ni foam (solid line, loading: Ni + Fe = 0.135 mg cm^{-2}), on the carbon fiber paper (dash line, loading: Ni + Fe = 0.135 mg cm^{-2}), and a bare Ni foam (dash dot line) in 1 M KOH at 5 mV s^{-1}.

The highest reported NiFe activities were obtained with NiFe LDH structures that were modified with oxidized graphene or carbon nanotubes and supported on Ni foam at high loadings (0.25 to 1 mg cm^{-2}).[236,238,243] For comparison, we prepared electrodes with higher mass loadings of $Ni_{0.75}Fe_{0.25}$ HO-np (Ni + Fe = 0.135 mg cm^{-2}) deposited on Ni foam and CF. Figure 6.14 compares the WOR LSVs of the $Ni_{0.75}Fe_{0.25}$ HO-np catalyst on Ni foam, on CF, and of a bare Ni foam. The redox peaks and WOR activity of the bare Ni foam were negligible compared to the $Ni_{0.75}Fe_{0.25}$ HO-np deposit. The LSV overpotential at 10 mA cm^{-2} was only 0.234 V (1.46 V_{RHE}) over $Ni_{0.75}Fe_{0.25}$ HO-np on Ni foam. This

activity is comparable to the best, modified Ni–Fe catalysts in the literature (0.210 V (0.25 mg cm^{-2})[238] and 0.224 V (1 mg cm^{-2})[243]). The onset potential over the $Ni_{0.75}Fe_{0.25}$ HO-np/Ni_{foam} electrode was 1.42 V_{RHE} (0.19 V overpotential), which compares well to the lowest in the literature (0.18 V).[438] The Tafel slope for the $Ni_{0.75}Fe_{0.25}$ HO-np/Ni_{foam} electrode also was low, 24 mV dec^{-1}. The 24 h galvanostatic WOR at 10 mA cm^{-2} (Figure 6.15B, only ~ 1.47 V_{RHE}, 0.24 V overpotential) and duty cycle stability tests (Figure 6.15A, E^{10} rose by ~ 13 mV after 5 duty cycles) showed that $Ni_{0.75}Fe_{0.25}$ HO-np were more active (per gram Fe + Ni) and stable over Ni_{foam} than over CF. The charges under the Ni(O)OH/$Ni(OH)_2$ cathodic peak (Figure 6.16A) showed that the utilization of Ni was 11% in the $Ni_{0.75}Fe_{0.25}$ HO-np/CF electrode at 0.135 mg cm^{-2} mass loading Ni + Fe. The utilization over Ni foam (48%) was substantially higher. When normalized to the electrochemically accessible Ni atoms estimated from the charges under the Ni(O)OH/$Ni(OH)_2$ cathodic peak (Figure 6.16B), $Ni_{0.75}Fe_{0.25}$ HO-np possessed nearly the same WOR activity. Therefore, the increased activity can come only from the increased utilization of Ni (48%) when supported on Ni foam. More research is required to understand why the catalyst utilization is higher over Ni_{foam}.

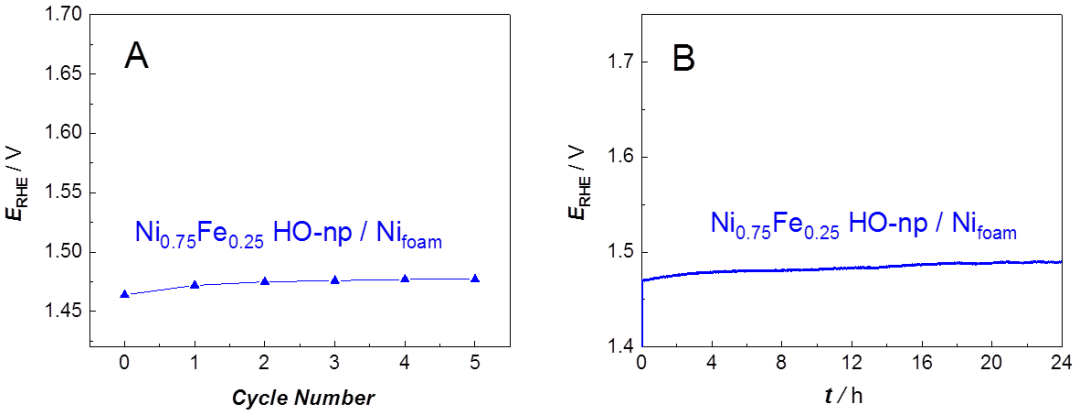

Figure 6.15 (A) Voltammetric potential at 10 mA cm^{-2} versus duty cycle numbers and (B) 24 h galvanostatic (10 mA cm^{-2}) WOR over the $Ni_{0.75}Fe_{0.25}$ HO-np/Ni_{foam} electrode (loading Ni + Fe = 0.135 mg cm^{-2}).

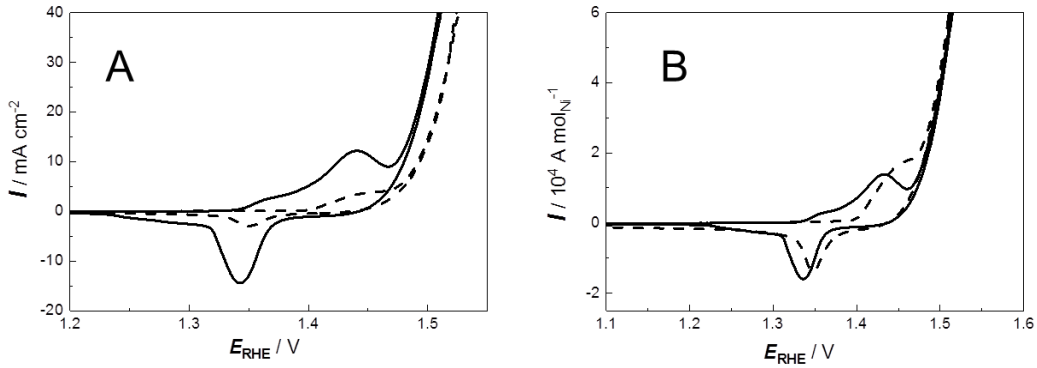

Figure 6.16 (A) CVs of the $Ni_{0.75}Fe_{0.25}$ HO-np/Ni_{foam} (solid line) and the $Ni_{0.75}Fe_{0.25}$ HO-np/CF (dashed line) electrodes in a 1.0 M KOH solution and (B) the current normalized to the mole of electrochemically accessible Ni atoms (sweep rate 5 mV s^{-1}, loading 0.135 mg cm^{-2}).

Regardless, these results show that the $Ni_{0.75}Fe_{0.25}$ HO-np/Ni_{foam} electrode, prepared in this simple manner, is comparable to the most active WOR catalysts reported to date. Also, $Ni_{0.75}Fe_{0.25}$ HO-np can be isolated by centrifugation, washed with distilled water, and redispersed in distilled water by sonication. A control experiment showed that isolated, washed, and dispersed $Ni_{0.75}Fe_{0.25}$ HO-np had the same activity with the as-synthesized catalyst (Figure 6.17).

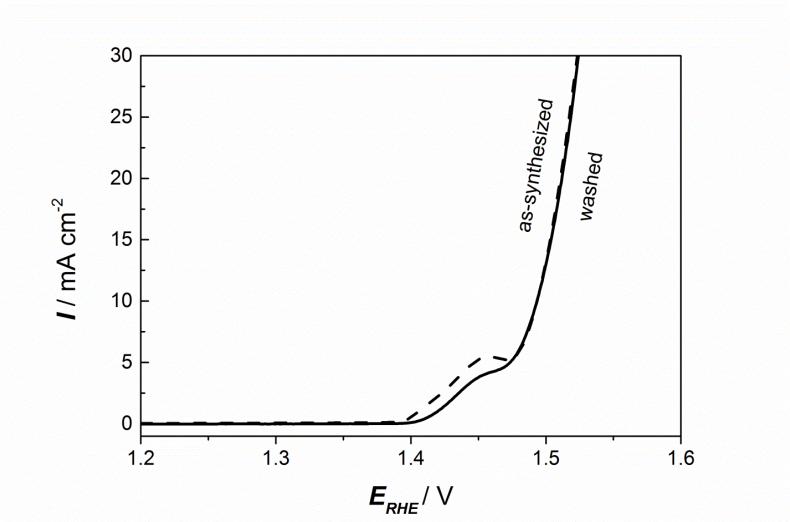

Figure 6.17 LSVs of the washed (solid line) and as-synthesized (dashed line) $Ni_{0.75}Fe_{0.25}$ HO-np/CF electrodes in 1.0 M KOH (sweep rate 5 mV s^{-1}) .

6.3 **Conclusions**

This Chapter describes a one-pot, open-air synthesis from simple Ni and Fe chlorides, which produced remarkably active and stable WOR catalysts. The synthesis is substrate-versatile and easily scaled. The hydrous oxide nanoparticles can be used directly from the reaction mixture or isolated as a solid without loss in activity. We suggest that the presence of Fe decreases the electron density at Ni, which enhances the rate of reaction between Ni-oxide species and dissolved hydroxide in the RDS. The simultaneous optimization of the activity of Ni by Fe, the fraction of Ni in the HO-np, and the catalyst utilization all contributed to the high activities and stabilities of these catalysts.

6.4 **Experimental**

6.4.1 Chemicals

Perchloric acid (Sigma-Aldrich, 70%, 99.999%), potassium hydroxide (Sigma-Aldrich, semiconductor grade, 99.99%), nickel chloride (Alfa Aesar, anhydrous, 98%), nickel chloride hydrate ($NiCl_2 \cdot 6H_2O$, Baker, 98%), iron(II) chloride ($FeCl_2 \cdot 4H_2O$, Fisher), iron(III) chloride ($FeCl_3 \cdot 6H_2O$, Fisher), Ni foam (Goodfellow, thickness 1.6 mm, porosity 95%), Toray carbon fiber paper (Electrochem. Inc.), and Nafion® (5 wt%, ElectroChem. Inc.) were used as received unless stated otherwise. Triply distilled water was used throughout the experiments.

6.4.2 Preparation of $Ni_{1-x}Fe_x$ HO-np

To prepare $Ni_{0.75}Fe_{0.25}$ HO-np, 0.0259 g (0.20 mmol) $NiCl_2$ or 0.0476 g (0.20 mmol) $NiCl_2 \cdot 6H_2O$ and 0.0133 g (0.067 mmol) $FeCl_2 \cdot 4H_2O$ or 0.0180 g (0.067 mmol) $FeCl_3 \cdot 6H_2O$ were dissolved in 20.0 mL triply distilled water in a 100 mL round-bottom flask. Then, 3.0 mL 0.8 M KOH solution were added dropwise over 2 min. The solution was stirred at 400 rpm for a total of 24 h in air. The use of the $FeCl_3 \cdot 6H_2O$ gave similar WOR activity and stability as the $FeCl_2 \cdot 4H_2O$ (Figure 6.18). For the synthesis of other $Ni_{1-x}Fe_x$ HO-np, appropriate masses of the metal precursors and 0.8 M KOH solutions (10 equivalent the total mole of the Ni^{2+} and Fe^{2+}) were utilized to yield the desired metal ratios. Table 6.4 provides details of the chemicals used for the synthesis. $Ni_{1-x}Fe_x$ HO-np can be

stored in the reaction mixture or washed and isolated. For the synthesis of Ni HO-np, purified KOH (Section 6.4.3) was used during the synthesis and the characterization.

Table 6.4 Amounts used for the synthesis of $Ni_{1-x}Fe_x$ HO-np

Composition	$NiCl_2$ (g)	$FeCl_2$ (g)	0.8 M KOH (mL)
Ni	0.0259	-	2.3
$Ni_{0.89}Fe_{0.11}$	0.0257	0.0030	2.5
$Ni_{0.80}Fe_{0.20}$	0.0261	0.0064	2.9
$Ni_{0.75}Fe_{0.25}$	0.0259	0.0085	3.0
$Ni_{0.66}Fe_{0.34}$	0.0259	0.0130	3.5
$Ni_{0.50}Fe_{0.50}$	0.0258	0.0253	4.6
Fe	-	0.0255	2.3

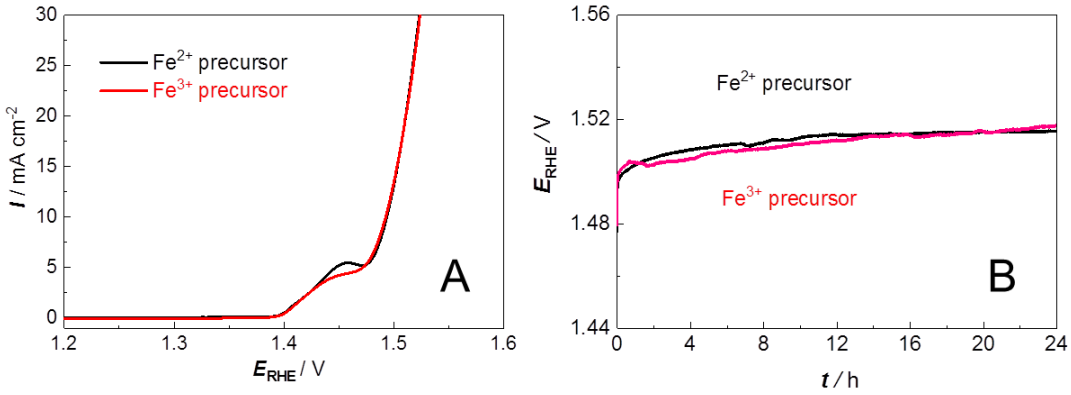

Figure 6.18 The WOR activities of the $Ni_{0.75}Fe_{0.25}$ HO-np/CF electrodes prepared using the Fe^{2+} or the Fe^{3+} as precursors in 1.0 M KOH; (A) LSVs with the sweep rate at 5 mV s^{-1} and (B) the 24 h 10 mA cm^{-2} galvanostatic test (loadings: 0.0675 mg cm^{-2}).

The as-prepared colloidal Ni HO-np, Fe HO-np, and $Ni_{1-x}Fe_x$ HO-np solutions were mixed with appropriate amounts of Nafion® to give a final 1 wt% Nafion® per total mass of Ni + Fe, calculated from the amounts in Table 6.4. Using a micropipette and graded microtips, appropriate volumes of the HO-np/Nafion® suspensions (sonicated for 2 min) were drop-coated onto ~ 1 cm^2 area of carbon fiber paper electrodes (1 × 3 cm^2) to give loadings ~ 67.5 μg or ~ 135 μg of the Ni+Fe in $Ni_{1-x}Fe_x$ HO-np or were drop-coated onto ~ 1 cm^2 area of Ni foam (Ni_{foam}; 1 × 3 cm^2) to give a loading of 135 μg Ni+Fe in $Ni_{0.75}Fe_{0.25}$ HO-np. The ink was dried at 60 °C for 20 min and left at room temperature for 20 min. The accuracy of the loading was checked by ICP–MS (~ 97%) (Table 6.2). Homemade graphite clips were used for electrochemical measurements to avoid metal contamination.

After 24 h, the synthesis solution was centrifuged at 4500 rpm for 20 min. The supernatant was decanted from the precipitated HO-np, which were then agitated mechanically with 30 mL triply distilled water for 5 min and centrifuged at 4500 rpm for 20 min. This process was repeated three times, and the resulting precipitates were dried in air for 48 h.

6.4.3 Purification of KOH solutions

The purification of KOH solutions follows the procedure described by Trotochaud et al.[221] It is necessary to remove any trace Fe from the KOH to measure the innate activity of the Ni HO-np/CF electrode (Figure 6.19). One gram of the $NiCl_2$ was mixed with 4 mL 1.0 M

KOH (semiconductor grade, as-received), then 20 mL water were added to form green precipitates ($Ni(OH)_2$). After centrifugation (4500 rpm, 15 min), the precipitates were washed with water (30 mL). The centrifugation and washing procedure was repeated three times. The washed $Ni(OH)_2$ was added to 1.0 M KOH (unpurified), and the mixture was agitated for 10 min to adsorb the Fe impurities. After allowing to settle for 3 h, the mixture was centrifuged for 0.5 h to separate the purified 1.0 M KOH solution. Figure 6.19 compares voltammetric responses of a Ni HO-np/CF electrode prepared and tested using as-received KOH with that of a Ni HO-np/CF electrode made and tested in purified (as described above) KOH solutions.

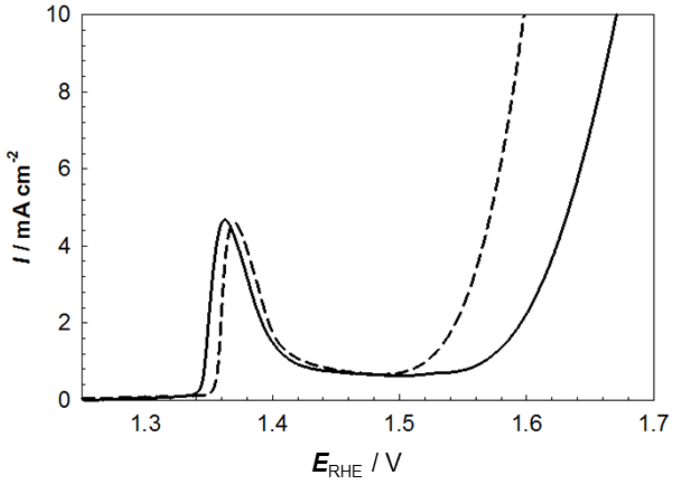

Figure 6.19 Voltammetric responses for the Ni HO-np/CF electrodes made and tested in as-received (dashed line) and purified (solid line) 1.0 M KOH solutions (sweep rate 5 mV s^{-1}).

6.4.4 Electrochemistry

The electrochemical experiments were performed with a Solartron SI 1287 Electrochemical Interface controlled by CorrWare for Windows Version 2-3d software. The reference electrode was a SCE. The measured potentials (E_{SCE}) were converted to the RHE scale and to the overpotentials (η) according to eqs 6.5 and 6.6.

$$E_{RHE} = E_{SCE} + 0.059pH + 0.241 \quad 6.5$$

$$\eta = E_{RHE} - 1.23V \quad 6.6$$

All electrochemistry experiments were performed in N_2-saturated 1.0 M KOH solutions (pH 13.6) at room temperature unless otherwise stated. A graphite rod formed the CE. Uncompensated resistance (1 Ω) was estimated by AC impedance[458] and corrected for. Each experiment has been repeated at least three times to ensure the reproducibility, and the experimental errors between measurements are less than 5%.

6.4.5 Calibration of the reference electrode

Calibration of the potential of the SCE was done by measuring against a Pt gauze electrode in a H_2-saturated 1.0 M KOH solution (Figure 6.20). The potential was swept from -0.943 to -1.143 V_{SCE} at 1 mV s^{-1}. The point of zero current was -1.044 V_{SCE}, consistent with the calculation using eq 6.5.

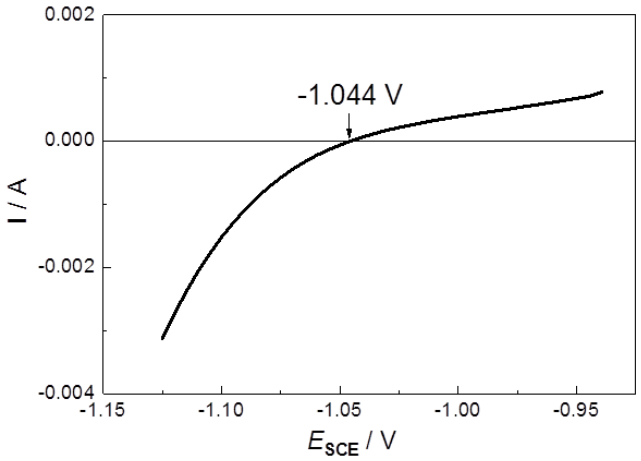

Figure 6.20 The reference electrode calibration curve at 1 mV s^{-1} in a H_2-saturated 1.0 M KOH solution.

6.4.6 Duty cycle experiment

The potential of the WE was set at E^5 (potential at which the current density reaches 5 mA cm^{-2}) and was increased by 0.02 V steps every 10 min (last potential E^{Final} would be E^5 + 0.1 V). The process of stepping the potential from E^5 to E^{Final} is one duty cycle. The duty cycle was repeated five times. After each cycle, a CV was collected and voltammetric potentials at 10 mA cm^{-2} were plotted as a function of the duty cycle number. The duty cycle process is displayed in Figure 6.21. Although the reported duty cycles in acid with $IrNiO_x$ were carried out starting at 0.5 mA cm^{-2} and the LSV potential was determined at 1 mA cm^{-2},[189] we started the cycles at 5 mA cm^{-2} to avoid the overlap with the $Ni(OH)_2$/Ni(O)OH peaks.

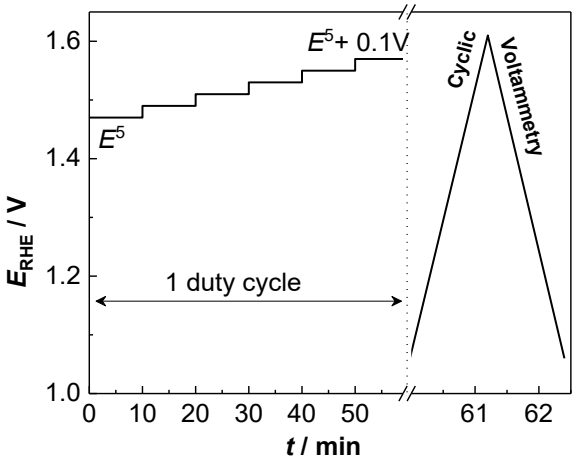

Figure 6.21 The potential versus time profile of a duty cycle process followed by a CV.

6.4.7 Instrumentation

BET measurements were carried out using Autosorb Quantachrome 1MP. The XRD patterns were measured with an Inel diffractometer equipped with a curved position-sensitive detector (CPS 120) and a Cu Kα1 radiation source operated at 40 kV and 20 mA with ($\lambda_{1/2}$ = 1.54060/1.54439 Å). HRTEM of washed $Ni_{0.75}Fe_{0.25}$ HO-np was performed at H-9500 with an accelerating voltage of 300 kV. STEM was conducted at JEM2200FS with an accelerating voltage of 200 kV. EDS was done under STEM mode. For the preparation of the sample for TEM, one drop of the suspension was placed onto a copper grid (carbon coated). Then, the sample was dried in the air for about 20 min. XPS measurements were performed on a Kratos Axis 165 instrument. The base pressure in the sample analytical chamber was lower than $1x10^{-9}$ torr. A monochromatized Al Kα source (hv = 1486.6 eV) was used at 12 mA and 14 kV. Survey scans spanned from a binding

energy of 1100 to 0 eV and collected with an analyzer pass energy of 160 eV in steps of 0.3 eV. Charge neutralization was applied to stabilize spectra during spectra collecting because the samples were not conductive adequately. To account for charging effects, all spectra were referred to C 1s at 284.8 eV. The binding energies of the peaks were calculated from the background-subtracted spectra using Shirley background. The peaks were fitted with Gaussian (70%)–Lorentzian (30%) curves.

Chapter 7 Modular Construction of Photoanodes with Covalently Bonded Ru- and Ir-Polypyridyl Visible Light Chromophores[a]

7.1 Introduction

Solar energy is essentially unlimited and can meet most of our future energy demands with minimal negative impact on the environment.[459,460] Cost-effective, efficient, and rapid large-scale storage is an inescapable requirement of the widespread utilization of renewable energy.[461] Solar energy can be stored with the WOR by converting the protons and electrons into H_2 or by using them to reduce carbon dioxide to form reusable fuels.[265,378,462–464] In 1972, Fujishima and Honda reported the first photoelectrochemical conversion of water into H_2 and O_2. This water splitting reaction utilized TiO_2 as the semiconductor/catalyst and UV illumination as the energy source.[250] Visible light constitutes ~ 44% of the solar spectrum,[465] and several approaches are being pursued to develop efficient visible light-driven water splitting systems.[378,462,463,466–469] For example, narrow band-gap SCs, including WO_3,[470] $BiVO_4$,[469,471] $SrTiO_3$,[472] and doped TiO_2[473–475] are

[a] *A version of this Chapter has been published. Wang, C.; Amiri, M.; Endean, R. T.; Martinez Perez, O.; Varley, S.; Rennie, B.; Rasu, L.; Bergens, S. H. ACS Appl. Mater. Interfaces 2018, DOI:10.1021/acsami.8b06605.*

being investigated as visible light-driven photoelectrodes. However, they generally absorb below 500 nm, exhibit poor hole transporting ability, and require large external voltages. Typically, dye-sensitized photoelectrochemical cells contain well-defined, separate chromophores and electrocatalysts. This distribution of function allows for independent optimization and for direct study of their roles and interactions within operating DSPECs.[248,265,266]

Ru- and Ir-polypyridyl complexes are common chromophores utilized in photoelectrochemical applications because they have strong, tunable MLCT (**m**etal-to-**l**igand **c**harge **t**ransfer) absorbance, they undergo efficient intersystem crossing, and their excited states have relatively long lifetimes.[476–480] Ru^{II}-polypyridine complexes have especially wide absorption ranges that extend into the visible and near infrared regions of the solar spectrum.[477,481,482]

The water oxidation photocurrent of DSPECs often decays from desorption of the chromophore and/or catalyst into water.[249,260,262,265] For aqueous environments, Ru chromophores are attached to SCs through phosphonate or carboxylate ester bonds made by condensation between SC surface hydroxides and acid groups on the ligands in the chromophores.[252,259,265] These chromophores suffer from desorption under basic conditions through hydrolysis of the esters.[254,256,289] Atomic layer deposition (ALD) of Al_2O_3 or TiO_2 layers improves the stability of the chromophore–catalyst layer on SCs.[288,483] Also, silatrane and hydroxamic acid anchoring groups have been utilized as binders, providing

enhanced stability towards hydrolysis up to pH 11.[273,274,276,282]

Typically, the rate of the WOR increases with pH.[248] Therefore, a wide variety of earth-abundant catalysts are stable under alkaline conditions but unstable in acid.[484] Finally, proton reduction is less competitive with CO_2 reduction at higher pHs.[102] For these reasons, it is necessary to develop anchoring/protection methods that stabilize chemical linkages between chromophore or catalyst molecules and SCs in strong alkaline solutions.[248] The electroreduction of aryl diazonium ions forms aryl radicals that have been grafted covalently to a variety of surfaces, including metals, metal oxides, and carbon.[291,292] In this process, the diazonium salt is generated in situ and is reduced to form covalent bonding with the surface by losing N_2 gas. Bélanger et al. deposited 1,10-phenanthroline on the GC surface with C5-covalently bonded to the surface using electrochemical reduction of the in situ generated 5-diazo-1,10-phenanthroline.[485] The direct grafting of diazonium-modified organometallic precursors to several electrode surfaces has been reported.[292,486–489] For example, Meyer et al. grafted a Ru^{II} diazonium-modified chromophore to a TiO_2 electrode. The resulting photoanode was more stable to alkaline conditions than phosphonic ester linkages.[290] However, this approach requires excess organometallic-diazonium compound that cannot be reused, and the lifetime of the radical intermediate depends upon the nature of the compound.[291,292]

In this Chapter, we report a reliable covalent grafting of 1,10-phenanthroline (phen) at C5 to ITO and TiO_2 surfaces by diazonium electroreduction, with the resulting SC-phen

bonds to Ru- and Ir- organometallic precursors forming corresponding chromophores (Scheme 7.1).

Scheme 7.1.

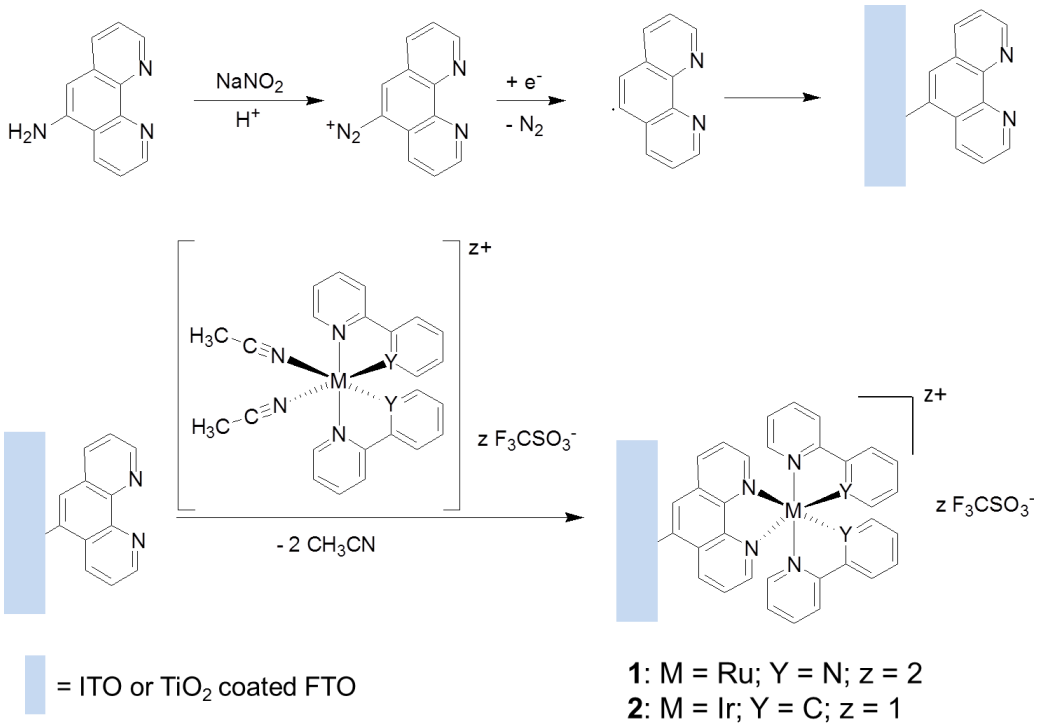

7.2 **Results and Discussion**

7.2.1 Deposition and characterization on ITO

The electroreduction of the in situ generated 5-diazo-1,10-phenanthroline over carbon electrodes was reported by the groups of Ekinci and Bélanger.[485,490] Figure 7.1A shows the CVs for the electroreduction of the 5-diazo-1,10-phenanthroline cation over ITO in 0.1 M H_2SO_4 (0.15 and -0.2 V_{SCE}, with a sweep rate of 50 mV s^{-1}). As reported for GC,[485] the first negative going sweep contains a large peak corresponding to the reduction of the diazonium ion. This peak decreases with cycling as the active atoms are blocked by the deposited 1,10-phenanthroline layer.[291] The phen grafted on GC undergoes irreversible reductions at potentials below -0.78 V_{SCE} and oxidations above 0.42 V_{SCE}. Therefore, we chose a potential window between 0.15 and -0.2 V_{SCE} to avoid these degradations.

Figure 7.1B shows the high resolution N 1s region XPS spectra of an ITO electrode before and after the diazonium reduction. The N 1s peak at 398.7 eV after the grafting indicates the pyridine-type nitrogen, hence the presence of 1,10-phenanthroline, on the ITO surface. Figure 7.1C shows that the redox peaks for the redox probe $Fe(CN)_6^{3-/4-}$ (5 mM $K_3[Fe(CN)_6]$) are diminished and separated over ITO-phen compared to bare ITO in CVs recorded in 0.1 M KCl. The increase in the peak separation from 118 mV for ITO to 204 mV for ITO-phen indicates inhibition of the electron transfer, and the decrease in the peak current is caused by some of the electrochemically active sites being blocked by

phen. These results suggest the presence of phen on the ITO surface. The $Fe(CN)_6^{3-/4-}$ redox peaks were not suppressed fully, indicating that the film is thin and/or porous.[485] The sigmoidal resemblance of the ITO-phen CV indicates hemispherical diffusion, suggesting that the pore size of the 1,10-phenanthroline film is small.

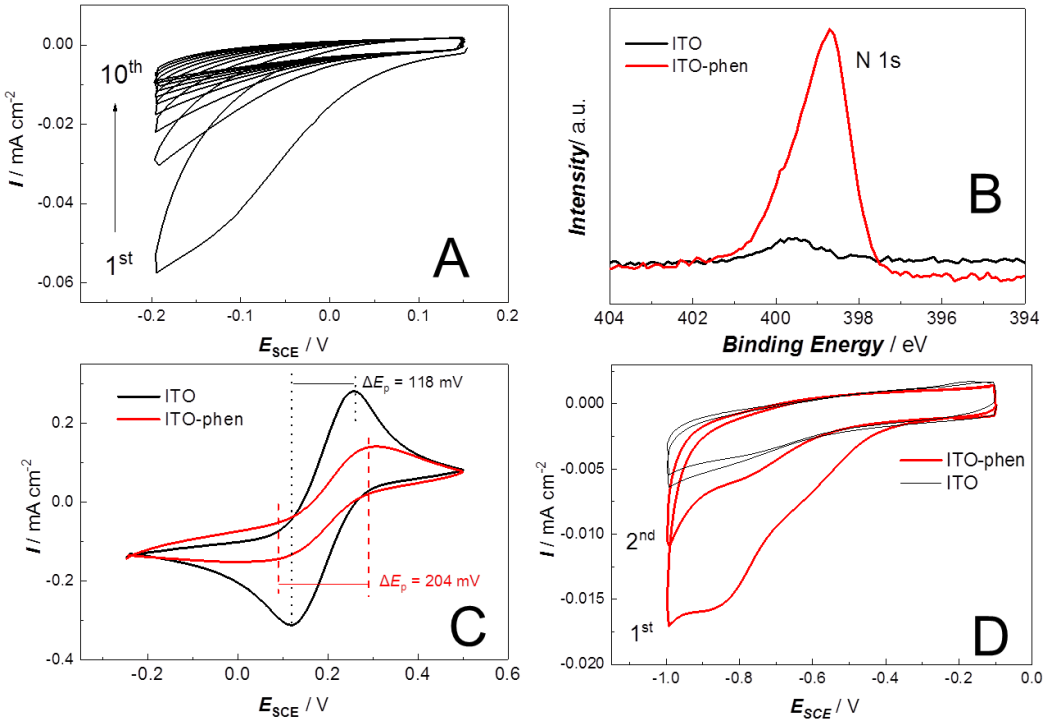

Figure 7.1 (A) CVs of the ITO electrode in a 0.1 M H_2SO_4 solution containing 5-amino-1,10-phenanthroline (1 mM) and $NaNO_2$ (2 mM) under N_2 with a sweep rate of 50 mV s^{-1}. (B) High resolution N 1s region XPS spectra of an ITO electrode before and after the 1,10-phenanthroline deposition. (C) CVs for the bare ITO and 1,10-phenanthroline modified ITO electrodes in a 5 mM $Fe(CN)_6^{3-}$ 0.1 M KCl solution under N_2 with a sweep rate of 20 mV s^{-1}. (D) CVs of the ITO-phen and bare ITO electrodes in a N_2-saturated 0.1 M Na_2SO_4 solution with a sweep rate of 50 mV s^{-1}.

Figure 7.1D shows CVs of the ITO-phen and bare ITO electrodes with a reducing lower limit (-0.1 to -1.0 V_{SCE}) in 0.1 M Na_2SO_4. The first negative going sweep with the ITO-phen electrode contained a strong reduction peak at -0.82 V_{SCE} with a shoulder at -0.57 V_{SCE} that was greatly diminished in the second sweep. This response is quite similar to that reported by Bélanger for phen grafted to GC and is attributed to $2e^-/2H^+$ reductions forming 1,4-dihydropyridine-type structures.[485,491] The charge under the reduction peak corresponds to an estimated surface coverage of 2.4×10^{-10} mol cm^{-2} by the grafted phen, assuming a two-electron process.

In principle, the ITO-phen ligand is protonated at the nitrogen under the acidic conditions of the electrografting. Indeed, it was necessary to rinse the ITO-phen ligand with ethanol ammonia aqueous solution, then with water and ethanol for the subsequent metalation reactions to occur. Exposing the neutralized ITO-phen to a 1:9 CH_2Cl_2/THF solution of the known compound[96] *cis*-$[Ru(bpy)_2(CH_3CN)_2]$ $(OTf)_2$ (**1**, 5 mM) at 50 °C for 2 h resulted in displacement of the acetonitrile ligands to form the photoanode ITO-$[(phen)Ru(bpy)_2](OTf)_2$, with the Ru-polypyridyl chromophore covalently bonded at C5 to ITO. The solution of **1** could be reused several times for the metalation provided it was stored under N_2. The steps in the construction of the ITO-chromophore photoanode were investigated with CV in a 0.1 M NBu_4PF_6 in CH_2Cl_2 solution. Figure 7.2A and 7.2B show the CVs of the ITO-phen and bare ITO electrodes in this non-aqueous electrolyte.

The CV of bare ITO was essentially featureless, while the CV of the ITO-phen contained a broad oxidation response > 1.0 V versus the ferrocenium/ferrocene redox couple ($V_{Fc+/Fc}$) and a broad reduction response < -1.0 $V_{Fc+/Fc}$. Figure 7.2C shows the CV of the ITO-$[(phen)Ru(bpy)_2]^{2+}$, starting at -0.35 $V_{Fc+/Fc}$ with the first sweep in the positive direction. There was an oxidation peak at 0.95 $V_{Fc+/Fc}$ in the first anodic sweep that matches the reported $Ru^{2+/3+}$ oxidation potential.[492] The corresponding reduction peak was absent in the reverse sweep, showing that the Ru^{III} complex was unstable under these conditions and decomposed by an unknown process. There was a cathodic peak at -1.62 $V_{Fc+/Fc}$ that may have arisen from the reduction of a phen-containing species remaining on ITO.[492] The estimated surface loading of the $[(phen)Ru(bpy)_2]^{2+}$ chromophore was 2.4×10^{-10} mol cm^{-2}, based upon the charge under the $Ru^{2+/3+}$ anodic peak. This coverage matches the coverage of ITO by phen in ITO-phen (2.4×10^{-10} mol cm^{-2}, estimated from the charge for the $2e^-$ reduction forming 1,4-dihydropyridines-type molecules). Further, the loading of Ru in ITO-$[(phen)Ru(bpy)_2]^{2+}$ was determined by ICP–MS (dissolved in aqua regia) to be 2.3×10^{-10} mol cm^{-2}, quite consistent with the coverage obtained from CV.

The metalation procedure can be repeated with the known compound[493] *cis*-$[Ir(ppy)_2(CH_3CN)_2]OTf$ (ppy = *ortho*-C_{phenyl} metalated 2-phenylpyridine) under the same conditions as for the Ru compound. Figure 7.2D shows the CV of the resulting ITO-$[(phen)Ir(ppy)_2]^+$ (0.1 M NBu_4PF_6, CH_2Cl_2), starting at -0.35 $V_{Fc+/Fc}$ with the first sweep in the positive direction. The $Ir^{3+/4+}$ redox couple peaks at 0.90 $V_{Fc+/Fc}$ and 0.81

$V_{Fc+/Fc}$ are similar to those for related Ir chromophores in the literature.[494] This redox couple is more reversible than the $Ru^{2+/3+}$ couple in ITO-$[(phen)Ru(bpy)_2]^{2+}$. The reduction peak in the first negative going sweep at -1.74 $V_{Fc+/Fc}$ may be attributed to the irreversible reduction of the phenanthroline ligand on the electrode.[494,495] The charge under the $Ir^{3+/4+}$ oxidation peak corresponds to a loading of Ir = 2.8×10^{-10} mol cm^{-2}. This loading agrees with the estimated coverage of phen in ITO-phen. Moreover, the ICP–MS results of Ir dissolved in aqua regia correspond to a loading of Ir = 2.6×10^{-10} mol cm^{-2}, consistent with the Ir and phen coverages estimated with CV. Taken together, the results from the Ru and Ir metalation show that this method is versatile and that little free phen ligand remains on the ITO surface after the metalation.

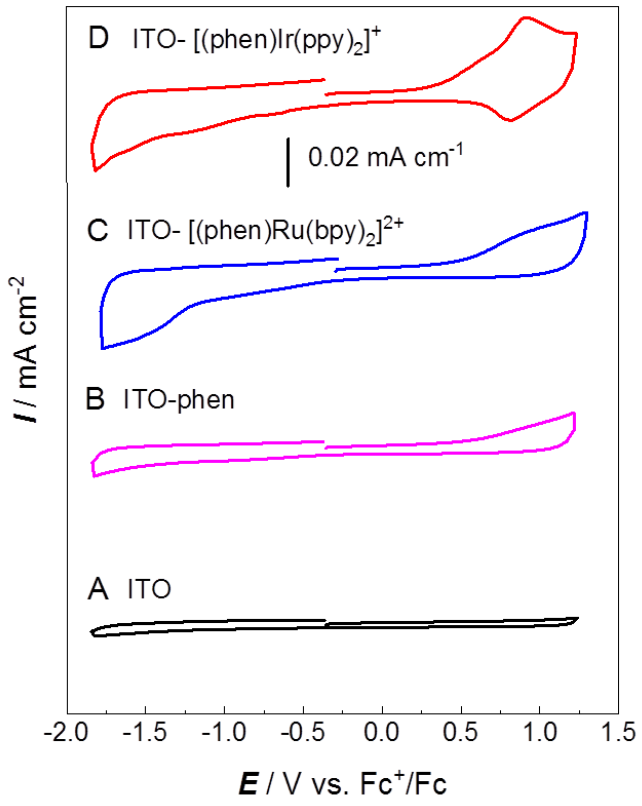

Figure 7.2 CVs of the ITO electrodes throughout the chromophore grafting process in a N_2-saturated CH_2Cl_2 solution containing 0.1 M NBu_4PF_6. The sweep rate was 200 mV s^{-1}.

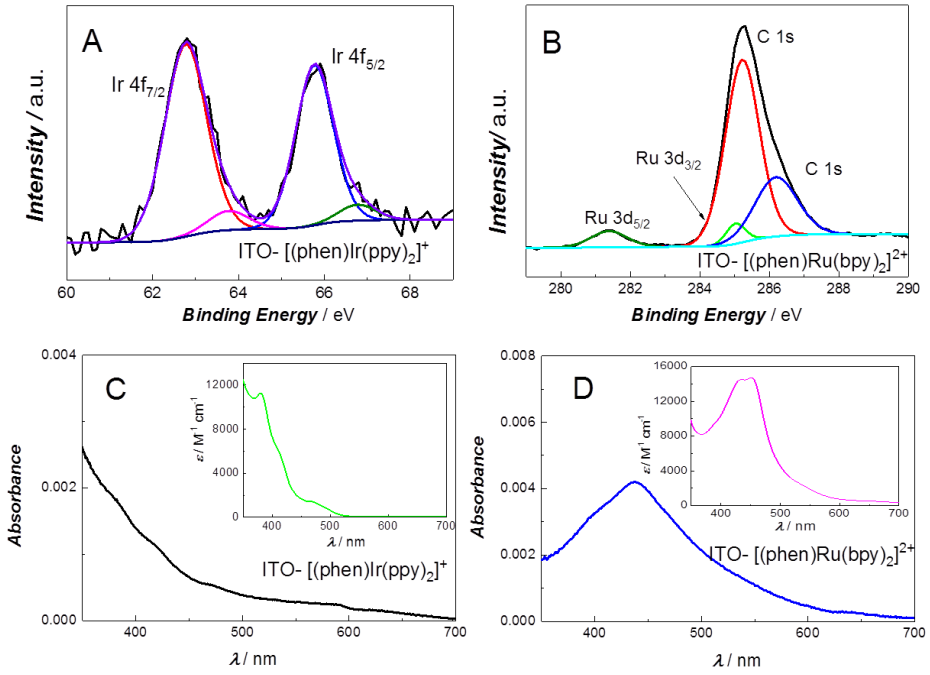

Figure 7.3 High resolution XPS spectra on (A) the Ir 4f region of the ITO-$[(phen)Ir(ppy)_2]^+$ electrode and (B) the Ru 3d region of the ITO-$[(phen)Ru(bpy)_2]^{2+}$ electrode. UV–vis absorption spectra of the (C) ITO-$[(phen)Ir(ppy)_2]^+$ and (D) ITO-$[(phen)Ru(bpy)_2]^{2+}$ electrodes with the ITO absorbance deducted. The insets correspond to the UV–vis absorption spectra of the *cis*-$[Ir(ppy)_2(phen)]$ OTf and $[Ru(bpy)_2(phen)]$ $(OTf)_2$ in CH_2Cl_2 solutions, respectively.

Figure 7.3A and 7.3B show the XPS spectra of Ir and Ru regions of the ITO-$[(phen)Ir(ppy)_2]^+$ and the ITO-$[(phen)Ru(bpy)_2]^{2+}$ electrodes, respectively. In Figure 7.3A, the XPS spectrum of the ITO-$[(phen)Ir(ppy)_2]^+$ shows well defined Ir 4f peaks. The binding energy for the Ir $4f_{7/2}$ peak was at 62.8 eV, indicating the 3^+ oxidation state of Ir on

the electrode.[489] Figure 7.3B exhibits the XPS spectrum of the Ru peaks. The binding energy for the Ru $3d_{5/2}$ peak was positioned at 281.4 eV, indicating the 2^+ oxidation state of Ru.[487,496] The estimated atomic ratios of N:Ir and N:Ru from the XPS data are ~ 4:1 and 6:1, respectively, suggesting that all the 1,10-phenanthroline groups are metalated and that azo-coupling did not occur during the diazonium reduction.[497]

Figure 7.3C and 7.3D show the solid-state UV–vis absorption spectra of the ITO-$[(phen)Ir(ppy)_2]^+$ and the ITO-$[(phen)Ru(bpy)_2]^{2+}$ photoelectrodes, respectively. The lower wavelength was set to 350 nm because the ITO absorbs strongly below this value. The UV–vis absorption spectrum of the ITO-$[(phen)Ir(ppy)_2]^+$ resembles that of the *cis*-$[Ir(ppy)_2(phen)]OTf$ in a CH_2Cl_2 solution (Figure 3C, inset). The visible absorption spectrum results from overlapping **m**etal-to-**l**igand **c**harge **t**ransfer (^{1}MLCT, ^{3}MLCT) ($d\pi(Ir)\rightarrow\pi^*(phen)$), **l**igand-to-**l**igand **c**harge **t**ransfer (^{1}LLCT, ^{3}LLCT), and **l**igand **c**entered (LC) $^3\pi\rightarrow\pi^*$ transitions.[498–500] The mixing of the formally spin-forbidden ^{3}MLCT, ^{3}LLCT, and (^{3}LC) $^3\pi\rightarrow\pi^*$ with higher-lying ^{1}MLCT transitions allows for relatively intense absorptions. This mixing arises from a strong spin-orbit coupling induced by the heavy Ir^{III} atom.

Figure 7.3D shows the solid-state UV–vis absorption spectrum of the ITO-$[(phen)Ru(bpy)_2]^{2+}$ photoelectrode. The absorption at 440 nm likely results from overlapping $d\pi(Ru)\rightarrow\pi(bpy)^*$ and $d\pi(Ru)\rightarrow\pi(phen)^*$ ^{1}MLCT absorptions.[477,501] The UV–vis spectrum of the $[Ru(bpy)_2(phen)]^{2+}$ in a CH_2Cl_2 solution contains a similar peak at 452

nm with a shoulder at 420 nm (Figure 3D, inset).[502]

The surface coverages (Γ) by the Ir and the Ru in the ITO-$[(phen)Ir(ppy)_2]^+$ and the ITO-$[(phen)Ru(bpy)_2]^{2+}$ were estimated from their solid-state UV–vis absorption spectra with eq 7.1, using the molar extinction coefficients (ε) measured for the *cis*-$[Ir(ppy)_2(phen)]^+$ and the $[Ru(bpy)_2(phen)]^{2+}$ in CH_2Cl_2 solutions at 440 nm.[460,503]

$$\Gamma(\text{mole per cm}^{-2}) = \frac{\text{Absorbance}}{\varepsilon(\text{M}^{-1}\text{cm}^{-1})} \qquad 7.1$$

The estimated coverages were 3.19×10^{-10} mol cm^{-2} for the ITO-$[(phen)Ir(ppy)_2]^+$ and 2.80×10^{-10} mol cm^{-2} for the ITO-$[(phen)Ru(bpy)_2]^{2+}$. These values are comparable with those obtained from CV and ICP–MS. Taken together, the results from CV, ICP–MS, XPS, and UV–vis all show that most, if not all, of the phen ligands in ITO-phen were converted into Ir- or Ru- chromophores by this procedure.

7.2.2 Deposition and characterization on TiO_2

High surface area TiO_2 (anatase, 10 μm film) on FTO is converted readily into the photoelectrodes TiO_2-$[(phen)Ir(ppy)_2]^+$ and TiO_2-$[(phen)Ru(bpy)_2]^{2+}$ utilizing the same procedure.

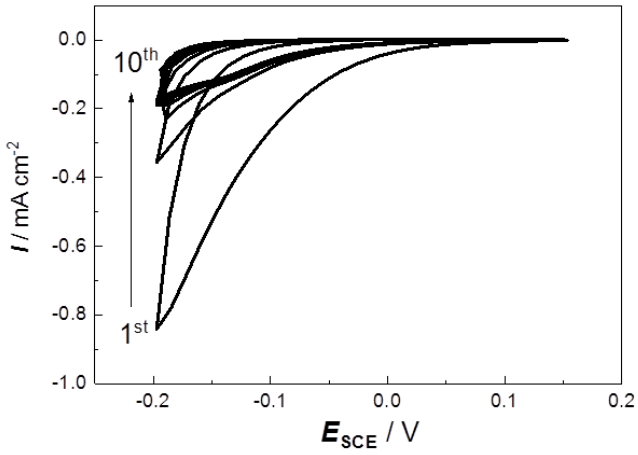

Figure 7.4 CVs of the TiO_2 electrode in a N_2-saturated 0.1 M H_2SO_4 solution containing 5-amino-1,10-phenanthroline (1 mM) and $NaNO_2$ (2 mM). The sweep rate was 50 mV s^{-1}.

Figure 7.4 shows the CVs of the electrochemical reduction of the diazonium salt using the TiO_2 electrode. Similar with the ITO electrode (Figure 7.1A), the first cycle exhibited a large reducing current, which decreased with cycling. This is an indication of the successful phen deposition on the TiO_2 surface.

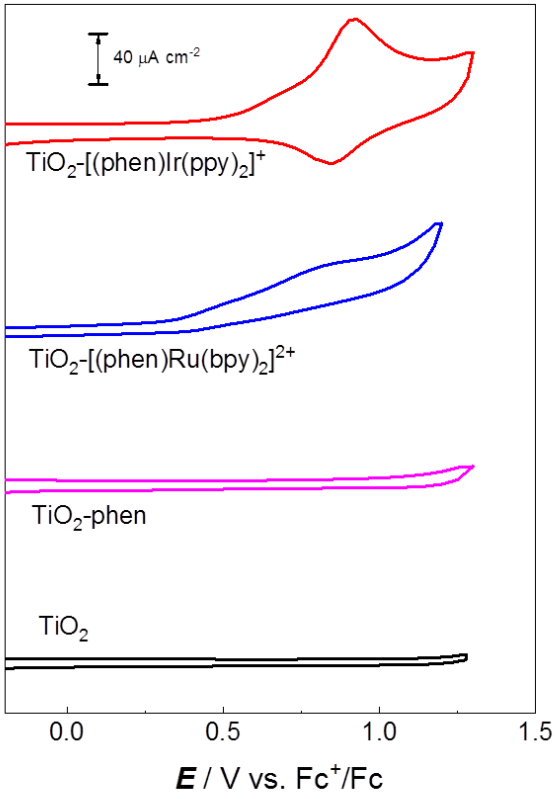

Figure 7.5 CVs of the TiO_2 electrodes throughout the chromophore grafting process in a N_2-saturated CH_2Cl_2 solution containing 0.1 M NBu_4PF_6. The sweep rate was 200 mV s^{-1}.

Figure 7.5 shows the CVs of the TiO_2-$[(phen)Ru(bpy)_2]^{2+}$, TiO_2-$[(phen)Ir(ppy)_2]^{+}$, TiO_2-phen, and bare TiO_2 electrodes. The bare TiO_2 electrode showed only capacitive currents in the applied potential range. The TiO_2-phen electrode displayed a broad oxidation peak higher than 1.0 $V_{Fc+/Fc}$. The TiO_2-$[(phen)Ru(bpy)_2]^{2+}$ and TiO_2-$[(phen)Ir(ppy)_2]^{+}$ electrodes exhibited the same features ascribed to the Ir and the Ru redox peaks, as discussed in Section 7.2.1. Based on the CVs, the coverages of the Ir

and the Ru on TiO_2 surfaces are estimated to be 2.2×10^{-9} mol cm^{-2} and 2.0×10^{-9} mol cm^{-2}, respectively. The ICP–MS data show that the coverage of the Ru and the Ir (dissolved in aqua regia) on the TiO_2-$[(phen)Ru(bpy)_2]^{2+}$ and TiO_2-$[(phen)Ir(ppy)_2]^{+}$ electrodes are 2.4×10^{-9} mol cm^{-2} and 2.6×10^{-9} mol cm^{-2}, respectively.

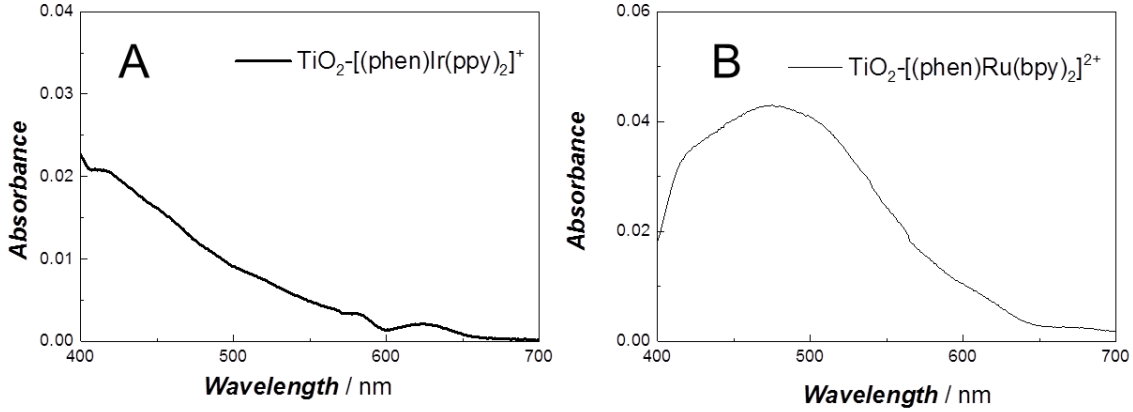

Figure 7.6 UV–vis spectra of (A) the TiO_2-$[(phen)Ir(ppy)_2]^{+}$ and (B) the TiO_2-$[(phen)Ru(bpy)_2]^{2+}$ electrodes with the TiO_2 absorbance deducted.

Figure 7.6 shows the UV–vis spectra of the TiO_2-$[(phen)Ir(ppy)_2]^{+}$ and the TiO_2-$[(phen)Ru(bpy)_2]^{2+}$ electrodes. The TiO_2-$[(phen)Ir(ppy)_2]^{+}$ electrode showed similar absorbance with the free molecule. The ^{1}MLCT peak of the TiO_2-$[(phen)Ru(bpy)_2]^{2+}$ electrode was at 475 nm, which is 23 nm higher than that of the free compound. This red shift in the ^{1}MLCT likely is caused by the strong coupling of the phenanthroline ligand with the TiO_2.[290] Based on eq 7.1, using the molar extinction coefficients and the absorbance at 450 nm, the surface coverages of Ir on the TiO_2-$[(phen)Ir(ppy)_2]^{+}$ and the

Ru on the TiO_2-$[(phen)Ru(bpy)_2]^{2+}$ electrodes are estimated to be 2.8×10^{-9} mol cm^{-2} and 2.2×10^{-9} mol cm^{-2}, respectively. We note that the surface coverages of the chromophores on TiO_2-$[(phen)Ir(ppy)_2]^{+}$ and TiO_2-$[(phen)Ru(bpy)_2]^{2+}$ electrodes obtained using CV, ICP–MS, and UV–vis methods are consistent.

In comparison, the $[Ru(bpy)_2(4,4'\text{-}(PO_3H_2)_2bpy)]^{2+}$, a commonly used chromophore in the literature, was synthesized and adsorbed on the TiO_2 surface using the reported method (denoted as RuP-TiO_2).[504,505] Figure 7.7A shows the CV of a RuP-TiO_2 electrode. Clear reversible peaks centered at 0.86 $V_{Fc+/Fc}$ could be assigned to the $Ru^{2+/3+}$ redox couple.[481] The Ru surface coverage, based on the integration of the charge, was 4×10^{-10} mol cm^{-2}. Figure 7.7B shows the UV–vis spectra of the RuP-TiO_2 electrode. The peak centered at 450 nm was the ^{1}MLCT peak.[481] Based on eq 7.1 ($\varepsilon = 14400$ M^{-1} cm^{-1}),[283] the Ru surface coverage of the RuP-TiO_2 electrode is estimated to be 9×10^{-9} mol cm^{-2}. ICP–MS on the Ru leached from the RuP-TiO_2 electrode using 1.0 M KOH and aqua regia shows that the Ru coverage on the electrode is 1.0×10^{-8} mol cm^{-2}, consistent with UV–vis estimation. The low surface coverage estimated from the CV indicates that only 5% of the Ru chromophore is electrochemically active on the TiO_2 surface. A similar observation was made by Meyer et al. on the TiO_2 surface-bound Ru^{II} complex.[506] However, for the electrodes fabricated using our diazonium deposition and metalation method, the estimated surface coverages of the chromophores are consistent with the results from the CV, UV–vis, and ICP–MS methods, which indicate that our method

deposits chromophores selectively at electrochemically active sites of the ITO and TiO_2 surfaces. In addition, the comparison between the chromophore coverages obtained using CVs (4×10^{-10} mol cm^{-2} for the RuP-TiO_2 and 2×10^{-9} mol cm^{-2} for the TiO_2-$[(phen)Ru(bpy)_2]^{2+}$) suggests that more electrochemically active TiO_2 sites are generated by our method, likely through the diazonium reduction process and/or the subsequent metalation process. The detailed mechanism requires further investigation.

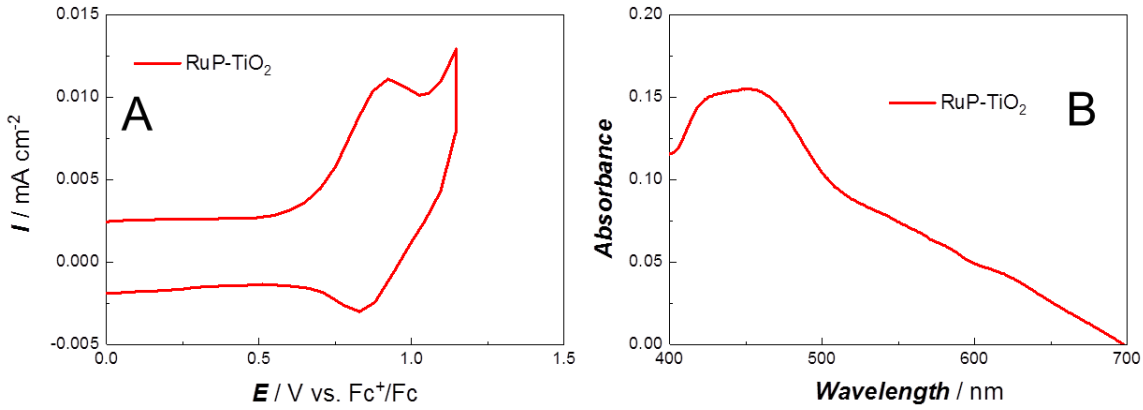

Figure 7.7 (A) CV of a RuP-TiO_2 electrode in a N_2-saturated CH_2Cl_2 solution containing 0.1 M NBu_4PF_6 at 200 mV s^{-1}. (B) UV–vis spectrum of the RuP-TiO_2 electrode with the TiO_2 absorbance deducted.

7.2.3 Photoelectrochemical activity

Figure 7.8A shows the IPCE (**i**ncident **p**hoton-to-current **c**onversion **e**fficiency) versus wavelength plots for the photoanodes towards the photoelectrochemical oxidation of 0.5 M TEA (**tri**ethyl**a**mine) in 0.1 M $NaClO_4$ solutions (-0.3 V_{SCE}, pH = 12.6). Unlike the

TiO_2-$[(phen)Ru(bpy)_2]^{2+}$ electrode, the control RuP-TiO_2 electrode bleached within 20 s of immersion into the alkaline solution. The IPCE for the TiO_2-$[(phen)Ru(bpy)_2]^{2+}$ was 1.4% at 450 nm, which was 12 times higher than the bleached RuP-TiO_2 control. Figure 7.8B shows the long-term photoelectrochemical oxidation of TEA (2.3 mW cm^{-2}, 450 nm incident light). The TiO_2-$[(phen)Ru(bpy)_2]^{2+}$ electrode was the most active. When the light was turned on at 300 s, a sharp increase in current occurred, followed by a rapid decline over the first 400 s of the illumination, then by a more stable region. The initial photocurrent reached 8 μA cm^{-2}, a value 6 times that of the TiO_2-phen electrode and 8 times that of the TiO_2. The initial TOF (**t**urn**o**ver **f**requency) was determined with eq 7.2 (i = photocurrent density, n = electron transfer number, Γ = surface coverage).[259,504]

$$\text{TOF } (h^{-1}) = \frac{3600\, i}{nF\Gamma} \qquad 7.2$$

The initial TOF for the TiO_2-$[(phen)Ru(bpy)_2]^{2+}$ electrode was 78 h^{-1} and dropped to 44 h^{-1} at 400 s illumination during the initial decline. From 400 to 3000 s illumination, the photocurrent only dropped by 7.6%. Figure 7.8C shows the photocurrent normalized to 200 s illumination time. The TiO_2-$[(phen)Ru(bpy)_2]^{2+}$ maintained 87% of the photocurrent after 1000 s and 81% after 3300 s.

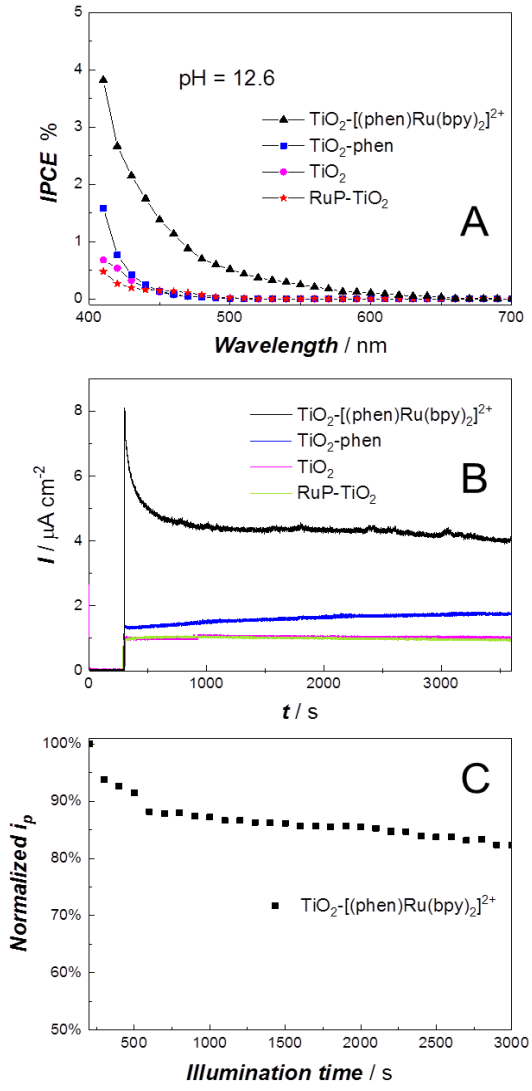

Figure 7.8 (A) The IPCE measurements of the TiO_2-$[(phen)Ru(bpy)_2]^{2+}$, TiO_2-phen, bare TiO_2 and RuP-TiO_2 electrodes at different wavelengths in 0.1 M $NaClO_4$ containing 0.5 M TEA at a constant potential of -0.3 V_{SCE} under Ar. (B) Photoelectrochemical responses of the electrodes under the same conditions with 450 nm monochromatic incident light (2.3 mW cm^{-2}). (C) Photocurrent of the TiO_2-$[(phen)Ru(bpy)_2]^{2+}$ electrode normalized to the photocurrent at 200 s illumination. All solutions were stirred at 500 rpm.

Figure 7.9A shows the IPCE versus wavelength plot for the photoelectrochemical oxidation of hydroquinone at neutral pH. The peak IPCE for the RuP-TiO_2 electrode was 6.3% at 450 nm. The IPCE for the TiO_2-$[(phen)Ru(bpy)_2]^{2+}$ electrode was 3.1% at 450 nm and reached 5.5% at 410 nm. We note that the coverage by chromophores in the RuP-TiO_2 control was 4.5 times that in TiO_2-$[(phen)Ru(bpy)_2]^{2+}$ (vide supra). Figure 7.9B shows the long-term stability results of the hydroquinone photoelectrochemical oxidation. The photocurrents were more stable for all the electrodes under neutral conditions than they were in base, and the large initial current drop was absent. The initial photocurrent for the TiO_2-$[(phen)Ru(bpy)_2]^{2+}$ electrode was 25 μA cm^{-2}, corresponding to TOF = 211 h^{-1}. Figure 7.9C compares the photocurrent for the TiO_2-$[(phen)Ru(bpy)_2]^{2+}$ and RuP-TiO_2 electrodes normalized to their Ru coverages. The normalized photocurrent for the TiO_2-$[(phen)Ru(bpy)_2]^{2+}$ electrode was 3 times that of the RuP-TiO_2 electrode throughout the process. The origin of this enhanced normalized photocurrent is under investigation. Figure 7.9D compares the stability of the TiO_2-$[(phen)Ru(bpy)_2]^{2+}$ and RuP-TiO_2 electrodes by normalizing activities to the current at 200 s of illumination. The TiO_2-$[(phen)Ru(bpy)_2]^{2+}$ electrode maintained 97% of the photocurrent after 1000 s and 85% after 3300 s. The control RuP-TiO_2 electrode dropped to 88% after 1000 s and down to 69% after 3300 s. The ICP–MS data showed that 33% of the surface Ru was lost to the solution after 3300 s for the control RuP-TiO_2, compared to 10% for the TiO_2-$[(phen)Ru(bpy)_2]^{2+}$.

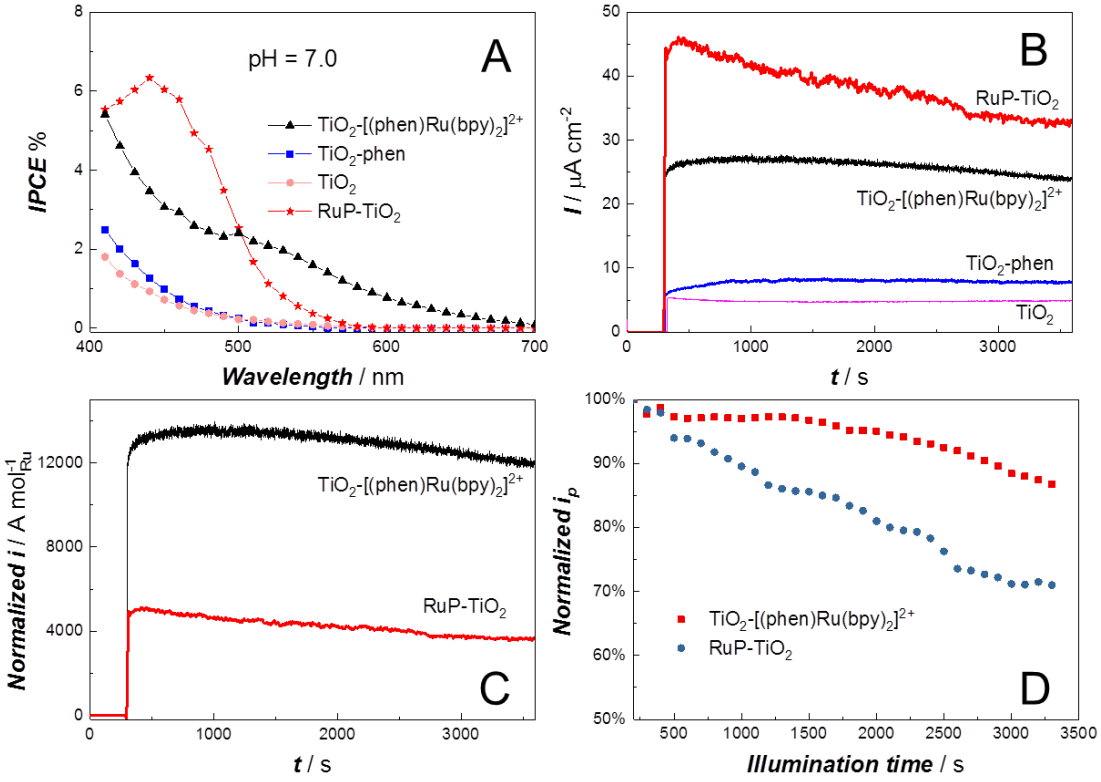

Figure 7.9 (A) and (B) IPCE and photoelectrochemical responses of the TiO_2-$[(phen)Ru(bpy)_2]^{2+}$, TiO_2-phen, bare TiO_2 and RuP-TiO_2 electrodes in 0.1 M $NaClO_4$ with 0.02 M hydroquinone under Ar at 0 V_{SCE}. (C) Photocurrent responses normalized to the moles of chromophores for the TiO_2-$[(phen)Ru(bpy)_2]^{2+}$ and RuP-TiO_2 electrodes under the same conditions. (D) Photocurrent stability comparison between the TiO_2-$[(phen)Ru(bpy)_2]^{2+}$ and RuP-TiO_2 electrodes normalized to the photocurrent at 200 s illumination. All solutions were stirred at 500 rpm.

Figure 7.10A shows the IPCE results of the TiO_2-$[(phen)Ir(ppy)_2]^{+}$ electrodes in neutral (hydroquinone) and basic (TEA) electrolytes. Under neutral conditions, the peak

IPCE for the TiO_2-$[(phen)Ir(ppy)_2]^+$ electrode reached 4.0% at 410 nm and decreased with increasing wavelength. Under alkaline conditions, the peak IPCE value reached 2.0% at 410 nm. Figure 7.10B shows the long-term photocurrent responses of the TiO_2-$[(phen)Ir(ppy)_2]^+$ electrode in neutral and basic conditions under 450 nm 2.3 mW cm^{-2} irradiation. Under neutral conditions, the initial photocurrent for the TiO_2-$[(phen)Ir(ppy)_2]^+$ electrode reached 22 μA cm^{-2}, corresponding to TOF = 187 h^{-1}. The TiO_2-$[(phen)Ir(ppy)_2]^+$ electrode maintained 74% photocurrent after 3300 s illumination relative to the photocurrent at 200 s. In base, the electrode reached 8 μA cm^{-2} (TOF = 68 h^{-1}) initially, then dropped quickly. Only 40% photocurrent was maintained after 3300 s relative to that of 200 s illumination. Compared with the TiO_2-$[(phen)Ru(bpy)_2]^{2+}$ electrode, the TiO_2-$[(phen)Ir(ppy)_2]^+$ electrode shows inferior stability in both neutral and basic solutions.

The IPCE of all the photoelectrodes were higher under neutral conditions than they were in base. Similar results were observed by Meyer et al, who attributed the higher IPCE to a decrease in the rate of back electron transfer as the pH is decreased.[504] Other factors, like the difference in the redox potentials of hydroquinone and triethylamine, could affect the electron transfer kinetics as well. More investigation is required to determine the origins of this phenomenon.

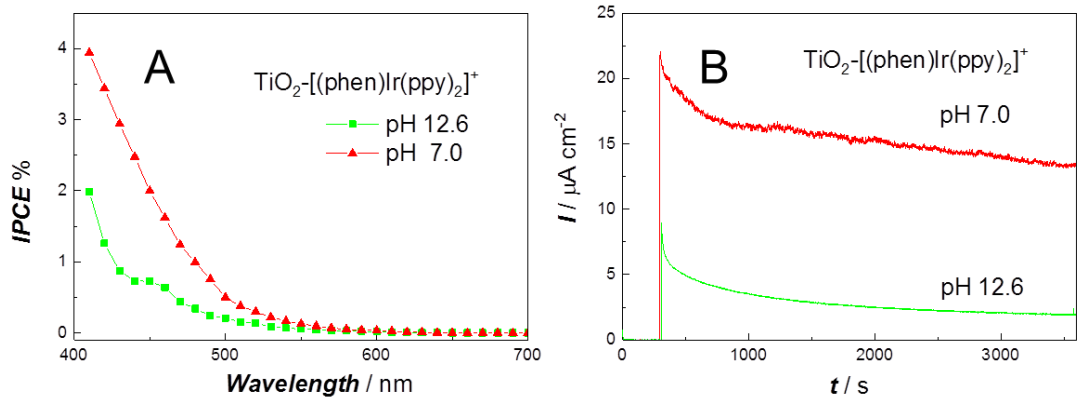

Figure 7.10 (A) The IPCE measurements of the TiO_2-$[(phen)Ir(ppy)_2]^+$ electrodes in 0.1 M $NaClO_4$ containing 0.5 M TEA at -0.3 V_{SCE} under Ar (green squares), and IPCE in 0.1 M $NaClO_4$ with 0.02 M hydroquinone under Ar at 0 V_{SCE} (red triangles). (B) Long-term photoelectrochemical responses of the electrodes under the same conditions. All solutions were stirred at 500 rpm.

7.2.4 Mechanism of photoelectrochemical reaction

The excited-state reduction potentials, $E(PS^+/PS^*)$, of the chromophores can be obtained using eq 7.3,

$$E(PS^+/PS^*) = E_{ox} - E_{0\text{-}0} \qquad 7.3$$

where E_{ox} is the oxidation potential of Ir^{III} or Ru^{II} compounds and $E_{0\text{-}0}$ is the zero-zero excitation energy[b] obtained from the optical spectra from literature.[479,495] The calculated

[b] Zero-zero excitation energy is the energy difference between the zero vibrational level of excited states and the zero vibrational level of ground states.

$E(PS^+/PS^*)$ values of the chromophores are more negative ($E(PS^+/PS^*)_{Ir}$ = -1.02 V_{NHE} and $E(PS^+/PS^*)_{Ru}$ = -0.71 V_{NHE}) than the conduction band edge potential of TiO_2 (~ -0.51 V_{NHE}), suggesting a feasible electron transfer from the photo-excited chromophores to the conduction band of the TiO_2.[289] Both the $E(PS^+/PS)_{Ir}$ = 1.38 V_{NHE} and $E(PS^+/PS)_{Ru}$ = 1.43 V_{NHE} are higher than the oxidation potential of TEA (0.93 V_{NHE})[507] and hydroquinone (0.37 V_{NHE}),[508] indicating that the electron transfer from the TEA or H_2Q (hydroquinone) to the PS^+ (i.e. SC-$[(phen)Ir^{IV}(ppy)_2]^{2+}$ and SC-$[(phen)Ru^{III}(bpy)_2]^{3+}$) is thermodynamically feasible. The energy diagram and the mechanism for the photoelectrochemical oxidation of the TEA and H_2Q are shown in Scheme 7.2, where Ru and Ir represent surface attached chromophores $[Ru(bpy)_2(phen)]^{2+}$ and $[Ir(ppy)_2(phen)]^+$, respectively.

Scheme 7.2.

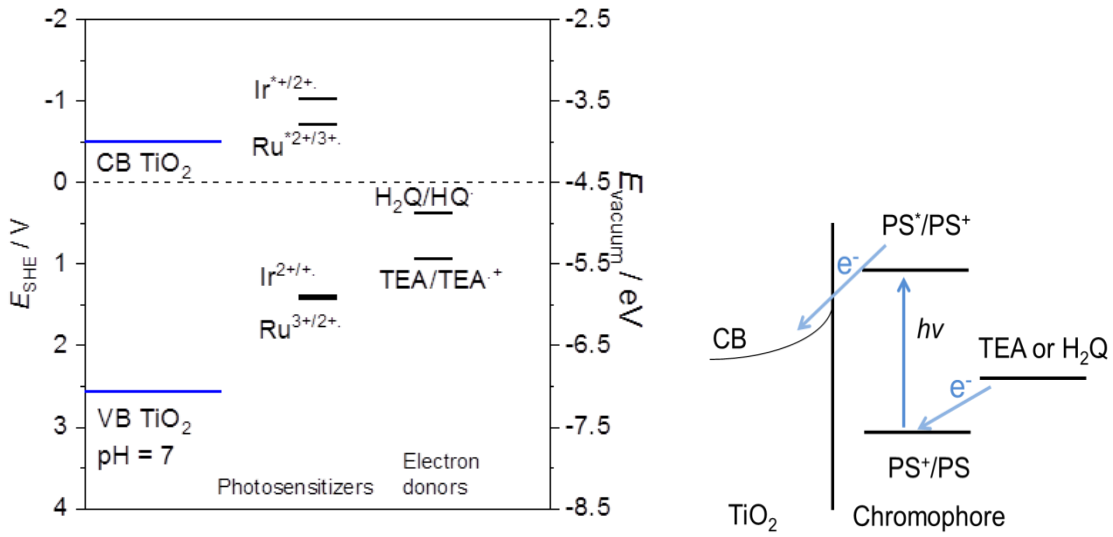

Upon light irradiation, the chromophore (PS) is excited to the singlet state and undergoes intersystem crossing, forming the long-lived excited triplet state (PS^*). Then, the excited-state chromophore injects an electron to the conduction band of TiO_2, forming PS^+. Next, the electron donors (TEA or H_2Q) give an electron to the PS^+ to regenerate the chromophore. The electron injected from PS^* to the conduction band of TiO_2 potentially could be used to generate hydrogen at the cathode. This process is described in eqs 7.4 to 7.7.

$$PS + h\upsilon \rightarrow PS^* \qquad 7.4$$

$$PS^* \rightarrow e^- + PS^+ \qquad 7.5$$

$$PS^+ + TEA \rightarrow PS + TEA^{\bullet+} \qquad 7.6$$

or

$$PS^+ + H_2Q \rightarrow PS + HQ^{\bullet} + H^+ \qquad 7.7$$

The $TEA^{\bullet+}$ (in eq 7.6) then deprotonates and rearranges into a carbon-centered radical, exhibiting highly reductive power. The iminium cation formed by oxidation of the carbon centered radical hydrolyzes to form diethylamine and acetaldehyde. This process is shown in Scheme 7.3.[509]

Scheme 7.3.

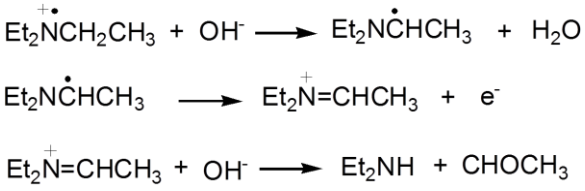

Two semiquinone radicals (eq 7.7) formed by the reduction of the PS^+ undergo disproportionation, forming hydroquinone and benzoquinone (Q), as shown in eq 7.8.[510]

$$2\ HQ^{\bullet} \rightarrow H_2Q + Q \qquad 7.8$$

7.3 **Conclusions**

In conclusion, we have demonstrated a versatile, two-step process to prepare a chromophore–SC assembly. We prepared demonstration photoelectrodes with Ru and Ir chromophores anchored to ITO or TiO_2 surfaces. The strong covalent C5–O^{surf} linkage between the chromophores and the TiO_2 is more stable under neutral and alkaline conditions than that with phosphonate ester bridges, and the sensitized electrodes can be paired with a suitable catalyst that could be used for photoelectrochemical oxidation of water in a wide pH range. Further studies to extend this method to other systems to construct water oxidation and CO_2 reduction photoelectrodes are under way in our laboratories.

7.4 **Experimental**

7.4.1 Chemicals

The following chemicals were used without purification, unless otherwise noted: 1,10-phenanthroline-5-amine (Sigma-Aldrich, 97%), H_2SO_4 (Sigma-Aldrich, 99.999%), anhydrous ethanol (Commercial Alcohols), triply distilled water, $NaNO_2$ (Sigma-Aldrich, ≥ 97.0%), 2-phenylpyridine (Sigma-Aldrich, 98%), acetone, distilled (Fischer Scientific), dichloromethane, distilled (Sigma-Aldrich, ACS reagent, ≥ 99.5%), toluene, distilled (Sigma-Aldrich, 99.9%), hexanes, distilled (Caledon, ACS), acetonitrile, distilled (≥ 99.5%), methanol (Sigma-Aldrich, ACS reagent, ≥ 99.8%), diethyl ether (Sigma-Aldrich, ACS reagent, ≥ 99%), KPF_6 (Sigma-Aldrich, ≥ 99%), $MgSO_4$ (Caledon, anhydrous), silver trifluoromethanesulfonate (Sigma-Aldrich, 99%), sodium perchlorate monohydrate (Sigma-Aldrich, ACS reagent, ≥ 98.0%), diethyl ether (Anachemia, ≥ 99.0%), pentane (Caledon, HPLC grade), tetrahydrofuran, distilled (Sigma-Aldrich, ACS reagent, ≥ 99.0%), NH_4OH (Caledon), 2-phenylpyridine (Sigma-Aldrich, 98%), 1,10-phenanthroline (Sigma-Aldrich, ≥ 99%), iridium chloride trihydrated (A.B. Mackay Chemicals), bis(2,2′-bipyridine)dichlororuthenium(II) $[Ru(bpy)_2(Cl)_2]$ (Sigma-Aldrich, 97%), ethoxyethanol (Sigma-Aldrich, 99%), TiO_2 nanoparticle (anatase, nanopowder < 25 nm particle size, 99.7% trace metals basis), Triton X-100 (EMD Millipore Corporation), 2,4-pentanedione (Sigma-Aldrich, ≥ 99%), tetraethyl tetrahydrofuran, distilled

(Sigma-Aldrich, ACS reagent, ≥ 99.0%), 2,2'-bipyridine-4,4'-diylphosphonate (Carbosynth Ltd., > 96%), $TiCl_4$ (Sigma-Aldrich, ≥ 99.995%, trace metals basis), $NaClO_4$ (Sigma-Aldrich, ACS reagent, ≥ 98.0%), HCl (Sigma-Aldrich, ACS reagent, 37%), HNO_3 (Sigma-Aldrich, ACS reagent, 70%), hydroquinone (Sigma-Aldrich, ReagentPlus, ≥ 99.5%), triethylamine, distilled (Sigma-Aldrich, ≥ 99.0%), Na_2SO_4 (Sigma-Aldrich, ACS reagent, ≥99.0%), ITO (Sigma-Aldrich, surface resistivity 8-12 Ω/sq), and FTO (Sigma-Aldrich, surface resistivity ~ 7 Ω/sq).

7.4.2 Preparation of chromophore–SC electrodes

7.4.2.1 Preparation of TiO_2 coated FTO electrodes

FTO slides were sonicated in ethanol and water for 30 min and treated in a 50 mM $TiCl_4$ solution at 70 ^oC for 30 min. TiO_2 pastes were prepared following a reported procedure.[511,512] Briefly, 2.0 g TiO_2 nanoparticles were mixed with 200 μL Triton X-100 surfactant and 200 μL 2,4-pentanedione in a 12 mL ethanol/water 1:1 solution. The solution was stirred for 2 h vigorously, followed by sonication for 30 min to give the TiO_2 paste, which was doctor-bladed on the FTO surface with four layers of the scotch tape as spacers. After they were dried in air, the TiO_2 on FTO electrodes were heated to 500 ^oC for 2 h, followed by immersion in a 50 mM $TiCl_4$ solution at 70 ^oC for 30 min, washed with water and ethanol, and heated at 450 ^oC for 30 min. Figure 7.11 shows the morphology and thickness of the TiO_2 film on FTO, and Figure 7.12 shows the TEM image of the TiO_2

nanoparticle.

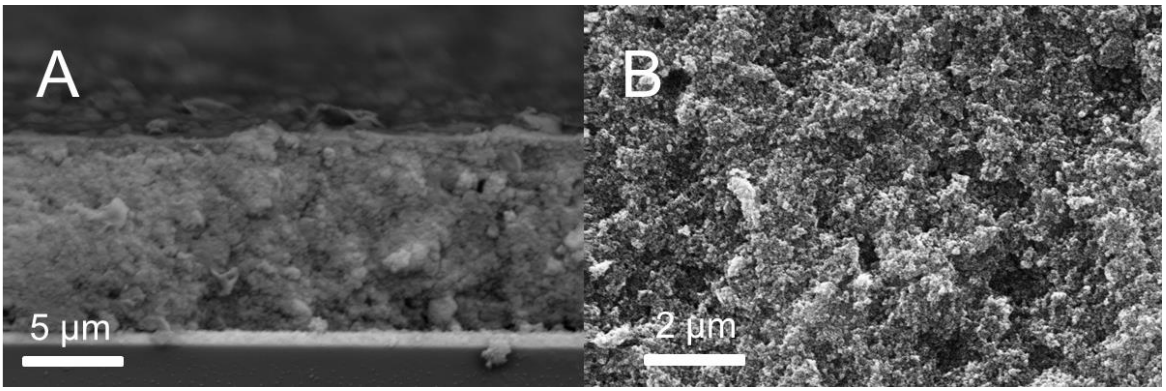

Figure 7.11 SEM images of the TiO_2 coated FTO glass slide. (A) The cross-section image and (B) the surface morphology.

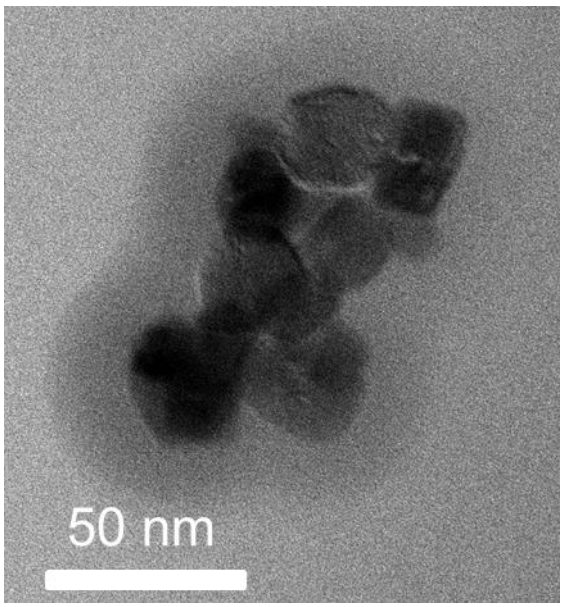

Figure 7.12 Transmission electron microscopy image of the TiO_2 nanoparticles.

7.4.2.2 Diazonium deposition

ITO coated glass slides were cut into a 2.5 × 1.2 cm^2 rectangular shape and were sonicated

for 15 min each in 5 mL acetonitrile, 5 mL 2-propanol, and 5 mL triply distilled water, then they were dried under N_2. The electrochemical grafting of the 1,10-phenanthroline onto the ITO slides (or TiO_2 coated FTO slides) was carried out according to the previous report.[485] Briefly, a 20 mL aqueous 0.1 M H_2SO_4 solution containing 1 mM 5-amino-1,10-phenanthroline (4 mg) was purged with N_2 for 15 min. One min after the addition of 2 mM $NaNO_2$ (3 mg), an ~ 1 cm^2 ITO slide was immersed into the solution as the WE and a graphite rod as the CE. The potential was scanned between 0.15 and -0.20 V_{SCE} with a sweep rate of 50 mV s^{-1} for 10 cycles. After electrochemical modification, the 1,10-phenanthroline coated ITO slide (ITO-phen) was rinsed and sonicated in water for 20 s to remove physically absorbed species. The TiO_2-phen (1,10-phenanthroline grafted to the TiO_2 coated FTO) electrodes did not undergo the sonication. The ITO-phen (or TiO_2-phen) electrodes were rinsed with distilled water and were immersed in a solution of ethanol and ammonium hydroxide (volume ratio 1:1) for 1 h to deprotonate the as-deposited 1,10-phenanthroline groups. Then, the electrodes were rinsed with water and ethanol and dried under air.

7.4.2.3 Metalation

The electrodes were placed in a Schleck tube and purged with N_2 for 15 min. $[Ir(ppy)_2(CH_3CN)_2]OTf$ (10 mg, 0.0130 mmol) or $[Ru(bpy)_2(CH_3CN)_2](OTf)_2$ (10 mg, 0.0126 mmol) was weighed out and 0.5 mL of dichloromethane were added to dissolve the

solid. The solution was cannulated into the Schlenk tube containing the electrodes and 4.5 mL of THF. The Schlenk tube was immersed in a paraffin oil bath and was heated to 50 °C for 2 h. After it cooled down to room temperature, the electrode was removed from the bath and rinsed with CH_2Cl_2 (5 mL) and water (2 mL). The resulting electrodes ITO-$[(phen)Ir(ppy)_2]^+$ and ITO-$[(phen)Ru(bpy)_2]^{2+}$ are stable in air under dark for over six months. The deposition on the TiO_2 electrode follows the same procedure, and the resulting electrodes are labeled as TiO_2-$[(phen)Ir(ppy)_2]^+$ and TiO_2-$[(phen)Ru(bpy)_2]^{2+}$.

7.4.2.4 Preparation of RuP-TiO_2 electrodes

A TiO_2 coated FTO electrode was immersed in a solution of 10 μM $[Ru(bpy)_2(4,4'\text{-}(PO_3H_2)_2bpy)]Br_2$ in 0.1 M $HClO_4$ for 12 h, followed by the immersion in a 0.1 M $HClO_4$ solution for another 12 h.[504] The resulting electrode (denoted as RuP-TiO_2) was washed with water, dried, and used.

7.4.3 Photoelectrochemistry

The electrolytes used for photoelectrochemistry studies consisted of 0.1 M $NaClO_4$ solutions containing either 0.5 M TEA (pH = 12.6) or 0.02 M hydroquinone (pH = 7.0), the CE was a coiled platinum wire, and the reference electrode was a SCE. The electrolyte was stirred using a magnetic stir bar at 500 rpm. A homemade 100 mL four-neck quartz flask with a flat window was used as the reaction flask for photoelectrochemical experiments. The solution was purged with Ar for 30 min prior to each measurement, and the Ar

atmosphere was maintained. The WE was washed with distilled water before use. The Newport QEPVSI-b system (300 W Xe lamp with Cornerstone M 260 monochromator) was calibrated against a silicon diode with known IPCE and was used for IPCE measurements. The incident light intensity was checked with a Thorlab S121C light meter. The IPCE values were calculated using eq 7.9,

$$\text{IPCE (\%)} = \frac{100 \times 1240 \times i}{P\lambda} \qquad 7.9$$

where i is the photocurrent density (mA cm^{-2}), P is the light power (mW cm^{-2}), and λ is the wavelength (nm). Each experiment has been repeated at least three times to ensure the reproducibility, and the experimental errors between measurements are less than 10%.

7.4.4 Synthesis of the Ru- and Ir- compounds

7.4.4.1 Synthesis of $[Ir_2Cl_2(ppy)_4]$

A literature procedure was used for the preparation of $[Ir_2Cl_2(ppy)_4]$.[513] 2-phenylpyridine (771 mg, 4.975 mmol, 5 equivalents) and $IrCl_3 \cdot 3H_2O$ (390 mg, 1.106 mmol, 1 equivalent) were dissolved in 30 mL of 2-ethoxyethanol and 10 mL of water, and the mixture was refluxed for 24 h. The precipitate was isolated via filtration and washed with ethanol, water, and acetone. 75 mL of dichloromethane were added, followed by toluene (25 mL) and hexane (10 mL). The solution was cooled overnight and filtered to yield the product as a yellow powder (428 mg, 71% yield). The ^1H NMR data were consistent with reported

values:[513] (ppm, in CD_2Cl_2, 498.119 MHz, *J*-values in Hz): 9.27 (d, 4H, *J* = 5.5); 7.95 (d, 4H, *J* = 8.0); 7.81 (t, 4H, *J* = 7.5); 7.57 (d, 4H, *J* = 7.5); 6.83 (m, 8H); 6.62 (t, 4H, *J* = 7.5); 5.89 (d, 4H, *J* = 7.5).

7.4.4.2 Synthesis of $[Ir(ppy)_2(CH_3CN)_2]OTf$

A reported procedure was used.[493] $[Ir_2Cl_2(ppy)_4]$ (165 mg, 0.153 mmol, 1 equivalent) was combined with AgOTf (112 mg, 0.437 mmol, 3 equivalents) in 15 mL acetonitrile under N_2. The mixture was stirred for 1 h, filtered through celite, and washed with acetonitrile. The filtrate was pumped down to ~ 5 mL, ether was added at -7 ^oC until a precipitate appeared, and the mixture was filtered and washed with ether and pentane. The precipitate was kept under vacuum for 18 h to yield the product as a yellow powder (148 mg, 70% yield). The ^1H NMR data agreed with reported values:[493] (ppm, in $CDCl_3$, 399.794 MHz, *J*-values in Hz) 9.11 (d, 2H, *J* = 5.6); 7.92 (m, 4H); 7.55 (d, 2H, *J* = 7.6); 7.43 (dt, 2H); 6.91(t, 2H, *J* = 7.2); 6.77 (t, 2H, *J* = 7.2); 6.10(d, 2H, *J* = 7.6); 2.40 (s, 6H).

7.4.4.3 Synthesis of $[Ru(bpy)_2(CH_3CN)_2](OTf)_2$

The synthesis of $[Ru(bpy)_2(CH_3CN)_2](OTf)_2$ is based on a previous report.[514] Under N_2, bis(2,2′-bipyridine)dichlororuthenium(II) $[Ru(Cl)_2(bpy)_2]$ (501.0 mg, 1.03 mmol, 1 equivalent) and AgOTf (530.3 mg, 2.06 mmol, 2 equivalents) were weighed into a 100 mL side-arm flask. 30 mL CH_3CN were added, and the solution was stirred for 2 h. Then, the

solution was filtered through Celite, washed with CH_3CN, and the filtrate collected. The filtration procedure was carried out three times to remove AgCl. Then, excess CH_3CN was removed via a liquid N_2 cold trap. The resulting solid was dissolved in ~ 5 mL CH_2Cl_2, and 4.0 mL ether were added to precipitate out an orange compound. The compound was washed with ether and dried as an orange compound (650 mg, yield 80%). The ^{1}H NMR data agreed with reported values: (499.798 MHz, $CDCl_3$,) δ 9.43 (d, 2H, *J* = 5.4 Hz), 8.46 (d, 2H, *J* = 8.2 Hz), 8.32 (d, 2H, *J* = 8.1 Hz), 8.24 (td, 2H, *J* = 8.0 Hz, 1.3 Hz), 7.96-7.90 (m, 4H), 7.56 (d, 2H, *J* = 5.5 Hz), 7.28-7.25 (m, 2H), 2.42 (s, 6H).

The synthesis of $[Ru(bpy)_2(4,4'\text{-}(PO_3H_2)_2\text{-}bpy)]Br_2$ is based on the reported literature procedure. [505] $[Ru(bpy)_2(4,4'\text{-}(PO_3H_2)_2\text{-}bpy)]Br_2$ (ppm, in CD_3OD, 399.794 MHz, *J*-values in Hz) 8.91 (d, 2H, *J* = 13); 8.73 (d, 4H, *J* = 8); 8.15 (t, 4H, *J* = 8); 8.01 (m, 2H); 7.82 (m, 4H); 7.75 (m, 2H); 7.51 (m, 4H).

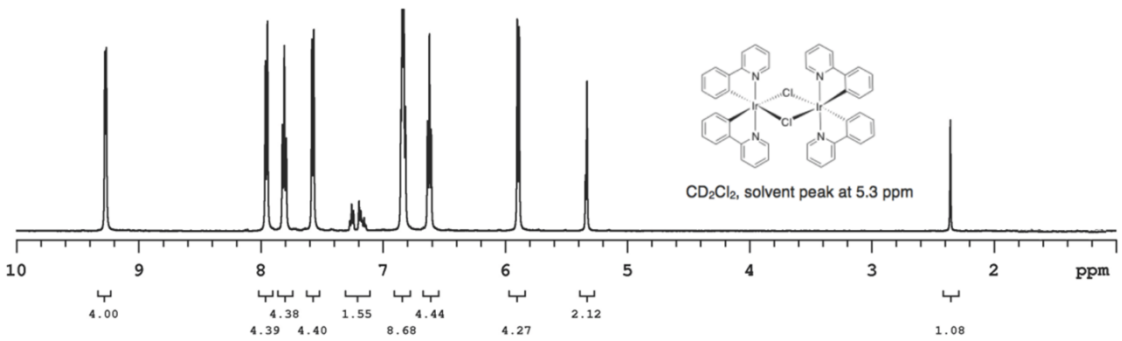
CD2Cl2, solvent peak at 5.3 ppm
10 9 8 7 6 5 4 3 2 ppm
4.00 4.38 4.39 4.40 1.55 8.68 4.44 4.27 2.12 1.08

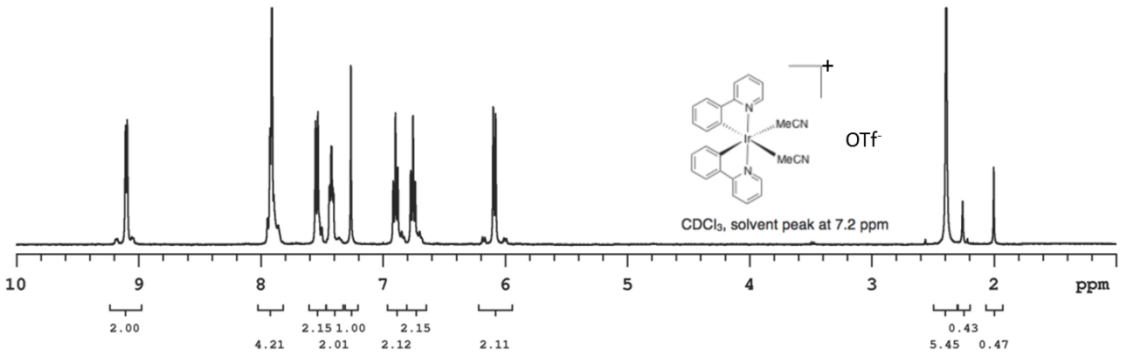
MeCN
MeCN
OTf-
CDCl3, solvent peak at 7.2 ppm
10 9 8 7 6 5 4 3 2 ppm
2.00 4.21 2.15 2.01 1.00 2.12 2.15 2.11 0.43 5.45 0.47

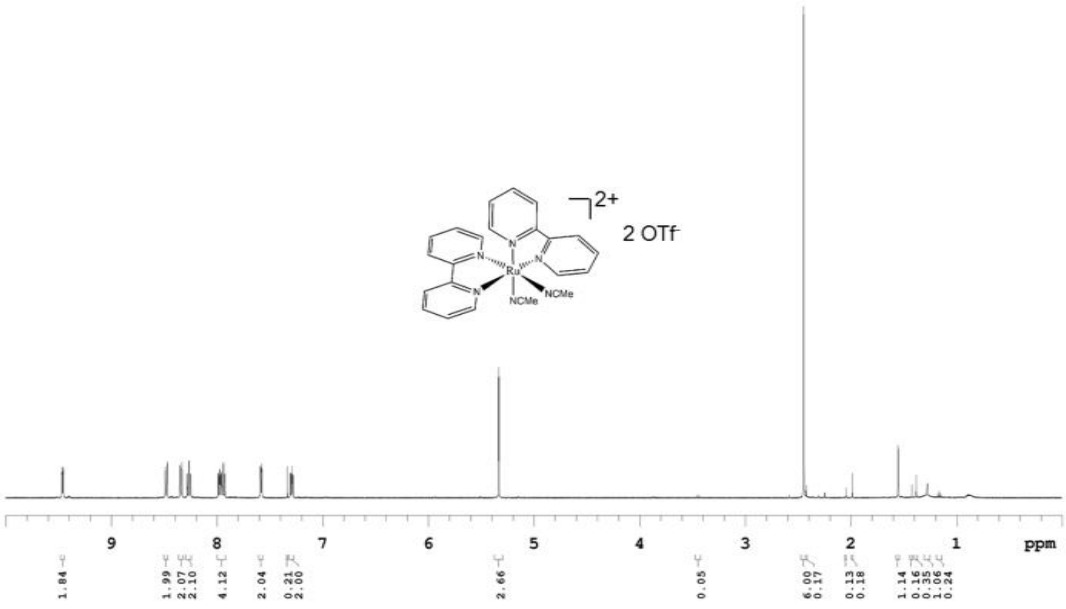
2+
2 OTf-
NCMe
NCMe
9 8 7 6 5 4 3 2 1 ppm
1.84 1.99 2.07 2.10 4.12 2.04 0.21 2.00 2.66 0.05 6.00 0.17 0.13 0.18 1.14 0.16 0.35 1.16 0.24

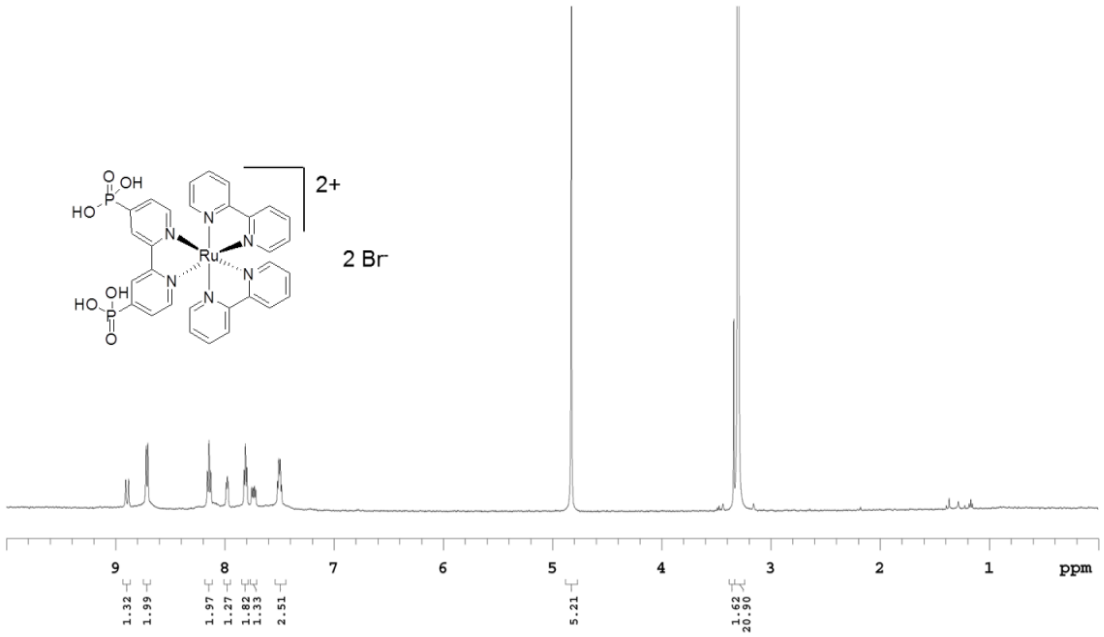

Figure 7.13 NMR spectra of the Ir and Ru complexes.

7.4.5 Instrumentation

Electrochemical studies were done using Solartron SI 1287 Electrochemical Interface controlled by CorrWare for Windows Version 2-3d software. XPS measurements were performed on a Kratos Axis 165 instrument. The base pressure in the sample analytical chamber was lower than 1×10^{-9} torr. A monochromatized Al Kα source (hv = 1486.6 eV) was used at 12 mA and 14 kV. Survey scans spanned from a binding energy of 1100 to 0 eV and collected with an analyzer pass energy of 160 eV in steps of 0.3 eV. ICP–MS analyses were performed with Perkin Elmer Elan 6000. The SC-$[(phen)Ru(bpy)_2]^{2+}$ and

SC-[(phen)Ir(ppy)$_2$]$^+$ electrodes were dissolved in aqua regia solutions for 24 h to etch the SC layer in order to assess the surface coverage of Ru- or Ir- chromophores. UV–vis spectra were acquired using Cary 400 UV–vis spectroscopy. To acquire UV–vis spectra on a SC surface, *n* pieces of SC-[(phen)Ru(bpy)$_2$]$^{2+}$ or SC-[(phen)Ir(ppy)$_2$]$^+$ were bonded together to enhance the signal (n = 5 for ITO and 1 for TiO_2). The spectra shown were the acquired spectra absorbance divided by *n*, with the ITO or TiO_2 absorbance deducted. TEM was done using JOEL JEM-ARM200CF S/TEM. The samples for TEM were prepared by sonication of the electrode in anhydrous ethanol, drop coated onto an ultrathin carbon film grid (Ted Pella. Inc.), and the grid dried under air. SEM was performed with a Hitachi S-4800 instrument. The ^{1}H NMR spectra were acquired using both 400 MHz and 500 MHz Varian Inova, and Varian DD2 M2 400 MHz NMR spectrometers. The chemical shifts are reported in ppm relatives to TMS with the solvent as the internal standard. Abbreviations used in reporting of NMR data are s (singlet), d (doublet), t (triplet), dt (doublet of triplet) and m (multiplet).

Chapter 8 Conclusions and Final Remarks

This dissertation describes the use of a platinum counter-electrode deposition method to prepare Pt overlayer Ni nanopillars extended structure catalysts for the ORR, a straightforward method to synthesize highly active WOC in acid and base, and a new method to form covalently-bound chromophores on SC surfaces. The catalysts were characterized fully by CV, SEM, TEM, XPS, ICP–MS, and XRD. The mechanisms for different catalysts towards electrochemical catalytic reactions were investigated, and attempts to correlate the electrocatalytic activity with the structure of the catalyst were made. In addition, their catalytic activities were compared with the state-of-art catalysts in the literature.

Chapter 2 and 3 show that we can control the Pt counter-electrode deposition to deposit a thin overlayer of Pt on Ni_{GLAD} nanopillars with desired loadings; the resulting Ni_{GLAD}{Pt}/GC electrodes were active towards the ORR in both acid and base. Under alkaline conditions, the ORR onset overpotential for the Ni_{GLAD}{Pt}/GC electrode was 30 mV less than for the {Pt}/GC electrode, and the mass activity was 2–3 times higher than that of the {Pt}/GC electrode at 0.85 V_{RHE}. Moreover, the Ni_{GLAD}{Pt}/GC electrode was more durable than the {Pt}/GC electrode with respect to a long-term potentiostatic ORR test. Under acidic conditions, dealloying was proven to be an effective method to increase the ORR activity of the Ni_{GLAD}{Pt}/GC electrode. By controlling the Pt deposition time, we are able to control the Pt layer thickness, thus tune the ORR activity of the

Ni_{GLAD}{Pt}/GC electrode. The most active catalyst was prepared with a bulk atomic composition of $Pt_{0.09}Ni_{0.91}$ with a Pt deposition time of 1500 s. The ORR onset overpotential for the dealloyed Ni_{GLAD}{Pt-1500}/GC electrode was 150 mV lower than that for the {Pt-1500}/GC electrode, and the mass activity was 30 times higher at 0.9 V_{RHE}. The 4-electron reduction path was identified, indicating the desirable full reduction of oxygen to water. XPS on the Ni_{GLAD}{Pt-1500}/GC and {Pt-1500}/GC electrodes suggested the existence of an electronic interaction between the substrate Ni and the Pt deposit.

There is room for optimization of our catalysts. Modifications of the parameters for GLAD like deposition time, oblique angle, and target rotation rate would affect the morphology of the Ni substrates. The spacing of the pillars (determined by the oblique angle), the shape of the pillar (determined by rotation rate), and the length of the pillar (determined by deposition time) would affect the mass transport of the reactants to the catalyst surface. Other transition metals, such as Cu, Co, and Fe, also could be used as the deposition source to form extended structured substrates by GLAD. Moreover, the effect of deposition current during galvanostatic Pt CE deposition on the morphology and activity needs to be investigated. We utilized a relatively low current in order to get more uniform Pt coverage at the substrate. Higher current may lead to higher Pt dissolution and deposition rate and higher hydrogen evolution rate at the working electrode; this may form a higher portion of under-coordinated surface Pt atoms, affecting the ORR activity.

Since the extended structure of ORR catalysts is attractive for their stability compared with nanoparticle catalysts, it would be interesting to incorporate the Ni_{GLAD}{Pt} catalysts into a fuel cell by depositing Ni_{GLAD} onto a membrane first, followed by Pt CE deposition. Finally, Ni_{GLAD}{Pt} catalysts are promising candidates towards other electrocatalytic reactions, like alcohol oxidation, water oxidation, and hydrogen evolution.

A straightforward synthetic method is developed and applied successfully to prepare active water oxidation catalysts in acidic (Chapter 4 and 5) and alkaline (Chapter 6) solutions. Both $Ir_{0.89}Ni_{0.11}$ HO-np and $Ir_{0.89}Cu_{0.11}$ HO-np were among the most active catalysts in the literature, with the onset overpotential as low as 0.19 V in acid. Both catalysts were stable towards long-term water oxidation, and the enhanced water oxidation activity was not caused just by the increase in the number of electrochemically active sites. XPS revealed higher electron density at the Ir site in both $Ir_{0.89}Ni_{0.11}$ and $Ir_{0.89}Cu_{0.11}$ HO-np relative to that in Ir HO-np, and we propose that the presence of Ir–O–M–O–Ir (M = Ni or Cu) in the HO-np is responsible for the enhanced activity and stability. The Tafel slopes at low overpotentials for $Ir_{0.89}Ni_{0.11}$, $Ir_{0.89}Cu_{0.11}$, and Ir HO-np were all around 60 mV dec^{-1}, indicating same mechanistic pathway for the WOR.

The synthesis and activity of $Ni_{0.75}Fe_{0.25}$ HO-np is described in Chapter 6; it is among the most active and stable WOC under alkaline conditions. Structural

characterization showed that $Ni_{0.75}Fe_{0.25}$ HO-np predominantly existed as double layered hydroxides. CF and Ni foam were used as supports, and the enhanced activity was caused by the increase in the Ni utilization when supported on Ni foam. Based on CV and XPS investigations, we proposed that the presence of Fe decreased the electron density at the Ni sites, which enhanced the rate of reaction between surface Ni–O or Ni–OH and the dissolved hydroxide species in the rate-determining step.

This new nanoparticle synthetic method opens up a direction for a cost-effective and facile scalable production of catalysts. We could envisage that more binary, tertiary, or quaternary hydrous oxide nanoparticle combinations will be discovered as efficient water oxidation catalysts and as catalysts for other electrochemical catalytic processes. Further investigation of the synthetic process could involve the effect of surfactants, ionic species, and temperature to the morphology and nanoparticle growth process. A deep understanding of the growth process would require the characterization of the synthetic solution using UV–vis, SEM, TEM, EDX, XRD, and other methods. Moreover, mechanistic investigations on active catalysts are needed to understand the origin of the activity enhancement and the WOR pathway. For example, measurements like in situ XPS, SERS, and IR are crucial in acquiring information regarding active intermediate species in water oxidation reactions. ^{18}O labeling coupled with online DEMS would reveal whether the mechanism went through the direct coupling pathway or the acid–base pathway. In addition, different substrates, like Ti and TiO_2 foam in acid and stainless steel

in base, are desirable to be applied to the water electrolyzers since carbon based materials undergo corrosion at high potentials. Also, it would be interesting to unveil the mechanism of the catalysts' degradation under a long-term study. Finally, the assembly of water electrolyzers using theses catalysts is one of the ultimate goals of these studies. These water oxidation electrocatalysts also can be applied in reversible fuel cells and in photoanodes of photoelectrochemical cells.

Chapter 7 describes a reliable method to form photoelectrodes by covalent grafting of 1,10-phenanthroline (phen) at C5 to ITO and TiO_2 surfaces via diazonium electroreduction and subsequently exposing them to Ru- and Ir- organometallic precursors to form corresponding chromophores. Surface characterizations confirmed that the chromophores SC-$[(phen)Ru(bpy)_2]^{2+}$ and SC-$[(phen)Ir(ppy)_2]^{+}$ formed in near quantitative yields by these reactions. The resulting photoanodes were active towards the oxidation of triethylamine in basic conditions and of hydroquinone in neutral ones. Photocurrent stability was investigated, with IPCE calculated. Under neutral conditions, better photocurrent stability was observed using the photoanodes with C5–O^{surf} covalently-bound chromophores compared those with the phosphonic acid anchors. Under strong alkaline conditions, the photoanodes with C5–O^{surf} covalently-bonded chromophores exhibited better IPCE and good photocurrent stability, while the phosphonic acid anchors hydrolyzed.

This novel deposition method opens up the possibility to fabricate a stable chromophore–SC assembly under strong alkaline conditions, expanding the application of the DSPECs to the alkaline environment. Though the IPCE is moderate compared with the literature value, various methods could be applied to improve it. Different electrochemical diazonium deposition methods (like potentiostatic, galvanostatic, etc.) could be applied to reach an optimum loading of the ligand on the surface. Other ligands could be used in the chromophore to tune the redox potential and absorption coefficient of the chromophores. Moreover, detailed mechanistic studies on the electron injection properties of the C5–O^{surf} covalently-bound chromophores and the back electron transfer process is needed to guide the selection of the optimum anchoring groups, ligands, and chromophores. The photocurrent degradation mechanism of the C5–O^{surf} covalently-bound chromophores needs to be identified so that protective methods could be applied to suppress the degradation. Finally, photoelectrodes fabricated using this method can be paired with catalysts to carry out photoelectrochemical catalytic reactions, including the WOR, carbon dioxide reduction, hydrogen evolution, alcohol oxidation, etc.; these, ultimately, can be integrated into the DSPECs.

Altogether, this thesis develops catalysts and electrodes that can be applied to energy conversion devices, including fuel cells, water electrolyzers, and dye-sensitized photoelectrochemical cells. With these approaches, we believe that the future of the

human species is bright, and that a world wholly supported by renewable and sustainable energy will be possible.

Bibliography

(1) Das, V.; Padmanaban, S.; Venkitusamy, K.; Selvamuthukumaran, R.; Blaabjerg, F.; Siano, P. *Renew. Sust. Energ. Rev.* **2017**, *73*, 10.

(2) Mekhilef, S.; Saidur, R.; Safari, A. *Renew. Sust. Energ. Rev.* **2012**, *16*, 981.

(3) Sharaf, O. Z.; Orhan, M. F. *Renew. Sust. Energ. Rev.* **2014**, *32*, 810.

(4) Bacon, F. T. *Electrochim. Acta* **1969**, *14*, 569.

(5) Choi, C. H.; Yu, S.; Han, I.; Kho, B.; Kang, D.; Lee, H. Y.; Seo, M.; Kong, J.; Kim, G.; Ahn, J. *Int. J. Hydrog. Energy* **2016**, *41*, 3591.

(6) Han, I.; Kho, B.; Cho, S. *J. Power Sources* **2016**, *304*, 244.

(7) Alaswad, A.; Baroutaji, A.; Achour, H.; Carton, J.; Al Makky, A.; Olabi, A. *Int. J. Hydrog. Energy* **2016**, *41*, 16499.

(8) Zhang, H.; Shen, P. K. *Chem. Rev.* **2012**, *112*, 2780.

(9) Luo, Y. *Handbook of bond dissociation energies in organic compounds*; CRC press, 2002.

(10) Breitwieser, M.; Klingele, M.; Vierrath, S.; Zengerle, R.; Thiele, S. *Adv. Energy Mater.* **2018**, *8*, 1701257.

(11) Brouzgou, A.; Song, S. Q.; Tsiakaras, P. *Appl. Catal., B* **2012**, *127*, 371.

(12) Igarashi, H.; Fujino, T.; Zhu, Y.; Uchida, H.; Watanabe, M. *Phys. Chem. Chem. Phys.* **2001**, *3*, 306.

(13) Roth, C.; Benker, N.; Buhrmester, T.; Mazurek, M.; Loster, M.; Fuess, H.; Koningsberger, D. C.; Ramaker, D. E. *J. Am. Chem. Soc.* **2005**, *127*, 14607.

(14) Shi, G.; Yano, H.; Tryk, D. A.; Iiyama, A.; Uchida, H. *ACS Catal.* **2016**, *7*, 267.

(15) Waszczuk, P.; Lu, G.; Wieckowski, A.; Lu, C.; Rice, C.; Masel, R. *Electrochim. Acta* **2002**, *47*, 3637.

(16) Sammes, N.; Bove, R.; Stahl, K. *Curr. Opin. Solid State Mater. Sci.* **2004**, *8*, 372.

(17) Elmer, T.; Worall, M.; Wu, S.; Riffat, S. B. *Renew. Sust. Energ. Rev.* **2015**, *42*, 913.

(18) Dodds, P. E.; Staffell, I.; Hawkes, A. D.; Li, F.; Grünewald, P.; McDowall, W.; Ekins, P. *Int. J. Hydrog. Energy* **2015**, *40*, 2065.

(19) Sulaiman, N.; Hannan, M.; Mohamed, A.; Majlan, E.; Daud, W. W. *Renew. Sust. Energ. Rev.* **2015**, *52*,

802.

(20) Das, H. S.; Tan, C. W.; Yatim, A. *Renew. Sust. Energ. Rev.* **2017**, *76*, 268.

(21) Dubau, L.; Castanheira, L.; Maillard, F.; Chatenet, M.; Lottin, O.; Maranzana, G.; Dillet, J.; Lamibrac, A.; Perrin, J. C.; Moukheiber, E. *Wiley Interdiscip. Rev.: Energy Environ.* **2014**, *3*, 540.

(22) Zhou, X.; Qiao, J.; Yang, L.; Zhang, J. *Adv. Energy Mater.* **2014**, *4*, 1301523.

(23) Daud, W.; Rosli, R.; Majlan, E.; Hamid, S.; Mohamed, R. *Renew. Energ.* **2017**, *113*, 620.

(24) Christensen, P. A.; Hamnett, A.; Linares Moya, D. *Phys. Chem. Chem. Phys.* **2011**, *13*, 5206.

(25) Yu, E. H.; Wang, X.; Krewer, U.; Li, L.; Scott, K. *Energy Environ. Sci.* **2012**, *5*, 5668.

(26) Wang, Y.; Li, L.; Hu, L.; Zhuang, L.; Lu, J.; Xu, B. *Electrochem. Commun.* **2003**, *5*, 662.

(27) Gülzow, E.; Schulze, M. *J. Power Sources* **2004**, *127*, 243.

(28) Varcoe, J. R.; Atanassov, P.; Dekel, D. R.; Herring, A. M.; Hickner, M. A.; Kohl, P. A.; Kucernak, A. R.; Mustain, W. E.; Nijmeijer, K.; Scott, K.; Xu, T.; Zhuang, L. *Energy Environ. Sci.* **2014**, *7*, 3135.

(29) Dekel, D. R. *J. Power Sources* **2018**, *375*, 158.

(30) Cheng, J.; He, G.; Zhang, F. *Int. J. Hydrog. Energy* **2015**, *40*, 7348.

(31) Dekel, D. R.; Amar, M.; Willdorf, S.; Kosa, M.; Dhara, S.; Diesendruck, C. E. *Chem. Mater.* **2017**, *29*, 4425.

(32) Carrette, L.; Friedrich, K. A.; Stimming, U. *ChemPhysChem* **2000**, *1*, 162.

(33) Shri Prakash, B.; Senthil Kumar, S.; Aruna, S. T. *Renew. Sust. Energ. Rev.* **2014**, *36*, 149.

(34) Mahato, N.; Banerjee, A.; Gupta, A.; Omar, S.; Balani, K. *Prog. Mater Sci.* **2015**, *72*, 141.

(35) Jun, A.; Kim, J.; Shin, J.; Kim, G. *ChemElectroChem* **2016**, *3*, 511.

(36) Galea, N. M.; Knapp, D.; Ziegler, T. *J. Catal.* **2007**, *247*, 20.

(37) Walters, K. M.; Dean, A. M.; Zhu, H.; Kee, R. J. *J. Power Sources* **2003**, *123*, 182.

(38) Khani, L.; Mahmoudi, S. M. S.; Chitsaz, A.; Rosen, M. A. *Energy* **2016**, *94*, 64.

(39) Wang, Y.; Leung, D. Y. C.; Xuan, J.; Wang, H. *Renew. Sust. Energ. Rev.* **2017**, *75*, 775.

(40) Zheng, Y.; Wang, J.; Yu, B.; Zhang, W.; Chen, J.; Qiao, J.; Zhang, J. *Chem. Soc. Rev.* **2017**, *46*, 1427.

(41) Chen, L.; Yuh, C. *Acta Metall. Sin. Engl. Lett.* **2017**, *30*, 289.

(42) Kirubakaran, A.; Jain, S.; Nema, R. *Renew. Sust. Energ. Rev.* **2009**, *13*, 2430.

(43) Czelej, K.; Cwieka, K.; Colmenares, J. C.; Kurzydlowski, K. J. *Appl. Catal., B* **2018**, *222*, 73.

(44) Antolini, E. *Appl. Energy* **2011**, *88*, 4274.

(45) Fergus, J. W. In *Engineering Solutions for Sustainability*; Springer: 2015, p 235.

(46) Barelli, L.; Bidini, G.; Campanari, S.; Discepoli, G.; Spinelli, M. *J. Power Sources* **2016**, *320*, 332.

(47) Chiodo, V.; Zafarana, G.; Maisano, S.; Freni, S.; Galvagno, A.; Urbani, F. *Int. J. Hydrog. Energy* **2016**, *41*, 18815.

(48) Hill, R.; Scott, S.; Butler, D.; Sit, S. P.; Burt, D.; Narayanan, R.; Cole, T.; Li, C.; Lightbown, V.; Zhou, Z. J. *Int. J. Greenhouse Gas Control* **2015**, *41*, 276.

(49) Huang, C.; Pan, Y.; Wang, Y.; Su, G.; Chen, J. *Energy Convers. Manage.* **2016**, *121*, 186.

(50) He, Q.; Shyam, B.; Nishijima, M.; Ramaker, D.; Mukerjee, S. *J. Phys. Chem. C* **2013**, *117*, 4877.

(51) Eapen, D. E.; Suseendiran, S. R.; Rengaswamy, R. In *Compendium of Hydrogen Energy*; Basile, A., Veziroğlu, T. N., Eds.; Woodhead Publishing: Oxford, 2016, p 57.

(52) Kanninen, P.; Borghei, M.; Sorsa, O.; Pohjalainen, E.; Kauppinen, E. I.; Ruiz, V.; Kallio, T. *Appl. Catal., B* **2014**, *156*, 341.

(53) Zakaria, Z.; Kamarudin, S. K.; Timmiati, S. *Appl. Energy* **2016**, *163*, 334.

(54) Akhairi, M. A. F.; Kamarudin, S. K. *Int. J. Hydrog. Energy* **2016**, *41*, 4214.

(55) Mota-Lima, A.; Silva, D. R.; Gasparotto, L. H.; Gonzalez, E. R. *Electrochim. Acta* **2017**, *235*, 135.

(56) Li, S.; Wang, L.; Chu, J.; Zhu, H.; Chen, Y.; Liu, Y. *Int. J. Hydrog. Energy* **2016**, *41*, 8583.

(57) Ong, B. C.; Kamarudin, S. K.; Basri, S. *Int. J. Hydrog. Energy* **2017**, *42*, 10142.

(58) Kamarudin, S. K.; Achmad, F.; Daud, W. R. W. *Int. J. Hydrog. Energy* **2009**, *34*, 6902.

(59) Tokarz, W.; Lota, G.; Frackowiak, E.; Czerwiński, A.; Piela, P. *Electrochim. Acta* **2013**, *98*, 94.

(60) Neto, A. O.; Dias, R. R.; Tusi, M. M.; Linardi, M.; Spinacé, E. V. *J. Power Sources* **2007**, *166*, 87.

(61) Wang, Y.; Zang, J.; Dong, L.; Pan, H.; Yuan, Y.; Wang, Y. *Electrochim. Acta* **2013**, *113*, 583.

(62) Kim, M.; Fang, B.; Chaudhari, N. K.; Song, M.; Bae, T.; Yu, J. *Electrochim. Acta* **2010**, *55*, 4543.

(63) Paul, B.; Andrews, J. *Renew. Sust. Energ. Rev.* **2017**, *79*, 585.

(64) Yao, W.; Yang, J.; Wang, J.; Nuli, Y. *Electrochem. Commun.* **2007**, *9*, 1029.

(65) Mitlitsky, F.; Myers, B.; Weisberg, A. H. *Energy Fuels* **1998**, *12*, 56.

(66) Shao, M.; Chang, Q.; Dodelet, J.-P.; Chenitz, R. *Chem. Rev.* **2016**, *116*, 3594.

(67) Nie, Y.; Li, L.; Wei, Z. *Chem. Soc. Rev.* **2015**, *44*, 2168.

(68) Yeager, E. *J. Mol. Catal.* **1986**, *38*, 5.

(69) Wroblowa, H. S.; Razumney, G. *J. Electroanal. Chem. Interfacial Electrochem.* **1976**, *69*, 195.

(70) Chandesris, M.; Vincent, R.; Guetaz, L.; Roch, J.; Thoby, D.; Quinaud, M. *Int. J. Hydrog. Energy* **2017**, *42*, 8139.

(71) Félix-Navarro, R.; Beltrán-Gastélum, M.; Reynoso-Soto, E.; Paraguay-Delgado, F.; Alonso-Nuñez, G.; Flores-Hernández, J. *Renew. Energ.* **2016**, *87*, 31.

(72) Vej-Hansen, U. G.; Escudero-Escribano, M.; Velázquez-Palenzuela, A.; Malacrida, P.; Rossmeisl, J.; Stephens, I.; Chorkendorff, I.; Schiøtz, J. *Electrocatalysis* **2017**, *8*, 594.

(73) Beermann, V.; Gocyla, M.; Kühl, S.; Padgett, E.; Schmies, H.; Goerlin, M.; Erini, N.; Shviro, M.; Heggen, M.; Dunin-Borkowski, R. E.; Muller, D. A.; Strasser, P. *J. Am. Chem. Soc.* **2017**, *139*, 16536.

(74) Kuttiyiel, K. A.; Sasaki, K.; Park, G.-G.; Vukmirovic, M. B.; Wu, L.; Zhu, Y.; Chen, J. G.; Adzic, R. R. *Chem. Commun.* **2017**, *53*, 1660.

(75) Miyatake, K.; Shimizu, Y. *ACS Omega* **2017**, *2*, 2085.

(76) Katsounaros, I.; Cherevko, S.; Zeradjanin, A. R.; Mayrhofer, K. J. J. *Angew. Chem. Int. Ed.* **2014**, *53*, 102.

(77) Keith, J. A.; Jacob, T. *Angew. Chem. Int. Ed.* **2010**, *49*, 9521.

(78) Keith, J. A.; Jerkiewicz, G.; Jacob, T. *ChemPhysChem* **2010**, *11*, 2779.

(79) Hyman, M. P.; Medlin, J. W. *J. Phys. Chem. B* **2005**, *109*, 6304.

(80) Nørskov, J. K.; Rossmeisl, J.; Logadottir, A.; Lindqvist, L.; Kitchin, J. R.; Bligaard, T.; Jónsson, H. *J. Phys. Chem. B* **2004**, *108*, 17886.

(81) Stamenkovic, V.; Mun, B. S.; Mayrhofer, K. J.; Ross, P. N.; Markovic, N. M.; Rossmeisl, J.; Greeley, J.; Nørskov, J. K. *Angew. Chem.* **2006**, *118*, 2963.

(82) Hammer, B.; Nørskov, J. K. In *Advances in Catalysis*; Academic Press: 2000; Vol. 45, p 71.

(83) Hammer, B.; Norskov, J. K. *Nature* **1995**, *376*, 238.

(84) Xin, H.; Vojvodic, A.; Voss, J.; Nørskov, J. K.; Abild-Pedersen, F. *Phys. Rev. B* **2014**, *89*, 115114.

(85) James, T. L. *J. Chem. Educ.* **1971**, *48*, 712.

(86) Weinert, M.; Watson, R. *Phys. Rev. B* **1995**, *51*, 17168.

(87) Pueyo Bellafont, N.; Bagus, P. S.; Illas, F. *J. Chem. Phys.* **2015**, *142*, 214102.

(88) Hu, Y.; Wu, P.; Yin, Y.; Zhang, H.; Cai, C. *Appl. Catal., B* **2012**, *111*, 208.

(89) Fu, X.; Liang, Y.; Chen, S.; Lin, J.; Liao, D. *Catal. Commun.* **2009**, *10*, 1893.

(90) Park, K.; Choi, J.; Kwon, B.; Lee, S.; Sung, Y.; Ha, H.; Hong, S.; Kim, H.; Wieckowski, A. *J. Phys. Chem. B* **2002**, *106*, 1869.

(91) Kim, D. B.; Chun, H.; Lee, Y. K.; Kwon, H.; Lee, H. *Int. J. Hydrog. Energy* **2010**, *35*, 313.

(92) Stamenkovic, V. R.; Fowler, B.; Mun, B. S.; Wang, G.; Ross, P. N.; Lucas, C. A.; Marković, N. M. *Science* **2007**, *315*, 493.

(93) Kitchin, J. R.; Nørskov, J. K.; Barteau, M. A.; Chen, J. G. *Phys. Rev. Lett.* **2004**, *93*, 156801.

(94) Adzic, R. R.; Zhang, J.; Sasaki, K.; Vukmirovic, M. B.; Shao, M.; Wang, J. X.; Nilekar, A. U.; Mavrikakis, M.; Valerio, J. A.; Uribe, F. *Top. Catal.* **2007**, *46*, 249.

(95) Nilekar, A. U.; Mavrikakis, M. *Surf. Sci.* **2008**, *602*, L89.

(96) Toyoda, E.; Jinnouchi, R.; Hatanaka, T.; Morimoto, Y.; Mitsuhara, K.; Visikovskiy, A.; Kido, Y. *J. Phys. Chem. C* **2011**, *115*, 21236.

(97) Zhou, W. P.; Lewera, A.; Larsen, R.; Masel, R. I.; Bagus, P. S.; Wieckowski, A. *J. Phys. Chem. B* **2006**, *110*, 13393.

(98) Kibler, L. A.; El‐Aziz, A. M.; Hoyer, R.; Kolb, D. M. *Angew. Chem. Int. Ed.* **2005**, *44*, 2080.

(99) Gorzkowski, M. T.; Lewera, A. *J. Phys. Chem. C* **2015**, *119*, 18389.

(100) Hyman, M. P.; Medlin, J. W. *J. Phys. Chem. C* **2007**, *111*, 17052.

(101) Hyman, M. P.; Loveless, B. T.; Medlin, J. W. *Surf. Sci.* **2007**, *601*, 5382.

(102) Watanabe, M.; Motoo, S. *J. Electroanal. Chem. Interfacial Electrochem.* **1975**, *60*, 275.

(103) Lu, C.; Rice, C.; Masel, R.; Babu, P.; Waszczuk, P.; Kim, H.; Oldfield, E.; Wieckowski, A. *J. Phys. Chem. B* **2002**, *106*, 9581.

(104) Zhang, J.; Mo, Y.; Vukmirovic, M. B.; Klie, R.; Sasaki, K.; Adzic, R. R. *J. Phys. Chem. B* **2004**, *108*, 10955.

(105) Yang, L.; Vukmirovic, M. B.; Su, D.; Sasaki, K.; Herron, J. A.; Mavrikakis, M.; Liao, S.; Adzic, R. R. *J. Phys. Chem. C* **2013**, *117*, 1748.

(106) Zhang, Y.; Ma, C.; Zhu, Y.; Si, R.; Cai, Y.; Wang, J. X.; Adzic, R. R. *Catal. Today* **2013**, *202*, 50.

(107) Karan, H. I.; Sasaki, K.; Kuttiyiel, K.; Farberow, C. A.; Mavrikakis, M.; Adzic, R. R. *ACS Catal.* **2012**, *2*, 817.

(108) Ghosh, T.; Vukmirovic, M. B.; DiSalvo, F. J.; Adzic, R. R. *J. Am. Chem. Soc.* **2010**, *132*, 906.

(109) Wang, J. X.; Inada, H.; Wu, L.; Zhu, Y.; Choi, Y.; Liu, P.; Zhou, W.-P.; Adzic, R. R. *J. Am. Chem. Soc.* **2009**, *131*, 17298.

(110) Cai, B.; Hübner, R.; Sasaki, K.; Zhang, Y.; Su, D.; Ziegler, C.; Vukmirovic, M. B.; Rellinghaus, B.; Adzic, R. R.; Eychmüller, A. *Angew. Chem. Int. Ed.* **2017**, *57*, 2963.

(111) Chen, G.; Kuttiyiel, K. A.; Su, D.; Li, M.; Wang, C.-H.; Buceta, D.; Du, C.; Gao, Y.; Yin, G.; Sasaki, K.; Vukmirovic, M. B.; Adzic, R. R. *Chem. Mater.* **2016**, *28*, 5274.

(112) Vukmirovic, M. B.; Zhang, J.; Sasaki, K.; Nilekar, A. U.; Uribe, F.; Mavrikakis, M.; Adzic, R. R. *Electrochim. Acta* **2007**, *52*, 2257.

(113) Zhang, J.; Vukmirovic, M. B.; Xu, Y.; Mavrikakis, M.; Adzic, R. R. *Angew. Chem. Int. Ed.* **2005**, *44*, 2132.

(114) Brankovic, S. R.; Wang, J. X.; Adžić, R. R. *Surf. Sci.* **2001**, *474*, L173.

(115) Stamenkovic, V. R.; Mun, B. S.; Arenz, M.; Mayrhofer, K. J. J.; Lucas, C. A.; Wang, G.; Ross, P. N.; Markovic, N. M. *Nat. Mater.* **2007**, *6*, 241.

(116) Stamenkovic, V. R.; Mun, B. S.; Mayrhofer, K. J. J.; Ross, P. N.; Markovic, N. M. *J. Am. Chem. Soc.* **2006**, *128*, 8813.

(117) Mani, P.; Srivastava, R.; Strasser, P. *J. Power Sources* **2011**, *196*, 666.

(118) Hasché, F.; Oezaslan, M.; Strasser, P. *J. Electrochem. Soc.* **2011**, *159*, B24.

(119) Rudi, S.; Tuaev, X.; Strasser, P. *Electrocatalysis* **2012**, *3*, 265.

(120) Beermann, V.; Gocyla, M.; Willinger, E.; Rudi, S.; Heggen, M.; Dunin Borkowski, R. E.; Willinger, M.; Strasser, P. *Nano Lett.* **2016**, *16*, 1719.

(121) Cui, C.; Gan, L.; Heggen, M.; Rudi, S.; Strasser, P. *Nat. Mater.* **2013**, *12*, 765.

(122) Choi, S. I.; Xie, S.; Shao, M.; Odell, J. H.; Lu, N.; Peng, H. C.; Protsailo, L.; Guerrero, S.; Park, J.; Xia, X. *Nano Lett.* **2013**, *13*, 3420.

(123) Huang, X.; Zhao, Z.; Cao, L.; Chen, Y.; Zhu, E.; Lin, Z.; Li, M.; Yan, A.; Zettl, A.; Wang, Y. M. *Science* **2015**, *348*, 1230.

(124) Fortunelli, A.; Goddard III, W. A.; Sementa, L.; Barcaro, G.; Negreiros, F. R.; Jaramillo-Botero, A. *Chem. Sci.* **2015**, *6*, 3915.

(125) Li, M.; Zhao, Z.; Cheng, T.; Fortunelli, A.; Chen, C.-Y.; Yu, R.; Zhang, Q.; Gu, L.; Merinov, B. V.; Lin, Z.; Zhu, E.; Yu, T.; Jia, Q.; Guo, J.; Zhang, L.; Goddard, W. A.; Huang, Y.; Duan, X. *Science* **2016**, *354*, 1414.

(126) Turner, J. A. *Science* **2004**, *305*, 972.

(127) Seyitoglu, S.; Dincer, I.; Kilicarslan, A. *Int. J. Hydrog. Energy* **2017**, *42*, 2592.

(128) Xiang, D.; Xiang, J.; Sun, Z.; Cao, Y. *Energy* **2017**, *140*, 78.

(129) Nikolaidis, P.; Poullikkas, A. *Renew. Sust. Energ. Rev.* **2017**, *67*, 597.

(130) Pletcher, D.; Li, X. *Int. J. Hydrog. Energy* **2011**, *36*, 15089.

(131) Ursua, A.; Gandia, L. M.; Sanchis, P. *Proc. IEEE* **2012**, *100*, 410.

(132) Zhang, J. *PEM fuel cell electrocatalysts and catalyst layers: fundamentals and applications*; Springer Science & Business Media, 2008.

(133) Millet, P.; Ngameni, R.; Grigoriev, S. A.; Mbemba, N.; Brisset, F.; Ranjbari, A.; Etiévant, C. *Int. J. Hydrog. Energy* **2010**, *35*, 5043.

(134) Zeng, K.; Zhang, D. *Prog. Energy Combust. Sci.* **2010**, *36*, 307.

(135) Santos, D. M.; Sequeira, C. A.; Figueiredo, J. L. *Quim. Nova* **2013**, *36*, 1176.

(136) Kreuter, W.; Hofmann, H. *Int. J. Hydrog. Energy* **1998**, *23*, 661.

(137) Rieger, P. *Englewood Cliffs, NJ* **1987**, 291.

(138) LeRoy, R. *Int. J. Hydrog. Energy* **1983**, *8*, 401.

(139) Marini, S.; Salvi, P.; Nelli, P.; Pesenti, R.; Villa, M.; Berrettoni, M.; Zangari, G.; Kiros, Y. *Electrochim. Acta* **2012**, *82*, 384.

(140) Rosa, V.; Santos, M.; Da Silva, E. *Int. J. Hydrog. Energy* **1995**, *20*, 697.

(141) Hickner, M. A.; Ghassemi, H.; Kim, Y. S.; Einsla, B. R.; McGrath, J. E. *Chem. Rev.* **2004**, *104*, 4587.

(142) Bockris, J.; Conway, B.; Yeager, E. *Comprehensive treatise of electrochemistry*; Springer, 1982.

(143) Pletcher, D.; Walsh, F. C. *Industrial electrochemistry*; Springer Science & Business Media, 2012.

(144) Götz, M.; Lefebvre, J.; Mörs, F.; Koch, A. M.; Graf, F.; Bajohr, S.; Reimert, R.; Kolb, T. *Renew. Energ.* **2016**, *85*, 1371.

(145) Hosseini, S. E.; Wahid, M. A. *Renew. Sust. Energ. Rev.* **2016**, *57*, 850.

(146) Carmo, M.; Fritz, D. L.; Mergel, J.; Stolten, D. *Int. J. Hydrog. Energy* **2013**, *38*, 4901.

(147) Wendt, H.; Imarisio, G. *J. Appl. Electrochem.* **1988**, *18*, 1.

(148) Rashid, M. M.; Al Mesfer, M. K.; Naseem, H.; Danish, M. *Int. J. Eng. Adv. Technol.* **2015**, *4*, 80.

(149) Cho, M. K.; Park, H. Y.; Choe, S.; Yoo, S. J.; Kim, J. Y.; Kim, H. J.; Henkensmeier, D.; Lee, S. Y.; Sung, Y. E.; Park, H. S. *J. Power Sources* **2017**, *347*, 283.

(150) Xiang, C.; Papadantonakis, K. M.; Lewis, N. S. *Mater. Horiz.* **2016**, *3*, 169.

(151) Bessarabov, D.; Wang, H.; Li, H.; Zhao, N. *PEM electrolysis for hydrogen production: principles and applications*; CRC Press, 2016.

(152) Chen, K.; Ai, N.; Jiang, S. P. *Electrochem. Commun.* **2012**, *19*, 119.

(153) Pan, W.; Chen, K.; Ai, N.; Lü, Z.; Jiang, S. P. *J. Electrochem. Soc.* **2016**, *163*, F106.

(154) Bi, L.; Boulfrad, S.; Traversa, E. *Chem. Soc. Rev.* **2014**, *43*, 8255.

(155) Laguna-Bercero, M. *J. Power Sources* **2012**, *203*, 4.

(156) Cinti, G.; Discepoli, G.; Bidini, G.; Lanzini, A.; Santarelli, M. *Int. J. Energy Res.* **2016**, *40*, 207.

(157) Choudhury, A.; Chandra, H.; Arora, A. *Renew. Sust. Energ. Rev.* **2013**, *20*, 430.

(158) Gupta, N.; Yadav, G. D. *Int. Res. Jou. Engg. & Tech.* **2016**, *3*, 5.

(159) Reier, T.; Nong, H. N.; Teschner, D.; Schlögl, R.; Strasser, P. *Adv. Energy Mater.* **2016**, *7*, 1601275.

(160) Suen, N. T.; Hung, S.; Quan, Q.; Zhang, N.; Xu, Y.; Chen, H. M. *Chem. Soc. Rev.* **2017**, *46*, 337.

(161) Dionigi, F.; Strasser, P. *Adv. Energy Mater.* **2016**, *6*, 1600621.

(162) Bockris, J. O. M. *J. Chem. Phys.* **1956**, *24*, 817.

(163) Rossmeisl, J.; Qu, Z. W.; Zhu, H.; Kroes, G. J.; Nørskov, J. K. *J. Electroanal. Chem.* **2007**, *607*, 83.

(164) Rao, R. R.; Kolb, M. J.; Halck, N. B.; Pedersen, A. F.; Mehta, A.; You, H.; Stoerzinger, K. A.; Feng, Z.; Hansen, H. A.; Zhou, H.; Giordano, L.; Rossmeisl, J.; Vegge, T.; Chorkendorff, I.; Stephens, I. E. L.;

Shao-Horn, Y. *Energy Environ. Sci.* **2017**, *10*, 2626.

(165) Busch, M.; Halck, N. B.; Kramm, U. I.; Siahrostami, S.; Krtil, P.; Rossmeisl, J. *Nano Energy* **2016**, *29*, 126.

(166) Fabbri, E.; Habereder, A.; Waltar, K.; Kotz, R.; Schmidt, T. J. *Catal. Sci. Technol.* **2014**, *4*, 3800.

(167) Kötz, R.; Lewerenz, H. J.; Stucki, S. *J. Electrochem. Soc.* **1983**, *130*, 825.

(168) Dau, H.; Limberg, C.; Reier, T.; Risch, M.; Roggan, S.; Strasser, P. *ChemCatChem* **2010**, *2*, 724.

(169) Antolini, E. *ACS Catal.* **2014**, *4*, 1426.

(170) Lim, J.; Park, D.; Jeon, S. S.; Roh, C.-W.; Choi, J.; Yoon, D.; Park, M.; Jung, H.; Lee, H. *Adv. Funct. Mater.* **2018**, *28*, 1704796.

(171) Casalongue, H. G. S.; Ng, M. L.; Kaya, S.; Friebel, D.; Ogasawara, H.; Nilsson, A. *Angew. Chem. Int. Ed.* **2014**, *53*, 7169.

(172) Pfeifer, V.; Jones, T. E.; Velasco Velez, J. J.; Massue, C.; Greiner, M. T.; Arrigo, R.; Teschner, D.; Girgsdies, F.; Scherzer, M.; Allan, J.; Hashagen, M.; Weinberg, G.; Piccinin, S.; Havecker, M.; Knop-Gericke, A.; Schlogl, R. *Phys. Chem. Chem. Phys.* **2016**, *18*, 2292.

(173) Minguzzi, A.; Lugaresi, O.; Achilli, E.; Locatelli, C.; Vertova, A.; Ghigna, P.; Rondinini, S. *Chem. Sci.* **2014**, *5*, 3591.

(174) Soldo, Y.; Hazemann, J.; Aberdam, D.; Inui, M.; Tamura, K.; Raoux, D.; Pernot, E.; Jal, J.; Dupuy Philon, J. *Phys. Rev. B* **1998**, *57*, 258.

(175) Fierro, S.; Nagel, T.; Baltruschat, H.; Comninellis, C. *Electrochem. Commun.* **2007**, *9*, 1969.

(176) Sivasankar, N.; Weare, W. W.; Frei, H. *J. Am. Chem. Soc.* **2011**, *133*, 12976.

(177) Zou, S.; Chan, H. Y. H.; Williams, C. T.; Weaver, M. J. *Langmuir* **2000**, *16*, 754.

(178) Marshall, A. T.; Sunde, S.; Tsypkin, M.; Tunold, R. *Int. J. Hydrog. Energy* **2007**, *32*, 2320.

(179) Cheng, J.; Zhang, H.; Ma, H.; Zhong, H.; Zou, Y. *Int. J. Hydrog. Energy* **2009**, *34*, 6609.

(180) Fuentes, R. E.; Farell, J.; Weidner, J. W. *Electrochem. Solid-State Lett.* **2011**, *14*, E5.

(181) Siracusano, S.; Baglio, V.; Di Blasi, A.; Briguglio, N.; Stassi, A.; Ornelas, R.; Trifoni, E.; Antonucci, V.; Arico, A. *Int. J. Hydrog. Energy* **2010**, *35*, 5558.

(182) Debe, M.; Hendricks, S.; Vernstrom, G.; Meyers, M.; Brostrom, M.; Stephens, M.; Chan, Q.; Willey, J.;

Hamden, M.; Mittelsteadt, C. K. *J. Electrochem. Soc.* **2012**, *159*, K165.

(183) Slavcheva, E.; Radev, I.; Bliznakov, S.; Topalov, G.; Andreev, P.; Budevski, E. *Electrochim. Acta* **2007**, *52*, 3889.

(184) Comninellis, C.; Vercesi, G. P. *J. Appl. Electrochem.* **1991**, *21*, 335.

(185) Terezo, A. J.; Bisquert, J.; Pereira, E. C.; Garcia-Belmonte, G. *J. Electroanal. Chem.* **2001**, *508*, 59.

(186) Marshall, A.; Børresen, B.; Hagen, G.; Sunde, S.; Tsypkin, M.; Tunold, R. *Russ. J. Electrochem.* **2006**, *42*, 1134.

(187) Zhang, J.; Hu, J.; Zhang, J.; Cao, C. *Int. J. Hydrog. Energy* **2011**, *36*, 5218.

(188) De Pauli, C. P.; Trasatti, S. *J. Electroanal. Chem.* **2002**, *538*, 145.

(189) Nong, H. N.; Gan, L.; Willinger, E.; Teschner, D.; Strasser, P. *Chem. Sci.* **2014**, *5*, 2955.

(190) Moghaddam, R. B.; Wang, C.; Sorge, J. B.; Brett, M. J.; Bergens, S. H. *Electrochem. Commun.* **2015**, *60*, 109.

(191) Nong, H. N.; Oh, H.-S.; Reier, T.; Willinger, E.; Willinger, M. G.; Petkov, V.; Teschner, D.; Strasser, P. *Angew. Chem. Int. Ed.* **2015**, *54*, 2975.

(192) Oh, H.-S.; Nong, H. N.; Reier, T.; Gliech, M.; Strasser, P. *Chem. Sci.* **2015**, *6*, 3321.

(193) Reier, T.; Pawolek, Z.; Cherevko, S.; Bruns, M.; Jones, T.; Teschner, D.; Selve, S.; Bergmann, A.; Nong, H. N.; Schlögl, R.; Mayrhofer, K. J. J.; Strasser, P. *J. Am. Chem. Soc.* **2015**, *137*, 13031.

(194) Lim, J.; Yang, S.; Kim, C.; Roh, C.; Kwon, Y.; Kim, Y.; Lee, H. *Chem. Commun.* **2016**, *52*, 5641.

(195) Papaderakis, A.; Pliatsikas, N.; Prochaska, C.; Vourlias, G.; Patsalas, P.; Tsiplakides, D.; Balomenou, S.; Sotiropoulos, S. *J. Phys. Chem. C* **2016**, *120*, 19995.

(196) Xu, S.; Chen, S.; Tian, L.; Xia, Q.; Hu, W. *J. Solid State Electrochem.* **2016**, *20*, 1961.

(197) Xu, S.; Liu, Y.; Tong, J.; Hu, W.; Xia, Q. *Russ. J. Electrochem.* **2016**, *52*, 1021.

(198) Kwon, T.; Hwang, H.; Sa, Y. J.; Park, J.; Baik, H.; Joo, S. H.; Lee, K. *Adv. Funct. Mater.* **2017**, *27*, 1604688.

(199) Sun, W.; Song, Y.; Gong, X.; Cao, L.; Yang, J. *Chem. Sci.* **2015**, *6*, 4993.

(200) Wang, C.; Sui, Y.; Xiao, G.; Yang, X.; Wei, Y.; Zou, G.; Zou, B. *J. Mater. Chem. A* **2015**, *3*, 19669.

(201) Yoon, D.; Bang, S.; Park, J.; Kim, J.; Baik, H.; Yang, H.; Lee, K. *CrystEngComm* **2015**, *17*, 6843.

(202) Pei, J.; Mao, J.; Liang, X.; Chen, C.; Peng, Q.; Wang, D.; Li, Y. *Chem. Commun.* **2016**, *52*, 3793.

(203) Hu, W.; Zhong, H.; Liang, W.; Chen, S. *ACS Appl. Mater. Interfaces* **2014**, *6*, 12729.

(204) Zaman, W. Q.; Wang, Z.; Sun, W.; Zhou, Z.; Tariq, M.; Cao, L.; Gong, X.-Q.; Yang, J. *ACS Energy Lett.* **2017**, *2*, 2786.

(205) Pfeifer, V.; Jones, T. E.; Velasco Velez, J. J.; Arrigo, R.; Piccinin, S.; Havecker, M.; Knop-Gericke, A.; Schlogl, R. *Chem. Sci.* **2017**, *8*, 2143.

(206) Frydendal, R.; Paoli, E. A.; Chorkendorff, I.; Rossmeisl, J.; Stephens, I. E. *Adv. Energy Mater.* **2015**, *5*, 1500991.

(207) Moreno-Hernandez, I. A.; MacFarland, C. A.; Read, C. G.; Papadantonakis, K. M.; Brunschwig, B. S.; Lewis, N. S. *Energy Environ. Sci.* **2017**, *10*, 2103.

(208) Risch, M.; Ringleb, F.; Kohlhoff, M.; Bogdanoff, P.; Chernev, P.; Zaharieva, I.; Dau, H. *Energy Environ. Sci.* **2015**, *8*, 661.

(209) McCrory, C. C. L.; Jung, S.; Ferrer, I. M.; Chatman, S. M.; Peters, J. C.; Jaramillo, T. F. *J. Am. Chem. Soc.* **2015**, *137*, 4347.

(210) Menezes, P. W.; Indra, A.; Levy, O.; Kailasam, K.; Gutkin, V.; Pfrommer, J.; Driess, M. *Chem. Commun.* **2015**, *51*, 5005.

(211) He, J.; Weekes, D. M.; Cheng, W.; Dettelbach, K. E.; Huang, A.; Li, T.; Berlinguette, C. P. *J. Am. Chem. Soc.* **2017**, *139*, 18174.

(212) McCrory, C. C. L.; Jung, S.; Peters, J. C.; Jaramillo, T. F. *J. Am. Chem. Soc.* **2013**, *135*, 16977.

(213) Jung, S.; McCrory, C. C. L.; Ferrer, I. M.; Peters, J. C.; Jaramillo, T. F. *J. Mater. Chem. A* **2016**, *4*, 3068.

(214) Bode, H.; Dehmelt, K.; Witte, J. *Z. Anorg. Allg. Chem.* **1969**, *366*, 1.

(215) Van der Ven, A.; Morgan, D.; Meng, Y.; Ceder, G. *J. Electrochem. Soc.* **2006**, *153*, A210.

(216) Hall, D. S.; Lockwood, D. J.; Bock, C.; MacDougall, B. R. *Proc. R. Soc. A* **2015**, *471*, 792.

(217) Oliva, P.; Leonardi, J.; Laurent, J.; Delmas, C.; Braconnier, J.; Figlarz, M.; Fievet, F.; De Guibert, A. *J. Power Sources* **1982**, *8*, 229.

(218) Lyons, M. E. G.; Brandon, M. P. *Int. J. Electrochem. Sci.* **2008**, *3*, 1386.

(219) Lu, P.; Srinivasan, S. *J. Electrochem. Soc.* **1978**, *125*, 1416.

(220) Bediako, D. K.; Lassalle-Kaiser, B.; Surendranath, Y.; Yano, J.; Yachandra, V. K.; Nocera, D. G. *J. Am. Chem. Soc.* **2012**, *134*, 6801.

(221) Trotochaud, L.; Young, S. L.; Ranney, J. K.; Boettcher, S. W. *J. Am. Chem. Soc.* **2014**, *136*, 6744.

(222) Landon, J.; Demeter, E.; noğlu, N.; Keturakis, C.; Wachs, I. E.; Vasić, R.; Frenkel, A. I.; Kitchin, J. R. *ACS Catal.* **2012**, *2*, 1793.

(223) Louie, M. W.; Bell, A. T. *J. Am. Chem. Soc.* **2013**, *135*, 12329.

(224) Li, N.; Bediako, D. K.; Hadt, R. G.; Hayes, D.; Kempa, T. J.; von Cube, F.; Bell, D. C.; Chen, L. X.; Nocera, D. G. *Proc. Natl. Acad. Sci.* **2017**, *114*, 1486.

(225) Tse, E. C. M.; Hoang, T. T. H.; Varnell, J. A.; Gewirth, A. A. *ACS Catal.* **2016**, *6*, 5706.

(226) Tichenor, R. L. *Ind. Eng. Chem.* **1952**, *44*, 973.

(227) Munshi, M.; Tseung, A.; Parker, J. *J. Appl. Electrochem.* **1985**, *15*, 711.

(228) Młynarek, G.; Paszkiewicz, M.; Radniecka, A. *J. Appl. Electrochem.* **1984**, *14*, 145.

(229) Corrigan, D. A. *J. Electrochem. Soc.* **1987**, *134*, 377.

(230) Yin, S.; Tu, W.; Sheng, Y.; Du, Y.; Kraft, M.; Borgna, A.; Xu, R. *Adv. Mater.* **2018**, *30*, 1705106.

(231) Khan, A. I.; O'Hare, D. *J. Mater. Chem.* **2002**, *12*, 3191.

(232) Fan, G.; Li, F.; Evans, D. G.; Duan, X. *Chem. Soc. Rev.* **2014**, *43*, 7040.

(233) Abellán, G.; Coronado, E.; Martí-Gastaldo, C.; Waerenborgh, J.; Ribera, A. *Inorg. Chem.* **2013**, *52*, 10147.

(234) Han, Y.; Liu, Z.-H.; Yang, Z.; Wang, Z.; Tang, X.; Wang, T.; Fan, L.; Ooi, K. *Chem. Mater.* **2008**, *20*, 360.

(235) Lu, Z.; Xu, W.; Zhu, W.; Yang, Q.; Lei, X.; Liu, J.; Li, Y.; Sun, X.; Duan, X. *Chem. Commun.* **2014**, *50*, 6479.

(236) Gong, M.; Li, Y.; Wang, H.; Liang, Y.; Wu, J. Z.; Zhou, J.; Wang, J.; Regier, T.; Wei, F.; Dai, H. *J. Am. Chem. Soc.* **2013**, *135*, 8452.

(237) Ting, X.; Yiwen, T.; Zhiyong, J.; Dawei, L.; Xiaoyan, H.; Bihui, L.; Lijuan, L. *Nanotechnology* **2009**, *20*, 475603.

(238) Long, X.; Li, J.; Xiao, S.; Yan, K.; Wang, Z.; Chen, H.; Yang, S. *Angew. Chem. Int. Ed.* **2014**, *53*, 7584.

(239) Tang, D.; Liu, J.; Wu, X.; Liu, R.; Han, X.; Han, Y.; Huang, H.; Liu, Y.; Kang, Z. *ACS Appl. Mater. Interfaces* **2014**, *6*, 7918.

(240) Diaz Morales, O.; Ledezma Yanez, I.; Koper, M. T. M.; Calle Vallejo, F. *ACS Catal.* **2015**, *5*, 5380.

(241) Oliver-Tolentino, M. A.; Vazquez-Samperio, J.; Manzo-Robledo, A.; Gonzalez-Huerta, R. D.; Flores-Moreno, J. L.; Ramirez-Rosales, D.; Guzman-Vargas, A. *J. Phys. Chem. C* **2014**, *118*, 22432.

(242) Gregoire, B.; Ruby, C.; Carteret, C. *Dalton Trans.* **2013**, *42*, 15687.

(243) Li, Z.; Shao, M.; An, H.; Wang, Z.; Xu, S.; Wei, M.; Evans, D. G.; Duan, X. *Chem. Sci.* **2015**, *6*, 6624.

(244) Batchellor, A. S.; Boettcher, S. W. *ACS Catal.* **2015**, *5*, 6680.

(245) Morales-Guio, C. G.; Mayer, M. T.; Yella, A.; Tilley, S. D.; Grätzel, M.; Hu, X. *J. Am. Chem. Soc.* **2015**, *137*, 9927.

(246) Lo, N. C.; Chung, P. C.; Chuang, W. J.; Hsu, S. C. N.; Sun, I. W.; Chen, P. Y. *J. Electrochem. Soc.* **2016**, *163*, D9.

(247) Song, F.; Hu, X. *Nat. Commun.* **2014**, *5*, 4477.

(248) Brennaman, M. K.; Dillon, R. J.; Alibabaei, L.; Gish, M. K.; Dares, C. J.; Ashford, D. L.; House, R. L.; Meyer, G. J.; Papanikolas, J. M.; Meyer, T. J. *J. Am. Chem. Soc.* **2016**, *138*, 13085.

(249) Ashford, D. L.; Gish, M. K.; Vannucci, A. K.; Brennaman, M. K.; Templeton, J. L.; Papanikolas, J. M.; Meyer, T. J. *Chem. Rev.* **2015**, *115*, 13006.

(250) Fujishima, A.; Honda, K. *Nature* **1972**, *238*, 37.

(251) Treadway, J. A.; Moss, J. A.; Meyer, T. J. *Inorg. Chem.* **1999**, *38*, 4386.

(252) Youngblood, W. J.; Lee, S.-H. A.; Kobayashi, Y.; Hernandez-Pagan, E. A.; Hoertz, P. G.; Moore, T. A.; Moore, A. L.; Gust, D.; Mallouk, T. E. *J. Am. Chem. Soc.* **2009**, *131*, 926.

(253) Moore, G. F.; Blakemore, J. D.; Milot, R. L.; Hull, J. F.; Song, H.-e.; Cai, L.; Schmuttenmaer, C. A.; Crabtree, R. H.; Brudvig, G. W. *Energy Environ. Sci.* **2011**, *4*, 2389.

(254) Hanson, K.; Brennaman, M. K.; Luo, H.; Glasson, C. R. K.; Concepcion, J. J.; Song, W.; Meyer, T. J. *ACS Appl. Mater. Interfaces* **2012**, *4*, 1462.

(255) Ashford, D. L.; Sherman, B. D.; Binstead, R. A.; Templeton, J. L.; Meyer, T. J. *Angew. Chem. Int. Ed.* **2015**, *54*, 4778.

(256) Hyde, J. T.; Hanson, K.; Vannucci, A. K.; Lapides, A. M.; Alibabaei, L.; Norris, M. R.; Meyer, T. J.; Harrison, D. P. *ACS Appl. Mater. Interfaces* **2015**, *7*, 9554.

(257) Sherman, B. D.; Ashford, D. L.; Lapides, A. M.; Sheridan, M. V.; Wee, K.-R.; Meyer, T. J. *J. Phys. Chem. Lett.* **2015**, *6*, 3213.

(258) Sherman, B. D.; Xie, Y.; Sheridan, M. V.; Wang, D.; Shaffer, D. W.; Meyer, T. J.; Concepcion, J. J. *ACS Energy Lett.* **2017**, *2*, 124.

(259) Gao, Y.; Ding, X.; Liu, J.; Wang, L.; Lu, Z.; Li, L.; Sun, L. *J. Am. Chem. Soc.* **2013**, *135*, 4219.

(260) Fan, K.; Li, F.; Wang, L.; Daniel, Q.; Gabrielsson, E.; Sun, L. *Phys. Chem. Chem. Phys.* **2014**, *16*, 25234.

(261) Ding, X.; Gao, Y.; Ye, L.; Zhang, L.; Sun, L. *ChemSusChem* **2015**, *8*, 3992.

(262) Li, F.; Fan, K.; Xu, B.; Gabrielsson, E.; Daniel, Q.; Li, L.; Sun, L. *J. Am. Chem. Soc.* **2015**, *137*, 9153.

(263) Li, H.; Li, F.; Wang, Y.; Bai, L.; Yu, F.; Sun, L. *ChemPlusChem* **2016**, *81*, 1056.

(264) Materna, K. L.; Crabtree, R. H.; Brudvig, G. W. *Chem. Soc. Rev.* **2017**, *46*, 6099.

(265) Yu, Z.; Li, F.; Sun, L. *Energy Environ. Sci.* **2015**, *8*, 760.

(266) Xu, P.; McCool, N. S.; Mallouk, T. E. *Nano Today* **2017**, *14*, 42.

(267) Zhao, Y.; Swierk, J. R.; Megiatto, J. D.; Sherman, B.; Youngblood, W. J.; Qin, D.; Lentz, D. M.; Moore, A. L.; Moore, T. A.; Gust, D.; Mallouk, T. E. *Proc. Natl. Acad. Sci.* **2012**, *109*, 15612.

(268) Gao, Y.; Zhang, L.; Ding, X.; Sun, L. *Phys. Chem. Chem. Phys.* **2014**, *16*, 12008.

(269) Ernstorfer, R.; Gundlach, L.; Felber, S.; Storck, W.; Eichberger, R.; Willig, F. *J. Phys. Chem. B* **2006**, *110*, 25383.

(270) Wang, L.; Ashford, D. L.; Thompson, D. W.; Meyer, T. J.; Papanikolas, J. M. *J. Phys. Chem. C* **2013**, *117*, 24250.

(271) Martini, L. A.; Moore, G. F.; Milot, R. L.; Cai, L. Z.; Sheehan, S. W.; Schmuttenmaer, C. A.; Brudvig, G. W.; Crabtree, R. H. *J. Phys. Chem. C* **2013**, *117*, 14526.

(272) McNamara, W. R.; Milot, R. L.; Song, H.-e.; Snoeberger III, R. C.; Batista, V. S.; Schmuttenmaer, C. A.; Brudvig, G. W.; Crabtree, R. H. *Energy Environ. Sci.* **2010**, *3*, 917.

(273) Materna, K. L.; Rudshteyn, B.; Brennan, B. J.; Kane, M. H.; Bloomfield, A. J.; Huang, D. L.; Shopov,

D. Y.; Batista, V. S.; Crabtree, R. H.; Brudvig, G. W. *ACS Catal.* **2016**, *6*, 5371.

(274) Brennan, B. J.; Koenigsmann, C.; Materna, K. L.; Kim, P. M.; Koepf, M.; Crabtree, R. H.; Schmuttenmaer, C. A.; Brudvig, G. W. *J. Phys. Chem. C* **2016**, *120*, 12495.

(275) McNamara, W. R.; Snoeberger III, R. C.; Li, G.; Richter, C.; Allen, L. J.; Milot, R. L.; Schmuttenmaer, C. A.; Crabtree, R. H.; Brudvig, G. W.; Batista, V. S. *Energy Environ. Sci.* **2009**, *2*, 1173.

(276) Brennan, B. J.; Llansola Portoles, M. J.; Liddell, P. A.; Moore, T. A.; Moore, A. L.; Gust, D. *Phys. Chem. Chem. Phys.* **2013**, *15*, 16605.

(277) Bae, E.; Choi, W.; Park, J.; Shin, H. S.; Kim, S. B.; Lee, J. S. *J. Phys. Chem. B* **2004**, *108*, 14093.

(278) Halasinski, T. M.; Weisman, J. L.; Ruiterkamp, R.; Lee, T. J.; Salama, F.; Head-Gordon, M. *J. Phys. Chem. A* **2003**, *107*, 3660.

(279) Norris, M. R.; Concepcion, J. J.; Glasson, C. R.; Fang, Z.; Lapides, A. M.; Ashford, D. L.; Templeton, J. L.; Meyer, T. J. *Inorg. Chem.* **2013**, *52*, 12492.

(280) Hanson, K.; Brennaman, M. K.; Ito, A.; Luo, H.; Song, W.; Parker, K. A.; Ghosh, R.; Norris, M. R.; Glasson, C. R.; Concepcion, J. J. *J. Phys. Chem. C* **2012**, *116*, 14837.

(281) Brennan, B. J.; Keirstead, A. E.; Liddell, P. A.; Vail, S. A.; Moore, T. A.; Moore, A. L.; Gust, D. *Nanotechnology* **2009**, *20*, 505203.

(282) Koenigsmann, C.; Ripolles, T.; Brennan, B.; Negre, C.; Koepf, M.; Durrell, A.; Milot, R.; Torre, J.; Crabtree, R. H.; Batista, V. *Phys. Chem. Chem. Phys.* **2014**, *16*, 16629.

(283) Bae, E.; Choi, W. *J. Phys. Chem. B* **2006**, *110*, 14792.

(284) Hudson, R.; Keay, L. *J. Chem. Soc.* **1956**, 2463.

(285) Hanson, K.; Losego, M. D.; Kalanyan, B.; Parsons, G. N.; Meyer, T. J. *Nano Lett.* **2013**, *13*, 4802.

(286) Hanson, K.; Losego, M. D.; Kalanyan, B.; Ashford, D. L.; Parsons, G. N.; Meyer, T. J. *Chem. Mater.* **2012**, *25*, 3.

(287) Lapides, A.; Sherman, B.; Brennaman, M.; Dares, C.; Skinner, K.; Templeton, J.; Meyer, T. *Chem. Sci.* **2015**, *6*, 6398.

(288) Wee, K.-R.; Brennaman, M. K.; Alibabaei, L.; Farnum, B. H.; Sherman, B.; Lapides, A. M.; Meyer, T. J. *J. Am. Chem. Soc.* **2014**, *136*, 13514.

(289) Takijiri, K.; Morita, K.; Nakazono, T.; Sakai, K.; Ozawa, H. *Chem. Commun.* **2017**, *53*, 3042.

(290) Bangle, R.; Sampaio, R. N.; Troian-Gautier, L.; Meyer, G. J. *ACS Appl. Mater. Interfaces* **2018**, *10*, 3121.

(291) Belanger, D.; Pinson, J. *Chem. Soc. Rev.* **2011**, *40*, 3995.

(292) Chung, D. J.; Oh, S. H.; Komathi, S.; Gopalan, A. I.; Lee, K. P.; Choi, S. H. *Electrochim. Acta* **2012**, *76*, 394.

(293) Feng, L.; Sun, X.; Yao, S.; Liu, C.; Xing, W.; Zhang, J. In *Rotating electrode methods and oxygen reduction electrocatalysts*; Elsevier: 2014, p 67.

(294) Jeon, M. K.; Lee, C. H.; Park, G. I.; Kang, K. H. *J. Power Sources* **2012**, *216*, 400.

(295) Ramaswamy, N.; Mukerjee, S. *J. Phys. Chem. C* **2011**, *115*, 18015.

(296) Jiang, J.; Gao, H.; Lu, S.; Zhang, X.; Wang, C.; Wang, W.; Yu, H. *J. Mater. Chem. A* **2017**, *5*, 9233.

(297) Estudillo-Wong, L. A.; Ramos-Sanchez, G.; Calvillo, L.; Granozzi, G.; Alonso-Vante, N. *ChemElectroChem* **2017**, *4*, 3264.

(298) Gan, L.; Cui, C.; Rudi, S.; Strasser, P. *Top. Catal.* **2014**, *57*, 236.

(299) Spendelow, J. S.; Wieckowski, A. *Phys. Chem. Chem. Phys.* **2007**, *9*, 2654.

(300) Hussain, S.; Kongi, N.; Matisen, L.; Kozlova, J.; Sammelselg, V.; Tammeveski, K. *Electrochem. Commun.* **2017**, *81*, 79.

(301) Castegnaro, M. V.; Paschoalino, W. J.; Fernandes, M. R.; Balke, B.; M. Alves, M. C.; Ticianelli, E. A.; Morais, J. *Langmuir* **2017**, *33*, 2734.

(302) Ge, X.; Sumboja, A.; Wuu, D.; An, T.; Li, B.; Goh, F. T.; Hor, T. A.; Zong, Y.; Liu, Z. *ACS Catal.* **2015**, *5*, 4643.

(303) García-Contreras, M.; Fernández-Valverde, S.; Vargas-Garcia, J. R. *J. Alloys Compd.* **2010**, *504*, S425.

(304) Pašti, I. A.; Gavrilov, N. M.; Baljozović, M.; Mitrić, M.; Mentus, S. V. *Electrochim. Acta* **2013**, *114*, 706.

(305) Jäger, R.; Härk, E.; Kasatkin, P.; Lust, E. *J. Electrochem. Soc.* **2014**, *161*, F861.

(306) Debe, M.; Steinbach, A.; Vernstrom, G.; Hendricks, S.; Kurkowski, M.; Atanasoski, R.; Kadera, P.; Stevens, D.; Sanderson, R.; Marvel, E. *J. Electrochem. Soc.* **2011**, *158*, B910.

(307) Liu, G. C.; Burns, C.; Sanderson, R.; Stevens, D.; Vernstrom, G. D.; Atanasoski, R. T.; Debe, M. K.; Dahn, J. *ECS Trans.* **2010**, *33*, 153.

(308) Liu, G. C.; Stevens, D.; Burns, J.; Sanderson, R.; Vernstrom, G.; Atanasoski, R.; Debe, M.; Dahn, J. *J. Electrochem. Soc.* **2011**, *158*, B919.

(309) Debe, M. K.; Steinbach, A. J.; Vernstrom, G. D.; Hendricks, S. M.; Kurkowski, M. J.; Atanasoski, R. T.; Kadera, P. J.; Stevens, D. A.; Sanderson, R. J.; Marvel, E. *ECS Trans.* **2010**, *33*, 143.

(310) Van der Vliet, D.; Wang, C.; Debe, M.; Atanasoski, R.; Markovic, N. M.; Stamenkovic, V. R. *Electrochim. Acta* **2011**, *56*, 8695.

(311) Gasda, M.; Eisman, G.; Gall, D. *J. Electrochem. Soc.* **2010**, *157*, B437.

(312) Gasda, M.; Eisman, G.; Gall, D. *J. Electrochem. Soc.* **2010**, *157*, B113.

(313) Gasda, M.; Eisman, G.; Gall, D. *J. Electrochem. Soc.* **2010**, *157*, B71.

(314) Gasda, M.; Teki, R.; Lu, T.-M.; Koratkar, N.; Eisman, G.; Gall, D. *J. Electrochem. Soc.* **2009**, *156*, B614.

(315) Bonakdarpour, A.; Tucker, R. T.; Fleischauer, M. D.; Beckers, N. A.; Brett, M. J.; Wilkinson, D. P. *Electrochim. Acta* **2012**, *85*, 492.

(316) Bonakdarpour, A.; Fleischauer, M.; Brett, M.; Dahn, J. *Appl. Catal., A* **2008**, *349*, 110.

(317) Khudhayer, W. J.; Kariuki, N. N.; Wang, X.; Myers, D. J.; Shaikh, A. U.; Karabacak, T. *J. Electrochem. Soc.* **2011**, *158*, B1029.

(318) Khudhayer, W. J.; Kariuki, N.; Myers, D. J.; Shaikh, A. U.; Karabacak, T. *J. Electrochem. Soc.* **2012**, *159*, B729.

(319) Hawkeye, M. M.; Brett, M. J. *J. Vac. Sci. Technol., A* **2007**, *25*, 1317.

(320) Robbie, K.; Brett, M. J. *J. Vac. Sci. Technol., A* **1997**, *15*, 1460.

(321) Krause, K. M.; Taschuk, M. T.; Brett, M. J. *J. Vac. Sci. Technol., A* **2013**, *31*, 031507.

(322) Francis, S. A.; Tucker, R. T.; Brett, M. J.; Bergens, S. H. *J. Power Sources* **2013**, *222*, 533.

(323) Menard, L. N.; Bergens, S. H. *J. Power Sources* **2009**, *194*, 298.

(324) Francis, S. A.; Bergens, S. H. *J. Power Sources* **2011**, *196*, 7470.

(325) Krause, K. M.; Thommes, M.; Brett, M. J. *Microporous Mesoporous Mater.* **2011**, *143*, 166.

(326) Debe, M. K. *J. Electrochem. Soc.* **2011**, *159*, B53.

(327) Hahn, F.; Beden, B.; Croissant, M.; Lamy, C. *Electrochim. Acta* **1986**, *31*, 335.

(328) Machado, S. A.; Avaca, L. *Electrochim. Acta* **1994**, *39*, 1385.

(329) Seghiouer, A.; Chevalet, J.; Barhoun, A.; Lantelme, F. *J. Electroanal. Chem.* **1998**, *442*, 113.

(330) Jiang, J.; Kucernak, A. *J. Electroanal. Chem.* **2005**, *576*, 223.

(331) Conway, B.; Angerstein-Kozlowska, H. *Acc. Chem. Res.* **1981**, *14*, 49.

(332) Kariuki, N. N.; Khudhayer, W. J.; Karabacak, T.; Myers, D. J. *ACS Catal.* **2013**, *3*, 3123.

(333) Guidelli, R.; Compton, R. G.; Feliu, J. M.; Gileadi, E.; Lipkowski, J.; Schmickler, W.; Trasatti, S. *Pure Appl. Chem.* **2014**, *86*, 245.

(334) Stacy, J.; Regmi, Y. N.; Leonard, B.; Fan, M. *Renew. Sust. Energ. Rev.* **2017**, *69*, 401.

(335) Markovic, N. M.; Gasteiger, H. A.; Ross, P. N. *J. Phys. Chem.* **1996**, *100*, 6715.

(336) Zhang, Z.; Liu, J.; Gu, J.; Su, L.; Cheng, L. *Energy Environ. Sci.* **2014**, *7*, 2535.

(337) Li, J.; Alsudairi, A.; Ma, Z.-F.; Mukerjee, S.; Jia, Q. *J. Am. Chem. Soc.* **2017**, *139*, 1384.

(338) Sui, S.; Wang, X.; Zhou, X.; Su, Y.; Riffat, S.; Liu, C.-j. *J. Mater. Chem. A* **2017**, *5*, 1808.

(339) Wang, C.; Markovic, N. M.; Stamenkovic, V. R. *ACS Catal.* **2012**, *2*, 891.

(340) Wu, J.; Yang, H. *Acc. Chem. Res.* **2013**, *46*, 1848.

(341) Chen, C.; Kang, Y.; Huo, Z.; Zhu, Z.; Huang, W.; Xin, H. L.; Snyder, J. D.; Li, D.; Herron, J. A.; Mavrikakis, M.; Chi, M.; More, K. L.; Li, Y.; Markovic, N. M.; Somorjai, G. A.; Yang, P.; Stamenkovic, V. R. *Science* **2014**, *343*, 1339.

(342) Zhao, X.; Chen, S.; Fang, Z.; Ding, J.; Sang, W.; Wang, Y.; Zhao, J.; Peng, Z.; Zeng, J. *J. Am. Chem. Soc.* **2015**, *8*, 2804.

(343) Han, B. H.; Carlton, C. E.; Kongkanand, A.; Kukreja, R. S.; Theobald, B. R.; Gan, L.; O'Malley, R.; Strasser, P.; Wagner, F. T.; Shao-Horn, Y. *Energy Environ. Sci.* **2015**, *8*, 258.

(344) Rudi, S.; Gan, L.; Cui, C.; Gliech, M.; Strasser, P. *J. Electrochem. Soc.* **2015**, *162*, F403.

(345) Kobayashi, S.; Wakisaka, M.; Tryk, D.; Iiyama, A.; Uchida, H. *J. Phys. Chem. C* **2017**, *121*, 11234.

(346) Marković, N. M.; Ross, P. N. *Surf. Sci. Rep.* **2002**, *45*, 117.

(347) Antolini, E. *Appl. Catal., B* **2017**, *217*, 201.

(348) Calle-Vallejo, F.; Pohl, M. D.; Reinisch, D.; Loffreda, D.; Sautet, P.; Bandarenka, A. S. *Chem. Sci.* **2017**, *8*, 2283.

(349) Zhou, W.-P.; Sasaki, K.; Su, D.; Zhu, Y.; Wang, J. X.; Adzic, R. R. *J. Phys. Chem. C* **2010**, *114*, 8950.

(350) Alonso-Vante, N. *ChemPhysChem* **2010**, *11*, 2732.

(351) Strasser, P.; Koh, S.; Anniyev, T.; Greeley, J.; More, K.; Yu, C. F.; Liu, Z. C.; Kaya, S.; Nordlund, D.; Ogasawara, H.; Toney, M. F.; Nilsson, A. *Nat. Chem.* **2010**, *2*, 454.

(352) Srivastava, R.; Mani, P.; Hahn, N.; Strasser, P. *Angew. Chem. Int. Ed.* **2007**, *46*, 8988.

(353) Strasser, P. *Rev. Chem. Eng.* **2009**, *25*, 255.

(354) Strasser, P.; Kühl, S. *Nano Energy* **2016**, *29*, 166.

(355) Feltham, A. M.; Spiro, M. *Chem. Rev.* **1971**, *71*, 177.

(356) Beden, B.; Floner, D.; Léger, J. M.; Lamy, C. *Surf. Sci.* **1985**, *162*, 822.

(357) Zhan, D.; Velmurugan, J.; Mirkin, M. V. *J. Am. Chem. Soc.* **2009**, *131*, 14756.

(358) Koutecky, J.; Levich, B. G. *Zh. Fiz. Khim.* **1958**, *32*, 1565.

(359) Yang, R. Z.; Leisch, J.; Strasser, P.; Toney, M. F. *Chem. Mater.* **2010**, *22*, 4712.

(360) Wang, D.; Yu, Y.; Xin, H. L.; Hovden, R.; Ercius, P.; Mundy, J. A.; Chen, H.; Richard, J. H.; Muller, D. A.; DiSalvo, F. J.; Abruña, H. D. *Nano Lett.* **2012**, *12*, 5230.

(361) Mukerjee, S.; Srinivasan, S.; Soriaga, M. P.; McBreen, J. *J. Phys. Chem.* **1995**, *99*, 4577.

(362) Stevens, D. A.; Mehrotra, R.; Sanderson, R. J.; Vernstrom, G. D.; Atanasoski, R. T.; Debe, M. K.; Dahn, J. R. *J. Electrochem. Soc.* **2011**, *158*, B905.

(363) Wang, J. X.; Uribe, F. A.; Springer, T. E.; Zhang, J.; Adzic, R. R. *Faraday Discuss.* **2009**, *140*, 347.

(364) Du, S.; Lu, Y.; Malladi, S. K.; Xu, Q.; Steinberger-Wilckens, R. *J. Mater. Chem. A* **2014**, *2*, 692.

(365) Xu, S.; Wang, C.; Francis, S. A.; Tucker, R. T.; Sorge, J. B.; Moghaddam, R. B.; Brett, M. J.; Bergens, S. H. *Electrochim. Acta* **2015**, *151*, 537.

(366) Zhao, Y.; E, Y.; Fan, L.; Qiu, Y.; Yang, S. *Electrochim. Acta* **2007**, *52*, 5873.

(367) Chang, Q.; Xu, Y.; Zhu, S.; Xiao, F.; Shao, M. *Front. Energy* **2017**, *11*, 254.

(368) Chen, T.; Kang, J.; Zhang, D.; Guo, L. *RSC Advances* **2016**, *6*, 71501.

(369) Antolini, E.; Salgado, J. R. C.; Giz, M. J.; Gonzalez, E. R. *Int. J. Hydrog. Energy* **2005**, *30*, 1213.

(370) Gasteiger, H. A.; Kocha, S. S.; Sompalli, B.; Wagner, F. T. *Appl. Catal., B* **2005**, *56*, 9.

(371) Nesselberger, M.; Ashton, S.; Meier, J. C.; Katsounaros, I.; Mayrhofer, K. J. J.; Arenz, M. *J. Am. Chem. Soc.* **2011**, *133*, 17428.

(372) Chandan, A.; Hattenberger, M.; El-kharouf, A.; Du, S.; Dhir, A.; Self, V.; Pollet, B. G.; Ingram, A.; Bujalski, W. *J. Power Sources* **2013**, *231*, 264.

(373) Buriak, J. M. *Chem. Mater.* **2015**, *27*, 1147.

(374) Lianos, P. *Appl. Catal., B* **2017**, *210*, 235.

(375) Montoya, J. H.; Seitz, L. C.; Chakthranont, P.; Vojvodic, A.; Jaramillo, T. F.; Nørskov, J. K. *Nat. Mater.* **2017**, *16*, 70.

(376) Bensaid, S.; Centi, G.; Garrone, E.; Perathoner, S.; Saracco, G. *ChemSusChem* **2012**, *5*, 500.

(377) Pachauri, R. K.; Chauhan, Y. K. *Renew. Sust. Energ. Rev.* **2015**, *43*, 1301.

(378) Roger, I.; Shipman, M. A.; Symes, M. D. *Nat. Rev. Chem.* **2017**, *1*, 3.

(379) Oh, H. S.; Nong, H. N.; Reier, T.; Gliech, M.; Strasser, P. *Chem. Sci.* **2015**, *6*, 3321.

(380) Reier, T.; Teschner, D.; Lunkenbein, T.; Bergmann, A.; Selve, S.; Kraehnert, R.; Schlögl, R.; Strasser, P. *J. Electrochem. Soc.* **2014**, *161*, F876.

(381) Lyons, M. E. G.; Doyle, R. L.; Fernandez, D.; Godwin, I. J.; Browne, M. P.; Rovetta, A. *Electrochem. Commun.* **2014**, *45*, 60.

(382) Berkermann, F. Ph. D. Dissertation, Ruhr-Universität Bochum, 2010.

(383) Kötz, R.; Stucki, S. *Electrochim. Acta* **1986**, *31*, 1311.

(384) Burke, L. D.; O'Meara, T. O. *J. Chem. Soc., Faraday Trans. 1* **1972**, *68*, 839.

(385) Blakemore, J. D.; Schley, N. D.; Olack, G. W.; Incarvito, C. D.; Brudvig, G. W.; Crabtree, R. H. *Chem. Sci.* **2011**, *2*, 94.

(386) Blakemore, J. D.; Mara, M. W.; Kushner-Lenhoff, M. N.; Schley, N. D.; Konezny, S. J.; Rivalta, I.; Negre, C. F. A.; Snoeberger, R. C.; Kokhan, O.; Huang, J.; Stickrath, A.; Tran, L. A.; Parr, M. L.; Chen, L. X.; Tiede, D. M.; Batista, V. S.; Crabtree, R. H.; Brudvig, G. W. *Inorg. Chem.* **2013**, *52*, 1860.

(387) Smith, R. D. L.; Sporinova, B.; Fagan, R. D.; Trudel, S.; Berlinguette, C. P. *Chem. Mater.* **2014**, *26*, 1654.

(388) Fu, L.; Yang, F.; Cheng, G.; Luo, W. *Nanoscale* **2018**, *10*, 1892.

(389) Takimoto, D.; Fukuda, K.; Miyasaka, S.; Ishida, T.; Ayato, Y.; Mochizuki, D.; Shimizu, W.; Sugimoto, W. *Electrocatalysis* **2016**, *8*, 144.

(390) Lee, S. H.; Lee, H.; Cho, M.; Lee, Y. *Carbon* **2017**, *115*, 50.

(391) Cosgrove, T. *Colloid Science Principles, Methods and Applications*; Blackwell Publishing: Bristol, 2005.

(392) Reetz, M. T.; Lopez, M.; Grunert, W.; Vogel, W.; Mahlendorf, F. *J. Phys. Chem. B* **2003**, *107*, 7414.

(393) Shen, J.; Ziaei-Azad, H.; Semagina, N. *J. Mol. Catal. A: Chem.* **2014**, *391*, 36.

(394) Zhao, Y. X.; Hernandez-Pagan, E. A.; Vargas-Barbosa, N. M.; Dysart, J. L.; Mallouk, T. E. *J. Phys. Chem. Lett.* **2011**, *2*, 402.

(395) Sherman, B. D.; Pillai, S.; Kodis, G.; Bergkamp, J.; Mallouk, T. E.; Gust, D.; Moore, T. A.; Moore, A. L. *Can. J. Chem.* **2011**, *89*, 152.

(396) Bock, C.; Birss, V. I. *J. Electroanal. Chem.* **1999**, *475*, 20.

(397) Gambardella, A. A.; Bjorge, N. S.; Alspaugh, V. K.; Murray, R. W. *J. Phys. Chem. C* **2011**, *115*, 21659.

(398) Zhao, Y.; Vargas-Barbosa, N. M.; Hernandez-Pagan, E. A.; Mallouk, T. E. *Small* **2011**, *7*, 2087.

(399) Da Silva, L. A.; Alves, V. A.; Da Silva, M. A. P.; Trasatti, S.; Boodts, J. F. C. *Can. J. Chem.* **1997**, *75*, 1483.

(400) Hu, J.; Zhang, J.; Cao, C. *Int. J. Hydrog. Energy* **2004**, *29*, 791.

(401) Da Silva, L. A.; Alves, V. A.; Trasatti, S.; Boodts, J. F. C. *J. Electroanal. Chem.* **1997**, *427*, 97.

(402) De Faria, L. A.; Boodts, J. F. C.; Trasatti, S. *J. Appl. Electrochem.* **1996**, *26*, 1195.

(403) Ryu, W.-H.; Lee, Y. W.; Nam, Y. S.; Youn, D.-Y.; Park, C. B.; Kim, I.-D. *J. Mater. Chem. A* **2014**, *2*, 5610.

(404) Fóti, G.; Mousty, C.; Reid, V.; Comninellis, C. *Electrochim. Acta* **1998**, *44*, 813.

(405) Wang, C.; Moghaddam, R. B.; Bergens, S. H. *J. Phys. Chem. C* **2017**, *121*, 5480.

(406) Wang, C.; Moghaddam, R. B.; Brett, M. J.; Bergens, S. H. *ACS Sustainable Chem. Eng.* **2017**, *5*, 1106.

(407) Dupin, J.-C.; Gonbeau, D.; Vinatier, P.; Levasseur, A. *Phys. Chem. Chem. Phys.* **2000**, *2*, 1319.

(408) Biesinger, M. C.; Payne, B. P.; Lau, L. W. M.; Gerson, A.; Smart, R. S. C. *Surf. Interface Anal.* **2009**, *41*,

324.

(409) Ali-Löytty, H.; Louie, M. W.; Singh, M. R.; Li, L.; Sanchez Casalongue, H. G.; Ogasawara, H.; Crumlin, E. J.; Liu, Z.; Bell, A. T.; Nilsson, A.; Friebel, D. *J. Phys. Chem. C* **2016**, *120*, 2247.

(410) Carley, A. F.; Jackson, S. D.; O'Shea, J. N.; Roberts, M. W. *Surf. Sci.* **1999**, *440*, L868.

(411) Shannon, R. *Acta Crystallogr., Sect. A* **1976**, *32*, 751.

(412) Tahir, M.; Pan, L.; Idrees, F.; Zhang, X.; Wang, L.; Zou, J.-J.; Wang, Z. L. *Nano Energy* **2017**, *37*, 136.

(413) Liu, J.; Liu, Y.; Liu, N.; Han, Y.; Zhang, X.; Huang, H.; Lifshitz, Y.; Lee, S.-T.; Zhong, J.; Kang, Z. *Science* **2015**, *347*, 970.

(414) Dincer, I.; Acar, C. *Int. J. Hydrog. Energy* **2015**, *40*, 11094.

(415) Abdol Rahim, A. H.; Tijani, A. S.; Kamarudin, S. K.; Hanapi, S. *J. Power Sources* **2016**, *309*, 56.

(416) Danilovic, N.; Subbaraman, R.; Chang, K.-C.; Chang, S. H.; Kang, Y. J.; Snyder, J.; Paulikas, A. P.; Strmcnik, D.; Kim, Y.-T.; Myers, D.; Stamenkovic, V. R.; Markovic, N. M. *J. Phys. Chem. Lett.* **2014**, *5*, 2474.

(417) Danilovic, N.; Subbaraman, R.; Chang, K. C.; Chang, S. H.; Kang, Y.; Snyder, J.; Paulikas, A. P.; Strmcnik, D.; Kim, Y. T.; Myers, D.; Stamenkovic, V. R.; Markovic, N. M. *Angew. Chem. Int. Ed.* **2014**, *53*, 14016.

(418) Lettenmeier, P.; Wang, L.; Golla-Schindler, U.; Gazdzicki, P.; Cañas, N. A.; Handl, M.; Hiesgen, R.; Hosseiny, S. S.; Gago, A. S.; Friedrich, K. A. *Angew. Chem.* **2016**, *128*, 752.

(419) Lee, B.-S.; Ahn, S. H.; Park, H.-Y.; Choi, I.; Yoo, S. J.; Kim, H.-J.; Henkensmeier, D.; Kim, J. Y.; Park, S.; Nam, S. W.; Lee, K.-Y.; Jang, J. H. *Appl. Catal., B* **2015**, *179*, 285.

(420) Cherevko, S.; Geiger, S.; Kasian, O.; Kulyk, N.; Grote, J.-P.; Savan, A.; Shrestha, B. R.; Merzlikin, S.; Breitbach, B.; Ludwig, A.; Mayrhofer, K. J. J. *Catal. Today* **2016**, *262*, 170.

(421) Park, J.; Sa, Y. J.; Baik, H.; Kwon, T.; Joo, S. H.; Lee, K. *ACS Nano* **2017**, *11*, 5500.

(422) Qiu, Y.; Xin, L.; Li, W. *Langmuir* **2014**, *30*, 7893.

(423) Li, Y.; Yu, Z.; Meng, J.; Li, Y. *Int. J. Hydrog. Energy* **2013**, *38*, 3898.

(424) Kötz, R.; Neff, H.; Stucki, S. *J. Electrochem. Soc.* **1984**, *131*, 72.

(425) Du, J.; Chen, Z.; Ye, S.; Wiley, B. J.; Meyer, T. J. *Angew. Chem. Int. Ed.* **2015**, *54*, 2073.

(426) Grosvenor, A. P.; Kobe, B. A.; McIntyre, N. S. *Surf. Sci.* **2004**, *572*, 217.

(427) Conway, B. E.; Mozota, J. *Electrochim. Acta* **1983**, *28*, 9.

(428) Lyons, M. E. G.; Floquet, S. *Phys. Chem. Chem. Phys.* **2011**, *13*, 5314.

(429) Acar, C.; Dincer, I. *Int. J. Energy Res.* **2015**, *39*, 1757.

(430) Nicoletti, G.; Arcuri, N.; Nicoletti, G.; Bruno, R. *Energy Convers. Manage.* **2015**, *89*, 205.

(431) Verhelst, S. *Int. J. Hydrog. Energy* **2014**, *39*, 1071.

(432) Asadi, M.; Kim, K.; Liu, C.; Addepalli, A. V.; Abbasi, P.; Yasaei, P.; Phillips, P.; Behranginia, A.; Cerrato, J. M.; Haasch, R.; Zapol, P.; Kumar, B.; Klie, R. F.; Abiade, J.; Curtiss, L. A.; Salehi-Khojin, A. *Science* **2016**, *353*, 467.

(433) Bonin, J.; Maurin, A.; Robert, M. *Coord. Chem. Rev.* **2017**, *334*, 184.

(434) Bodner, M.; Hofer, A.; Hacker, V. *Wiley Interdiscip. Rev.: Energy Environ.* **2015**, *4*, 365.

(435) Kim, J.-H.; Youn, D. H.; Kawashima, K.; Lin, J.; Lim, H.; Mullins, C. B. *Appl. Catal., B* **2018**, *225*, 1.

(436) Subbaraman, R.; Tripkovic, D.; Chang, K.-C.; Strmcnik, D.; Paulikas, A. P.; Hirunsit, P.; Chan, M.; Greeley, J.; Stamenkovic, V.; Markovic, N. M. *Nat. Mater.* **2012**, *11*, 550.

(437) Smith, R. D. L.; Prevot, M. S.; Fagan, R. D.; Trudel, S.; Berlinguette, C. P. *J. Am. Chem. Soc.* **2013**, *135*, 11580.

(438) Smith, R. D. L.; Prévot, M. S.; Fagan, R. D.; Zhang, Z.; Sedach, P. A.; Siu, M. K. J.; Trudel, S.; Berlinguette, C. P. *Science* **2013**, *340*, 60.

(439) Swierk, J. R.; Klaus, S.; Trotochaud, L.; Bell, A. T.; Tilley, T. D. *J. Phys. Chem. C* **2015**, *119*, 19022.

(440) Zhao, Z.; Wu, H.; He, H.; Xu, X.; Jin, Y. *J. Mater. Chem. A* **2015**, *3*, 7179.

(441) Zhang, D.; Meng, L.; Shi, J.; Wang, N.; Liu, S.; Li, C. *Electrochim. Acta* **2015**, *169*, 402.

(442) Gong, M.; Dai, H. *Nano Res.* **2015**, *8*, 23.

(443) Merrill, M. D.; Dougherty, R. C. *J. Phys. Chem. C* **2008**, *112*, 3655.

(444) Zhang, B.; Zheng, X.; Voznyy, O.; Comin, R.; Bajdich, M.; García-Melchor, M.; Han, L.; Xu, J.; Liu, M.; Zheng, L.; García de Arquer, F. P.; Dinh, C. T.; Fan, F.; Yuan, M.; Yassitepe, E.; Chen, N.; Regier, T.; Liu, P.; Li, Y.; De Luna, P.; Janmohamed, A.; Xin, H. L.; Yang, H.; Vojvodic, A.; Sargent, E. H. *Science* **2016**, *352*, 333.

(445) Friebel, D.; Louie, M. W.; Bajdich, M.; Sanwald, K. E.; Cai, Y.; Wise, A. M.; Cheng, M. J.; Sokaras, D.; Weng, T. C.; Alonso-Mori, R.; Davis, R. C.; Bargar, J. R.; Nørskov, J. K.; Nilsson, A.; Bell, A. T. *J. Am. Chem. Soc.* **2015**, *137*, 1305.

(446) Lu, Z.; Qian, L.; Tian, Y.; Li, Y.; Sun, X.; Duan, X. *Chem. Commun.* **2016**, *52*, 908.

(447) Saiah, F. B. D.; Su, B.-L.; Bettahar, N. *J. Hazard. Mater.* **2009**, *165*, 206.

(448) Zhou, L.; Huang, X.; Chen, H.; Jin, P.; Li, G.; Zou, X. *Dalton Trans.* **2015**, *44*, 11592.

(449) Ruano-Casero, R. J.; Pérez-Bernal, M. E.; Rives, V. *Z. Anorg. Allg. Chem.* **2005**, *631*, 2142.

(450) Grosvenor, A. P.; Kobe, B. A.; Biesinger, M. C.; McIntyre, N. S. *Surf. Interface Anal.* **2004**, *36*, 1564.

(451) Kim, M. S.; Kim, K. B. *J. Electrochem. Soc.* **1998**, *145*, 507.

(452) Li, X.; Walsh, F. C.; Pletcher, D. *Phys. Chem. Chem. Phys.* **2011**, *13*, 1162.

(453) Trotochaud, L.; Young, S. L.; Ranney, J. K.; Boettcher, S. W. *J. Am. Chem. Soc.* **2014**, *136*, 6744.

(454) Bates, M. K.; Jia, Q.; Doan, H.; Liang, W.; Mukerjee, S. *ACS Catal.* **2016**, *6*, 155.

(455) Zou, S. H.; Burke, M. S.; Kast, M. G.; Fan, J.; Danilovic, N.; Boettcher, S. W. *Chem. Mater.* **2015**, *27*, 8011.

(456) Castro, E. B.; Gervasi, C. A. *Int. J. Hydrog. Energy* **2000**, *25*, 1163.

(457) Yeo, B. S.; Bell, A. T. *J. Phys. Chem. C* **2012**, *116*, 8394.

(458) Gao, M.; Sheng, W.; Zhuang, Z.; Fang, Q.; Gu, S.; Jiang, J.; Yan, Y. *J. Am. Chem. Soc.* **2014**, *136*, 7077.

(459) Lewis, N. S. *Science* **2016**, *351*, 353.

(460) O'Regan, B.; Gratzel, M. *Nature* **1991**, *353*, 737.

(461) Grätzel, M. *Nature* **2001**, *414*, 338.

(462) Walter, M. G.; Warren, E. L.; McKone, J. R.; Boettcher, S. W.; Mi, Q.; Santori, E. A.; Lewis, N. S. *Chem. Rev.* **2010**, *110*, 6446.

(463) Tachibana, Y.; Vayssieres, L.; Durrant, J. R. *Nature Photonics* **2012**, *6*, 511.

(464) Yang, J.; Wang, D.; Han, H.; Li, C. *Acc. Chem. Res.* **2013**, *46*, 1900.

(465) Schultz, D. M.; Yoon, T. P. *Science* **2014**, *343*, 985.

(466) Han, X.-B.; Zhang, Z.-M.; Zhang, T.; Li, Y.-G.; Lin, W.; You, W.; Su, Z.-M.; Wang, E.-B. *J. Am. Chem. Soc.* **2014**, *136*, 5359.

(467) Moniz, S. J. A.; Shevlin, S. A.; Martin, D. J.; Guo, Z.-X.; Tang, J. *Energy Environ. Sci.* **2015**, *8*, 731.

(468) Hisatomi, T.; Kubota, J.; Domen, K. *Chem. Soc. Rev.* **2014**, *43*, 7520.

(469) Higashi, T.; Kaneko, H.; Minegishi, T.; Kobayashi, H.; Zhong, M.; Kuang, Y.; Hisatomi, T.; Katayama, M.; Takata, T.; Nishiyama, H.; Yamada, T.; Domen, K. *Chem. Commun.* **2017**, *53*, 11674.

(470) Liu, X.; Wang, F.; Wang, Q. *Phys. Chem. Chem. Phys.* **2012**, *14*, 7894.

(471) Wang, S.; Chen, P.; Yun, J. H.; Hu, Y.; Wang, L. *Angew. Chem.* **2017**, *129*, 8620.

(472) Wang, Q.; Hisatomi, T.; Jia, Q.; Tokudome, H.; Zhong, M.; Wang, C.; Pan, Z.; Takata, T.; Nakabayashi, M.; Shibata, N.; Li, Y.; Sharp, I. D.; Kudo, A.; Yamada, T.; Domen, K. *Nat. Mater.* **2016**, *15*, 611.

(473) Liu, Q.; Ding, D.; Ning, C.; Wang, X. *Int. J. Hydrog. Energy* **2015**, *40*, 2107.

(474) Asahi, R.; Morikawa, T.; Ohwaki, T.; Aoki, K.; Taga, Y. *Science* **2001**, *293*, 269.

(475) Goto, Y.; Seo, J.; Kumamoto, K.; Hisatomi, T.; Mizuguchi, Y.; Kamihara, Y.; Katayama, M.; Minegishi, T.; Domen, K. *Inorg. Chem.* **2016**, *55*, 3674.

(476) Qin, Y.; Peng, Q. *Int. J. Photoenergy* **2012**, *2012*, 21.

(477) Ji, S.; Wu, W.; Wu, W.; Song, P.; Han, K.; Wang, Z.; Liu, S.; Guo, H.; Zhao, J. *J. Mater. Chem.* **2010**, *20*, 1953.

(478) Kohle, O.; Grätzel, M.; Meyer, A. F.; Meyer, T. B. *Adv. Mater.* **1997**, *9*, 904.

(479) Takizawa, S.; Aboshi, R.; Murata, S. *Photochem. Photobiol. Sci.* **2011**, *10*, 895.

(480) Evans, R. C.; Douglas, P.; Winscom, C. J. *Coord. Chem. Rev.* **2006**, *250*, 2093.

(481) Caspar, J. V.; Meyer, T. J. *Inorg. Chem.* **1983**, *22*, 2444.

(482) Burian, M.; Syrgiannis, Z.; La Ganga, G.; Puntoriero, F.; Natali, M.; Scandola, F.; Campagna, S.; Prato, M.; Bonchio, M.; Amenitsch, H.; Sartorel, A. *Inorg. Chim. Acta* **2017**, *454*, 171.

(483) Alibabaei, L.; Dillon, R. J.; Reilly, C. E.; Brennaman, M. K.; Wee, K.-R.; Marquard, S. L.; Papanikolas, J. M.; Meyer, T. J. *ACS Appl. Mater. Interfaces* **2017**, *9*, 39018.

(484) Surendranath, Y.; Kanan, M. W.; Nocera, D. G. *J. Am. Chem. Soc.* **2010**, *132*, 16501.

(485) Shul, G.; Weissmann, M.; Bélanger, D. *Electrochim. Acta* **2015**, *162*, 146.

(486) Nguyen, V. Q.; Sun, X.; Lafolet, F.; Audibert, J.-F.; Miomandre, F.; Lemercier, G.; Loiseau, F.; Lacroix, J.-C. *J. Am. Chem. Soc.* **2016**, *138*, 9381.

(487) Agnes, C.; Arnault, J.-C.; Omnes, F.; Jousselme, B.; Billon, M.; Bidan, G.; Mailley, P. *Phys. Chem. Chem. Phys.* **2009**, *11*, 11647.

(488) Piper, D. J. E.; Barbante, G. J.; Brack, N.; Pigram, P. J.; Hogan, C. F. *Langmuir* **2011**, *27*, 474.

(489) deKrafft, K. E.; Wang, C.; Xie, Z.; Su, X.; Hinds, B. J.; Lin, W. *ACS Appl. Mater. Interfaces* **2012**, *4*, 608.

(490) Yeşildağ, A.; Ekinci, D. *Electrochim. Acta* **2010**, *55*, 7000.

(491) Shul, G.; Weissmann, M.; Bélanger, D. *Langmuir* **2014**, *30*, 6612.

(492) Caspar, J. V.; Meyer, T. J. *Inorg. Chem.* **1983**, *22*, 2444.

(493) Schmid, B.; Garces, F. O.; Watts, R. J. *Inorg. Chem.* **1994**, *33*, 9.

(494) Dragonetti, C.; Falciola, L.; Mussini, P.; Righetto, S.; Roberto, D.; Ugo, R.; Valore, A.; De Angelis, F.; Fantacci, S.; Sgamellotti, A.; Ramon, M.; Muccini, M. *Inorg. Chem.* **2007**, *46*, 8533.

(495) Kim, J. I.; Shin, I.; Kim, H.; Lee, J. *J. Am. Chem. Soc.* **2005**, *127*, 1614.

(496) Liu, G.; Klein, A.; Thissen, A.; Jaegermann, W. *Surf. Sci.* **2003**, *539*, 37.

(497) Lund, T.; Nguyen, P. T.; Ruhland, T. *J. Electroanal. Chem.* **2015**, *758*, 85.

(498) Tang, H.; Li, Y.; Chen, Q.; Chen, B.; Qiao, Q.; Yang, W.; Wu, H.; Cao, Y. *Dyes Pigm.* **2014**, *100*, 79.

(499) Yu, X.-M.; Kwok, H.-S.; Wong, W.-Y.; Zhou, G.-J. *Chem. Mater.* **2006**, *18*, 5097.

(500) Wong, W. Y.; Zhou, G. J.; Yu, X. M.; Kwok, H. S.; Lin, Z. *Adv. Funct. Mater.* **2007**, *17*, 315.

(501) Li, M.; Zhou, X.; Xia, B.; Zhang, H.; Pan, Q.; Liu, T.; Fu, H.; Sun, C. C. *Inorg. Chem.* **2008**, *47*, 2312.

(502) Felcmann, C.; Alt, R.; Greiner, G.; Rau, H.; Worner, M. *Phys. Chem. Chem. Phys.* **2000**, *2*, 3483.

(503) Sabuzi, F.; Tiravia, M.; Vecchi, A.; Gatto, E.; Venanzi, M.; Floris, B.; Conte, V.; Galloni, P. *Dalton Trans.* **2016**, *45*, 14745.

(504) Brennaman, M. K.; Patrocinio, A. O. T.; Song, W.; Jurss, J. W.; Concepcion, J. J.; Hoertz, P. G.; Traub, M. C.; Murakami Iha, N. Y.; Meyer, T. J. *ChemSusChem* **2011**, *4*, 216.

(505) Gillaizeau-Gauthier, I.; Odobel, F.; Alebbi, M.; Argazzi, R.; Costa, E.; Bignozzi, C. A.; Qu, P.; Meyer, G. J. *Inorg. Chem.* **2001**, *40*, 6073.

(506) Chen, Z.; Concepcion, J. J.; Jurss, J. W.; Meyer, T. J. *J. Am. Chem. Soc.* **2009**, *131*, 15580.

(507) Pellegrin, Y.; Odobel, F. *Comptes Rendus Chimie* **2017**, *20*, 283.

(508) Quan, M.; Sanchez, D.; Wasylkiw, M. F.; Smith, D. K. *J. Am. Chem. Soc.* **2007**, *129*, 12847.

(509) Cline, E. D.; Adamson, S. E.; Bernhard, S. *Inorg. Chem.* **2008**, *47*, 10378.

(510) Gallagher, L. A.; Serron, S. A.; Wen, X.; Hornstein, B. J.; Dattelbaum, D. M.; Schoonover, J. R.; Meyer, T. J. *Inorg. Chem.* **2005**, *44*, 2089.

(511) Dragonetti, C.; Valore, A.; Colombo, A.; Righetto, S.; Trifiletti, V. *Inorg. Chim. Acta* **2012**, *388*, 163.

(512) Xu, S.; Zhou, C.; Yang, Y.; Hu, H.; Sebo, B.; Chen, B.; Tai, Q.; Zhao, X. *Energy Fuels* **2011**, *25*, 1168.

(513) Sprouse, S.; King, K. A.; Spellane, P. J.; Watts, R. J. *J. Am. Chem. Soc.* **1984**, *106*, 6647.

(514) Liu, Y.; Turner, D. B.; Singh, T. N.; Angeles-Boza, A. M.; Chouai, A.; Dunbar, K. R.; Turro, C. *J. Am. Chem. Soc.* **2009**, *131*, 26.